CAVITATION AND WAKE STRUCTURE OF UNSTEADY TIP VORTEX FLOWS

Thesis by
Douglas P. Hart
Division of Engineering and Applied Science

In Partial Fulfillment
of the Requirements for the Degree of
Doctor of Philosophy

California Institute of Technology
Pasadena, California 91125
1993
(Submitted November 10, 1992)

ACKNOWLEDGMENTS

The thrown pebble's ring
widening in the still pond
at last reaches shore.
---- C. J. Hart

I would like to express my deepest graditude to my advisors, Professor Allan Acosta and Professor Christopher Brennen. Their professional and personal guidance made the completion of this work possible. Furthermore, I would like to thank the members of my defense committee including, Professors Anthony Leonard, Fred Raichlen, and Joel Burdick.

This thesis relied heavily upon the professional staff of Caltech, and I thank all those people that contributed. I would especially like to thank Marty Gould for his expert machining and advice, and Cecilia Lin for her help in preparation of figures. I would also like to express my graditude to Jackie Beard and Dana Young for their support and encouragement.

I gratefully acknowledge the help of my fellow graduate students, especially Elizabeth McKenney, Steven Ceccio, Yan Kuhn de Chizelle, and Sanjay Kumar. I would also like to acknowledge the numerous undergraduates who have assisted in this work with special thanks to Celina Mikolajczak, Anna Yeakley, and Anthea Howell.

Funding for this work was provided by the Office of Naval Research under contract number N00167-85-K-0165, Technical Monitor J. Fein . This support and support from the General Electric Foundation for my first year at the California Institute of Technology is gratefully acknowledged.

I thank my wife, Anne, and my family for their invaluable patience and encouragement. I dedicate this thesis to my grandfather Clarence J. Hart who passed away while I was in the final throes of completing my graduate studies. He was the only true intellectual I have ever known. I will miss him dearly.

ABSTRACT

Unsteady flows are prevalent in virtually every fluid application yet, because of their intrinsic complexity, few attempts have been made to measure them or explain their behavior. This thesis presents an experimental study of one of the simplest unsteady flow induced effects, the periodic change in angle of attack of a lifting surface. Of particular interest is the influence this effect has on the tip vortex structure of a finite aspect ratio hydrofoil and the part it plays in the inception of cavitation.

An aspect ratio 2.3 hydrofoil was reflection-plane mounted to the test section floor of the Caltech Low Turbulence Water Tunnel and harmonically oscillated in pitch near its center of pressure. Observations of the growth and collapse of surface and tip vortex cavitation were made along with detailed observations of the interaction of the tip vortex formation with the spanwise wake structure. Measurements of the cavitation inception number for surface cavitation and tip vortex cavitation were made relative to the phase of the hydrofoil and the reduced frequency, $k=\omega c/2U_\infty$, of oscillation. Studies of the oscillation-induced spanwise trailing vortex structures and the Kármán vortex street generated by the boundary layer were made of a two-dimensional hydrofoil. Laser Doppler Velocimetry (LDV) measurements were taken of the tip vortex velocity profile and the flow at the trailing edge of both the two- and the three-dimensional hydrofoils at reduced frequencies ranging from 0.5 to 2.0. Dynamic changes in bound circulation and shed vorticity in the streamwise and spanwise directions relative to the freestream were calculated from these measurements at three locations along the span of the foil. The results of these measurements are compared to theoretical flow calculations and related to measurements of the cavitation inception number in the tip vortex region of the three-dimensional foil.

TABLE OF CONTENTS

Contents *Page*

Contents *Page*

NOMENCLATURE

δ = Boundary layer thickness, *m*

σ = Cavitation number = $(p - p_v)/(\frac{1}{2}\rho U_\infty^2)$

σ_i = Cavitation inception index = $(p_i - p_v)/(\frac{1}{2}\rho U_\infty^2)$

Γ = Circulation = $\oint_C \bar{u} \cdot d\bar{y}$, m^2/s

Γ_B = Bound circulation, m^2/s

μ = Dynamic viscosity, kg/ms

ρ = Fluid density, kg/m^3

α = Hydrofoil angle of attack, *degrees*

ω = Hydrofoil excitation frequency, *rad/s*

ϕ = Hydrofoil phase angle, *degrees*

γ = Vorticity = $\nabla \times \bar{u}$, *rad/s*

λ = Wave-length, *m*

$\Delta\alpha$ = Hydrofoil oscillation amplitude, *degrees*

α_m = Hydrofoil mean angle of attack, *degrees*

A = Hydrofoil surface area, m^2

AR = Aspect ratio = 2s/c

c = Hydrofoil chord length, 0.152*m* (6*in*)

C(k) = Theodorsen's lift deficiency factor

C_D = Drag coefficient of three-dimensional foil

C_d = Drag coefficient of two-dimensional foil

C_L = Lift coefficient of three-dimensional foil

C_l = Lift coefficient of two-dimensional foil

C_p = Pressure coefficient = $(p - p_o)/(\frac{1}{2}\rho U_\infty^2)$

DAC = Dissolved air content, *ppm*

Nomenclature (cont'd)

$d\Gamma/dy$ = Rate of change of bound circulation, *m/s*

f = Excitation frequency, *Hz*

F = Force, *N*

g = Gravitational acceleration, m/s^2

Hz = Hertz, s^{-1}

k = Reduced frequency = $\omega c/2U_\infty$

L = Lift, *N*

LDV = Laser Doppler Velocimetry

L_Q = Quasi-steady lift, *N*

LTWT = Low Turbulence Water Tunnel

PDA = Particle Diameter Analyzer

p_o = LTWT test section pressure, *kPa*

ppm = Parts-per-million

p_v = Water vapor pressure, *kPa*

Re = Reynolds number = $\rho U_\infty c/\mu$

s = Semispan of foil, *m*

St = Strouhal number = fc/U_∞

t = Time, *s*

u = Flow velocity in streamwise direction, *m/s*

U_∞ = LTWT test section velocity, *m/s*

U_θ = Velocity tangential to vortex core, *m/s*

v = Flow velocity in spanwise direction, *m/s*

w = Flow velocity perpendicular to foil, *m/s*

x = Downstream distance from leading edge, *m*

y = Spanwise distance from foil root, *m*

z = Distance orthogonal to x-y plane, *m*

Nomenclature (cont'd)

Subscripts

u_∞ = Far field

u_D = Drag

u_d = Desinence condition

u_g = Gas

u_{LO} = Zero lift condition

u_{max} = Maximum

u_{min} = Minimum

u_p = Pressure side

u_s = Suction side

u_{sp} = Spanwise

u_{st} = Streamwise

u_{tv} = Tip vortex

Superscripts

$\vec{u}$ = Vector quantity

u' = Fluctuating quantity

$u*$ = Non-dimensionalized quantity

$\dot{u}$ = Derivative with respect to time

$\overline{u}$ = Time averaged quantity

LIST OF FIGURES

Figure *Page*

Figure *Page*

Figure *Page*

Figure *Page*

Figure *Page*

Figure *Page*

Figure *Page*

LIST OF TABLES

CHAPTER 1

INTRODUCTION

All things come into being by necessity, the cause of the coming into being of all things being the vortex, which Democritus calls "law of nature."

----Diogenes Laertius

1.1 Motivation and Background

The study of streamlined lifting surfaces, critical to the technological advancement of virtually every type of fluid-based device, is one of the cardinal research topics of fluid dynamics. The bulk of the theoretical, numerical, and experimental accomplishments to date, however, has dealt with steady flows, despite the fact that nearly every real-world application involves highly unsteady, nonlinear fluid behavior. Unsteady flows, as intricate as they are fascinating, have until recently remained out of reach, except through the crudest of models. With the advent of powerful tools and innovative techniques for computation and instrumentation, significant progress is now possible in the investigation of these flows.

As summarized by McCroskey [1982], research on unsteady flows over streamlined lifting surfaces has primarily been directed by efforts to understand undesirable effects such as flutter, vibration, buffeting, gust response, dynamic stall, and cavitation. Some attention has also been given to understanding the beneficial effects of unsteadiness such as the flapping propulsion of birds and fish, controlled periodic vortex generation, stall delay, and to improving the performance of turbomachinery, helicopter rotors, and wind turbines. The studies presented in this thesis, while

primarily motivated by a desire to understand the intricacies of the general behavior of unsteady flows, were directed by an interest in a phenomenon observed in the performance of propellers rotating in ship wakes.

Propellers typically encounter fluctuations in the freestream due to disturbances generated by the hull of the vessel being propelled. As Figure 1.1 illustrates, each blade of the propeller experiences a periodic fluctuation in flow velocity as it rotates in and out of the wake. These fluctuations result in a change in angle of attack of the blade as well as an apparent heaving motion (see Figure 1.2). This often results in premature cavitation in the tip vortex region and across the surface of the propeller, leading to increased noise and erosion of the propeller as well as a loss in thrust. Virtually all high-performance rotating machinery as well as devices such as valves and turning vanes operating in unsteady conditions encounter similar problems. Thus, a basic understanding of unsteady flow on lifting surfaces is important and often critical in the design of fluid-based equipment and equipment dependent on fluid-based machinery.

Theoretical studies of unsteady flows began in the early 1930's. Among the best known and more perceptive analyses are those by Theodorsen [1935] and von Kàrmàn and Sears [1938], who studied the periodic oscillation of a two-dimensional flat plate. They showed that the fluid dynamic phenomena associated with this problem are characterized by a non-dimensional frequency parameter, $k=\omega c/2U_\infty$, and that the solution can be expressed in terms of standard Bessel functions whose argument is k. Experimental studies have been conducted as well (For example: [Abramson, Chu, Irick 1967; Acosta, Delong 1971; DeLaurier, Harris 1981; Koochesfahani 1989. Shen, Gowing 1986]). Like the majority of theoretical analyses, however, most of

this research has concentrated on the simpler case of unsteady flow on two-dimensional lifting surfaces.

In recent years, numerical work on unsteady flow problems has met with varying degrees of success (Figure 1.3) [Chen, Sheu 1989; Spalart, Leonard 1981; Spalart 1985; Zabusky 1989]. Often, it is a lack of experimental data for comparison that has hindered the progress of these analyses. Without this data, there is no basis for determining the accuracy of codes nor is there guidance for their development.

The experimental studies presented in this thesis provide a basic understanding of the effects of unsteady flow on three-dimensional lifting surfaces as well as useful data for the development of unsteady numerical codes. The following sections, Sections 1.2 and 1.3, present a brief introduction to the behavior of the type of three-dimensional lifting surface flows studied in the present work and how unsteady freestream conditions affect this behavior.

1.2 Nature of Tip Vortex Flows

The primary characteristic that distinguishes flow over a two-dimensional, or infinite aspect ratio, lifting surface from that over a lifting surface of finite aspect ratio is that the latter must consider flow traversing over the end of the surface from the pressure side to the suction side. As fluid passes over the end, it forms a vortex emanating from the tip and extending far downstream. This *tip vortex flow* drastically alters the characteristics of the lifting surface and requires more complicated mathematics and more sophisticated instrumentation in its study than the two-dimensional surface flow. To understand the added effect of unsteadiness in these already

complex flows, an understanding of the fundamentals of tip vortex flows under steady conditions is necessary.

Tip vortex flows historically have been of interest in the aerodynamics of flight and propulsion because of their connection to aerodynamic theory and because of the profound effects strong trailing vortices have on the surrounding flow, as many studies have documented. In hydrodynamic applications an additional phenomenon must be considered, as the core of the tip vortex may sustain a pressure low enough to cause cavitation with its consequent effects of hydrodynamic noise and erosion (see Figure 1.4).

While much is still unknown about the nature of tip vortex flows, considerable advancements have been made since the early days of fluid dynamics. The extension of knowledge of the relatively well understood two-dimensional flows into three dimensions is often a complex process. Lanchester in 1907, however, grasped the essence of lift on a three-dimensional surface when he proposed the *Lifting-Line Model.* This insightful explanation of tip vortex flows was later put into mathematical form by Prandtl in 1918.

Consider a finite wing or foil, such as the one shown in Figure 1.5, at a positive angle of attack α relative to the freestream. As the wing begins to accelerate from rest, a circulation Γ develops around the wing, resulting in a force component in the lift direction as well as a component in the drag direction. A vortex forms and is left behind as the wing moves forward. This *starting* vortex induces a circulation in the flow equal but opposite to the circulation around the foil, such that the net circulation in the flow as a whole remains zero. As Lanchester illustrated, the circulation around the wing can be modeled as the result of a number of horseshoe vortices, Figure 1.6. A

point in the wake of this vortex system experiences a velocity component in the direction from the suction side of the wing to the pressure side, Figure 1.7. This velocity component is commonly referred to as the *downwash*, ω_i, of the wing and results in an effective change in the angle of attack, as shown in Figure 1.8. Along the span of the wing, the local effective angle of attack is $\alpha_e = \alpha - \alpha_i - \alpha_{LO}$ where α is the geometric angle of attack of the wing relative to a line from the leading-edge to the trailing-edge, α_{LO} is the angle of zero lift due to asymmetry (camber) of the foil, and α_i is the angle resulting from the downwash due to the trailing vortex system. For high aspect ratio, elliptically loaded wings at small angles of attack, the lifting-line model predicts (as shown in [Kundu 1990]) a bound circulation of

$$\Gamma_B = \frac{\pi c U_\infty}{1+2/AR}(\alpha - \alpha_{LO}) \tag{1.1}$$

a lift coefficient of

$$C_L = \frac{2\pi}{1+2/AR}(\alpha - \alpha_{LO}) \equiv C_{L_\alpha}(\alpha - \alpha_{LO}) \tag{1.2}$$

and an induced drag coefficient of

$$C_{D_i} = \frac{1}{\pi AR} C_L^2. \tag{1.3}$$

These results, because of their simplicity and connection to the fundamental concepts of lift, have become the basis for which the performance of lifting surfaces are often compared.

Most three-dimensional lifting surfaces develop a strong gradient in the circulation, $|d\Gamma/ds|$, near the tip. This gradient is the result of flow over the tip from the pressure side of the wing to the suction side deflecting the streamlines passing over the foil – toward the tip on the suction side, and

away from the tip on the pressure side. Owing to the induced downwash velocity in the wake, the wake flow rolls up to form a concentrated vortex near the tip. This *tip vortex*, as can be seen in Figure 1.9, is a prominent feature of three-dimensional lifting surface flows. Tip vortices can be quite strong on high lift devices; they are often the primary source of noise and loss in performance of fluid-based machinery. More importantly, they are a disturbance in the flow that does not dissipate quickly, potentially influencing all mechanisms operating in their wake.

1.3 Effects of Unsteady Flow

> *Before our eyes opens forth now the splendid prospect of three-dimensional kinematics, the mother tongue for man's perception of the changing world about him. It is the vorticity vector, for whose existence it is both requisite and sufficient that the number of dimensions be three.*
>
> ---- C. Truesdell

Unsteady flow drastically complicates the wake structure generated by three-dimensional lifting surfaces. No longer can the wake be modeled as a simple horseshoe vortex structure with the tip vortices linking to a starting vortex. Even the simplest of unsteady flows results in a highly complex three-dimensional vortex formation.

Unsteady flows encountered by lifting surfaces can be grouped into a few general categories. As shown in Figure 1.10, these flows, from the frame of reference of the freestream, include lateral or vertical heaving of the lifting surface, incremental changes in angle of attack, periodic pitching or heaving, as well as combinations of these motions. Perhaps the best illustration of how these flows affect the performance of a finite aspect ratio lifting surface can be

seen in the wake of a wing experiencing a flow that induces a periodic change in angle of attack (this type of unsteady flow is of great concern in problems such as control surface flutter and wake cutting). The periodic change in angle of attack of a finite wing results in the formation of two vortex systems, Figure 1.11. As the angle of attack — and thus the circulation around the wing — increases, a pair of spanwise vortices are shed with a circulation around this pair equal in strength but opposite to the change in circulation around the wing. This vortex formation is in essence a *starting* vortex, except that the circulation around this formation is equal to the *change* in circulation rather than the *total* circulation around the wing. The total circulation about the wing at any given instant is then equal to the original starting vortex plus the sum of the periodic shed vorticity. As the wing decreases in angle of attack and the circulation about the wing decreases, another spanwise vortex pair is shed – an *ending* vortex. The circulation around this formation is equal but opposite to the vortex pair formed when the angle of attack of the wing was increasing. The result is a series of vortex pairs which link to each other by wrapping around the tip vortex. The total circulation around the two sets of vortex pairs is zero, corresponding to a net zero change in circulation about the wing during an oscillation cycle.

Although somewhat simplistic, this description is useful as a general outline of the trailing wake structure formation of finite wings in unsteady flow conditions. In actuality, a number of spanwise vortices roll up and link within the wake making the trailing vortex structure extremely complex as will be discussed in Chapter 4.

1.4 Scope of Present Work

The purpose of the work presented in this thesis is to analyze the effect of unsteady motion on the tip-vortex structure of a finite aspect ratio hydrofoil, and the subsequent effects upon cavitation inception in the tip vortex region. This study concentrates on a periodic sinusoidal change in incidence angle of a finite aspect ratio hydrofoil, examining in detail the full three-dimensional, unsteady oscillating lifting surface problem from an experimental perspective. For the first time, detailed observations have been made of the unsteady wake structure, and of the bound circulation and shed vorticity of an oscillating finite aspect ratio foil. These results, along with an understanding of the formation of the unsteady wake structure behind a finite aspect ratio foil in unsteady flow conditions and its effect on the inception of cavitation, are the main contributions of this thesis.

The work presented in this thesis is organized into seven chapters. Chapter 1 provides a general background on the formation of the wake structure of finite aspect ratio foils in unsteady flow, and the motivation for investigating this phenomenon. Chapter 2 describes the facilities used to conduct the experimental investigations, and Chapter 3 details the techniques used to investigate the trailing wake structure and development of tip vortex cavitation and surface cavitation. Chapter 4 discusses in detail the formation of the unsteady wake structure and factors influencing its formation. Chapter 5 discusses the effects unsteady flow has on surface and tip vortex cavitation. Chapter 6 introduces a novel technique used to measure the rate of change in circulation about the hydrofoil as it oscillates and presents the results of these measurements. Finally, Chapter 7 provides a brief summary and conclusion.

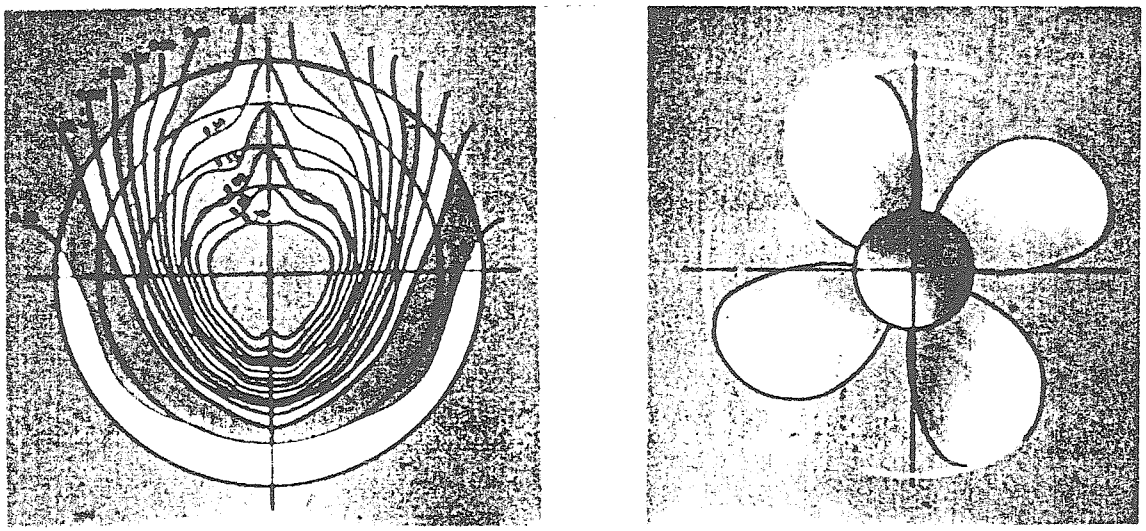

Figure 1.1 Schematic of Propeller Rotating in the Wake of a Ship
Propellers typically rotate through the turbulent boundary layer of ship wakes. The reduced freestream velocity generated by these wakes results in an oscillatory change in angle of attack over each blade of the propeller. This effect often results in premature cavitation.

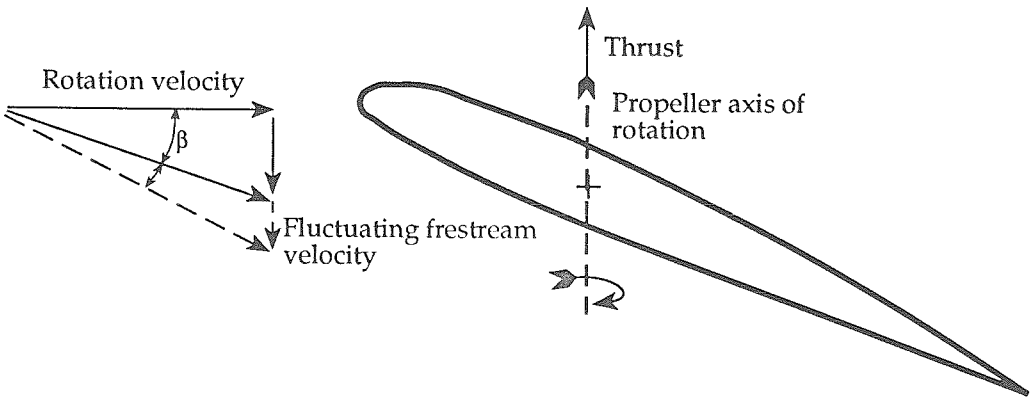

Figure 1.2 Schematic Showing Effective Change in Leading-Edge Angle of Attack

This schematic illustrates how the angle of attack of a propeller is effected by the freestream. Changes in the freestream velocity in which a propeller operates result in a change in the angle of attack of the blades of the propeller as well as a heaving motion in the direction of thrust

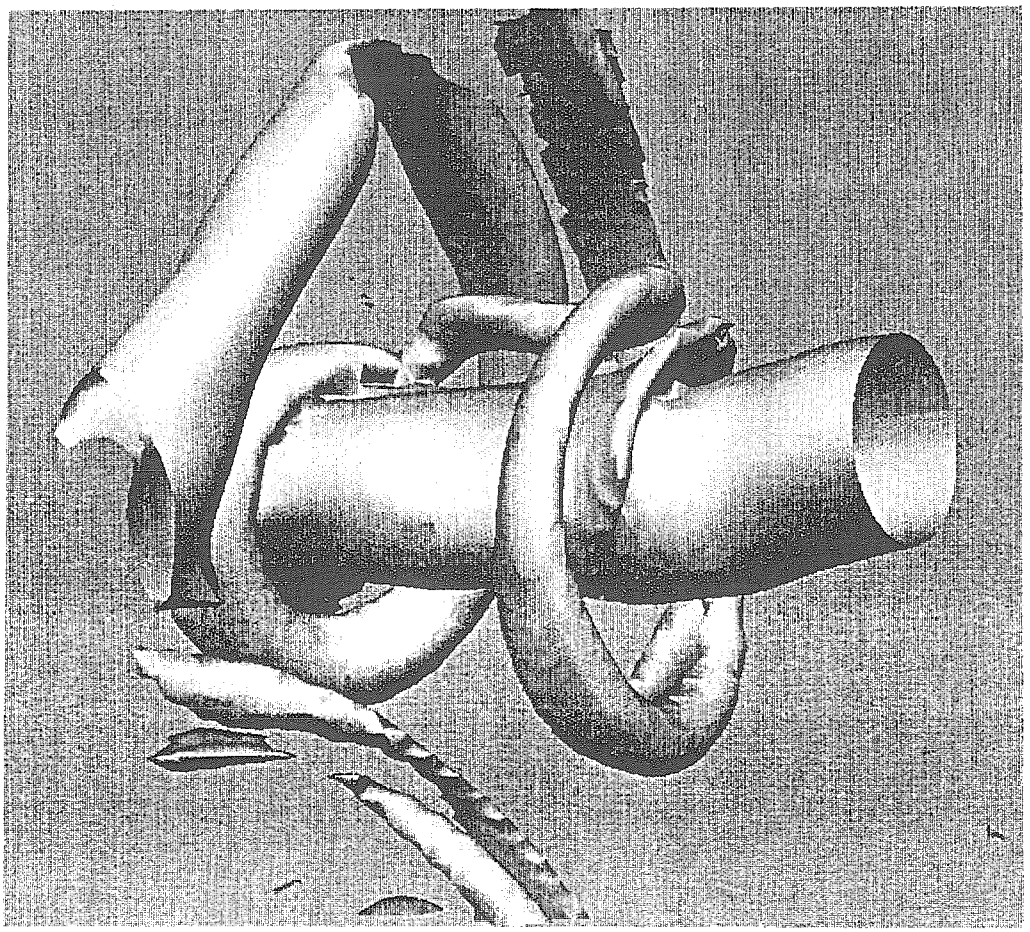

Figure 1.3 Numerical Solution of Orthogonal Vortices
This figure is an example of a numerical solution of a time dependent three-dimensional flow. It illustrates the structure of orthogonal vortices of different strengths when located in proximity to each other. The weaker vortex is stretched as it rolls into the stronger vortex. One of the difficulties in developing codes to solve these types of problems is a lack of experimental data for comparison (From Zabusky, Melander [1989]).

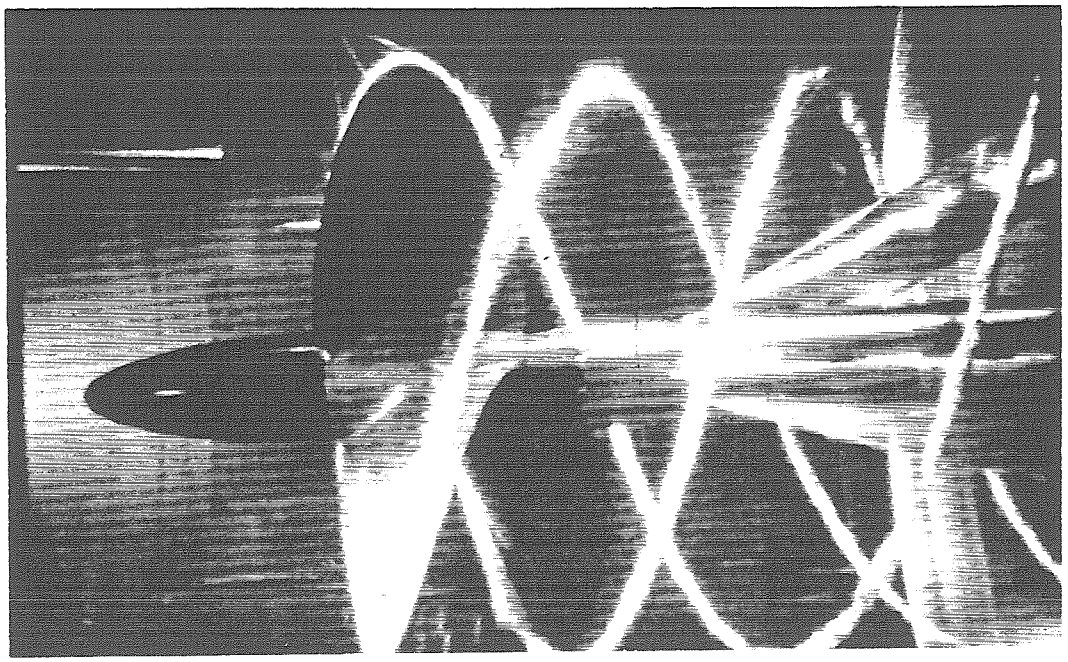

Figure 1.4 Tip Vortex Cavitation on a Propeller
Cavitation in the tip vortex region of a propeller rotating in a water tunnel generates a helical trailing wake structure. The low pressure region in the core of the tip vortex is typically the location where cavitation first initiates.

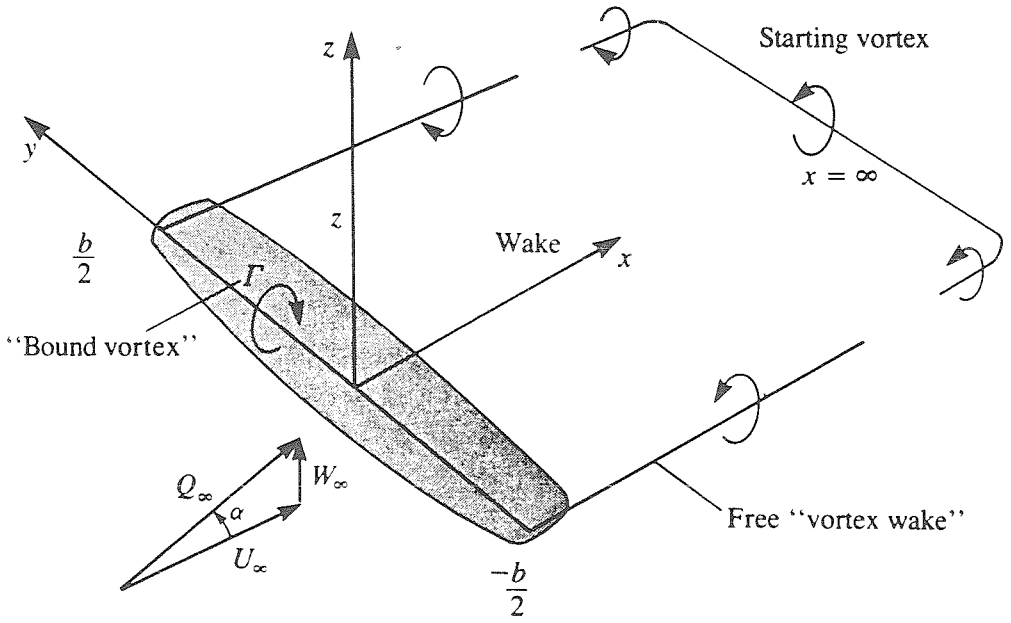

Figure 1.5 Far-Field Horseshoe Model of a Finite Wing
This figure shows a finite wing at a positive angle of attack, α, relative to the freestream. As the wing begins to accelerate from rest, a circulation, Γ, develops around the wing resulting in a force component in the lift direction as well as a component in the drag direction. A starting vortex also forms and is left behind as the wing moves forward. This vortex induces a circulation in the flow equal and opposite to the circulation around the foil such that the net circulation in the flow as a whole remains zero (From Katz and Plotkin [1991]).

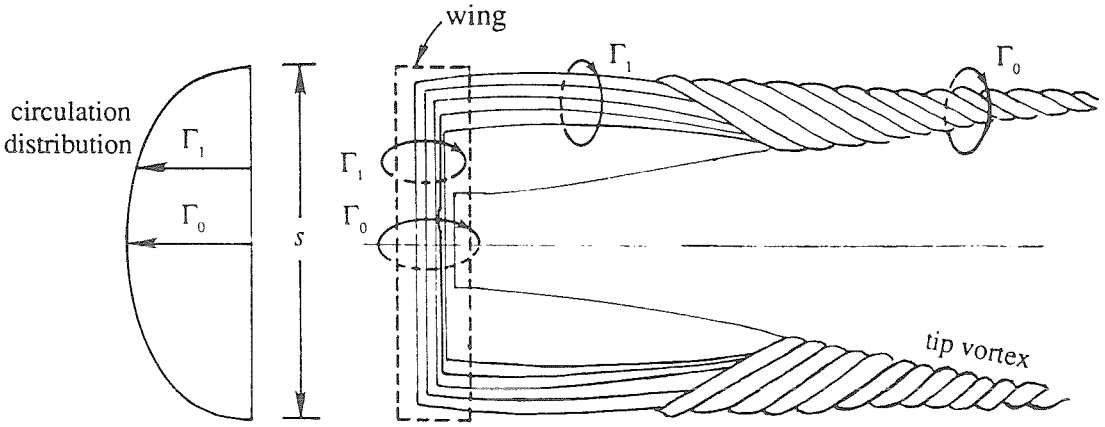

Figure 1.6 Lifting-Line Model
Horseshoe vortices distributed along the wing induce circulation around the wing. The bound vortex segment of all vortices is placed along the y axis (From Kundu [1990]).

A. Foil from bird's eye view.
B. Foil from behind.

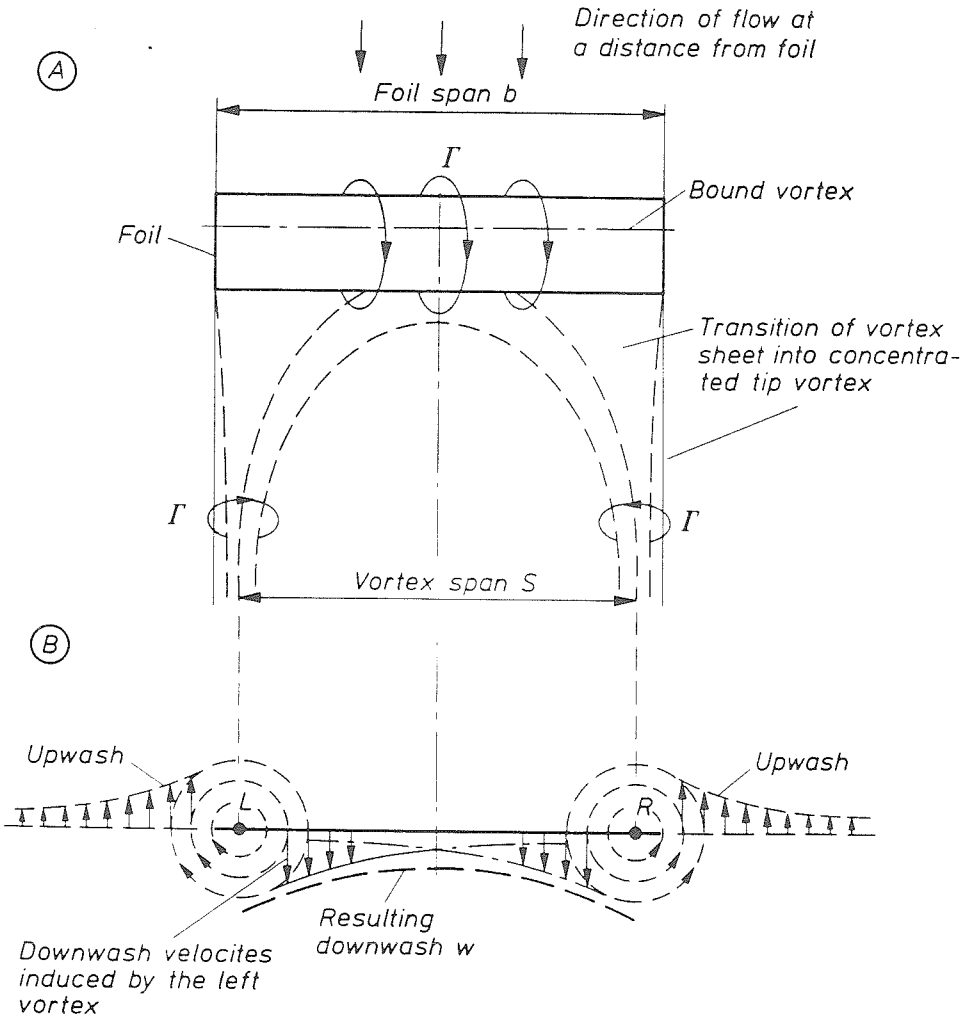

Figure 1.7 Trailing Vortex Induced Downwash
Horseshoe vortices induce a downward velocity component in the flow in the wake of a finite wing. This downward velocity component, known as the downwash of the wing, results in a decrease in the effective angle of attack (From Marchaj [1989]).

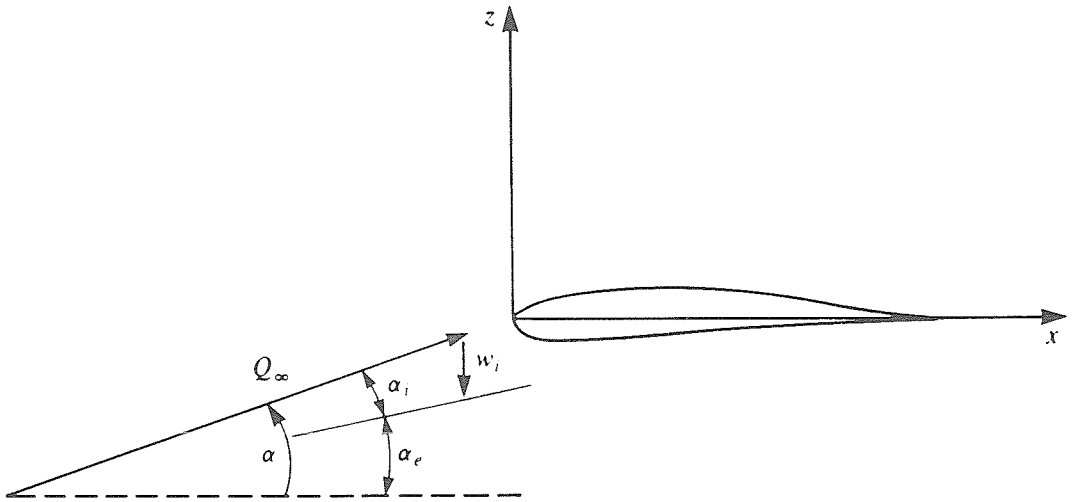

Figure 1.8 Effective Angle of Attack
The effective angle of attack of a finite wing is equal to the geometric angle of attack minus the angle of attack due to the vortex induced downwash minus the angle of attack of zero lift resulting from foil chamber (From Katz and Plotkin [1991]).

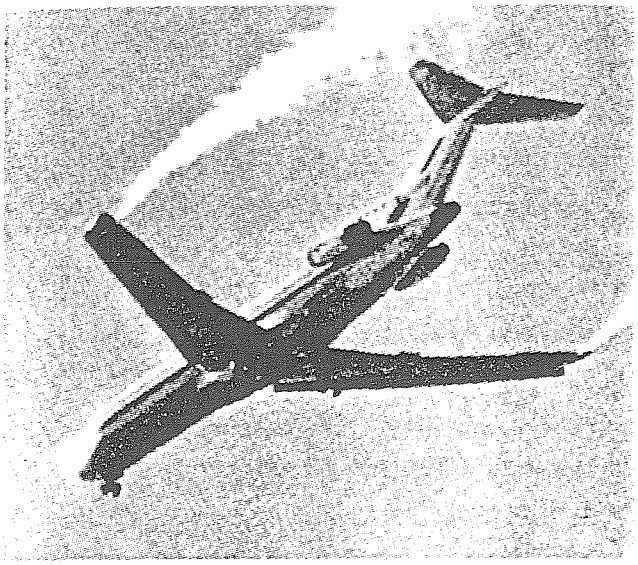

Figure 1.9 Tip Vortex Flow Visualization
Flow visualization of the tip vortices formed on an airplane wing (wing tip vortices made visible by injecting smoke at the wing tips of a Boeing 727 airplane) (From Katz and Plotkin [1991]).

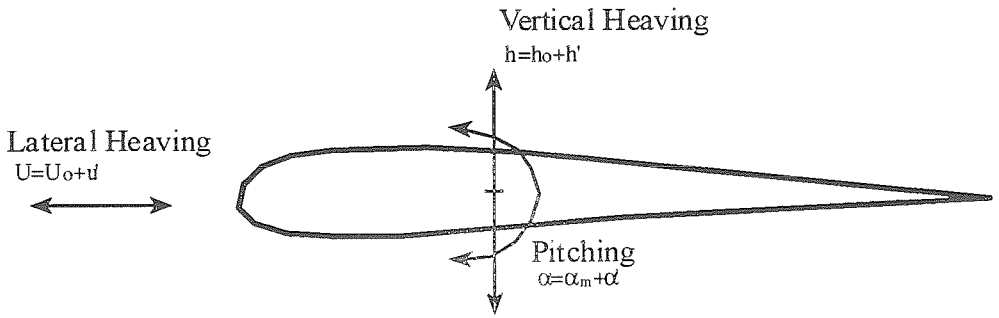

Figure 1.10 Schematic Showing Components of Unsteady Motion
There are a number of unsteady flow components which fluid-based machinery typically experience. These motions include vertical heaving, lateral heaving, pitching and combinations of these motions. The unsteady motions can be periodic, such as experienced by a propeller rotating in the wake of a ship, or they can be incremental changes such as occurs when a gust of wind passes over an aircraft wing.

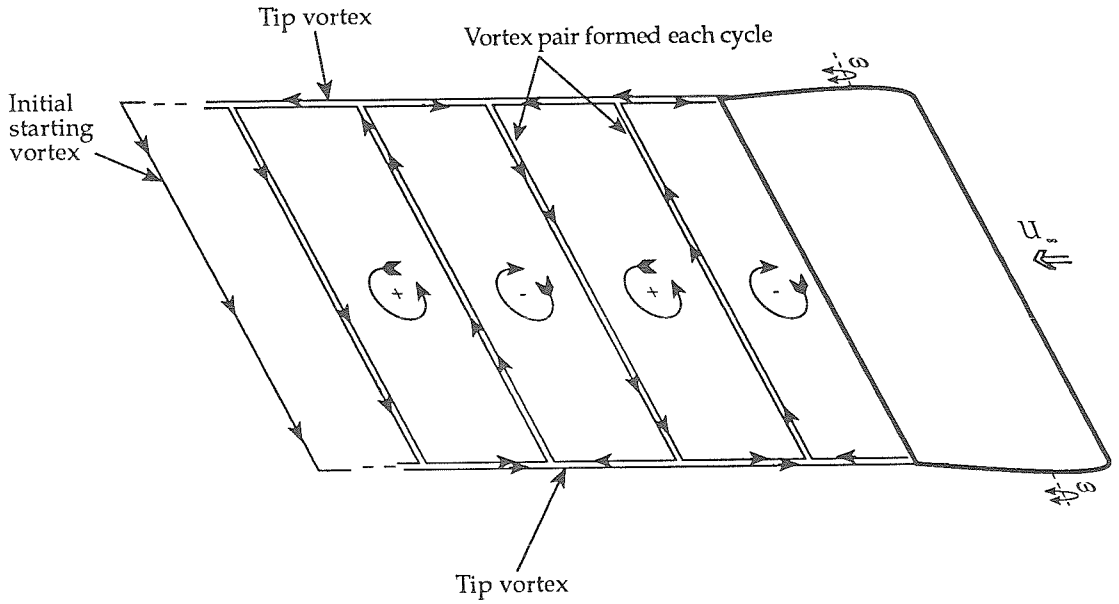

Figure 1.11 Simplified Illustration of Wake Structure Behind an Oscillating Wing

This schematic shows a simplified model of the trailing vortex structure in the wake of a finite aspect ratio oscillating wing. During each oscillation cycle a pair of spanwise vortices is formed. The net circulation around the pair is zero, corresponding to a zero net change in circulation about the hydrofoil. These spanwise vortices link to each other by wrapping around the tip vortex, which results in periodic changes in the circulation along the tip vortex.

CHAPTER 2

EXPERIMENTAL FACILITY

Described in this chapter are the equipment and facilities used to conduct the experiments presented in this document. Included in this description are details of the Caltech Low Turbulence Water Tunnel (LTWT), the hydrofoil oscillation mechanism, the two-dimensional flow setup, the LDV system, the holographic system, and the digital data recording system (most of this equipment is shown in the photograph in Figure 2.1). Specialized equipment used only in specific tests (e.g., photographic equipment, flow visualization equipment, cavitation detection equipment, etc.) is explained in Chapter 3.

2.1 Low Turbulence Water Tunnel

The Caltech Low Turbulence Water Tunnel (LTWT), described in detail by Gates [1977], is a closed-circuit facility with a 16:1 contraction ratio (see Table 2.1 and Figure 2.2). It is driven by a $14kW$ ($30hp$) DC motor at velocities up to $10m/s$. The tunnel has a $30cm \times 30cm \times 250cm$ rectangular test section which is enclosed by ground, polished glass side windows and two top and two bottom transparent Plexiglas removable windows. The test section diverges slightly along the top and bottom, compensating for the increase in boundary layer thickness from the inlet to the exit. A low turbulence level (<0.04%) is maintained over the full tunnel velocity range through use of vaned turning elbows and a settling chamber containing two honeycombs and three turbulence damping screens. A $4kW$ ($5hp$) vacuum pump controls the tunnel pressure from $120kPa$ down to $15kPa$.

The LTWT contains approximately $23m^3$ (6,000 *gal.*) of water. Roughly half of this water can be pumped into storage tanks above the tunnel, enough

to drop the water level in the tunnel below the level of the test section. Water quality is maintained by filtration and deaeration systems. The tunnel is equipped with two filtration systems which can be run independently or in series: A diatomaceous earth system removes particles down to $20\mu m$ at a rate of approximately $8.0m^3$ per hour. A filtration bag system removes particles down to $5\mu m$ at a rate of approximately $5.0m^3$ per hour. The dissolved air content of the water (measured by a van Slyke Blood Gas Analyzer) is controlled by spraying tunnel water inside a vacuum chamber. This deaeration system can reduce the dissolved air content of the water from $15ppm$ (saturation) down to $6ppm$ in about two hours and down to $3ppm$ in about 6 hours. Deaeration and filtration of the tunnel water are done between experiments. No noticeable change in water quality occurs during a typical experiment.

Corrosion of metallic parts in the LTWT is minimized by adding a weak concentration ($700ppm$) of sodium chromate (Na_2CrO_4) to the tunnel water. Efficient use of sodium chromate requires a basic environment. Therefore, along with sodium chromate, potassium hydroxide (KOH) is added to the LTWT until a *pH* greater than 8.0 is reached.

Velocity and pressure measurements are made either with mercury-water manometers or with absolute and differential pressure transducers. A Zenith Intel-8086 based computer continually monitors the tunnel operating parameters during tests including the cavitation number. The accuracy of these measurements is within 0.5%.

2.2 Hydrofoil Oscillation Mechanism

As shown in Figure 2.3, the hydrofoil is connected to a 750 watt DC motor by a four-bar linkage such that it oscillates nearly sinusoidally in pitch about a point near the center of pressure, x/c=0.38. The oscillation system including the motor, foil mount, and oscillation linkage is mounted to a two inch thick aluminum plate that fits into the base of the LTWT test section. The entire oscillation system is removed from the test section as a complete unit with the aid of an overhead crane. A collet connecting the oscillation linkage to a coupling shaft allows adjustment of the mean angle of attack of the foil. In addition, by changing the pivot point of the oscillation linkage connection to the motor spindle, adjustments of oscillation amplitudes ranging from ±1° to ±5° can be made (see Figure 2.4). The coupling shaft on which the hydrofoil pivots, shown in Figure 2.5, has a hole bored through its center allowing dye and air to be pumped into the foil section for flow visualization as well as allowing wiring for instrumentation to be passed out of the test section. This coupling shaft rides on a Rulon bearing inside the tunnel and a ball bearing outside the tunnel. A ceramic/carbon sliding seal prevents air from leaking into the tunnel under vacuum conditions and it prevents water from leaking out when the tunnel is at rest. The hydrofoil mounts to a circular plate that fastens to the coupling shaft. A Teflon ring is used as a bearing, taking up some of the moment generated by the fluid dynamic loads on the foil. The oscillation rate of the hydrofoil can be adjusted from 0 to 50*Hz* by a Sabina DC motor control unit operating under open loop control. An optical shaft encoder mounted to the DC motor provides a digital signal (1024 pulses/revolution), used to synchronize flow measurements with the phase of the foil.

2.3 NACA 64A309 Hydrofoil

The experiments presented in this thesis were conducted using a hydrofoil with an NACA 64A309 asymmetric foil section, shown in Figure 2.6. The "A" classification is a linear fit modification from the 80% chord position to the trailing edge, providing a stronger trailing edge structure with minimal effect on the flow characteristics (details of the foil geometry are tabulated in Table 2.2 for reference). The hydrofoil made from this section has a rectangular planform, with an 15.2*cm* (6*in*) chord length, and a span of 17.5*cm* (7*in*). It was reflection plane mounted to the floor of the LTWT test section giving it an effective aspect ratio of 2.3. The hydrofoil is constructed out of stainless steel and polished to a smooth finish. A removable rounded brass tip cap at the end of the foil allowed access to instrumentation and flow visualization equipment within the foil.

2.4 Finite Aspect Ratio Hydrofoil Setup

Figure 2.7 shows the experimental setup used to investigate the flow around the finite aspect ratio hydrofoil oscillating in pitch. The foil oscillated about the 0.38c chord position near the center of pressure. This helped reduce the torsional loading on the drive mechanism, allowing the 750 watt drive motor to oscillate the foil at frequencies up to 50*Hz*. At frequencies greater than 30*Hz*, however, the unsteady moments caused by surface cavitation, as well as the added mass loads resulting from the acceleration of fluid about the foil at these frequencies, caused structural difficulties with the foil mount. Therefore, experiments were generally conducted at oscillation frequencies less than 30*Hz*.

2.5 Two-Dimensional Hydrofoil Setup

Investigations of the flow around a two-dimensional hydrofoil were accomplished by removing the tip section of the finite aspect ratio foil and mounting a Plexiglas panel over the top of it (Figure 2.8.). The panel was held in place by two Plexiglas struts bolted to the top window. Nylon bushings were used to seal out water and air as well as to adjust the clearance of the panel relative to the foil tip. Tip clearance was maintained at a distance less than $1mm$.

2.6 Laser Doppler Velocimetry System

A Dantec Particle Dynamics Analyzer (PDA) was configured as shown in Figure 2.9 as a Laser Doppler Velocimeter (LDV) to measure velocities at the trailing edge of the foil. The Dantec system was used as a single axis $500mW$ LDV with separate receiver and transmitter. A manual traversing system was built to position the LDV to collect data along the span of the foil and across the trailing edge. Measurements of both streamwise and spanwise velocities were taken at seven locations across the wake and at four different spanwise locations. The software provided with the Dantec system allowed the data collection to be synchronized with the encoder pulses, so that information about the flow at a given foil angle could later be extracted. Details of these measurements are presented in Chapter 6.

2.7 Holographic System

A holographic system has been developed and used in numerous cavitation experiments at Caltech [Gates 1977; Katz 1981, 1984; O'Hern 1987; Green 1988]. In the study presented in this thesis, the holographic system was used primarily to establish the direction of rotation of the flow in the wake.

To accomplish this, the system was modified from a two-pulse to a three-pulse system with independently adjustable time delays between pulses, providing information on the sign of the local flow velocity as well as its magnitude. Attempts were made to use this system to take instantaneous velocity measurements of the flow in the wake of the hydrofoil. Unfortunately, the complexity of these flows made it extremely difficult to establish a consistent flow pattern from the limited information available in each hologram.

The holographic system, or holocamera, shown in Figure 2.10, is an in-line system (the reference beam and the subject beam are the same) based on a Pockels Cell switched ruby laser. At a selected time, the laser flash lamp is triggered and high-voltage ($5kV$) energy stored in a capacitor bank is discharged through the flash lamp, causing the lamp to emit intense light for approximately $1500\mu s$. The light excites a ruby rod located in the center of the flash lamp. After a time delay preset by the holocamera operator, the Pockels Cell is activated and light emitted from the ruby rod bounces between the partially reflective front mirror in the laser cavity and the completely reflective back mirror. This results in an avalanche effect that discharges the ruby rod in a very short period — typically $20ns$-$50ns$. This discharge is referred to as *lasing*. Multiple exposures (up to three pulses) are accomplished by switching the Pockels Cell on and off. Delays up to $200\mu s$ between exposures are possible (Appendix C details the circuit that controls the Pockels Cell pulse delays and the main control circuit). The light emitted during lasing is attenuated with neutral density filters which are adjusted to provide the correct exposure. The light then passes through a beam expander and a pinhole spatial filter. The beam expander is used to reduce the energy

per unit area of the beam to help prevent burning of the special filter optics. The spatial filter strips off the majority of non-coherent light caused by imperfections in the optics. The beam is then collimated and diverted by mirrors to the location of interest in the LTWT test section. The holograms are recorded on Agfa Gevaert 10E75 holographic film mounted in a camera on the opposite side of the test section. After development of the film, the hologram is reconstructed by illuminating it with collimated He-Ne laser light (see Figure 2.11). Measurements are made on highly magnified portions of the holographic image.

2.8 Digital Data Recorder

Data was recorded digitally on an Intel-8086 based computer using an R.C. Electronics, Inc. ISC-16 Computerscope system. This system is made up of a 16-channel A/D board, an external instrument interface, and a software package. It is capable of receiving up to 16 channels of data input at an aggregate sampling rate of up to 1*MHz*. Digital conversion is achieved with 12 bit accuracy over an input range of -10 to +10 volts. This system emulates a digital oscilloscope storing up to 64k words of data in a memory buffer each time it is triggered.

A synchronization circuit, described in detail in Appendix D, was developed to synchronize the data recorded by the Computerscope with the phase of the oscillating hydrofoil. The synchronization circuit outputs a standard TTL pulse (+5 volts) each time a preset hydrofoil phase position was reached (measured from the optical shaft encoder). This pulse was fed into the external trigger input of the Computerscope. The data could be recorded in a single burst each time a particular hydrofoil phase was reached, or it

could be synchronized to track the phase of the foil. This was accomplished by inputting the 1024 pulse per revolution encoder output (converted to TTL levels) to the external clock input of the Computerscope and setting the Computerscope to take 1024 data points per channel (Figure 2.12). Software, described in detail in Appendix E, allowed recorded data to be ensemble averaged with the phase of the hydrofoil over hundreds of oscillation cycles.

Table 2.1 Low Turbulence Water Tunnel Specifications

Cavitation Number	0.04 (min.)
Contraction Ratio	16:1
Corrosion Control	Sodium Chromate, Na_2CrO_4 (700*ppm*) *pH* maintained >8.0 with KOH
Deaeration Level	3*ppm* (min.)
Deaeration Time	6*ppm* (2 hours), 3*ppm* (6 hours)
Drive Power	14*kW* (30*hp*)
Filtration (2 systems)	20μm (diatomaceous earth), ≈ $8m^3$/hour 5μm (filter bags), ≈$5m^3$/hour
Freestream Turbulence	< 0.04%
Maximum Velocity	10*m/s*
Pressure (absolute)	120*kPa* (max), 10*kPa* (min)
Test Section Dimensions	30*cm* x 30*cm* x 250*cm*
Volume	$23m^3$ (6000 *gals.*)
Water Temperature	19°C (±2°C)

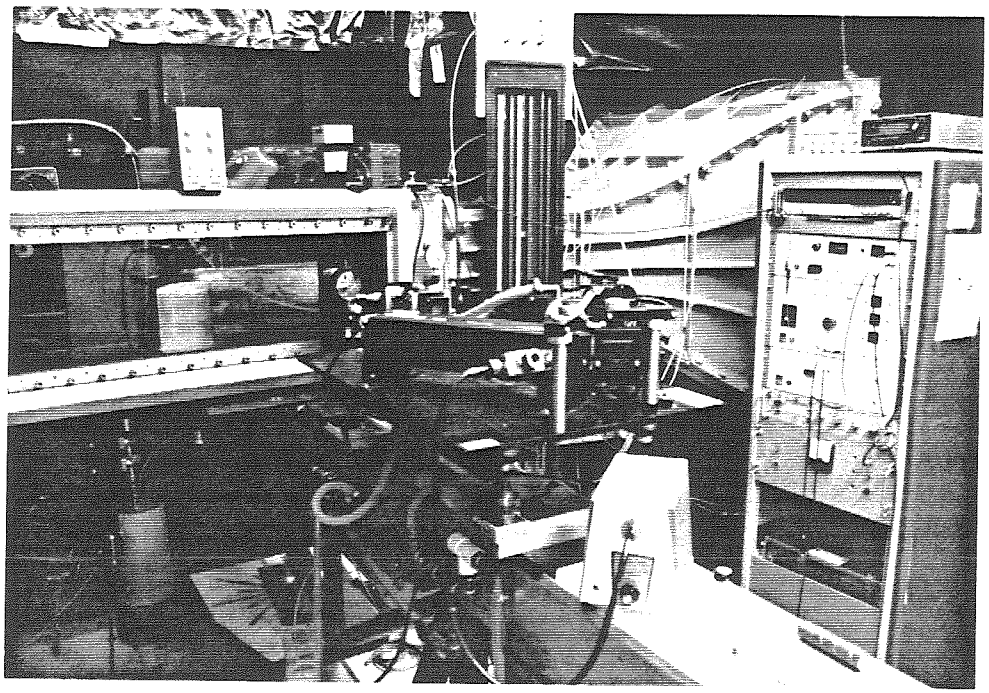

Figure 2.1 Oscillating Hydrofoil Experimental Facilities
Photograph showing the major components of the oscillating hydrofoil experimental setup. The NACA 64A309 hydrofoil can be seen in the test section of the LTWT. In the foreground is the holocamera system. The controls for the oscillation mechanism and the holocamera are on the right side mounted to a rack. Also on the right, mounted to the throat of the tunnel, are manometers used to calibrate the computer monitoring system.

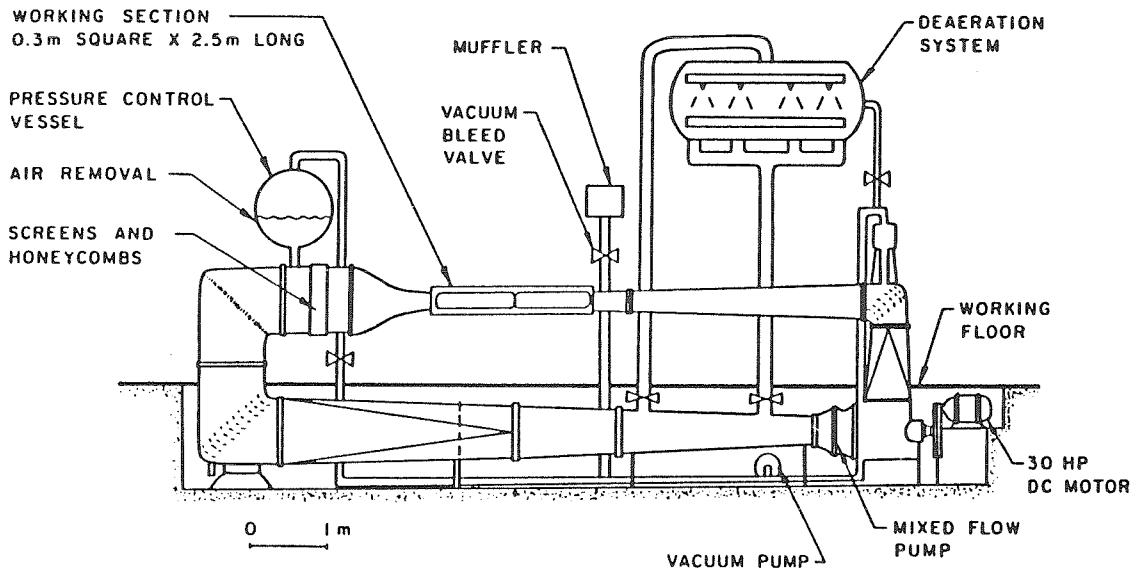

Figure 2.2 Caltech Low Turbulence Water Tunnel
The LTWT has a 30cm × 30cm × 250cm test section with parallel quartz windows on each side and Plexiglas hatches above and below. A 16:1 contraction ratio and a 14kW DC motor allow the tunnel to operate at speeds up to 10m/s. Pressure in the tunnel is controlled by a vacuum pump system and can be brought from 120kPa down to 15kPa. Air content is controlled by spraying the tunnel water over a bed of blocks under vacuum. The tunnel air content can be brought down from saturation (15ppm) to 6ppm in about two hours. Tunnel operating conditions are monitored continuously by computer.

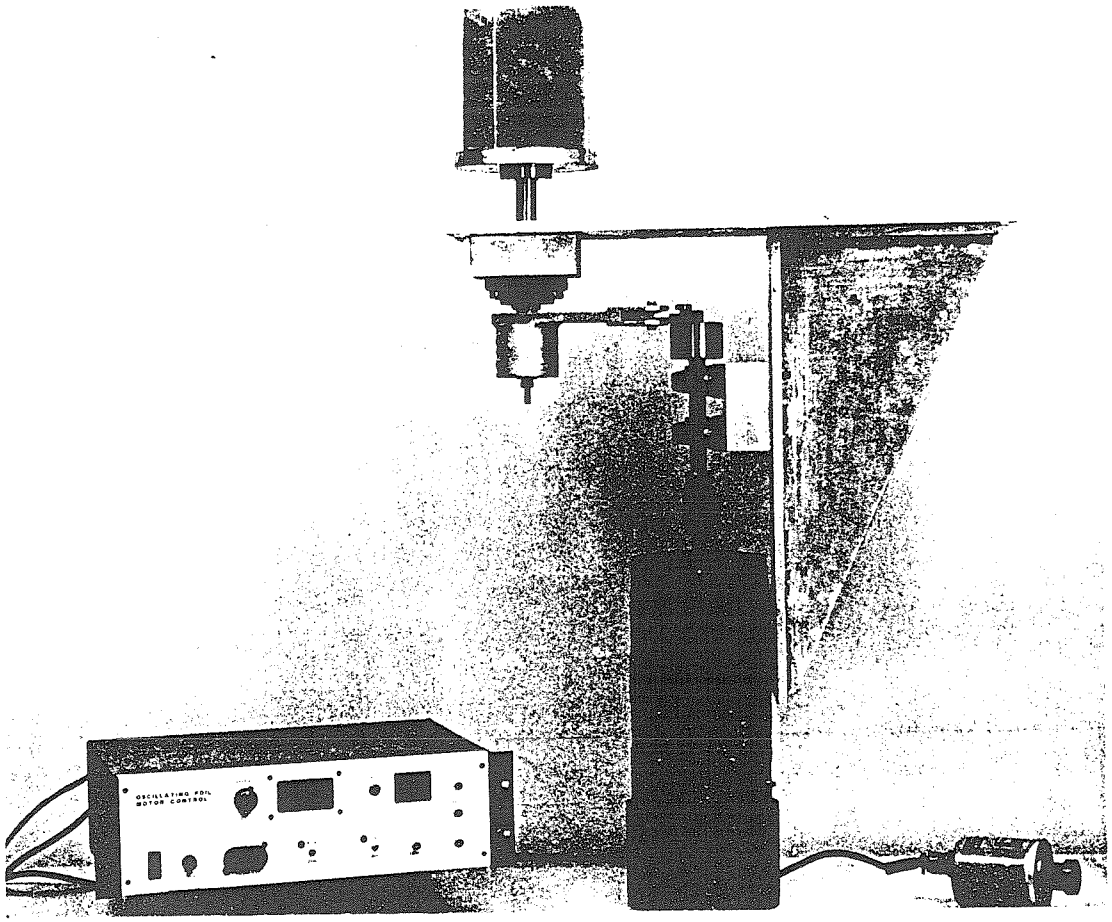

Figure 2.3 Hydrofoil Oscillation Mechanism
The hydrofoil is oscillated in a sinusoidal fashion by a 750 watt DC motor that drives a four bar linkage connected to a shaft at the base of the hydrofoil. The entire oscillation system is mounted to a two inch thick aluminum plate that fits into the base of the LTWT test section. The oscillation mechanism is removed from the test section as a complete unit with the aid of an overhead crane.

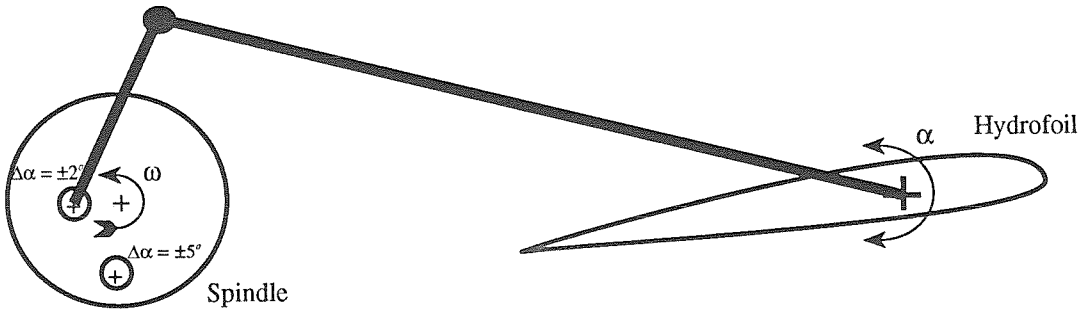

Figure 2.4 Hydrofoil Oscillation Linkage
A four-bar linkage oscillates the hydrofoil in a nearly sinusoidal motion. An elliptical spindle allows the amplitude of the foil oscillations to be adjusted from ±1° to ±5° in 1° increments. A collar fastened to the spindle can be adjusted to allow the hydrofoil to oscillate about any mean angle of attack from 0° to 360°. An angle vernier mounted to the spindle provides a means of measuring the mean angle of attack to within a quarter of a degree.

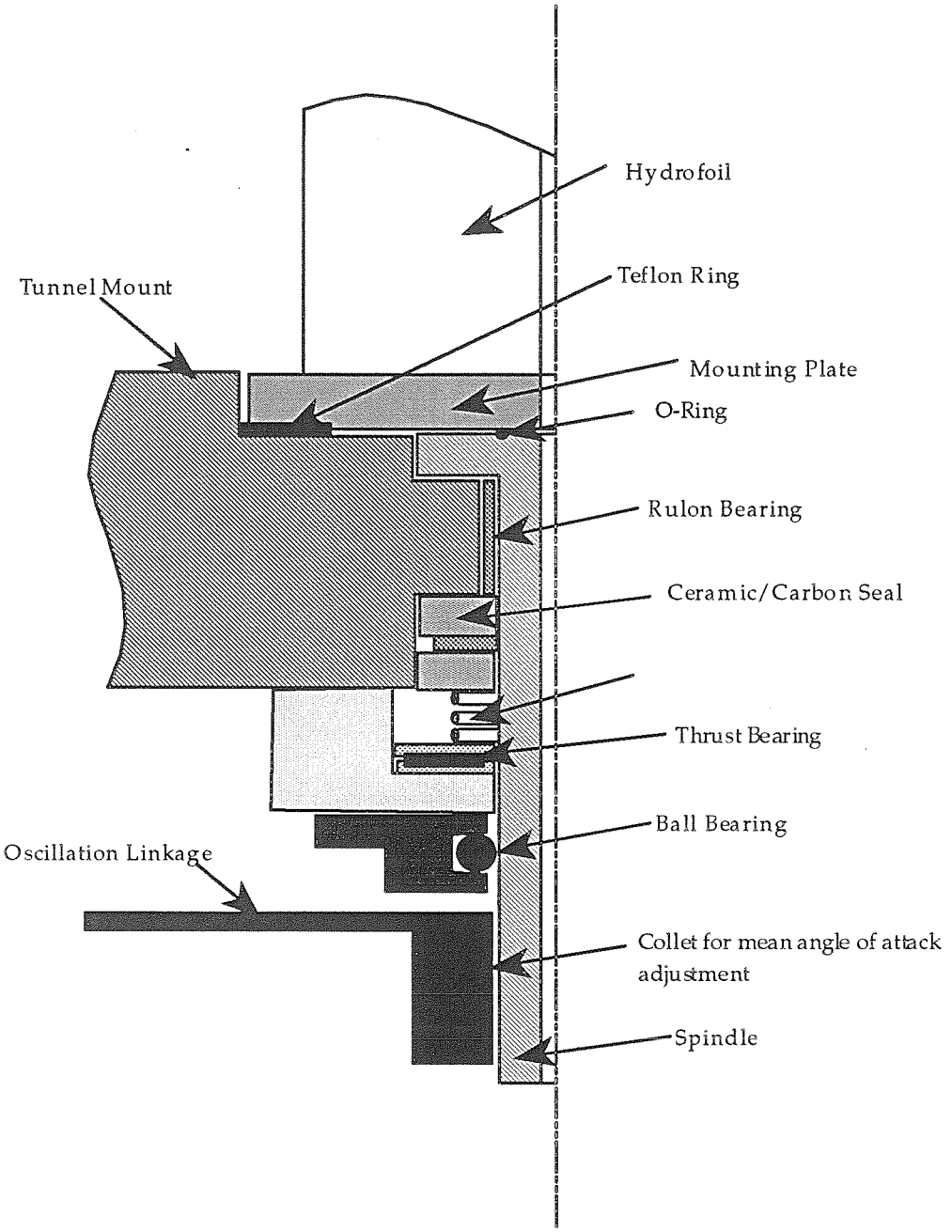

Figure 2.5 Detail of Hydrofoil Spindle Seal and Bearings
An NACA 64A309 hydrofoil mounts to an aluminum plate recessed in the LTWT test section floor. The plate rotates on a Teflon bearing and is driven by a spindle bolted to the bottom. The spindle passes through a Rulon bearing and then through a ceramic/carbon seal that prevents water from leaking out under atmospheric conditions and prevents air from entering the tunnel when the tunnel is operated under vacuum. The spindle then passes through a bulkhead mounted ball bearing and is connected to the drive linkage.

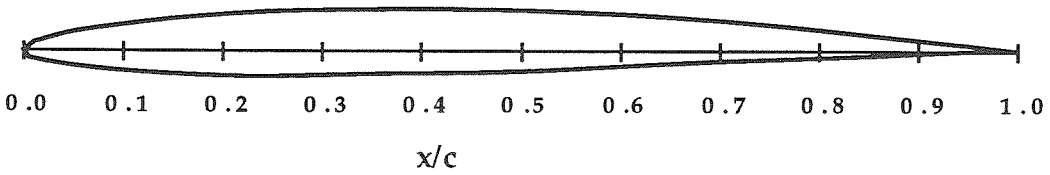

Figure 2.6 NACA 64A309 Hydrofoil Cross-Section
The NACA 64A309 modified hydrofoil which was tested is an asymmetric hydrofoil made from stainless steel and polished to a smooth finish. The "A" modification is a linear fit from the 80% chord position to the trailing-edge. This allows the foil to be easily manufactured and increases the structural integrity of the trailing-edge section. This type of modification has very little effect on the performance. The hydrofoil has a chord length of 0.152m (6in) and a semispan of 0.18m (7in), AR=2.3. A brass rounded tip section with the radius of curvature equal to the width of the hydrofoil at each chord position was bolted to the tip of the hydrofoil for tip vortex studies.

Table 2.2 NACA 64A309 Hydrofoil Geometry

Measurements taken directly from the experimental hydrofoil are shown in parentheses. True specifications were formulated from information presented in the Theory of Wing Sections. Abbot, von Doenhoff [1959].

x/c	Thickness/c*	Mean/c**	Suction Surface	Pressure Surface
0.00	0.000 (0.000)	0.000 (0.000)	0.000 (0.000)	0.000 (0.000)
0.02	0.013 (0.018)	0.003 (0.002)	0.010 (0.011)	-0.004 (-0.007)
0.05	0.042 (0.036)	0.005 (0.004)	0.026 (0.022)	-0.016 (-0.014)
0.10	0.058 (0.054)	0.008 (0.007)	0.037 (0.034)	-0.021 (-0.020)
0.15	0.069 (0.065)	0.010 (0.010)	0.045 (0.042)	-0.025 (-0.023)
0.20	0.077 (0.074)	0.012 (0.012)	0.051 (0.049)	-0.026 (-0.025)
0.25	0.083 (0.080)	0.013 (0.014)	0.055 (0.053)	-0.028 (-0.026)
0.30	0.087 (0.083)	0.015 (0.015)	0.059 (0.056)	-0.029 (-0.027)
0.35	0.089 (0.086)	0.015 (0.016)	0.060 (0.059)	-0.030 (-0.027)
0.40	0.090 (0.086)	0.016 (0.017)	0.061 (0.060)	-0.029 (-0.026)
0.45	0.088 (0.086)	0.016 (0.017)	0.060 (0.061)	-0.028 (-0.026)
0.50	0.085 (0.083)	0.017 (0.018)	0.060 (0.060)	-0.026 (-0.024)
0.55	0.079 (0.079)	0.016 (0.018)	0.056 (0.057)	-0.024 (-0.022)
0.60	0.073 (0.073)	0.016 (0.017)	0.053 (0.054)	-0.021 (-0.019)
0.65	0.065 (0.066)	0.015 (0.017)	0.048 (0.050)	-0.018 (-0.016)
0.70	0.057 (0.058)	0.015 (0.016)	0.044 (0.045)	-0.014 (-0.013)
0.75	0.048 (0.049)	0.013 (0.015)	0.037 (0.039)	-0.011 (-0.010)
0.80	0.038 (0.037)	0.012 (0.012)	0.031 (0.031)	-0.007 (-0.006)
0.85	0.029 (0.028)	0.010 (0.010)	0.025 (0.024)	-0.005 (-0.004)
0.90	0.019(0.019)	0.008 (0.007)	0.018 (0.016)	-0.002 (-0.003)
0.95	0.010 (0.010)	0.005 (0.004)	0.009 (0.008)	-0.001(-0.001)
1.00	0.000 (0.000)	0.000 (0.000)	0.000 (0.000)	0.000 (0.000)
L.E. radius: 0.494c				
T.E. radius: 0.023c				

*$Thickness/c \approx 0.38\left[(x/c)^{0.75} - (x/c)^{1.4}\right]$

**$Mean/c \approx \sqrt{48.3504 - (x/c - 0.5)^2} - 6.9354$

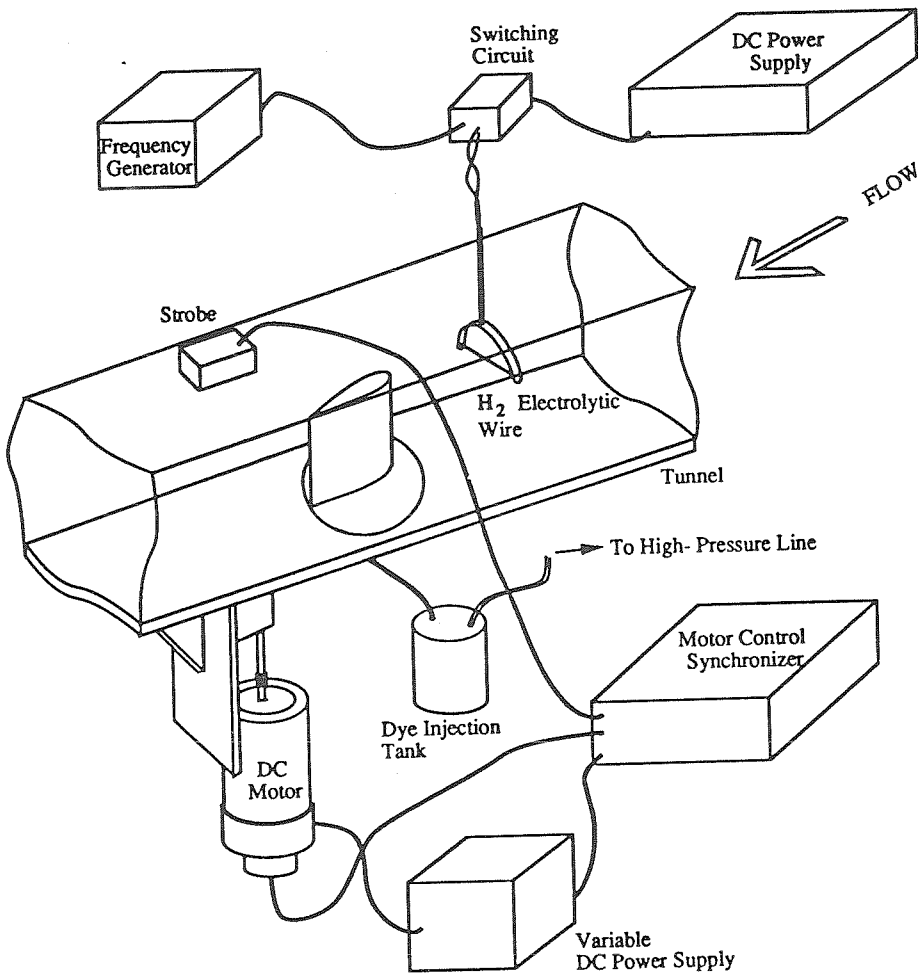

Figure 2.7 Finite Aspect Ratio Oscillating Hydrofoil Experimental Schematic
A 750 watt DC motor connected by a four bar linkage oscillates the hydrofoil sinusoidally in pitch about the 0.38c chord position. The oscillation mechanism mounts to a plate which fits into the lower window of the test section of the LTWT. An encoder at the base of the drive motor allows synchronization of instrumentation with the phase of the foil.

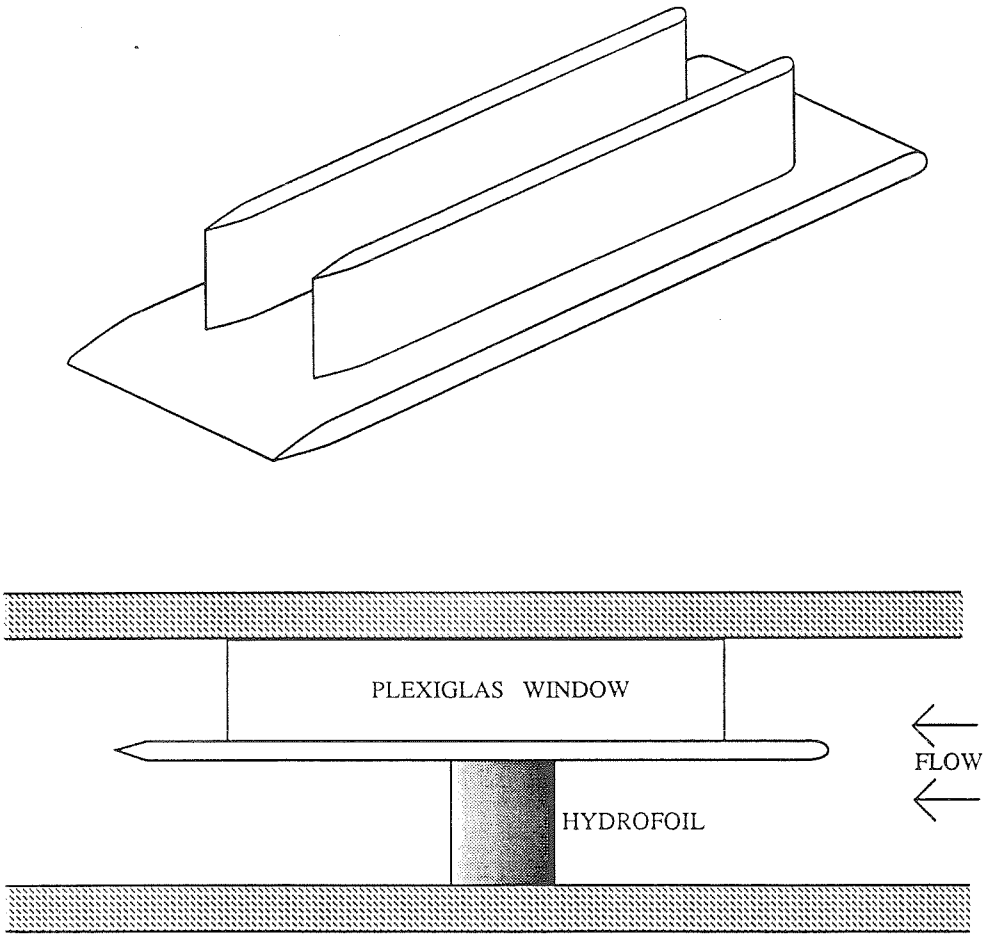

Figure 2.8 Two-Dimensional Hydrofoil Setup
Studies of a two-dimensional oscillating hydrofoil were made by removing the tip of the three-dimensional foil and placing a Plexiglas panel on top. The panel was bolted to the top window of the LTWT. Nylon bushings were used to seal the bolts and to space the panel less than 1mm from the top of the foil.

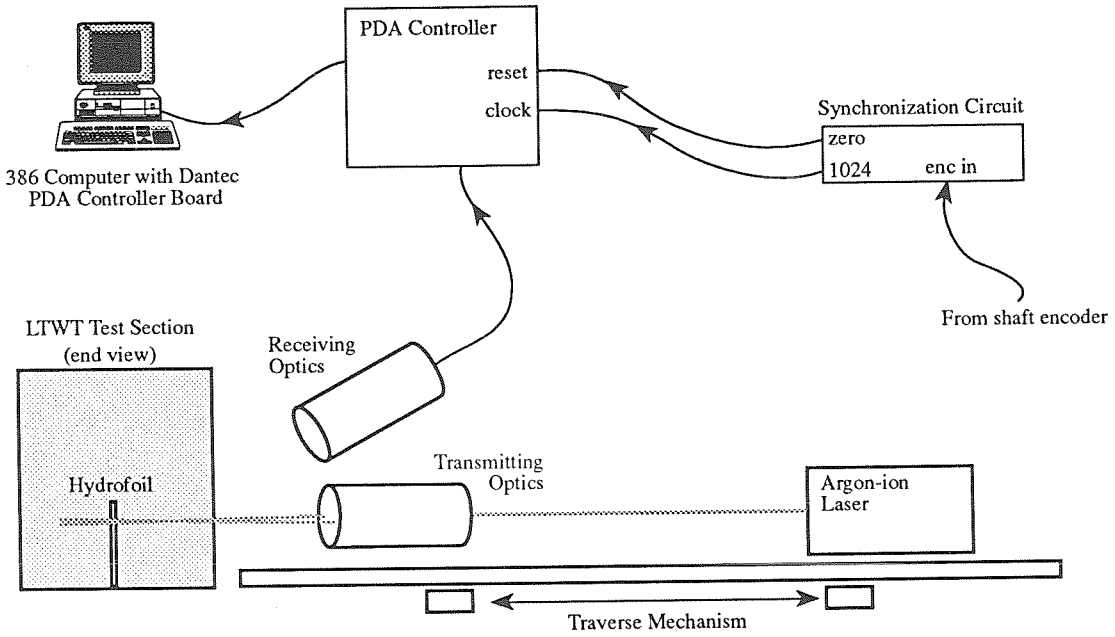

Figure 2.9 Schematic of Laser Doppler Velocimetry System
Velocity measurements of the flow near the trailing edge of the hydrofoil were made using a Dantec PDA system in its LDV mode. The data from this single-axis LDV system was encoded to the phase of the hydrofoil and ensemble averaged over several hundred oscillations. Measurements in the streamwise and spanwise directions were made at seven locations perpendicular to the hydrofoil for each of four locations along the span of the foil.

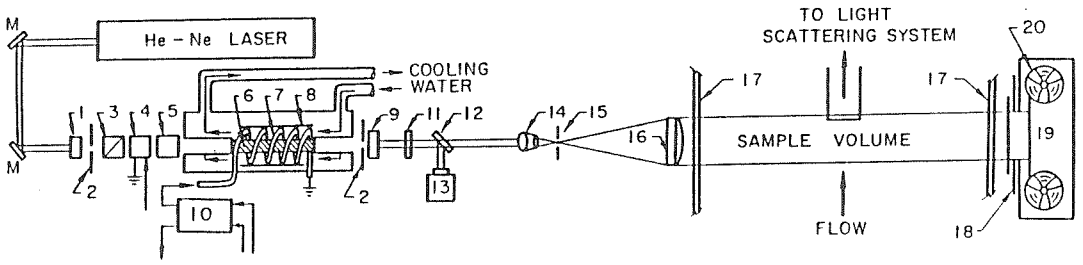

1. BACK MIRROR
2. IRIS APERTURE
3. POLARIZER
4. POCKEL'S CELL
5. POLARIZER
6. RUBY ROD
7. XENON FLASH LAMP
8. REFLECTOR
9. FRONT MIRROR-SAPPHIRE ETALON
10. TRIGGER TRANSFORMER
11. N.D. FILTER
12. BEAM SPLITTER (4% REFLECTIVETY)
13. PIN DIODE
M. MIRROR
14. MICROSCOPE OBJECTIVE
15. SPATIAL FILTER-10μ PIN HOLE
16. COLLIMATING LENS
17. GLASS WINDOWS OF THE TUNNEL
18. SHUTTER
19. AUTOMATIC FILM DRIVE
20. HOLOGRAPHIC FILM

Figure 2.10 Schematic of Holocamera Setup

Triple pulsed ruby laser (λ=694nm, red) passes through a neutral density filter used to adjust the hologram illumination, travels through a spatial pinhole filter to reduce the non-monochromatic light content, passes through a collimating lens and illuminates the flow before being recorded on film. The area of illumination can be adjusted by adjusting a series of mirrors used to divert the laser to different parts of the LTWT test section.

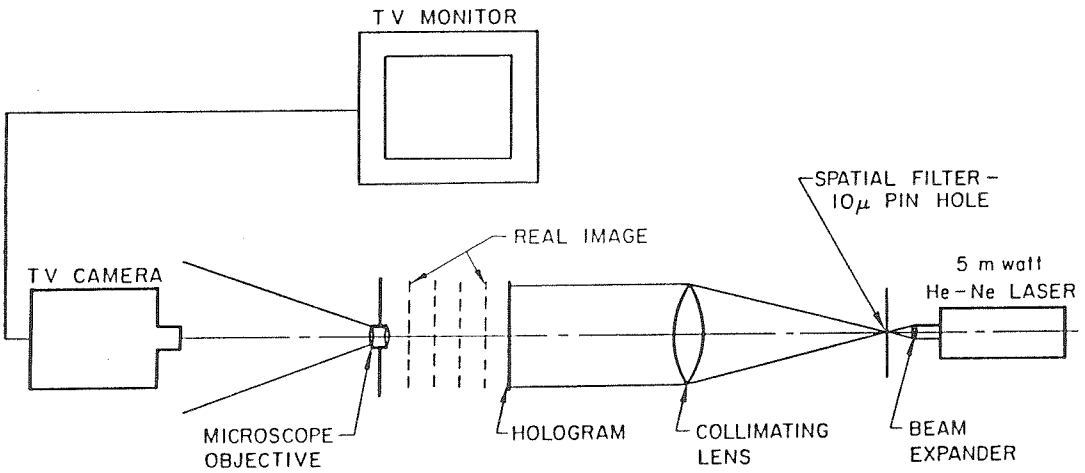

Figure 2.11 Holographic Reconstruction System
A He-Ne laser beam is expanded and collimated. It is then passed through the hologram and is focused onto an image array. The output of the image array is converted and displayed on a monitor.

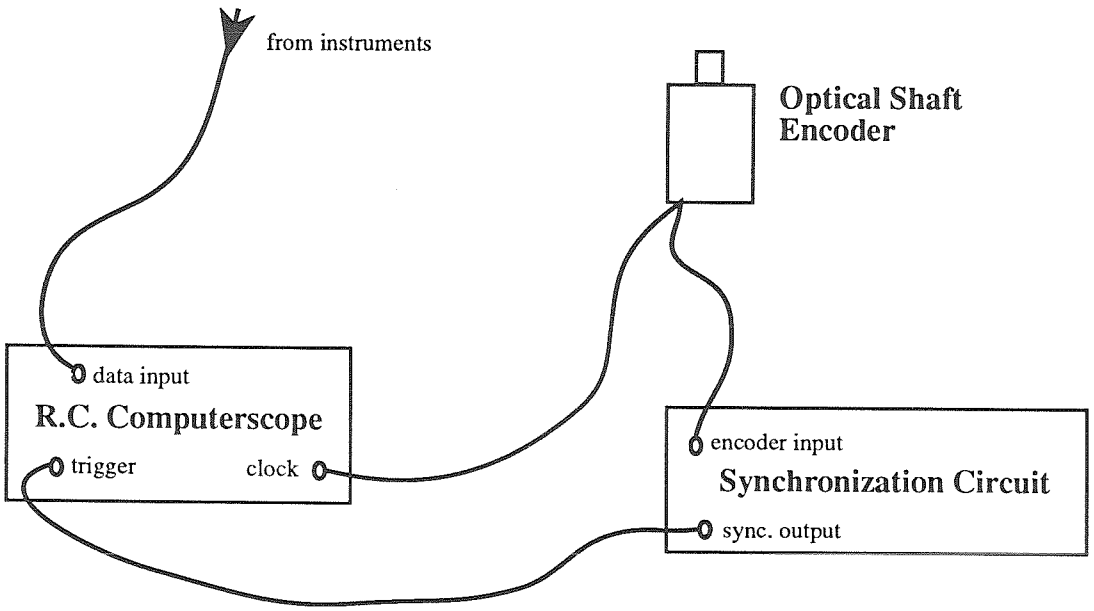

Figure 2.12 Schematic of Data Recorder Setup
Data can be recorded in a single burst each time a particular hydrofoil phase is reached or it can be synchronized to track the phase of the foil. This was accomplished by inputting the 1024 pulse per revolution encoder output (converted to TTL levels) to the external clock input of the Computerscope and setting the Computerscope to take 1024 data points per channel. Software allowed recorded data to be ensemble averaged with the phase of the hydrofoil over hundreds of oscillation cycles.

CHAPTER 3

EXPERIMENTAL TECHNIQUES

This chapter describes the experimental techniques employed in the research presented in this thesis. Some of these techniques are variations of methods developed by other researchers and adapted to the present study. Others were developed in the process of conducting this research. Included in this chapter are descriptions of specialized equipment used in specific tests.

3.1 Flow Visualization

Flow visualization was used to observe the formation of the unsteady trailing wake structure and to determine the mean flow direction over the surface of the hydrofoil. Flow patterns were recorded using standard video techniques as well as high speed 8*mm* film (500 frames/second). In addition, photographs of the flow were taken using open shutter photography with 3200 ASA color film and synchronizing two Strobotac 1531-A strobe lights (10μs flash duration) to the phase of the oscillating hydrofoil. The phase of the hydrofoil at which the strobes triggered could be adjusted to allow the formation of the tip vortex structure to be observed.

3.1.1 Wake Flow Visualization

Two techniques, hydrogen micro-bubble generation and injection of dye or air, were used to visualize the flow in the wake of the hydrofoil. Air and dye injection into the tip vortex core allowed direct observations of the vortex structure while hydrogen micro-bubbles, due to their small but finite size, provided an indication of the flow streamlines.

Injection of dye into the tip vortex core, as illustrated in Figure 3.1, was accomplished by forcing dye out of a tank with pressurized air into a tube that led past a valve and up through the center of the foil. A channel cut into the brass tip of the hydrofoil diverted this dye to the trailing edge where it oozed through a small hole into the flow near the tip vortex. The low pressure of the tip vortex core entrained the low density dye, tracing the vortex structure.

Selection of a satisfactory dye was difficult due to the unsteadiness of the flow in the wake of the foil. A dye was required that was lighter than water so that it would be entrained into the low pressure region of the trailing vortex structure and would not quickly dissipate in the wake flow. Water based dyes, while convenient, were found to dissipate too quickly and could not be injected in enough concentration to allow the flow visualization to be recorded on film. It was found that a solution of milk and alcohol provided the best results (see Figure 3.2). The fat in the milk held the solution together, preventing dispersion in the flow, and the alcohol allowed adjustment of the density of the solution. Even then, this mixture illuminated the flow clearly only at very low flow velocities and the density could not be made low enough to trace the entire trailing vortex structure – only the tip vortex, where the pressure was the lowest, could be traced effectively with this technique.

To obtain a clearer understanding of the formation of the trailing wake structure of the oscillating hydrofoil, air was used in place of dye and injected into the tip vortex region of the foil. Air, being considerably less dense than dye, traced many of the small complex vortex structures in the wake (see Figure 3.3). It is not known, however, whether or not the air significantly influenced the formation of the trailing vortices. By displacing the fluid at the

core of these structures where the shear forces are the greatest, the air may have slowed the viscous diffusion of the vortices and altered their axial flow profiles. Vortices tend not to diffuse quickly under normal conditions due to the low velocity gradient just outside the core. It is believed that the injection of air for flow visualization did not significantly alter the wake structure in the region near the foil.

Hydrogen micro-bubbles were also used to visualize the wake flow. As shown in Figure 3.4, a $25\mu m$ tungsten wire was used to generate a hydrogen micro-bubble sheet.

This wire was placed across the width of the LTWT perpendicular to the span of the hydrofoil at a distance of one chord upstream from the leading edge. The wire was mounted to a traversing mechanism, allowing the hydrogen micro-bubble sheet to be positioned at any desired location along the span of the hydrofoil. A DC power supply provided -60V and 1.5 amperes to the wire, resulting in a dense hydrogen micro-bubble sheet of bubbles roughly 50 - 100μm in diameter (see Figure 3.5). The density of the hydrogen micro-bubble sheet was controlled by placing a switching circuit in line with the DC power supply and switching the tungsten wire voltage on and off with a frequency generator at a rate of 100 to 1000Hz.

3.1.2 Surface Flow Visualization

Concern about the possibility of flow separation near the trailing edge of the hydrofoil, and the difficulties this would cause in trying to measure the flow in this area, prompted several tests where surface flow visualization was used to indicate the flow patterns inside the boundary layer of the foil. Two techniques for surface flow visualization were used in these tests; paint dots

which indicate the mean flow pattern, and telltales which provide an instantaneous view of the flow direction.

Paint dot surface flow visualization is an old but effective technique. A viscous oil-based paint is mixed with linseed oil and dotted in a grid pattern on the surface of the object being tested in an area of interest. The test object is then placed in the flow conditions of interest and the paint dots are allowed to smear out along the direction of flow. Green [1988] describes in detail how this technique is used for surface flow visualization on a non-oscillating hydrofoil in the LTWT. For surface flow visualization of an oscillating hydrofoil, the paint linseed mixture had to be made particularly viscous to allow the foil to reach test conditions before the paint mixture would begin to smear significantly. Typically a mixture of 1 part linseed oil to 10 parts Pictor oil-based white paint was used. Figure 3.6 shows the result of a typical paint drop flow visualization trace on an oscillating hydrofoil. This technique was useful because it provided a global, non-intrusive view of the surface flow on the foil, though it only provided information on the mean flow along the surface. No indication of flow separation was evident during any of the tests made using this technique.

To obtain an instantaneous view of the surface flow pattern, telltales were used. Pieces of cotton thread long enough to reach the trailing edge were adhered to the leading edge of the foil using a cyanoacrylate-based glue (see Figure 3.7). Smaller telltales, attached at key points over the surface of the foil, would have provided more detailed information about the boundary layer flow, but adhesion to the smoothly polished stainless steel proved very difficult. The longer telltales, however, provided useful information when care was taken to observe the direction of flow indicated only at the very ends

of the telltales. The tension generated by the drag of the telltales in the flow distorted the indicated flow direction of the rest of the thread. The telltales clearly indicated a slight flow separation at the trailing edge of the foil, as well as a large phase lag in the motion of the flow in the boundary layer of the foil relative to the phase of the oscillating foil.

3.2 Triple-Pulsed Holographic Measurements of Instantaneous Velocity

Attempts were made to obtain velocity information in the wake of the hydrofoil using the holocamera described in Chapter 2. The complexity of the unsteady wake, however, made measurements of instantaneous velocity extremely difficult. Even in the clearest holograms, it was nearly impossible to relate a particular feature in the hologram to any known location in the wake structures observed in flow visualization studies. As a result, the holographic data was not used for quantitative information. Triple-pulsed holograms of the flow, however, did provide general information about the direction of rotation of the flow in the wake. Hydrogen bubbles ranging in size from $10\mu m$ to $100\mu m$ were generated near the trailing edge of the hydrofoil (see Figure 3.8). Triple-pulsed holograms of the flow in the wake region of the hydrofoil taken with a $150\mu s$ delay between first and second pulse and $80\mu s$ delay between the second and third pulse, such as the one shown in Figure 3.9, allowed measurement of the direction and magnitude of the hydrogen bubbles. For the complex flows in the wake of the oscillating hydrofoil, knowledge of the sign of the velocity vectors was critical in determining the structure of the trailing vorticity. This information could not be determined from two-pulsed holograms.

3.3 LDV Measurements of Hydrofoil Wake

Laser Doppler Velocimetry (LDV) measurements were taken of the flow in the spanwise and streamwise directions at the trailing edge of the two-dimensional and the three-dimensional hydrofoils (see Figure 3.10). These measurements were used to determine the change in streamwise and spanwise circulation due to the pitching motion of the foils. The technique used to make these measurements is unique to the study of unsteady lifting surface research. Because of the complexity involved in taking these measurements and reducing the data and because of the significance of these measurements, Chapter 6 has been devoted to describing this technique.

3.4 Cavitation Inception Measurements

Cavitation inception studies are notoriously difficult. Cavitation nucleates from small bubbles in the freestream. Due to surface tension effects, the conditions under which these bubbles cavitate depends on the size of the bubble. Since a given fluid will tend to contain bubbles of a variety of sizes, the flow conditions will not change suddenly from a non-cavitating state to a cavitating state. Instead, as the local pressure of the fluid decreases the larger bubbles in the flow will cavitate. As the pressure continues to decrease, the cavitation rate will increase as smaller and smaller bubbles begin to cavitate. This rate of cavitation events is typically exponential in growth relative to the cavitation number of the flow, $\sigma = (p - p_v)/\frac{1}{2}\rho U_\infty^2$. Because this process is extremely dependent on the number and size distribution of bubbles in the freestream, and because there is no instrument available that will clearly and accurately measure this distribution, defining the inception of cavitation necessarily remains an imprecise task.

3.4.1 Visual Cavitation Detection

The simplest technique for determining the inception of cavitation, visual inspection, is also the most subjective. The cavitation number is lowered, usually by lowering the test section pressure, until the first cavitation bubbles appear. The computer that monitors the tunnel parameters calculates and reports the cavitation number as well, and its current value can simply be read off the screen. This technique was used extensively to determine cavitation inception on the hydrofoil surface when operating at very high reduced frequencies, when other techniques proved problematic. The main difficulty with this technique lies in establishing an objective definition for inception, which is further complicated by the difficulty in clearly identifying a cavitation event in the highly complex pattern of the wake of the oscillating foil. In addition, even after a criterion for determining cavitation inception has been established, the visual technique still provides no means for identifying the phase of the oscillating hydrofoil at which inception occurs.

3.4.2 Acoustic Cavitation Detection

Some of the problems associated with visual determination of cavitation inception can be solved by detecting cavitation acoustically. Cavitation bubbles create strong sharp pressure pulses in the fluid when they collapse. These pulses are easily sensed by placing a hydrophone in or near the flow. Figure 3.11 illustrates the acoustical technique used to measure cavitation event rates in the wake of the oscillating hydrofoil. A piezo-ceramic based hydrophone with a bandwidth greater than $100MHz$ was placed in a tank of water on top of the test section of the LTWT (the tank of water allowed close acoustic coupling to the flow in the tunnel without having to place the hydrophone directly in the tunnel). The output of the hydrophone was

amplified and passed through a 4*kHz* high-pass electronic filter to isolate cavitation noise from the background noise of the tunnel and foil oscillation mechanism. The hydrophone output was then input to a threshold detection circuit which output a pulse when a level greater than a certain preset value was reached. In addition, the circuit locked out any incoming pulse for a short interval (also adjustable) to prevent rebounds of the cavitation bubble collapse and reverberations off the tunnel walls from being counted as cavitation events. The output from this circuit was input into an HP Digital Frequency Counter where the frequency of cavitation events was determined. A digital data taker was also connected to the output of the hydrophone as well as to the output of the optical encoder of the hydrofoil oscillation mechanism via a synchronization circuit. The data taker allowed the acoustic output of the hydrophone to be recorded in phase with the oscillation of the hydrofoil, making it possible (as shown by Figure 3.12) to determine the phase of the hydrofoil when a particular cavitation event occurred. This technique, as Chapter 5 will describe, was useful in analyzing the effects of unsteady flow on the inception of cavitation on the surface of the hydrofoil. It, however, has several disadvantages. Cavitation typically occurs in the tip vortex region of the oscillating foil as well as on both surfaces. This method of detecting cavitation events does not discriminate between these types of cavitation. In addition, as shown in the acoustic trace in Figure 3.13, the noise generated by the flow around the foil as it oscillates at very high frequencies makes this technique difficult if not impossible to use in that regime.

3.4.3 Optical Cavitation Detection

An optical system was developed as an improvement on the acoustic method of determining cavitation event rates in order to analyze cavitation in the wake region of the oscillating hydrofoil. An array of six photo-diodes was fastened to an adjustable Plexiglas mount, as shown in Figure 3.14. A halogen light was placed on one side of the LTWT test section and the photo-diode array was placed on the other and positioned so that shadows created by cavitation bubbles in the tip vortex region of the oscillating hydrofoil passed over the photo-diodes. Cavitation in the tip vortex region of the foil occurred within a very well defined area making positioning of the light source and the photo-diodes relatively simple. Only slight adjustments had to be made as test conditions changed. The outputs of the photo-diodes were recorded by an HP Digital Frequency Counter and by a digital data taker in the same way as the acoustical traces of cavitation events were recorded. The photo-diodes provided a very high signal-to-noise ratio allowing measurements of cavitation events to be taken at all operating conditions of interest. Figure 3.15 shows a typical trace of the photo-diode outputs relative to the phase of the oscillating hydrofoil. By cross-correlating between diodes, the multiple diode array provides a means of detecting not only the cavitation event rate but also the phase at which the hydrofoil generated the vortex structure where cavitation first appears as well as the downstream location where this cavitation initiated.

Figure 3.16 shows a plot of cavitation event rates in the wake of a non-oscillating hydrofoil as a function of cavitation number for angles of attack ranging from 2° to 12°. Measurements of this type are typical of the ones used to determine the cavitation inception number in the tip vortex region of the

oscillating hydrofoil. The photo-diode optical technique provides very reproducible results. These were compared with measurements made by Green [1988] and found to agree well as shown in Figure 3.17.

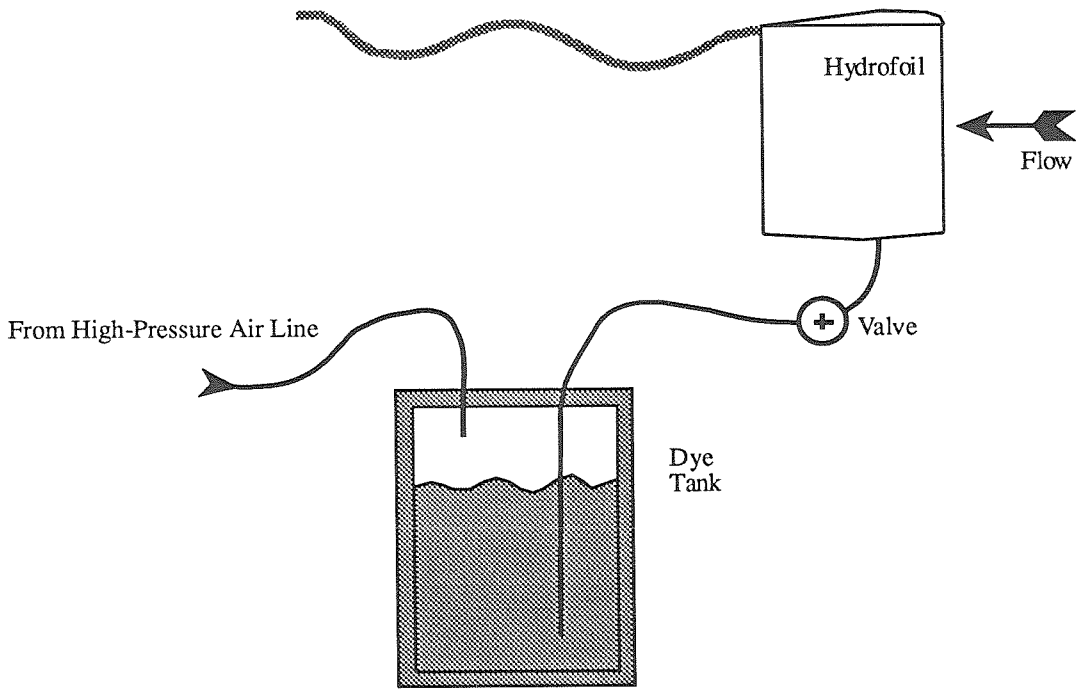

Figure 3.1 Dye Injection System
A Plexiglas tank holds a dye solution for flow visualization. Pressurized air entering the top of the tank forces dye out a tube through the drive spindle of the hydrofoil oscillation mechanism, up through a shaft in the hydrofoil and out the tip into the core of the tip vortex. The dye solution was made from whole milk and alcohol. Alcohol was added to the milk until the desired density of the dye was achieved.

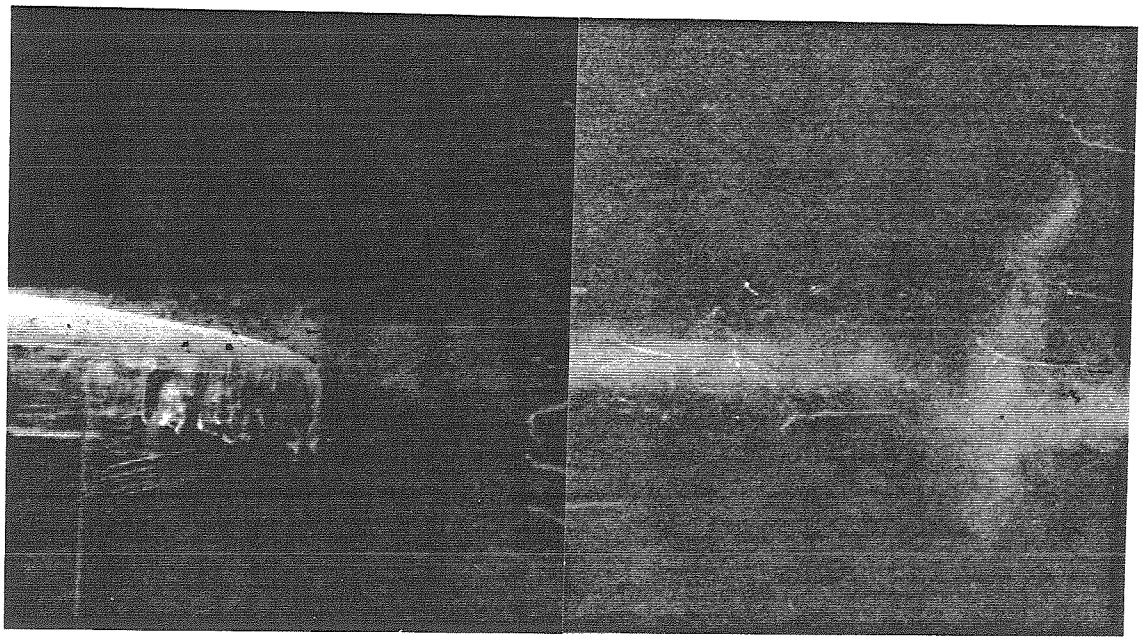

Figure 3.2 Tip Vortex Structure Made Visible by Dye Injection
Dye made from alcohol and whole milk is injected into the tip vortex structure of the oscillating hydrofoil. The 'puffy' formations are caused by dispersion of the dye in a weakened region of the tip vortex formation. This region is the result of vortex filament connecting the spanwise vortices wrapping around the tip vortex.

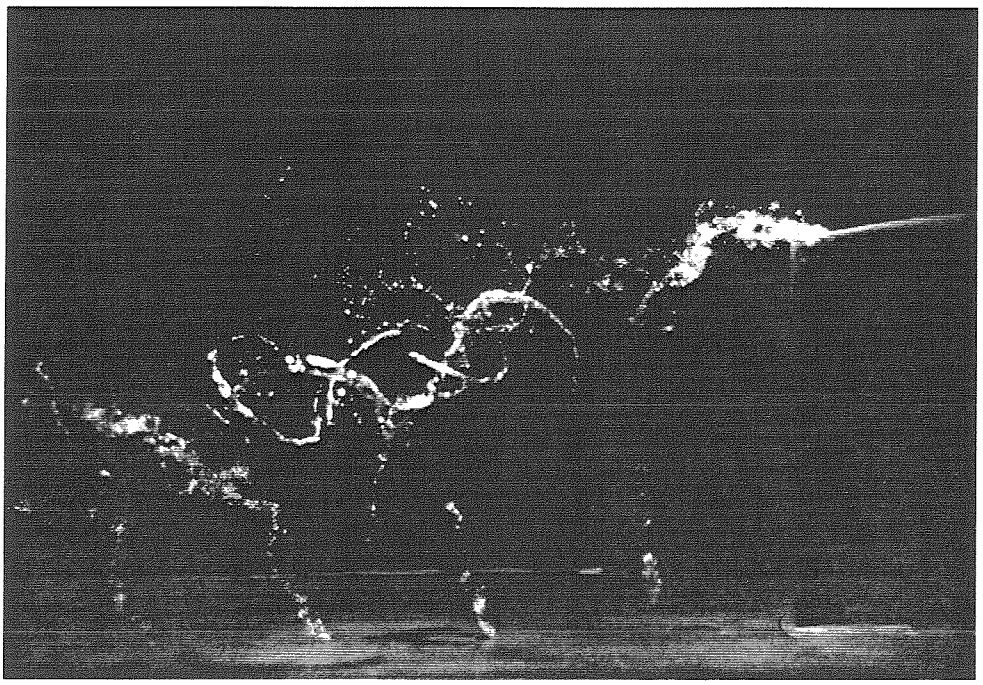

Figure 3.3 Tip Vortex Structure Made Visible by Air Injection
Air is injected into the tip vortex structure of the hydrofoil oscillating at a high reduced frequency. The air is entrained into the low pressure region of the trailing wake structures providing clear visualization of the complex vortex structures.

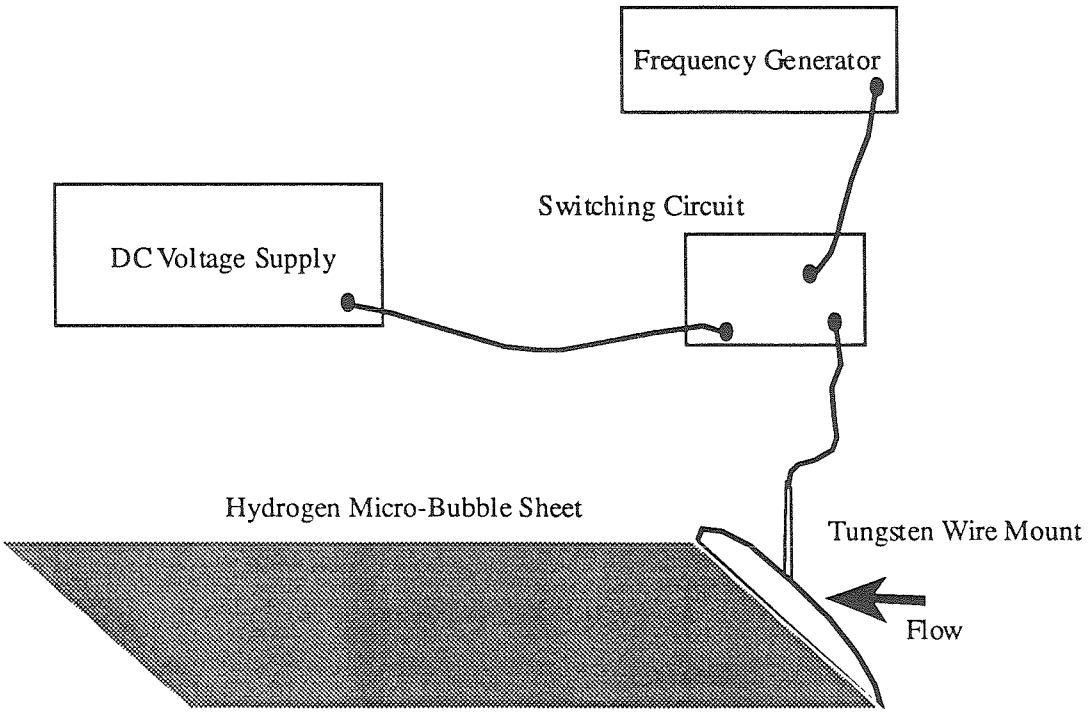

Figure 3.4 Hydrogen Micro-Bubble Flow Visualization Setup
A 25μm tungsten wire connected to a 60V, 1 amp. DC power supply generates a sheet of 50μm hydrogen bubbles . Two halogen lamps illuminate the micro-bubble sheet from below. The hydrogen bubbles, because of their small size, closely follow the flow. Near the core of the trailing vortex formations, however, there is a strong pressure gradient and a slight drift between the fluid and the hydrogen bubbles exist.

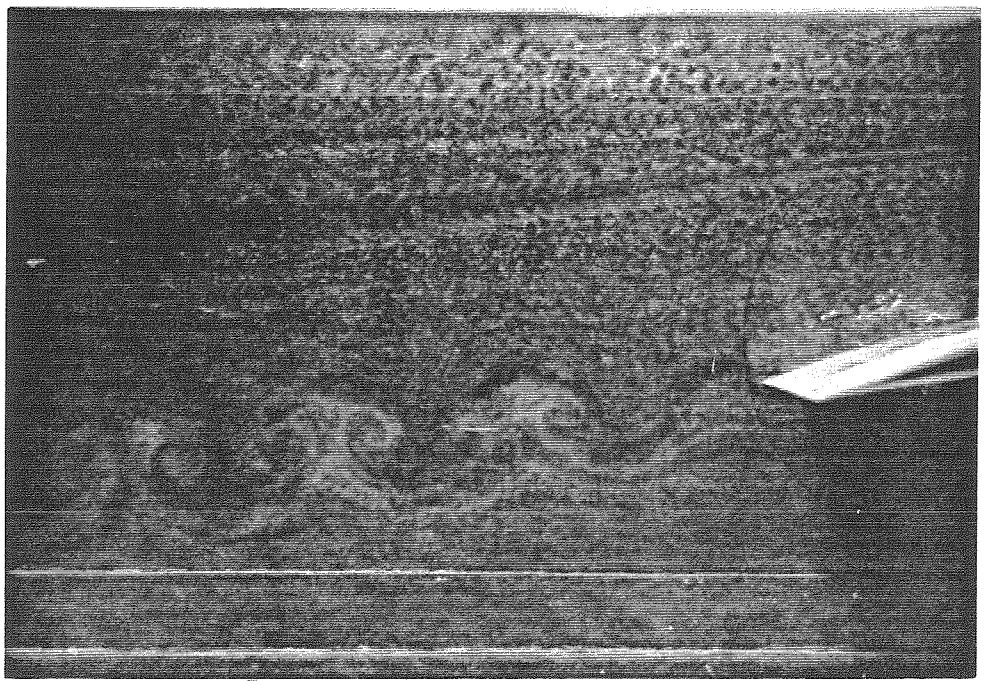

Figure 3.5 Wake Structure of an Oscillating Two-Dimensional Hydrofoil Made Visible by Hydrogen Micro-Bubbles

Hydrogen micro-bubbles generated by a 25μm tungsten wire mounted upstream of the foil trace the flow around a hydrofoil oscillating in pitch in two-dimensional flow conditions. This flow visualization technique provides a means of studying fine details of the formation of the vortex structures in the wake.

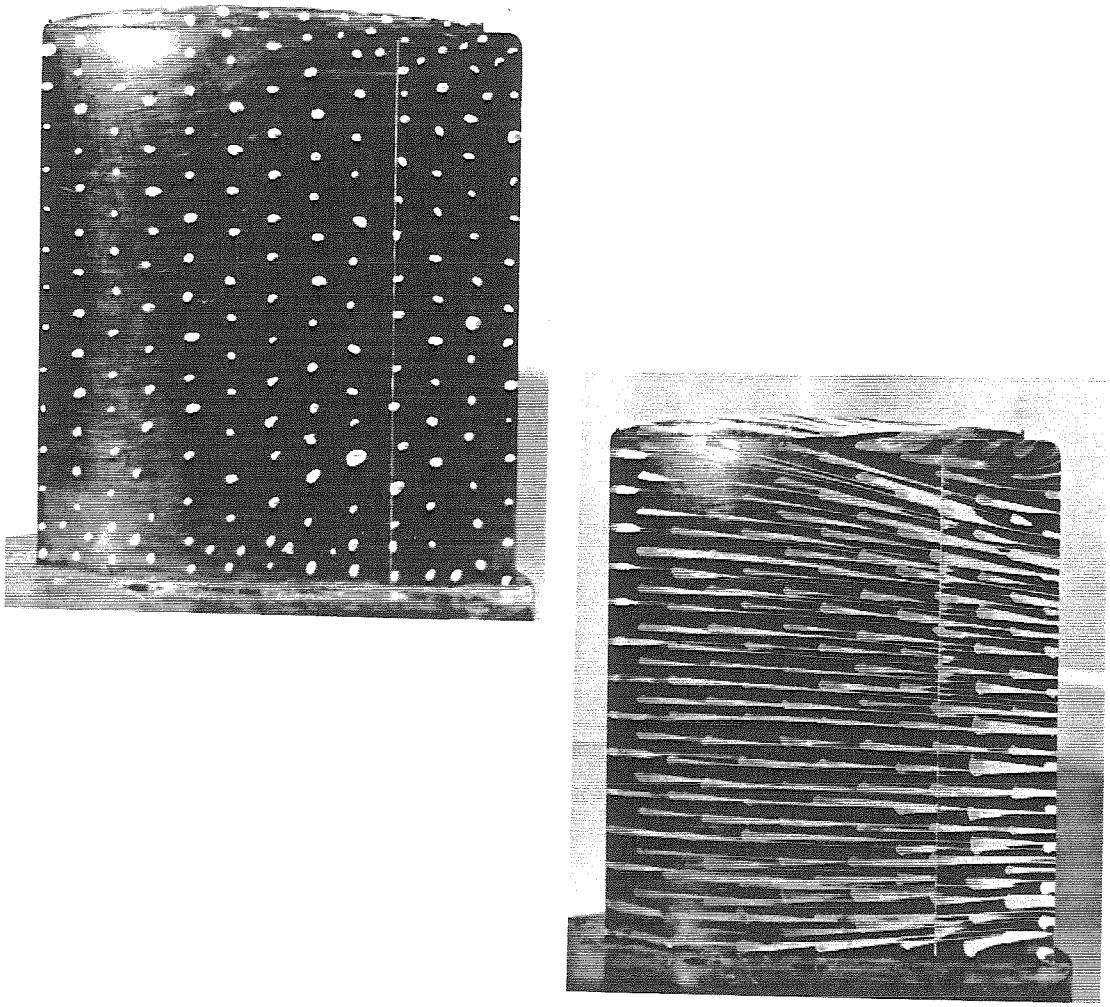

Figure 3.6 Paint Dot Surface Flow Visualization
Paint dots made from oil based paint and linseed oil are placed in a grid pattern on the surface of the hydrofoil. These paint dots indicate the mean flow direction on the surface of the hydrofoil by forming streaks in the direction of the local flow.

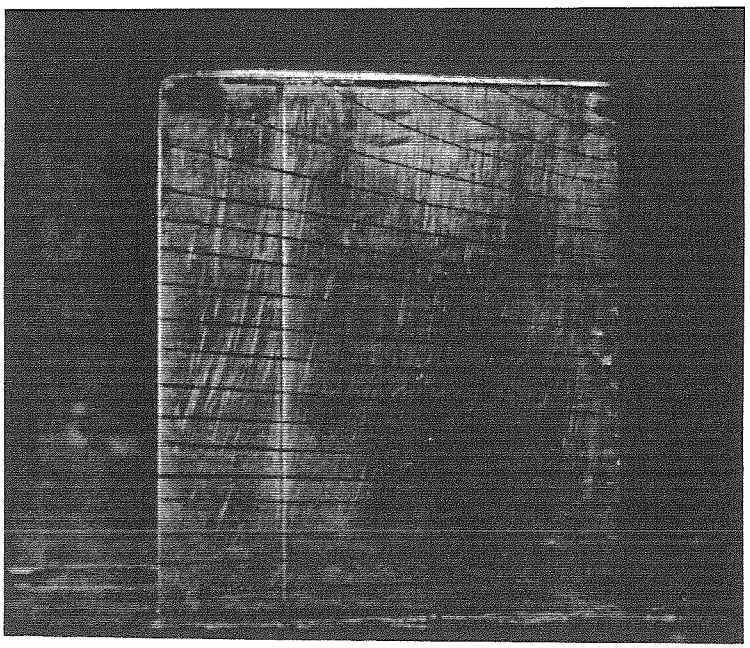

Figure 3.7 Surface Flow Visualization Using Telltales
Cotton thread is glued to the leading edge of the hydrofoil. The ends of these treads indicate the direction of flow near the trailing edge. This method of surface flow visualization clearly indicated the presence of a phase lag between the motion of the fluid and the phase of the hydrofoil.

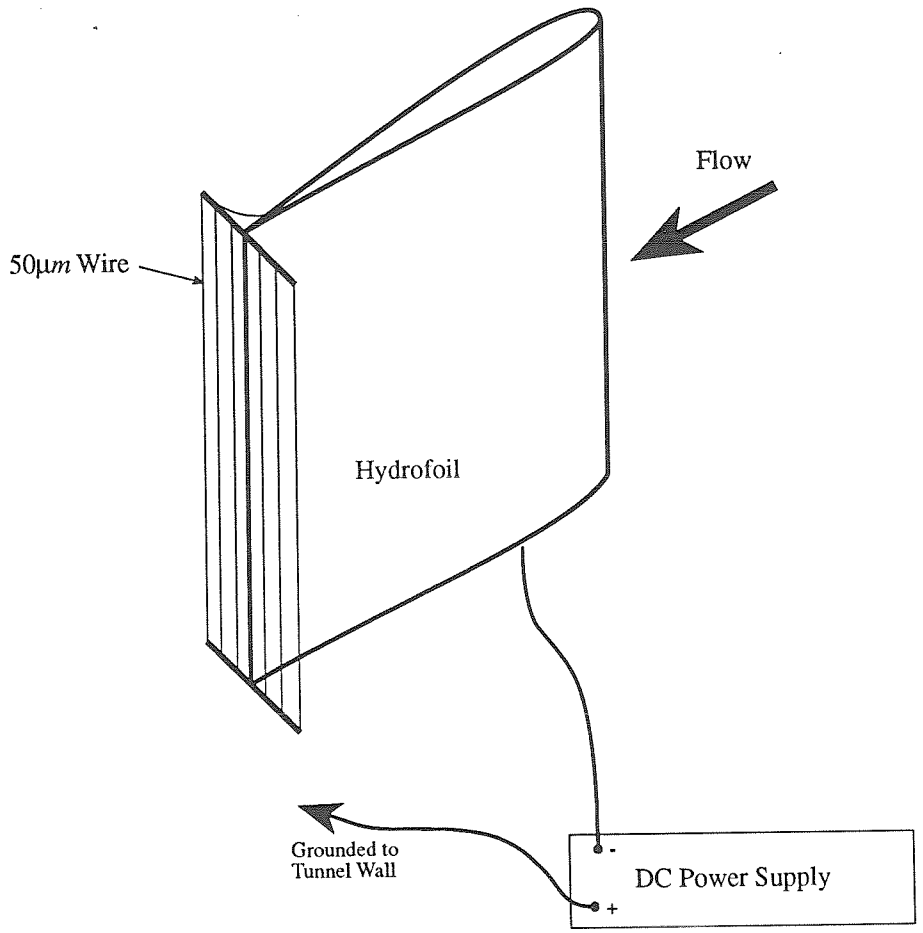

Figure 3.8 Hydrogen Bubble Seeding of Wake Flow
Wires fastened to brackets on the hydrofoil generated hydrogen bubbles ranging in size from 10μm to 100μm. Triple-pulsed holograms of the wake flow determined the velocity of these hydrogen bubbles providing information on the direction of rotation of the trailing vortex structures. The complexity of the unsteady wake of the oscillating hydrofoil prevented use of this type of flow measurement for quantitative studies of unsteady induced vorticity.

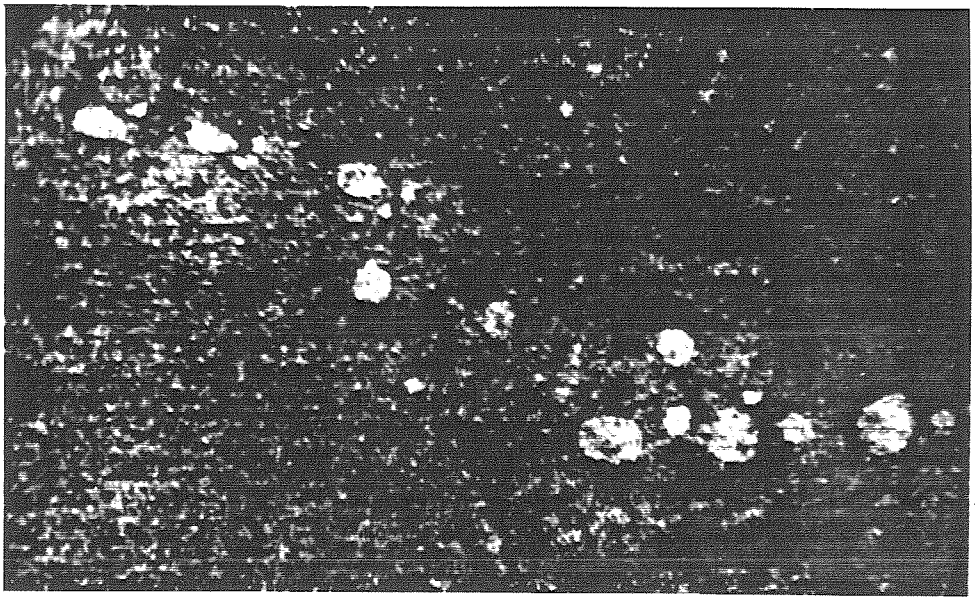

Figure 3.9 Typical Three-Pulsed Holographic Image
This is a photograph of a typical reconstructed three-pulsed holographic image showing bubbles in the flow behind an oscillating hydrofoil. The average bubble size shown in this photograph is 150μm. The duration between the first and second pulse is 150μs and between the second and third pulse is 80μs. By taking triple pulsed images with varying time delays in this fashion, the sign of the velocity vector can be determined, which is critical to the analysis of complex flows.

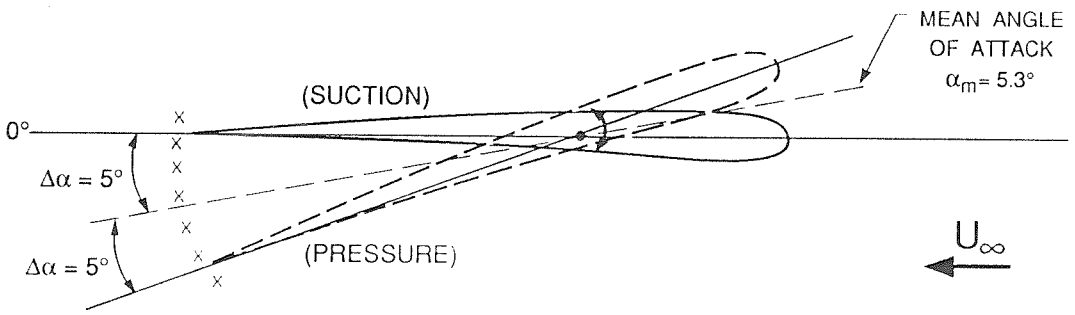

Figure 3.10 Schematic Showing Location of LDV Measurements in the Wake of an Oscillating Hydrofoil

A Dantec Particle Dynamic Analyzer, PDA, was used as a single axis LDV to measure the velocity in the wake of an oscillating hydrofoil. Schematic shows the locations at which data was obtained relative to the hydrofoil. LDV data was recorded in phase with the hydrofoil motion at seven locations perpendicular to the hydrofoil span at the 20%, 50%, and 80% span of the hydrofoil.

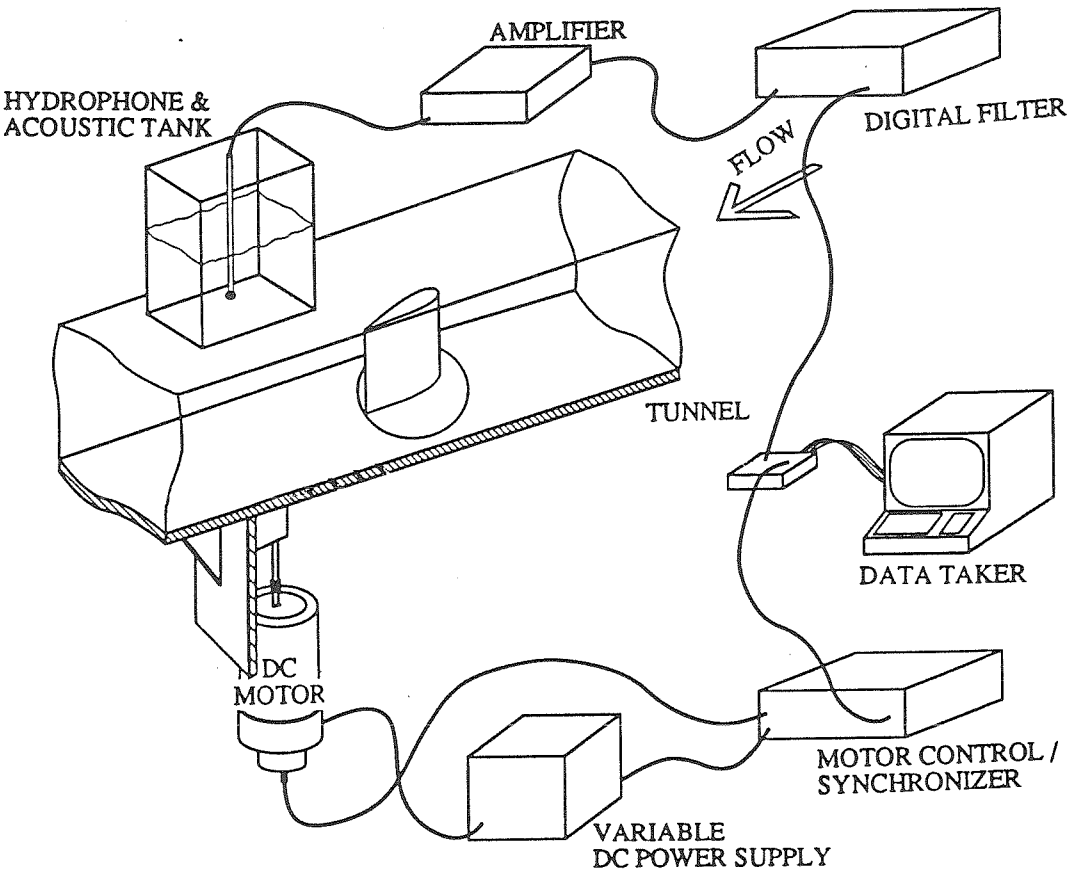

Figure 3.11 Acoustical Detection System Used to Determine Cavitation Inception on the Surface of the Hydrofoil

Hydrophone mounted in water in a Plexiglas tank on top of the LTWT test section detects cavitation events. The output of the hydrophone is amplified with a high bandwidth amplifier and high-pass filtered with a four-pole 8kHz butterworth electronic filter to rid the signal of tunnel operation noises. The output is then fed to a digital data taker which records the cavitation events along with the phase of the hydrofoil.

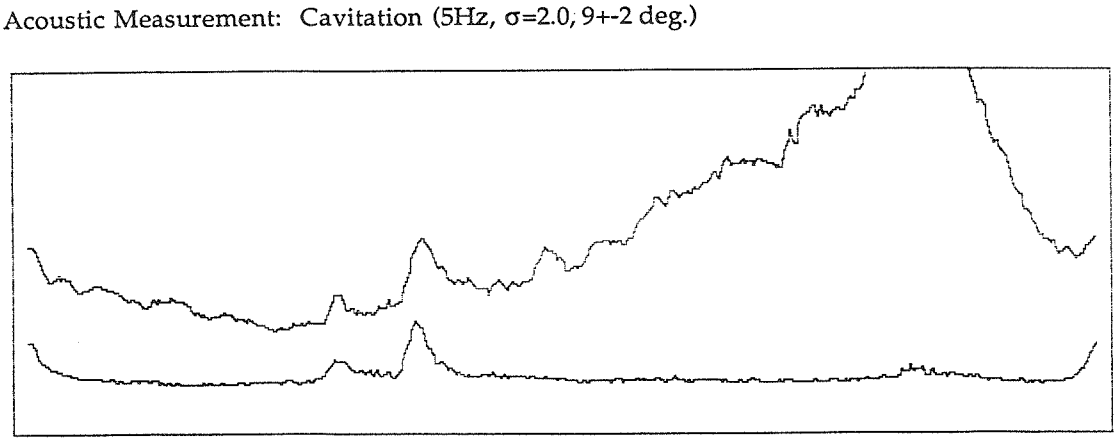

Figure 3.12 Typical Acoustical Data Trace Showing Cavitation Event
Acoustical determination of cavitation events is a common experimental technique for determining the inception of cavitation. At low tunnel speeds and low oscillation frequencies this technique works very well with the oscillating hydrofoil. The top acoustical data trace shown here was taken with the hydrofoil cavitating. The bottom trace was taken under non-cavitating conditions.

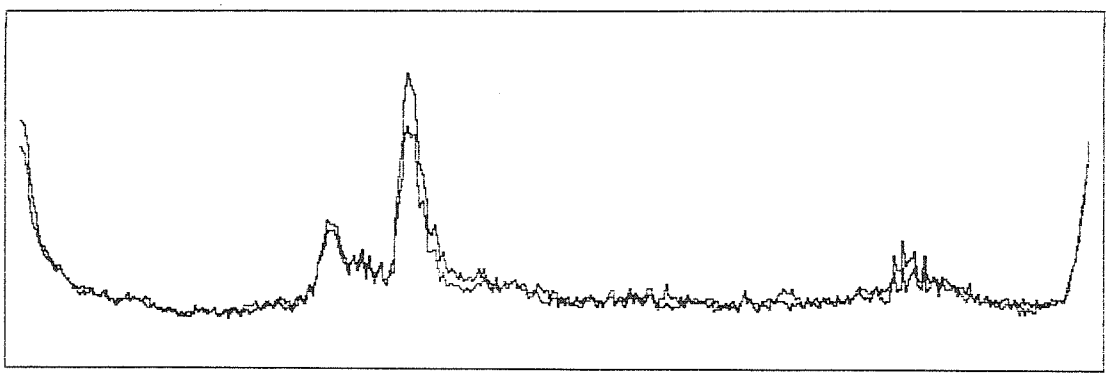

Figure 3.13 Acoustical Data Trace at a High Hydrofoil Oscillation Rate
At high tunnel speeds and at high hydrofoil oscillation frequencies, the mechanical noises that are generated become significant preventing accurate determination of cavitation events. The above acoustical data traces demonstrate this. The top trace shows the acoustical output when the hydrofoil is cavitating and the bottom trace shows the oscillating hydrofoil under non-cavitating conditions.

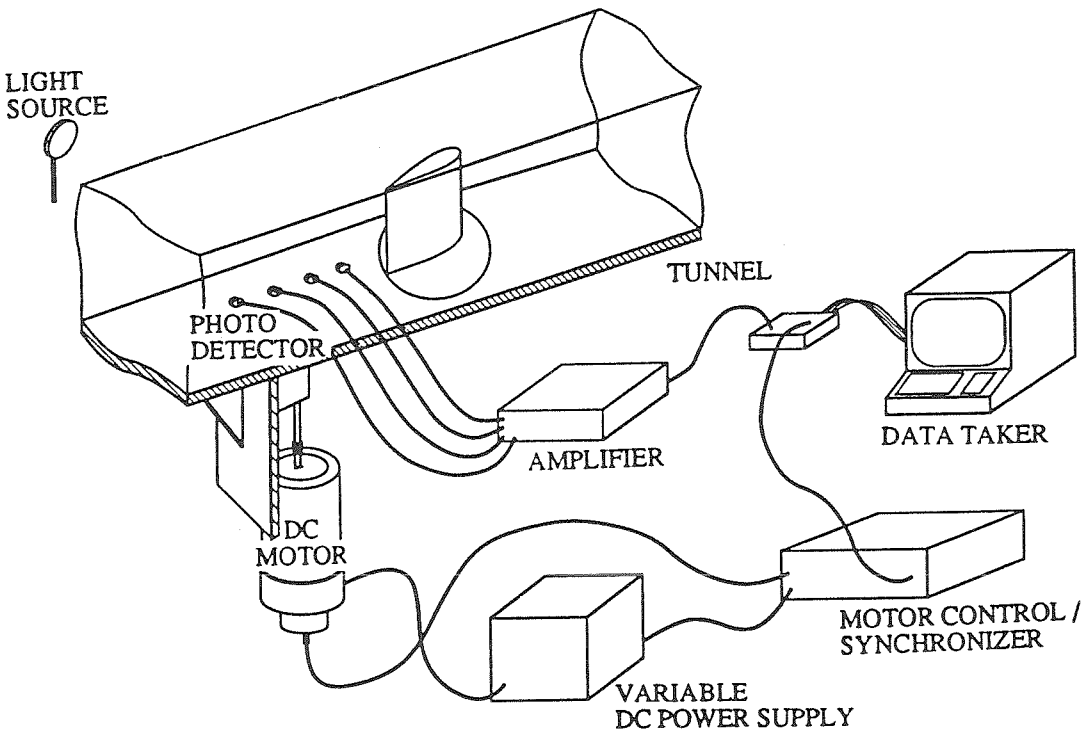

Figure 3.14 Schematic of Photo-Diode System Used to Detect Cavitation Inception

An array of six photo-diodes mounted to an adjustable frame located against the test section window was used to detect the inception of cavitation. A halogen light illuminated the flow. Cavitation occurring in the vortex cores cast shadows on the photo-diode array. A digital data taker recorded the cavitation events along with the phase of the hydrofoil. By cross-correlating between diodes, the multiple diode array provided a means of detecting not only the cavitation event rate but also the phase at which the hydrofoil generated the vortex structure where cavitation first appeared as well as the downstream location where cavitation initiated.

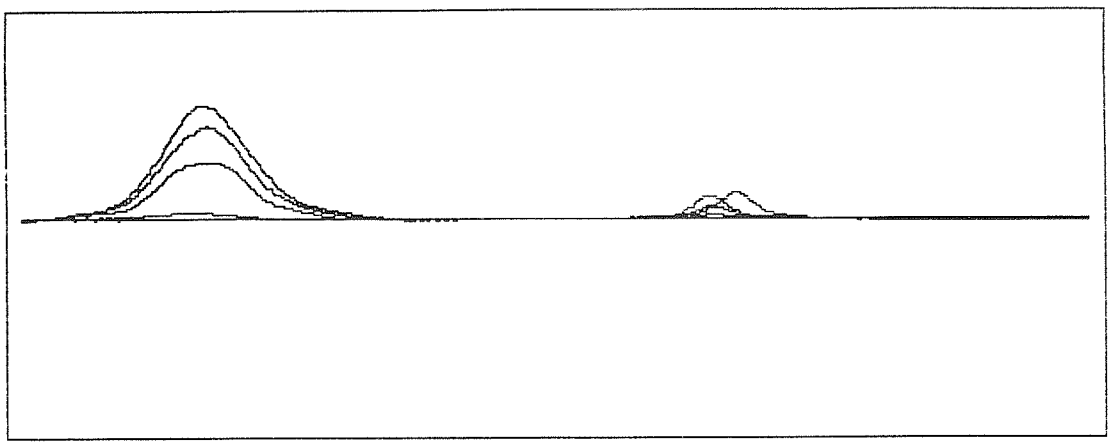

Figure 3.15 Typical Photo-Diode Array Data Trace
Data traces from six photo-diodes showing cavitation traveling downstream. Cavitation appears between the third and fourth diodes and re-absorbs near the fifth. Diode traces are plotted as a function of hydrofoil phase, allowing the position of the hydrofoil during the formation of the cavitating trailing vortex structure to be determined by cross-correlation.

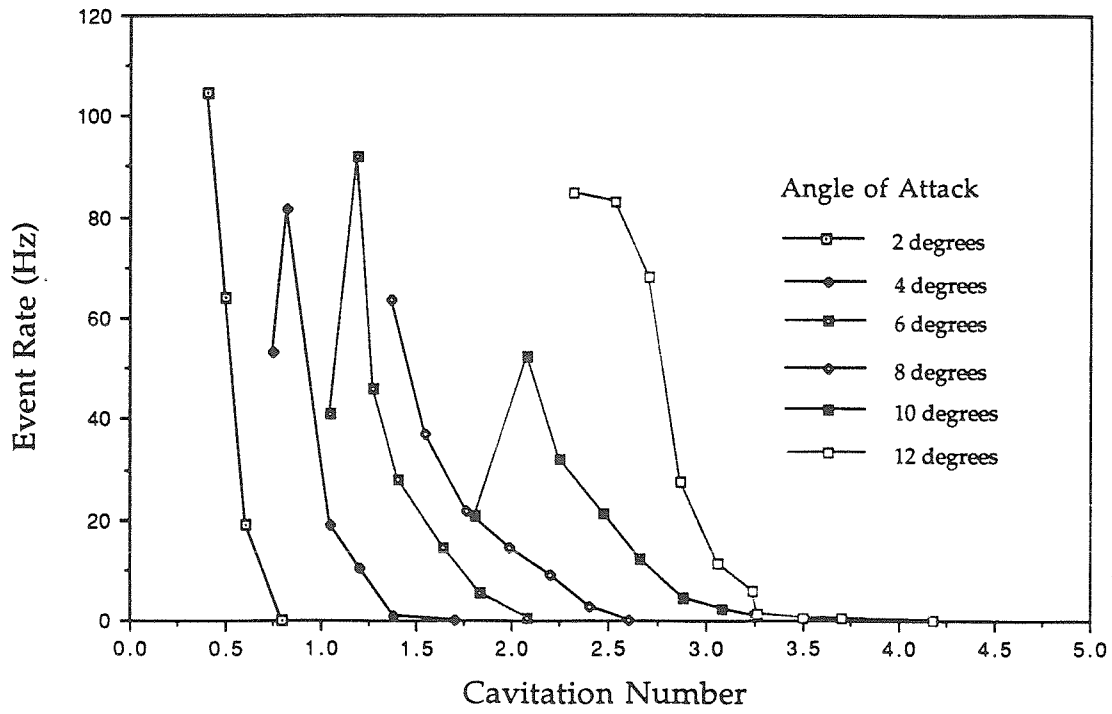

Figure 3.16 Cavitation Event Rate as a Function of Cavitation Number for Angles of Attack Ranging from 2° to 12°

Photo-diodes detect cavitation in the tip vortex region of the hydrofoil wake. The hydrofoil is not oscillating in this case. The photo-diodes provide a means of clearly defining a transition point which can be thought of as the inception of cavitation. Here, the sharp bends in the cavitation event rate curves are taken as the point of cavitation inception. Note also the drop in event rate at the low cavitation numbers in three of the traces. This is the result of attached cavitation forming at the foil tip.

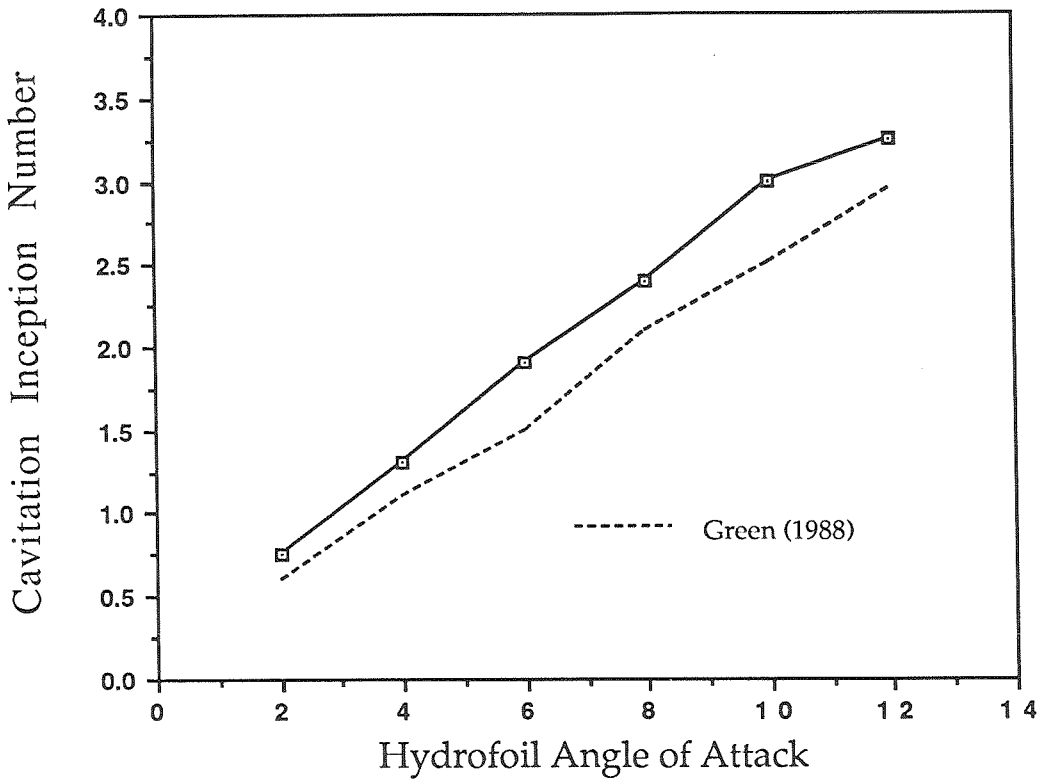

Figure 3.17 Comparison of Cavitation Inception Number For a Non-Oscillating Hydrofoil

Cavitation inception measurements of a non-oscillating hydrofoil using a photo-diode optical technique are compared with data taken by Green [1988] who used a visual technique. The slight discrepancy between the two curves may be the result of a difference in devolved air content. Both of the curves were taken with an assumed air content of 6ppm. The actual air content of the LTWT often drifts slightly as the tunnel is operated.

CHAPTER 4

UNSTEADY WAKE STRUCTURE

This chapter describes the unsteady wake structure generated by the oscillation of the hydrofoil. The intricacy of the three-dimensional wake evolves from two distinct sources of vorticity: The changes in circulation about the foil caused by the oscillatory motion generate periodically shed spanwise vortices, and flow over the foil tip rolls up into a tip vortex which extends far downstream and interacts with the spanwise vortices. The spanwise vortex generation was isolated by observing the hydrofoil in the two-dimensional configuration described earlier, providing a baseline for analyzing the wake structure formed by the finite aspect ratio foil.

4.1 Spanwise Vortex Structure

Previous experimental studies of two-dimensional, harmonically pitching hydrofoils have shown the formation of vortices in the wake that are shed periodically with the change in angle of attack of the foil [Abramson, Chu, Irick 1967; DeLaurier, Harris 1981; Katz 1981; Koochesfahani 1989; Satyanarayana 1978]. Figure 4.1 shows that these vortices are also significant components in the wake of oscillating finite aspect ratio hydrofoils. Their generation can be explained from both analytical and physical perspectives.

Analytically, the vortices must be shed if Kelvin's Theorem is to be satisfied, i.e., for the circulation in the flow as a whole to remain unchanged. As the angle of attack of a foil increases, the circulation about the foil also tends to increase, until stall occurs. By Kelvin's Theorem, then, this increase in spanwise circulation must be matched by a corresponding decrease elsewhere in the flow. Thus, a spanwise vortex forms at the trailing edge of

the foil, its circulation equal and opposite to the change in circulation induced by the change in angle of attack, and is subsequently swept downstream with the flow. As the foil oscillates and the circulation around the foil increases and decreases, then, the vorticity in the wake will do the same.

In physical terms, consider first that the fluid around the hydrofoil is not perfectly coupled to the foil. As the foil oscillates it creates a force on the fluid, pulling it in the direction of oscillation. When the foil reaches an extremum in the oscillation cycle and begins to change its direction, the inertia of the fluid hinders it from precisely following the motion of the foil. A shear force is generated in the fluid pushing past the leading and trailing edges of the foil (see Figure 4.2). This force causes the fluid to roll up into vortex structures which travel downstream with the flow.

4.1.1 Experimental Observations

The two-dimensional component of the wake was examined by removing the tip of the hydrofoil and installing a Plexiglas panel over the top, as described in Chapter 3. An illuminated hydrogen bubble sheet highlighted a cross-section of the wake flow, tracing the formation and interaction of the spanwise vortices shed from the trailing edge of the oscillating foil. From photographs and video tape recordings of the flow two distinct vortex shedding regimes were observed.

For low reduced frequencies (k<4) and low oscillation amplitudes ($\Delta\alpha$ <5°), the wake consisted primarily of a train of small Kàrmàn vortices which traced the sinusoidal path of the trailing edge of the foil, as shown in Figure 4.3. These vortices were shed at a frequency much higher than the foil oscillation frequency. When the excitation frequency or oscillation amplitude

were sufficiently increased, however, distinct larger vortices began to roll up at the trailing edge, appearing to absorb the smaller vortices. As the larger vortices convected downstream they were seen to draw together in pairs within the wake, merging and drifting away from the center of the tunnel.

The transition between the two regimes depended on both frequency and amplitude. For an oscillation amplitude of ±2°, for example, the vortices tended to start rolling up when $k>4$, whereas for an amplitude of ±5°, $k>2$ was sufficient. Figure 4.4 shows the two-dimensional wake in the *rollup* regime, defined by the occurrence of vortex rollup within two chord lengths of the trailing edge of the foil. The transition from a smooth sinusoidal wake flow to a regime where vortex pairs are formed is illustrated in Figures 4.5 to 4.8.

4.1.2 Discussion

The flow mechanism that distinguishes the two shedding regimes appears to be the balance between the strength of the shed vortices and the diffusion of vorticity — for the lower reduced frequencies or smaller oscillation amplitudes, the vorticity shed by the motion of the trailing edge diffuses before any discernible rollup can take place.

In the rollup regime, the vortices interact with one another within the wake as they are swept downstream. Due to the dynamic coupling of the fluid to the foil, the phase at which these formations are shed relative to the foil phase is dependent on the reduced frequency and amplitude of oscillation, thus the pattern of these vortex formations as they leave the foil depends largely on the motion of the foil. In the wake the vortices tend to draw together in opposite-rotating pairs. Once paired, the mutual induced

velocities of the vortices drive them away from the center of the tunnel as they travel downstream.

Katz and Weihs [1978] and Koochesfahani [1989] have theorized that the angle the vortex pairs make with one other is related to the thrust generated by the motion of the foil. Garrick [1936] theorized based on Theodorsen's analyses that, neglecting viscous losses, a two-dimensional hydrofoil oscillating in pitch about the center of pressure will develop thrust at a reduced frequency of oscillation greater than one, $k>1$. This is clearly a much lower reduced frequency than that at which the vortex pairs are seen to form in the wake of an experimental oscillating foil.

4.2 Tip Vortex Formation

Many theoretical, numerical, and experimental studies have been made of steady tip vortex flows. In certain real-world applications, such as the airliner wake shown in Figure 1.10, a steady flow is a reasonable and useful approximation, since the spanwise wake component is negligible compared to the strength of the tip vortices and has negligible effect on the downwash of the wing. In highly unsteady three-dimensional flows, however, such as a propeller rotating in the wake of a ship or the oscillating hydrofoil of the current study, the introduction of the tip vortex flow greatly complicates the structure of the vortex formations in the wake. As illustrated in Figure 4.9, the tip vortex links to the spanwise vortices forming a complex chain.

4.2.1 Experimental Observations

As discussed in Chapter 3, two techniques were used to observe the tip vortex structure in the wake of the finite aspect ratio hydrofoil. In Figure 4.10, dye has been injected into the tip vortex core of the oscillating hydrofoil. The

photographs in this figure show one complete cycle of oscillation of the hydrofoil. The dye forms puffy structures as it traces the flow in the tip vortex region. As can be seen in this figure, these structures are very stable and travel downstream with the flow. In Figures 4.11 and 4.12, air has been injected into the low pressure region of the tip vortex core. The air is pulled into the cores of the spanwise vortex formations, tracing the complex interaction between the tip vortex and the shed spanwise vortices. (For clarity, Figure 4.13 shows a sketch of the vortex structure in Figure 4.11 and 4.12.)

An intriguing component of the vortex interaction in the wake structure is the pairing of the spanwise vortices. For high reduced frequencies and/or oscillation amplitudes, the injected air shows a link between the vortex shed at the minimum angle of attack with that shed at the maximum angle, one such structure for each oscillation cycle. This pattern is shown in the photograph in Figure 4.14 and sketched in Figure 4.15 for an oscillation amplitude of ±5°. When the frequency or amplitude is sufficiently low, however, the pairing changes. The linking now appears to occur between vortices of consecutive oscillation cycles, i.e. between the vortex shed at the minimum angle of one cycle with the one shed at the maximum angle of the subsequent cycle. The sketch in Figure 4.13, for an amplitude of ±2°, shows this type of pairing. The mean angle of attack does not seem to affect the vortex pairing, as long as the hydrofoil remains at a positive angle of attack over the entire oscillation cycle.

Under all oscillation conditions, the trailing vortex structure slopes toward the base of the hydrofoil as it leaves the trailing edge. Further downstream, the structure appears to break down, forming a helical spiral

around the position where the tip vortex would be located on a stationary hydrofoil. This helical vortex formation continues downstream beyond the end of the test section with no apparent change in structure.

4.2.2 Discussion

The structure of the wake of the finite aspect ratio hydrofoil is dramatically more complicated than the simple introduction of a tip vortex to the two-dimensional wake discussed earlier in this chapter. As described in Chapter 1, *two* spanwise vortices now appear to be shed by the trailing edge at each extremum of the oscillation cycle. Both vortices rotate in the same direction, and thus their mutual induced effect is to twist about one another, as Figure 4.16 indicates. Where the spanwise vortices meet the tip vortex the pair splits apart again, and each vortex wraps around the tip vortex as shown in Figure 4.9. One vortex wraps in the upstream direction and one wraps downstream from the intersection; thus one of the vortices will be rotating in the same direction as the tip vortex and the other will be rotating in the opposing direction. The former will augment the strength of the tip vortex and the latter will attenuate it, resulting in a periodic change in the effective strength of the tip vortex.

The attenuated segments of the tip vortex, where the vortex core pressure will be highest, appeared in the dye injection study as puffs and in the air injection case as small clouds of bubbles. In the air injection case, the apparent changes in vortex pairing can be attributed to the entrainment of the air into lower pressure regions of the vortex structure. For large oscillation amplitudes, the strength of the spanwise vortices approaches that of the tip vortex, so the wrapping of the vortices produces a greater variation in the tip

vortex strength. The pressure at the vortex core will be lowest where the tip vortex is augmented, thus more of the injected air will be entrained into those segments.

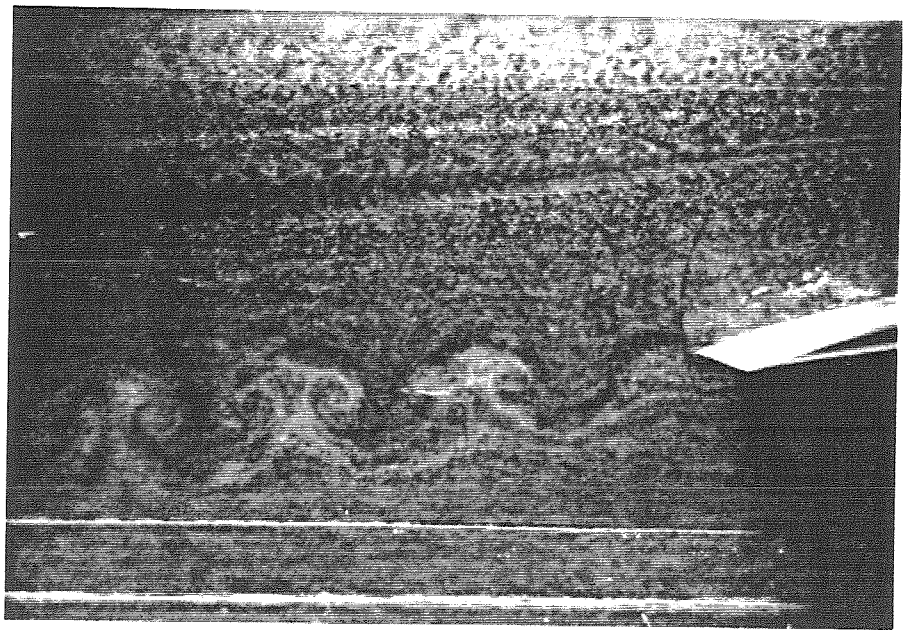

Figure 4.1 Spanwise Vortices in the Wake of a Finite Aspect Ratio Oscillating Hydrofoil, k=7

A hydrogen micro-bubble sheet illuminates the rollup of spanwise vortex pairs shed from an aspect ratio 2.3 rectangular planform hydrofoil The micro-bubble sheet cuts the foil near the root at the 20% span of the foil (α_m=5°, $\Delta\alpha$=±5°, k=5).

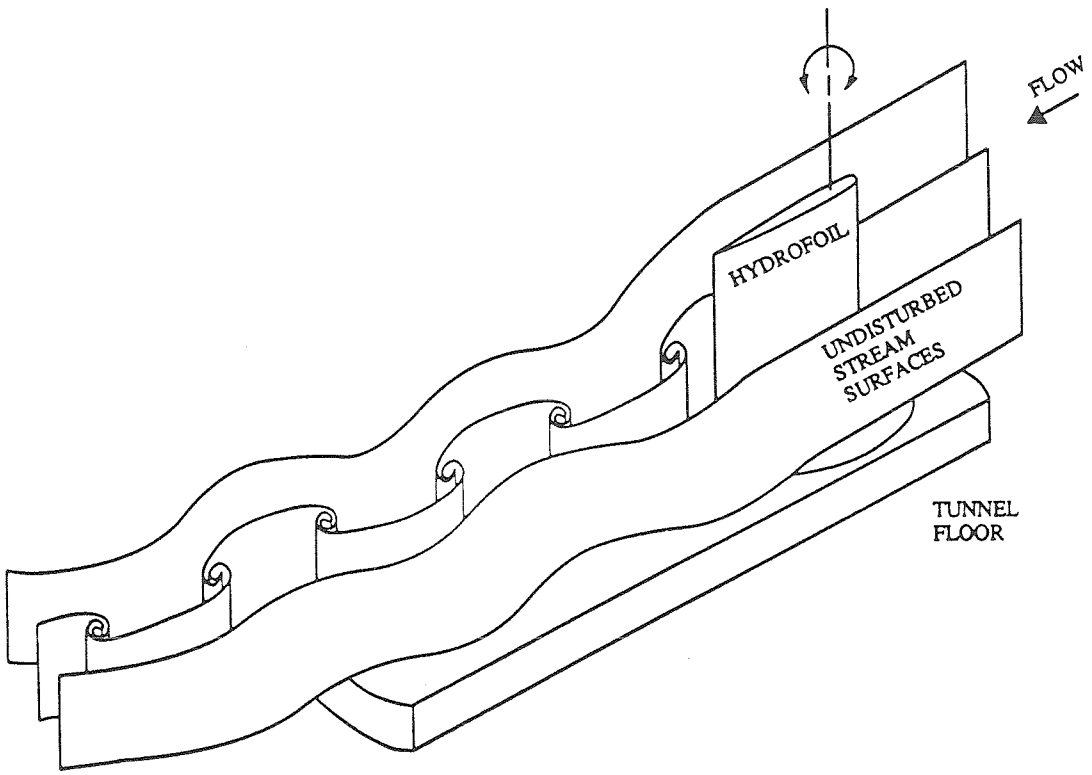

Figure 4.2 Schematic of Spanwise Vortex Formation in the Wake of a Two-Dimensional Oscillating Hydrofoil

This schematic illustrates the vortex formations in the wake of an oscillating two-dimensional hydrofoil. A pair of these vortices form during each oscillation cycle. The circulation around each vortex is equal but opposite to the change in circulation about the foil as the angle of attack of the foil changes.

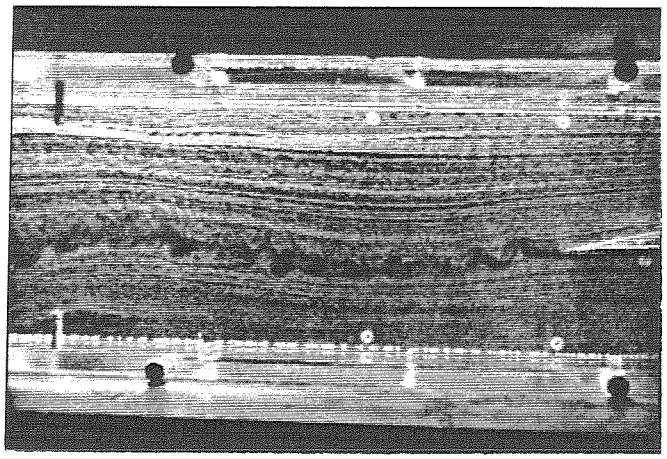

Figure 4.3 Kármán Vortices Shed from an Oscillating Two-Dimensional NACA 64A309 Hydrofoil

A hydrogen micro-bubble sheet traces the flow in the wake of a two-dimensional oscillating foil. The Kármán vortex street formed by the boundary layer of the foil can be seen along the sinusoidal path of the oscillating wake structure of the foil (α_m=5°, $\Delta\alpha$=±2°, *k*=2).

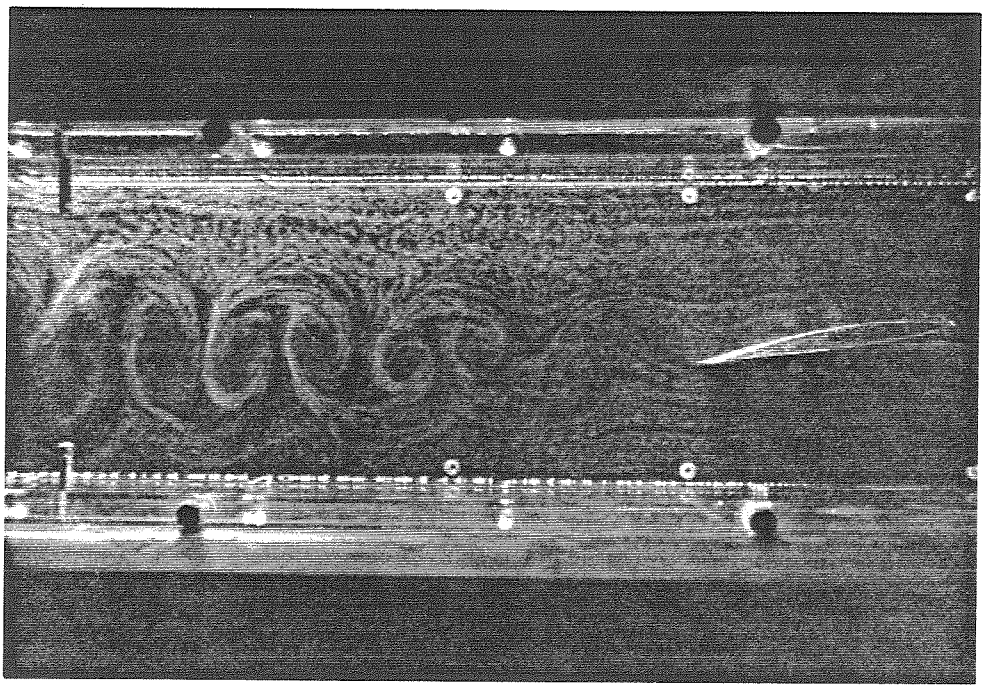

Figure 4.4 Spanwise Vortices in the Wake of an Oscillating Two-Dimensional NACA 64A309 Hydrofoil

A hydrogen micro-bubble sheet illuminates the rollup of spanwise vortex pairs shed from the two-dimensional hydrofoil during each oscillation period (α_m=5°, $\Delta\alpha$ =±2°, *k*=7).

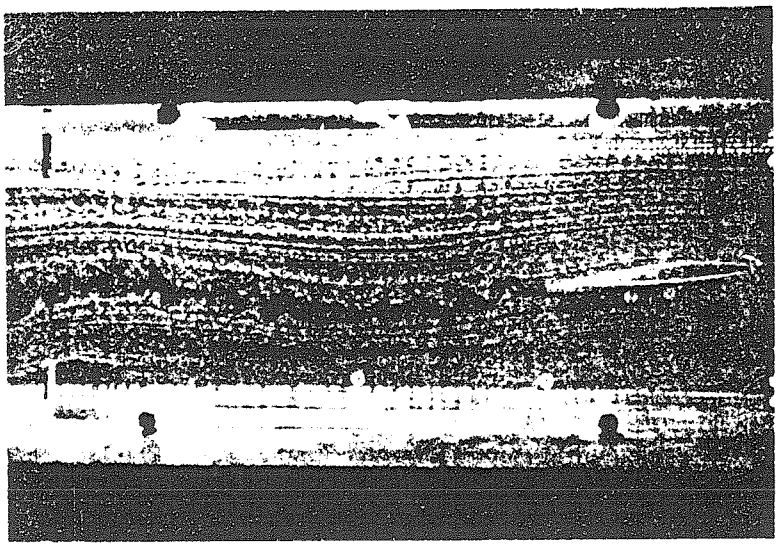

Figure 4.5 Kármán Vortex Street in the Wake of a Two-Dimensional Hydrofoil
Kármán vortex street can be seen in the sinusoidal track of the wake behind a two-dimensional hydrofoil. The reduced frequency of oscillation is too low to form vortex structures (α_m=7°, $\Delta\alpha$=±2°, k=2).

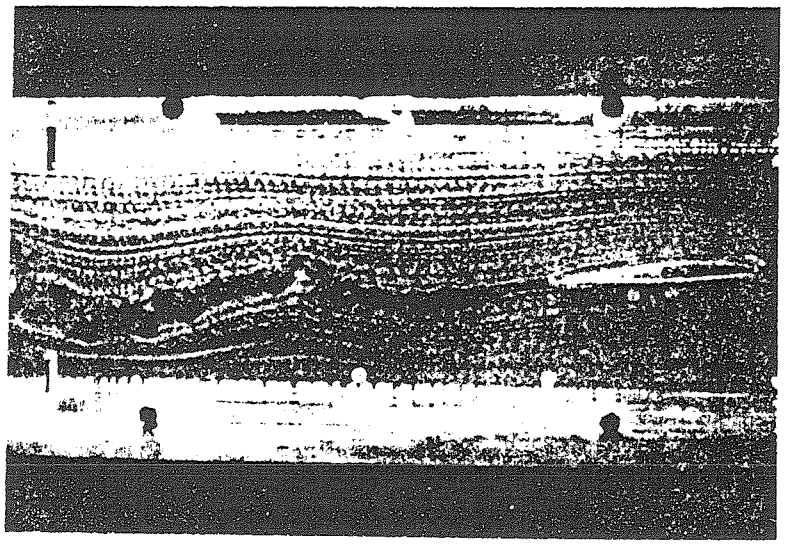

Figure 4.6 Beginning of Roll Up of Two-Dimensional Wake Structure
Spanwise vortex structures can be seen beginning to form in the wake of this two-dimensional oscillating hydrofoil wake(α_m=7°, $\Delta\alpha$=±2°, *k*=4).

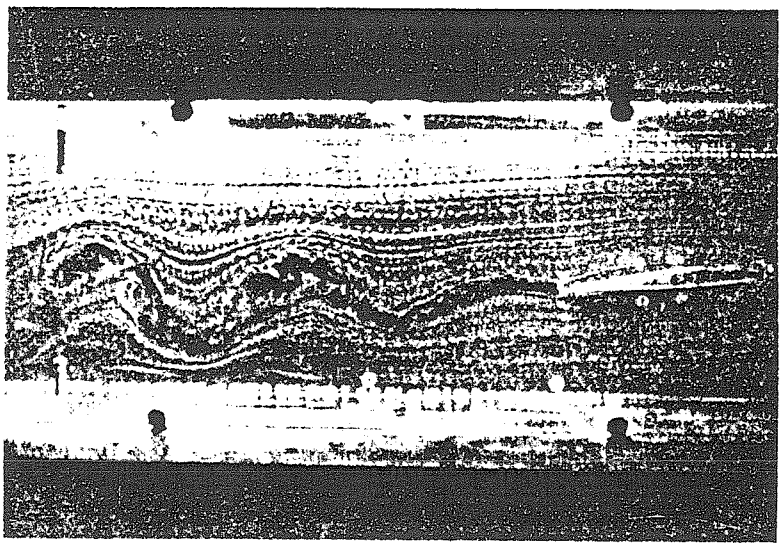

Figure 4.7 Spanwise Vortex Pairs in the Wake of a Two-Dimensional Hydrofoil
Pairs of spanwise vortex structures are apparent in the wake of the hydrofoil. These vortex structures stretch the Kármán vortices as they roll up into them(α_m=7°, $\Delta\alpha$=±2°, *k*=6).

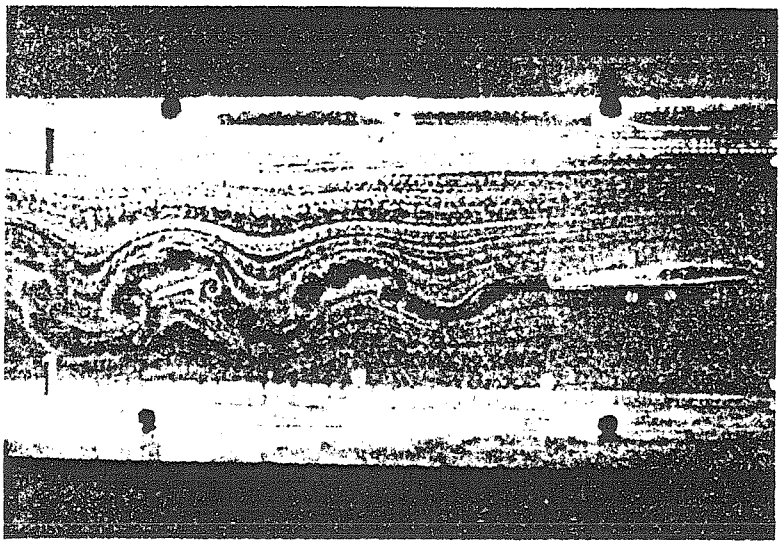

Figure 4.8 Wake Formation of Two-Dimensional Hydrofoil at High Reduced Frequency

At these very high reduced frequency, the spanwise vortex formation are clearly visible in the wake of this two-dimensional hydrofoil as it oscillates in pitch. The vortex pairs angle in the flow direction. It is theorized that this angling of these structures is indicative of the generation of thrust by the oscillating foil (α_m=7°, $\Delta\alpha$=±2°, k=7).

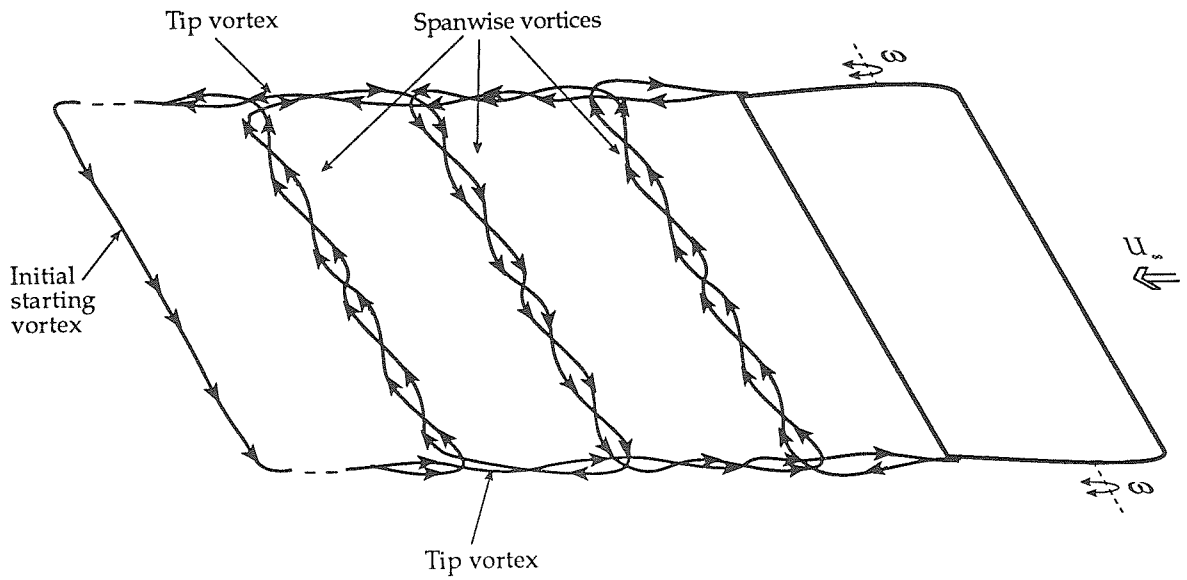

Figure 4.9 Schematic of Vortex Structure in the Wake of a Three-Dimensional Hydrofoil Oscillating in Pitch.

This schematic shows a simplified model of the trailing vortex structure in the wake of a finite aspect ratio oscillating hydrofoil. During each oscillation cycle a pair of spanwise vortices is formed. The net circulation around the pair is zero corresponding to a zero net change in circulation about the hydrofoil. These spanwise vortices link to each other by wrapping around the tip vortex, which produces periodic changes in the circulation of the tip vortex structure.

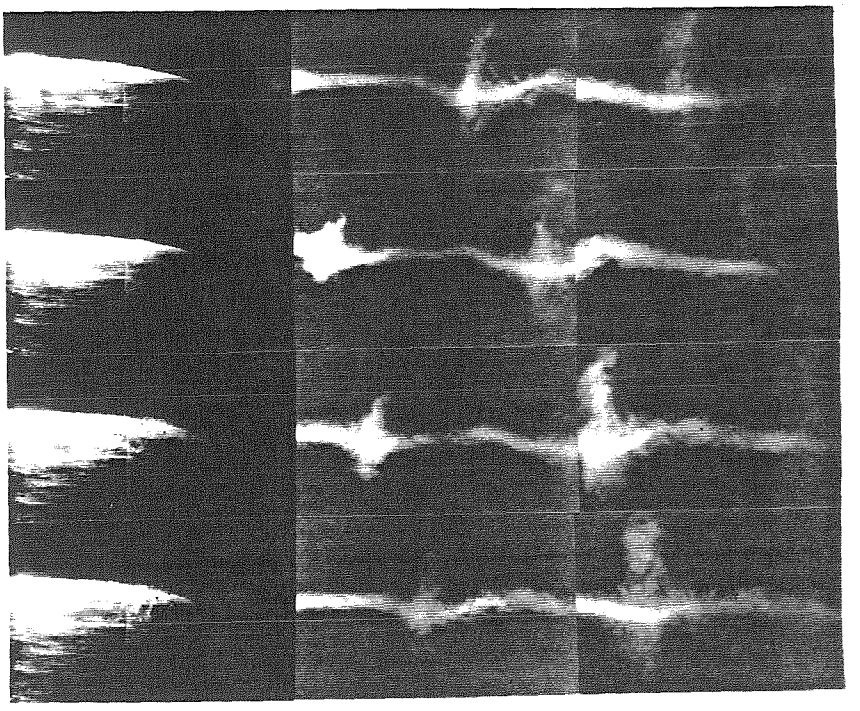

Figure 4.10 Photograph Showing Dye Injection Into the Tip Vortex Region of an Oscillating Hydrofoil, k=5.5

This is a series of photographs taken of one cycle of a hydrofoil oscillating ±5° about a 5° mean angle of attack. Each photograph shows a 5° change in angle of attack. Dye is injected into the tip vortex of the hydrofoil. The small "puffs" that occur at regular intervals down stream are regions where the spanwise vortex formations interact with the tip vortex formation. These are regions where the strength of the tip vortex is weakened.

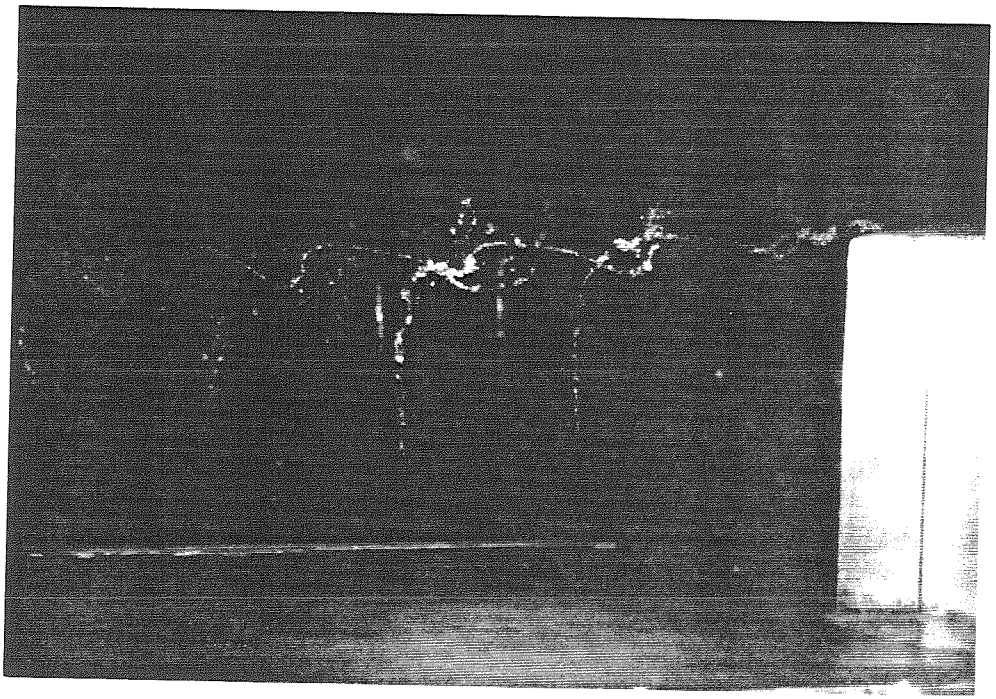

Figure 4.11 Photograph Showing Air Injection Into the Tip Vortex Region of a Hydrofoil Oscillating ±2° about a 7° Mean Angle of Attack, k=5.5
Air injected into the tip vortex is entrained into the vortex core providing a means of visualizing its structure. Interactions between the span-wise vorticity and the tip vortex results in a complex chain.

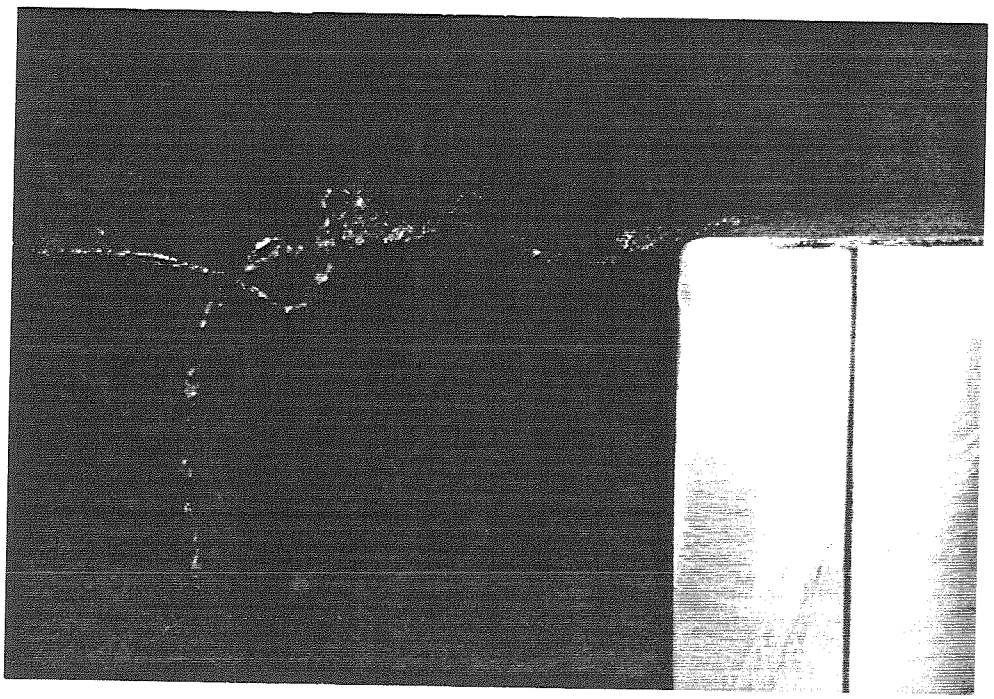

Figure 4.12 Close-up of Air Injection into the Tip Vortex Region of a Hydrofoil Oscillating ±2° about a 7° Mean Angle of Attack, k=5.5
This is a more detailed view of the wake structure shown in Figure 4.12.

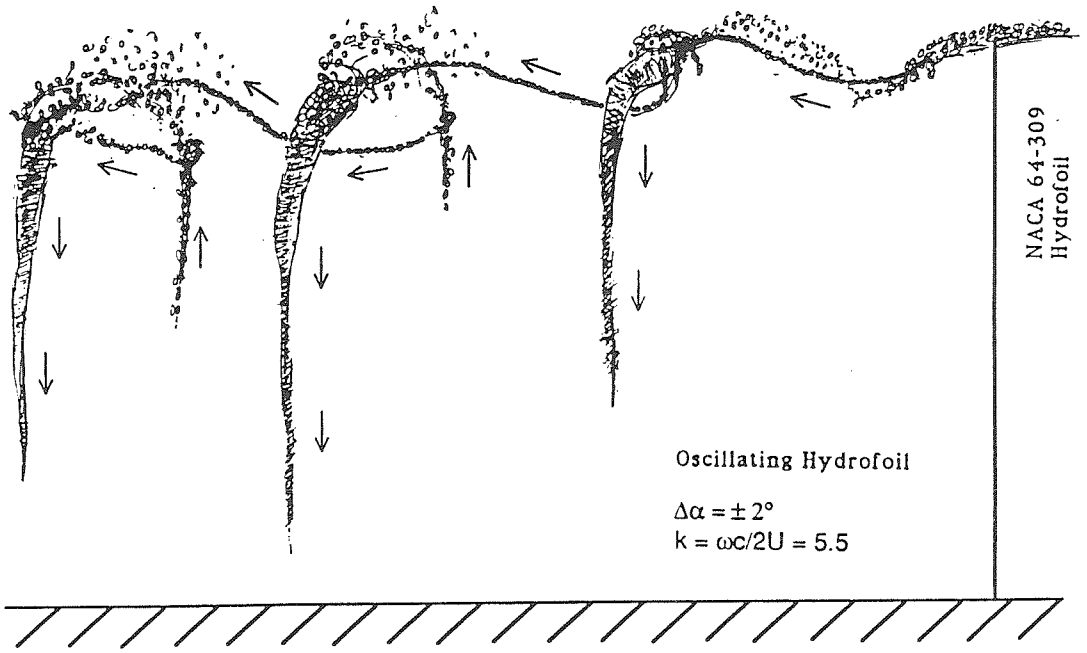

Figure 4.13 Schematic of the Tip Vortex Structure of a Hydrofoil Oscillating ±2° about a 7° Mean Angle of Attack, *k*=5.5

At an oscillation amplitude of ±2°, a strong link between the spanwise vortex structure formed at the minimum angle of attack of the hydrofoil and the spanwise formation formed at the maximum angle of attack during the proceeding cycle is prominent. The arrows in this schematic indicate the direction of the vorticity.

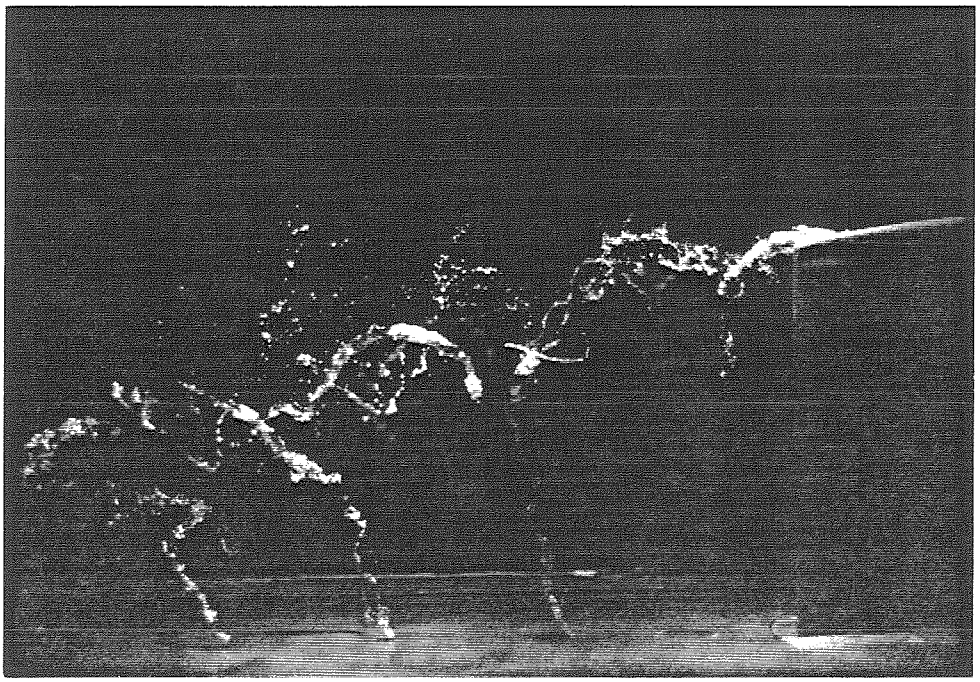

Figure 4.14 Photograph Showing Air Injection Into the Tip Vortex Region of a Hydrofoil Oscillating ±5° about a 7° Mean Angle of Attack, k=5.5
Air injected into the tip vortex is entrained into the vortex core providing a means of visualizing its structure. Interactions between the span-wise vorticity and the tip vortex results in a complex chain.

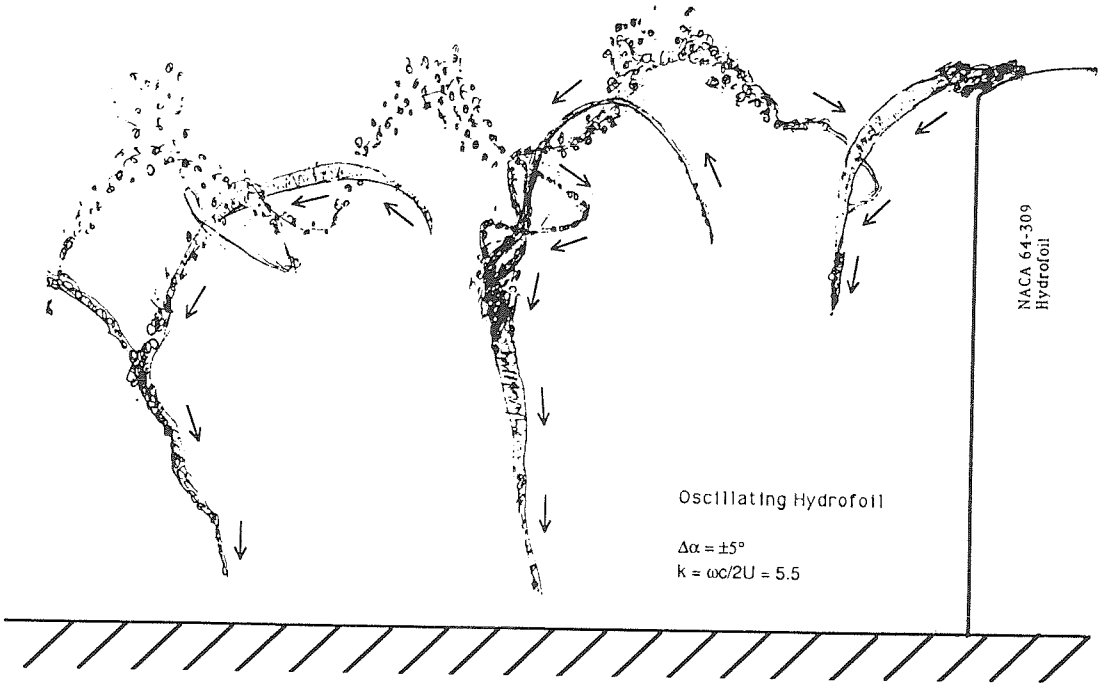

Figure 4.15 Schematic of the Tip Vortex Structure of a Hydrofoil Oscillating ±5° about a 7° Mean Angle of Attack, *k*=5.5

At an oscillation amplitude of ±5°, a strong link between the spanwise vortex structure formed at the minimum angle of attack of the hydrofoil and the spanwise formation formed at the maximum angle of attack during the same cycle is prominent. The arrows in this schematic indicate the direction of the vorticity.

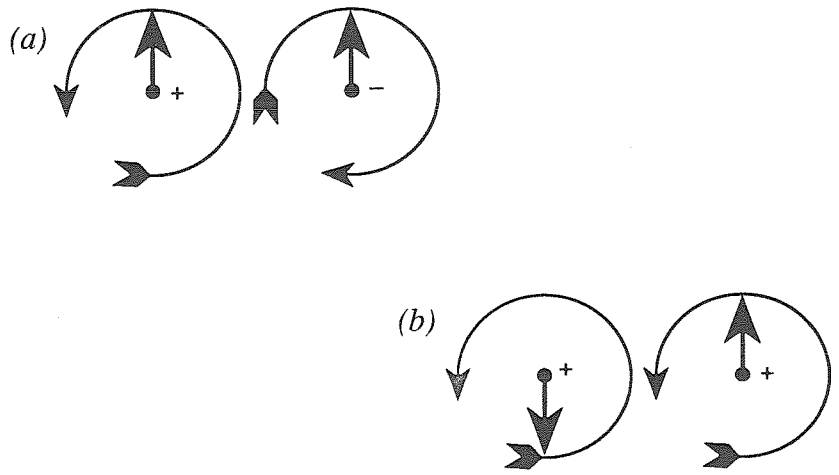

Figure 4.16 Illustration of Induced Velocities on Adjacent Vortex Filaments
This figure illustrates the velocities induced by neighboring vortices. Vortices with rotations in opposite direction (A) propel each other in the same directions. Vortices with the same rotations (B) induce velocities on each other which twist the pair about one another.

CHAPTER 5

EFFECTS OF UNSTEADY FLOW ON CAVITATION

Presented in this chapter are observations and measurements of surface and tip vortex cavitation on a hydrofoil harmonically pitching with an amplitude of ±2° at a mean angle of attack of 7°. The experimental tests presented here were made for reduced frequencies ranged from 0.2 to 2.0, and Reynolds numbers ranged from 11×10^5 to 13×10^5. A dissolved air content of *6ppm* was maintained throughout these tests. In all cases, cavitation inception was first observed in the tip vortex about three chords downstream from the trailing edge and occurred at a cavitation inception number of about 2.1. As the tunnel pressure was decreased, the cavitation moved upstream until it attached to the foil tip on the suction side near the trailing edge. Surface cavitation was first observed at a cavitation number of about 1.0, approximately half that of tip vortex cavitation inception.

5.1 Surface Cavitation

Experimental measurements and observations were made of the inception, growth, and collapse of surface cavitation on the hydrofoil. Surface cavitation was detected both by visual inspection and by the acoustical detection technique described in Chapter 3. Strobe lights were synchronized to the phase of the hydrofoil using the synchronization circuit described in Appendix D. The cavitation inception number at a particular phase of the foil was determined by setting the strobes to trigger at that phase and then lowering the tunnel pressure until cavitation was observed. The cavitation number was then read from the computers monitoring the tunnel. The criteria chosen for the identification of cavitation inception was the consistent

appearance of at least one bubble on the hydrofoil surface at the selected phase.

5.1.1 Growth and Collapse of Surface Vapor Cavity

Surface cavitation on the suction side of the hydrofoil first appears as traveling bubble cavitation which, as the cavitation number is reduced, quickly becomes attached cavitation near the base of the foil. With further reduction, the cavitation grows from the base outward towards the tip. The trailing edge of this attached cavity has a parabolic shape, following the pressure contour characteristic of this foil, except near the tunnel floor. The boundary layer of the tunnel floor appears to suppress cavitation near the mid-chord and trailing edge of the foil. When the surface cavity collapses (due to the natural shedding frequency of the cavitation, the oscillation of the foil or a combination of both), a bubbly cloud near the base of the hydrofoil is formed. A ring vortex often emerges from the downstream side of this cloud as the cloud begins to detach from the foil, and both cloud and vortex then dissipate several chords downstream of the trailing edge.

Cavitation on the surface of the foil sheds and reforms at a frequency not only dependent on the excitation frequency but also on the Reynolds number of the flow. In general, surface cavitation forms and collapses with the oscillation of the hydrofoil. There exists a phase lag, however, between the extent of the surface cavitation and the foil oscillation, which tends to increase with increased frequency. At lower reduced frequencies, surface cavitation forms and grows appreciably before the hydrofoil has reached its maximum angle of attack. The cavitation then remains until the hydrofoil angle of attack is well below that at which inception occurs. At higher reduced foil frequencies (0.3 or greater) surface cavitation does not grow significantly until

well after the hydrofoil has reached its maximum oscillation amplitude, but again it persists until the hydrofoil angle of attack is below the point of inception. This seems to suggest that the natural shedding frequency of the cavitation is not completely dominated by the hydrofoil excitation frequency, and that the variation in the phase lag may in some way represent the changing roles of the two frequencies in the unsteady cavitation process.

The photographs in Figures 5.1, 5.2, and 5.3 illustrate this interaction between the natural shedding frequency and the excitation frequency. They show the suction side of the hydrofoil operating at a Reynolds number of 12×10^5 and a cavitation number of 0.5 as it oscillates from 9° to 5° in 0.5° increments. Figure 5.1 shows the hydrofoil at a reduced frequency of 0.35, slightly below the cavity shedding reduced frequency of 0.47 observed when the hydrofoil was held stationary at 7° angle of attack. Notice the two distinct cavities that exist at 7.5° angle of attack and the ring vortex that remains from a previous cavity collapse.

As the excitation frequency is increased to 0.47 (Figure 5.2), two separate collapses no longer occur. Observations at this frequency reveal that the points of cavitation formation and collapse during an oscillation cycle are very inconsistent. At an excitation frequency of 0.70 (Figure 5.3) the pattern of cavity formation and collapse remains very similar to that at 0.47, but the points during the oscillation cycle at which they occur have now become quite consistent. In addition, both the 0.47 and the 0.70 excitation cases result in a loud pounding sound as the cavities collapse. Note the phase lag between the hydrofoil angle of attack and the extent of cavitation that exists in all three sets of photographs.

Figure 5.4 summarizes the observations of leading edge cavitation on the oscillating hydrofoil. Points on the various curves represent minimum cavitation numbers at which cavitation was observed on the foil at the given phase and reduced frequency. For a stationary hydrofoil such curves would be symmetrical, since without oscillation only the position of the foil is important. For the oscillating case, however, the effect of the motion of the foil is illustrated by the asymmetry of the curves. The motion tends to delay inception in the first half of the cycle and to delay desinence in the latter half, as has just been discussed.

The extent to which the motion delays both inception and desinence is better illustrated in Figure 5.5. Here the measurements are plotted in the form of a hysteresis diagram, with the lower traces representing an increasing angle of attack and the upper traces representing a decreasing angle of attack. As the excitation frequency increases, the hysteresis increases as well. This appears to be due to the changing angle of attack of the leading edge of the foil, as will be discussed in the following section.

5.1.2 Effect of Kinematic Change in Angle of Attack

As the hydrofoil oscillates, a velocity component normal to chord of the foil is induced. This induced velocity causes a change in the effective angle of attack of the foil at the leading edge (see Figure 5.6), which can be expressed as

$$\alpha_e = \alpha - \tan^{-1}\left[\frac{1}{U_\infty}\left(\tfrac{c}{2} - a\right)\omega\Delta\alpha\cos(\omega t)\cos(\alpha)\right] \tag{5.1}$$

where a is the distance from the center of the foil to the point of oscillation and the motion of the foil is $\alpha = \alpha_m + \Delta\alpha\sin(\omega t)$. When the surface cavitation

inception measurements are plotted relative to this angle of attack (Figure 5.7), the data collapses well enough to suggest a universal relationship between inception and the instantaneous hydrodynamic angle of attack. For the range of reduced frequencies investigated, then, it appears that the increase in cavitation inception number is primarily due to the increase in hydrodynamic angle of attack resulting from the kinematics of the oscillating foil.

5.2 Tip Vortex Cavitation

Experimental measurements and observations were made of the inception, growth, and collapse of tip vortex cavitation on the finite aspect ratio hydrofoil as it oscillated in pitch. Tip vortex cavitation was detected using the optical photo-diode detection technique described in Chapter 3.

Under conditions of low to moderate reduced frequencies, $k<1.5$, and moderate angles of attack, $0^\circ<\alpha<10^\circ$, cavitation first appears in the tip vortex region about three chords downstream of the hydrofoil trailing edge. At higher reduced frequencies, cavitation first appears at the trailing edge of the hydrofoil attached to the tip (apparently the result of the high acceleration forces generated by the oscillating motion). This cavitation, however, does not remain attached to the foil – shedding as the foil oscillates to a lower angle of attack and collapsing downstream. As the cavitation number is lowered at these high reduced frequencies, cavitation begins to appear three chords downstream as in the case of the hydrofoil oscillating at a lower reduced frequency. The following sections of this chapter concentrate of the inception of cavitation in the tip vortex formation downstream of the trailing edge of the foil.

5.2.1 Influence of Reduced Frequency on the Inception of Tip Vortex Cavitation

The oscillation phase at which cavitation inception occurs within the tip vortex is largely dependent on the reduced frequency and mean angle of attack of the hydrofoil. At low cavitation numbers or high mean angles of attack, cavitation develops near the maximum angle of attack of the hydrofoil where the tip vortex is strongest. At high reduced frequencies, cavitation inception does not occur in the vortex formation produced at the hydrofoil maximum angle of attack as one might expect, but occurs instead near the minimum. This is due to the dynamic interaction of the oscillating foil with the surrounding fluid. Cavitation in this case begins where the spanwise vortex merges with the tip vortex, and the bubbles are swept rapidly into the cores of both the spanwise vortices and the tip vortex formation (Figure 5.8).

Surface cavitation at the trailing edge of the hydrofoil near the tip is relatively independent of the reduced frequency of the hydrofoil. Cavitation in the tip vortex region downstream of the hydrofoil, on the other hand, is very dependent on the reduced frequency of the hydrofoil as shown in Figure 5.9. Here cavitation inception number is plotted as a function of hydrofoil reduced frequency for 5°, 7°, and 9° angles of attack. Note that the cavitation inception number decreases with increased reduced frequency and then increases as the reduced frequency is increased beyond about k=1.5. This is apparent at the 5°, and 7° mean angles of attack. At 9° mean angle of attack, the foil oscillates between 7° and 11°. This is close to the 12° angle of attack at which separation occurs on this particular hydrofoil and may account for the difference in the trend of this curve.

5.2.2 Cavitation Inception Mechanism

At the minimum angle of attack the spanwise vortex shed by the trailing edge of the foil rotates in the same direction as the tip vortex, resulting in a strong vortex formation near the tip of the hydrofoil where the two vortices merge. The reverse occurs at the maximum angle of attack of the hydrofoil, where the spanwise vortex formed at this phase angle rotates opposite to the tip vortex. The net result in this case appears to be a weakening of the vortex formation at the junction. This was shown in Figure 4.16, where arrows were used to indicate the direction of the vortex vectors. The weakening of the vortex formation in the figure is marked by a dispersion of air bubbles where the vortex core pressure is too weak to entrain the air effectively. As discussed in Appendix A, Theodorsen predicted the existence of a phase shift in the fluid loading of an oscillating foil. This phase shift is apparent on the NACA 64A309 hydrofoil in Figure 5.8. Near the trailing edge of the foil, on what would be the pressure side of a non-oscillating hydrofoil, traveling bubble cavitation can be seen as a consequence of the low pressure caused by a phase shift in the loading of the foil. On a finite aspect ratio hydrofoil, this phase shift results in a vortex formation near the tip of the hydrofoil which is weaker than that generated at the minimum angle of attack in an oscillation cycle. At moderate reduced frequencies, the location of cavitation initiation in the tip vortex between the spanwise vortex pairs is dependent on this phase shift. It moves from the region formed at the maximum angle of attack of the hydrofoil to the region formed at the minimum angle of attack as the reduced frequency is increased.

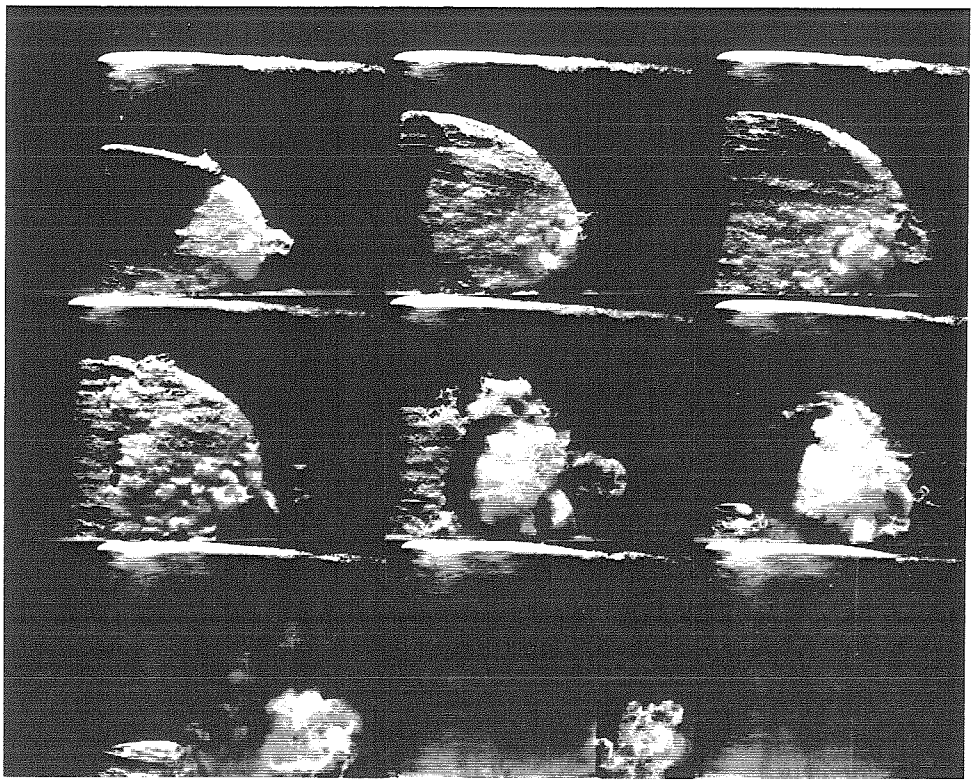

Figure 5.1 Photograph Showing Surface Cavitation on an Oscillating Hydrofoil During a Half Cycle of Oscillation at k=0.35

Surface cavitation starts as traveling bubble cavitation and quickly attaches at the leading edge of the hydrofoil to form a vapor cavity. This cavity grows and collapses with the hydrofoil oscillation. At hydrofoil oscillation frequencies equal to the frequency at which these vapor cavities form and collapse under non-oscillating conditions, the vapor cavities resonate creating a very violent collapse ($\Delta\alpha=\pm2°$, $\alpha_m=7°$, $Re=12\times10^5$, $\sigma=0.5$).

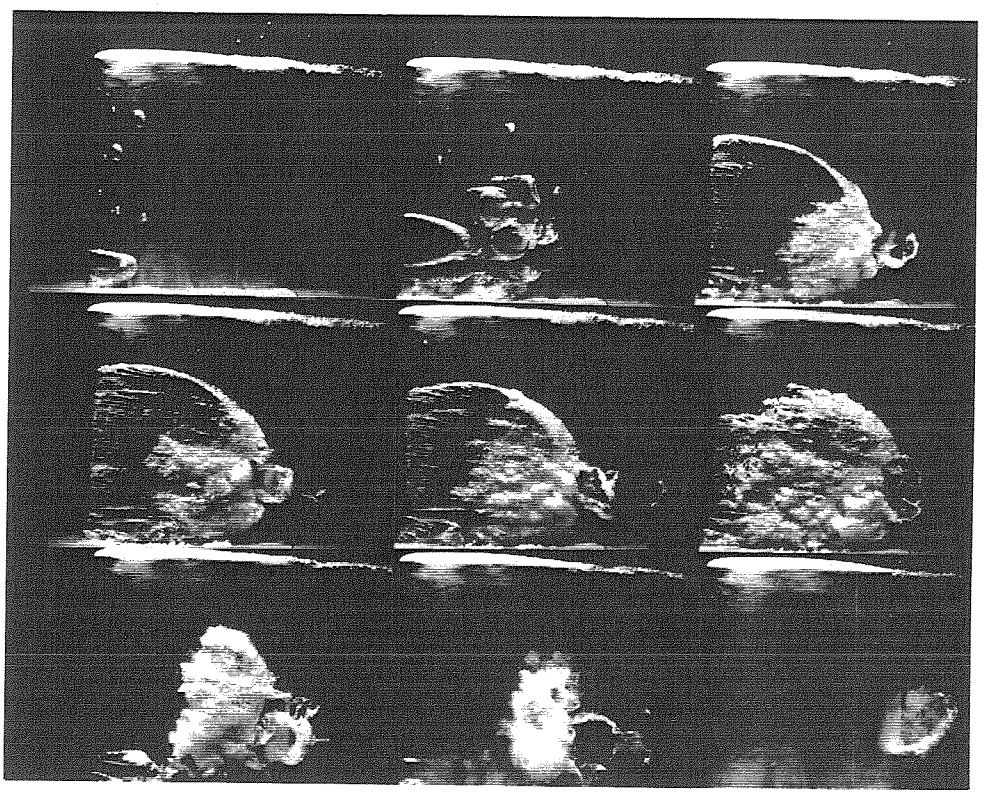

Figure 5.2 Photograph Showing Surface Cavitation on an Oscillating Hydrofoil During a Half Cycle of Oscillation at k=0.47

The hydrofoil in this series of photographs is oscillating at the same frequency the cavity at the leading edge of the hydrofoil forms an collapses under non-oscillating conditions. The magnitude of the cavity that results from the oscillatory motion results in an extremely violent collapse ($\Delta\alpha=\pm2°$, $\alpha_m=7°$, $Re=12\times10^5$, $\sigma=0.5$).

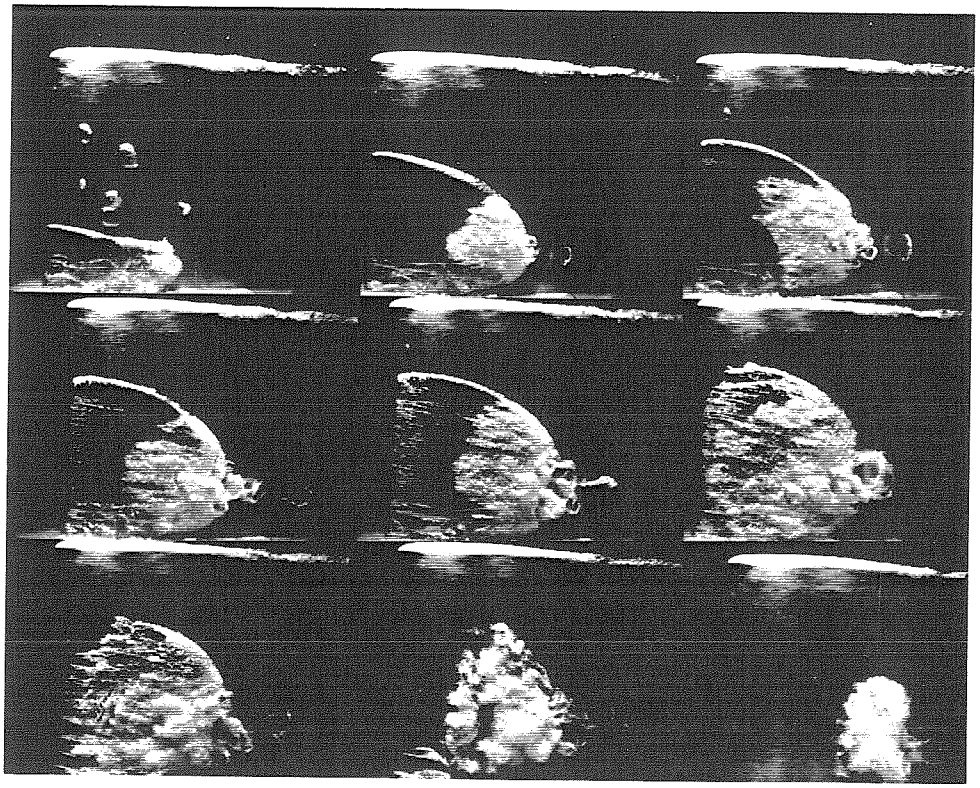

Figure 5.3 Photograph Showing Surface Cavitation on an Oscillating Hydrofoil During a Half Cycle of Oscillation at k=0.7

The hydrofoil in this series of photographs is oscillating at frequency slightly higher than the cavity at the leading edge of the hydrofoil forms and collapses under non-oscillating conditions. The vapor cavity that forms under these conditions does not result in the same violent collapse as the one in Figure 5.2 ($\Delta\alpha=\pm2°$, $\alpha_m=7°$, $Re=12\times10^5$, $\sigma=0.5$)

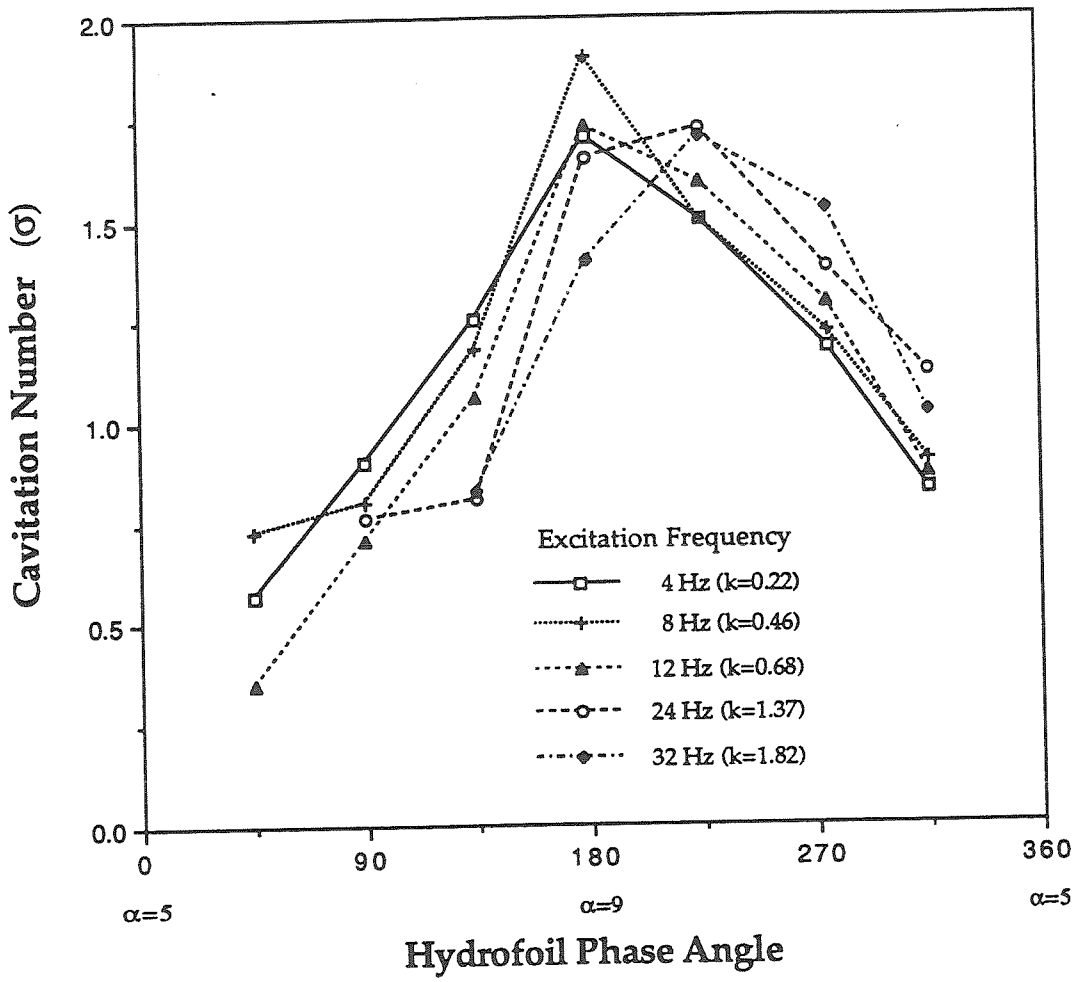

Figure 5.4 Cavitation Inception Number for Surface Cavitation as a Function of Hydrofoil Angle of Attack Relative to the Freestream

The cavitation inception number for surface cavitation on the hydrofoil versus angle of attack are shown here for several reduced frequencies. At high reduced frequencies, a significant phase shift becomes apparent in the cavitation inception curve. This effect is due primarily to an increase in the relative angle of attack of the hydrofoil leading edge.

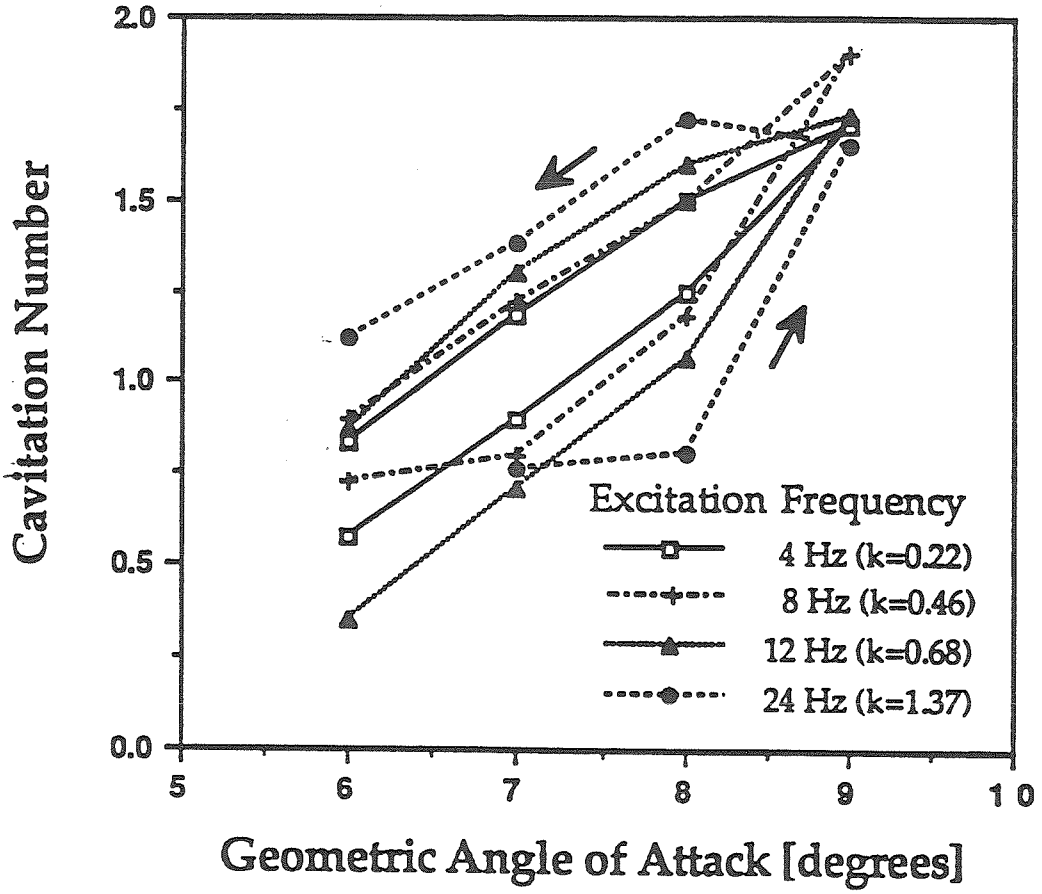

Figure 5.5 Cavitation Inception Number for Surface Cavitation as a Function of Hydrofoil Angle of Attack Relative to the Angle of Attack of the Foil
The lower traces in this plot represent an increasing angle of attack and the upper traces represent a decreasing angle of attack of the foil. As the reduced frequency increases, there is an increased hysteresis between cavitation inception and desinence.

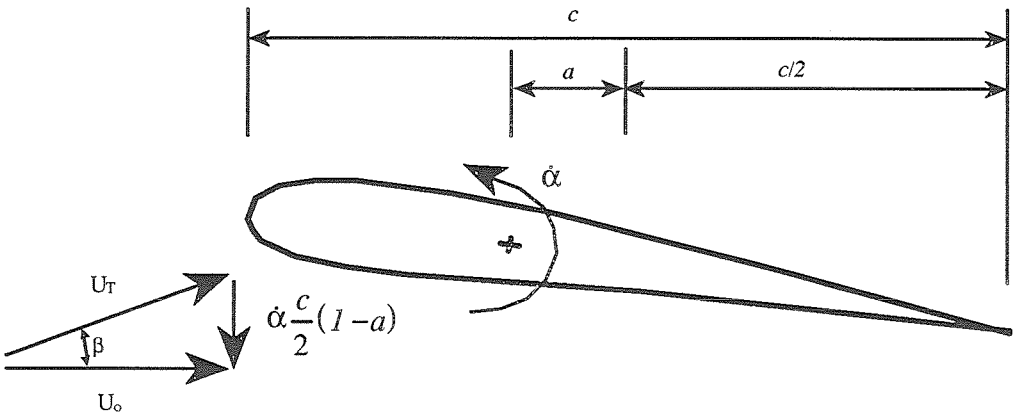

Figure 5.6 Schematic Showing Kinematic Change in Leading-Edge Effective Angle of Attack

The pitching motion of the hydrofoil results in an induced velocity component normal to the chord of the foil at the leading edge. This velocity component results in a change in the effective angle of attack of the leading edge of the foil. U_T in the figure represents the true freestream velocity observed by the leading edge of the foil, and β represents the change in angle of attack due to the kinematics of the foil oscillation.

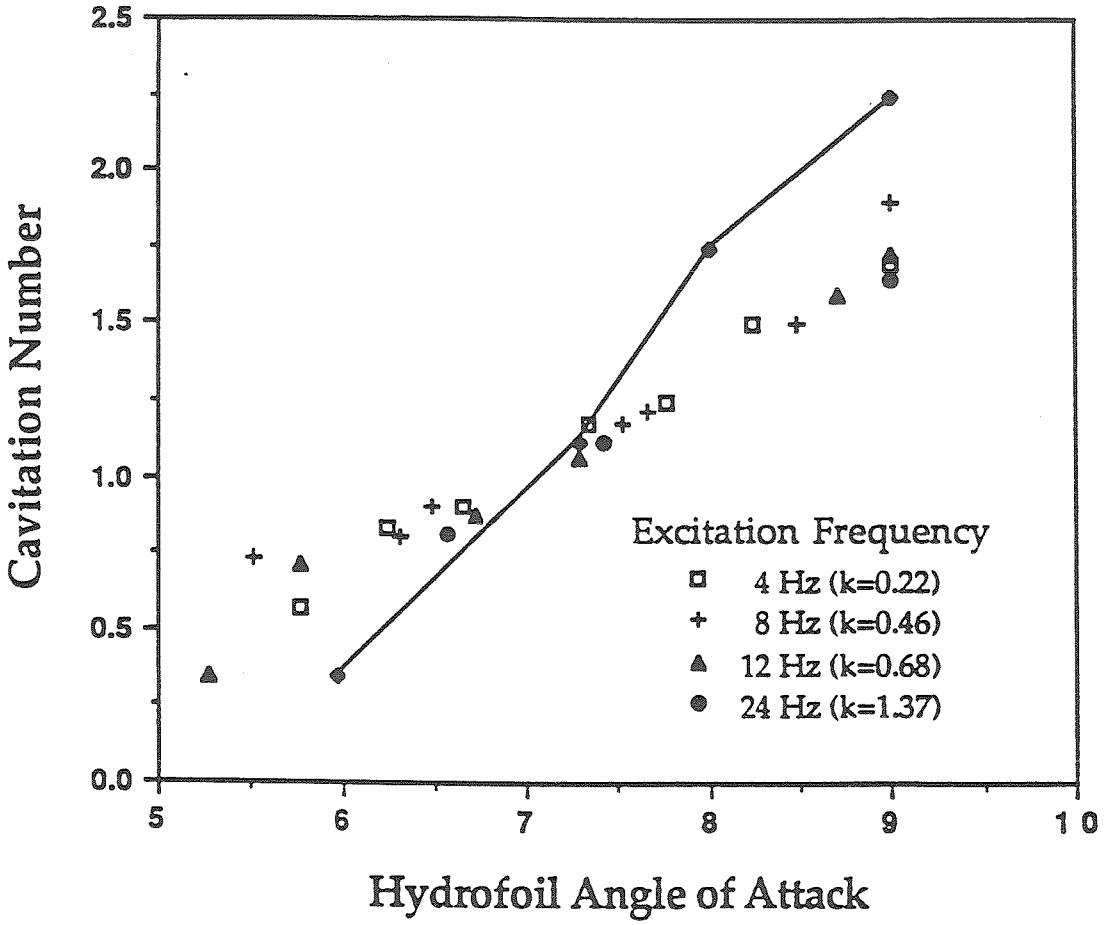

Figure 5.7 Cavitation Inception Number for Surface Cavitation as a Function of Hydrofoil Angle of Attack Relative to the Leading Edge Flow

When the cavitation inception number for surface cavitation is plotted relative to the true angle of attack seen by the leading edge of the hydrofoil, it deviates very little from the curve showing the cavitation inception number for a non-oscillating hydrofoil at increasing angles of attack.

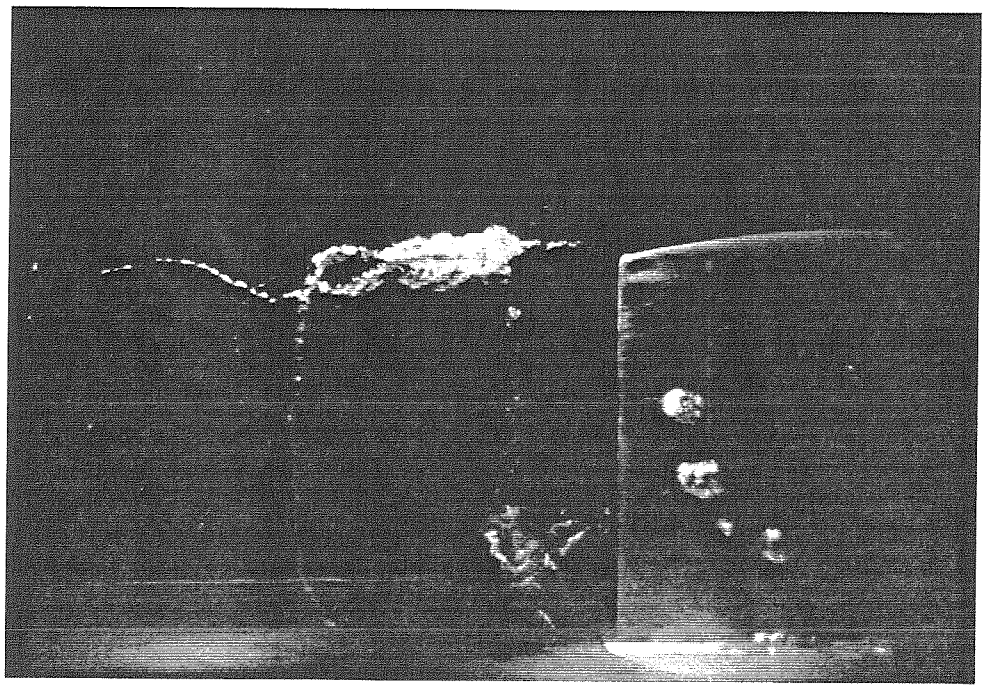

Figure 5.8 Photograph of Tip Vortex Cavitation Downstream of a Hydrofoil Oscillating at a High Reduced Frequency, k=2.4

Cavitation initiates in the knee of the vortex formation where the tip vortex links with the spanwise vortex formed when the hydrofoil is at the minimum angle of attack in an oscillation cycle. Cavitation rapidly spreads into the tip vortex region between the spanwise vortex formed at the minimum angle of attack of the hydrofoil and the spanwise vortex formed at the maximum angle of attack of the hydrofoil in an oscillation cycle ($Re=12x10^5$, $\alpha_m=5^\circ$, $\Delta\alpha=\pm5^\circ$, $k=2.4$).

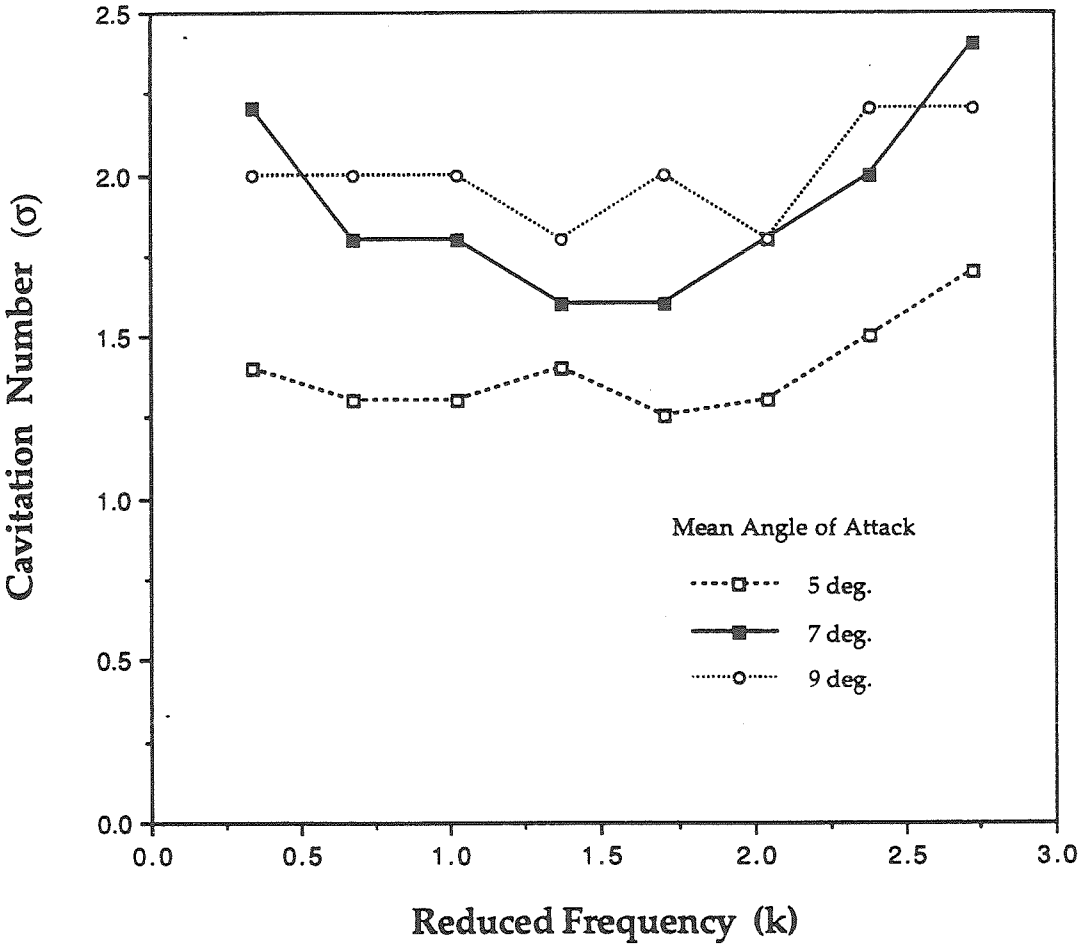

Figure 5.9 Cavitation Inception Number for the Tip Vortex as a Function of Reduced Frequency

The cavitation inception number versus reduced frequency is shown for angles of attack of $\alpha = 5^\circ$, $\alpha = 7^\circ$, *and* $\alpha = 9^\circ$. *As the reduced frequency is increased, the cavitation inception number decreases and then increases. This is the result of a reduction in the circulation about the foil with reduced frequency. At high reduced frequencies, the forces on the foil are dominated by added mass effects and the cavitation inception number increases with reduced frequency.*

CHAPTER 6

MEASUREMENT OF UNSTEADY CIRCULATION

This chapter describes the techniques used to determine the changes in circulation due to the oscillation of the hydrofoil and the techniques used to measure the velocity profile of the tip vortex. Included are experimental measurements for both the two- and the three-dimensional foils.

6.1 Calculation of the Rate of Change of Circulation

The structure of the wake, the lift, the drag, and the inception of cavitation on the surface and in the wake of a hydrofoil are all functions of the bound circulation around the foil and the shed vorticity. To measure these parameters experimentally requires either taking many measurements of velocity throughout the flow field and calculating the circulation from the definition of circulation (Equation 6.2), or measuring the forces on the foil and calculating the circulation from a relation such as the Kutta-Joukowski formula,

$$L/s = \rho U_\infty \Gamma \tag{6.1}$$

or an analogous equation relating circulation to the measured force component. Taking velocity measurements throughout the flow field would require enormous amounts of data for an accurate determination of the circulation, making this method impractical. Using unsteady force measurements is tricky, since interpreting the results would be complicated by the need to consider the inertial forces contributed by the foil and the oscillation mechanism as well as the added mass component of the fluid-foil interaction. It is considerably easier to determine simply the *changes* in circulation due to the oscillation of the foil, and it will be seen that, for the

purposes of calculating the effects of the oscillation on the flow, this is quite sufficient.

We begin with the definition of circulation,

$$\Gamma = \oint_C \vec{u} \cdot d\vec{y} \tag{6.2}$$

which by Stokes's theorem can be written

$$\Gamma = \int_A \vec{\omega} \cdot d\vec{A}. \tag{6.3}$$

The Lagrangian time derivative of this equation, by the Reynolds Transport Theorem [Kundu 1990], is

$$\frac{D\Gamma}{Dt} = \frac{d}{dt}\int_A \vec{\omega} \cdot d\vec{A} = \int_A \frac{d\vec{\omega}}{dt} \cdot d\vec{A} + \int_{x_i} \omega_i u_j \cdot dx_i \tag{6.4}$$

but, by Kelvin's theorem,

$$\frac{D\Gamma}{Dt} = 0 \tag{6.5}$$

so that

$$\int_A \frac{d\vec{\omega}}{dt} \cdot d\vec{A} = -\int_{x_i} \omega_i u_j \cdot dx_i. \tag{6.6}$$

However, the Eulerian time derivative of the circulation is [Kundu 1990]

$$\frac{d\Gamma}{dt} = \int_A \frac{d\vec{\omega}}{dt} \cdot d\vec{A}. \tag{6.7}$$

Therefore,

$$\frac{d\Gamma}{dt} = -\int_{x_i} \omega_i u_j \cdot dx_i. \tag{6.8}$$

Thus, the rate of change in circulation around the hydrofoil in the spanwise direction can be written as

$$\frac{\partial \Gamma_{sp}}{\partial t} = \int_{\delta_p}^{\delta_s} u\, \omega_{sp}\, dy \approx \frac{u_p^2 - u_s^2}{2} \tag{6.9}$$

(where δ_p is the thickness of the boundary layer on the pressure side of the foil, and δ_s the thickness on the suction side of the foil), since $\omega_{sp} = \frac{dw}{dx} - \frac{du}{dy} \approx -\frac{du}{dy}$ assuming the flow is nearly parallel at the trailing edge of the hydrofoil. Because the flow is essentially irrotational outside the boundary layer of the hydrofoil, the limits of integration can be taken from the boundary layer edges.

Similarly, the change in streamwise circulation along the span of the foil at the trailing edge can be expressed, from the fundamental definition of a vortex sheet [Kundu 1990], as

$$\frac{\partial \Gamma_{st}}{\partial s} = v_p - v_s. \tag{6.10}$$

Thus, the change in circulation about an unsteady hydrofoil can be determined simply by measuring the instantaneous velocities at the trailing edge of the hydrofoil.

6.2 Measurement of Trailing Edge Flow Velocities

The current experiments used Laser Doppler Velocimetry to acquire quantitative measurements of instantaneous streamwise and spanwise velocities at the trailing edge of the oscillating two-dimensional and three-dimensional hydrofoils. The LDV measurements were taken as close as possible to the trailing edge of the foil at reduced frequencies of k= 0.48, 0.96, and 1.92. In each case, the mean angle of attack was 5.3° and the oscillation amplitude was ±5°. The freestream velocity was held constant at 5m/s. Four different locations along the span of the finite aspect ratio foil were measured: 20% span (just above the test section floor boundary layer), 50% span, 80% span (just below the tip vortex region), and at the foil tip. At each spanwise

location and for each frequency, streamwise and spanwise velocity data were collected at seven different stations across the wake of the foil (perpendicular to the freestream – see Figure 6.1). Plots of the velocity data vs. phase at each station, such as the one in Figure 6.2, show a clear drop in the freestream velocity each time the foil boundary layer sweeps by that location.

6.3 Data Reduction

The LDV measurements were encoded with the phase position of the foil and collected into a file. The data were ensemble-averaged and transposed into the coordinate frame of the oscillating hydrofoil based on the sinusoidal oscillation motion of the foil, as discussed in Section 6.3.1, and, as discussed in Section 6.3.2, fit to the first and second harmonics of the foil frequency. This technique provided a means of accurately interpolating the flow field behind the hydrofoil improving the resolution of the irregularly spaced data locations. The change in velocity across the trailing edge was then extrapolated through the boundary layer, as discussed in Section 6.3.3, by linearly fitting the data in the direction perpendicular to the foil span.

6.3.1 Transformation to Hydrofoil Frame of Reference

The hydrofoil phase information, recorded with the LDV measurements, was used to transform the velocity data into the frame of reference of the moving foil. This was accomplished by introducing a new variable, η, to represent the changing position of the trailing edge. η is defined to be the distance from each location where instantaneous velocities were measured to the trailing edge of the foil (note that η is a function of the oscillation phase ϕ of the hydrofoil). This means that each velocity measurement, taken at a given location x and phase ϕ, can now be expressed in terms of its distance

from the trailing edge at the time it was taken. As Figure 6.3 shows, lines of constant η represent positions in the flow at a constant distance from the trailing edge, e.g., η=0 tracks the trailing edge itself. Mathematically, if x is the variable indicating cross-stream distance in the tunnel coordinate frame, then the transformation can be expressed as

$$\eta = x\text{-}A_0\sin(\phi)$$

where A_0 is the amplitude of oscillation of the trailing edge, or

$$\eta = A\sin(\omega t) - x_0 \tag{6.11}$$

where $A = c(1-0.38)\sin(\Delta\alpha)$ and x_o equals the offset from the data location relative to the tunnel to the trailing edge of the hydrofoil at the mean angle of attack of the hydrofoil. We can now consider the data in the moving frame of reference of the trailing edge (see Figure 6.4).

6.3.2 Fitting of Data

Since the velocity measurements were ensemble phase averaged, they could be assumed to be periodic with respect to the phase of the oscillating hydrofoil. The data set could therefore be transformed into the frame of reference of the moving foil, i.e., the η-ϕ coordinate frame, and then fit to a harmonic function. Five of the seven LDV data locations were crossed by the trailing edge of the hydrofoil twice during each cycle of oscillation. As illustrated in Figure 6.4, this resulted in a total of ten data points per oscillation cycle at each value of η in the η-ϕ plane. Therefore with consideration for aliasing errors, a first and second-order harmonic function relative to the frequency of the foil oscillation was selected for fitting of the data;

$$\frac{u}{U_\infty} = a_o\sin(\omega t) + b_o\cos(\omega t) + c_o\sin(2\omega t) + d_o\cos(2\omega t) + e_o, \tag{6.12}$$

where a_o, b_o, etc. are functions of η. The actual velocities were found to fit very closely to this function, with standard deviations on the order of 0.005 for most values of η. The values of c_o and d_o were found, on the average, to be very small. This technique provided a means of accurately interpolating the flow field behind the hydrofoil by providing an analytic smooth function to replace the discrete data locations (see Figure 6.5).

6.3.3 Interpolation of Trailing Edge Velocities

As mentioned, the vorticity field can be inferred from the velocity measurements by considering the velocity difference across the trailing edge as it changes with the phase of the hydrofoil. The calculation is quite straightforward, but the determination of the exact thickness of the boundary layer is less certain. Since the identification of the trailing edge velocities depends upon accurately locating the boundary layer edge, this uncertainty can cause some error in calculating the circulation in this manner. The velocity profiles outside the boundary layer, however, were noted to taper off gradually with distance from the foil making this a relatively small error (<10%) (see Figure 6.6). In order to improve the accuracy of the estimated velocity jump, for each value of phase ϕ the shape of the velocity profile outside the boundary layer on each side of the foil was fit to a straight line, $\frac{u}{U_\infty} = a_1 \frac{\eta}{c} + a_2$. The functions defined by the resulting coefficients, a_1 and a_2, were then used to calculate the pressure side and suction side trailing edge velocities at each phase of the foil oscillation cycle, as shown in Figure 6.7.

Figure 6.8 shows a comparison of the change in circulation with hydrofoil phase calculated from the transposed ensemble-averaged data outside the

boundary layer to the change in circulation calculated by fitting the data in this manner.

6.4 Results

The following sections present the results of measurements of the rate of change of the spanwise circulation of the two- and three-dimensional hydrofoils. Also presented are the change in streamwise circulation, the boundary layer profile and the tip vortex axial and tangential velocity profiles of the three-dimensional hydrofoil. Only a fraction of the total data collected is presented here. Additional data, not relevant to explaining the observed results, can be found in Appendix B.

6.4.1 Spanwise Circulation

Figure 6.9 shows the rate of change in spanwise circulation at the trailing edge of a two-dimensional hydrofoil. The curves presented in this figure show that the magnitude of the rate of change of spanwise circulation increases linearly with reduced frequency of oscillation. In addition, a phase shift is evident between the sinusoidal shape of these curves and the phase of the foil. This phase lag increases with increased reduced frequency.

A similar trend exists at the trailing edge of the finite aspect ratio hydrofoil, as illustrated in Figure 6.10. This figure shows results from measurements taken near the root of the foil. Measurements taken at the mid-chord and near the tip (Figure 6.11) show that the rate of change of spanwise circulation at the trailing edge of the foil varies very little in magnitude along the entire span.

6.4.2 Streamwise Circulation

Figure 6.12 shows a plot of the change in streamwise circulation as a function of hydrofoil phase for three span locations. Note that the majority of change in streamwise circulation, like the shed spanwise vorticity, occurs within the last 30% of the span of the foil and, like the shed spanwise vorticity, lags the phase of the hydrofoil motion. This streamwise vorticity rolls up downstream to form the tip vortex of the foil. As Figure 6.13 illustrates, the change in streamwise circulation decreases slightly with an increase in reduced frequency from k=0.48 to k=0.96 and then increases with a further increase in reduced frequency. This non-monatonic phenomenon has also been noted in the occurrence of the inception of cavitation in the tip vortex region (Figure 5.18). Also apparent in Figure 6.13 is a slight phase lag between the change in streamwise circulation near the tip of the foil and the change in streamwise circulation near root. This phase difference increases with an increase in reduced frequency of oscillation.

6.4.3 Measurement of Boundary Layer Profile

The streamwise velocity profiles acquired for calculation of the rate of change of spanwise circulation indicated a change in the boundary layer profile of the finite aspect ratio hydrofoil as it oscillated in pitch (see Figure 6.14). The average boundary layer thickness was found to be approximately 3*mm* on the suction side of the hydrofoil and 2*mm* on the pressure side. As shown in Figure 6.15, the fluctuations of the boundary layer thickness with hydrofoil phase on both sides of the foil increased with an increase in reduced frequency. The limited resolution of the velocity measurements at the trailing edge of the foil prevented accurate comparisons of the small changes between the boundary layer profiles along the span of the foil.

6.4.4 Measurement of Tip Vortex Flow

The technique used to determine the change in circulation and boundary layer profile of the hydrofoil lends itself well to measuring the axial and tangential velocity of the tip vortex near the trailing edge of the foil. The magnitudes of the measured values, however, are likely to be slightly low. The reason for this is that the exact position of the tip vortex relative to the hydrofoil wonders with time. The measurements are taken from a fixed location and ensemble averaged and do not show the actual peak velocities. Observations of the tip vortex in this region using air injection flow visualization, however, indicates that the actual wandering of the tip vortex is very slight. It is believed, therefore, that the measured values are reasonably close to the actual instantaneous values.

Figure 6.16 shows the spanwise (tangential) velocity profile of the tip vortex taken at the maximum and minimum angle of attack of the hydrofoil at reduced frequencies of k=0.48, 0.96, and 1.92. The core of the tip vortex is slightly to the suction side of the foil. The velocity profile is not symmetrical about the core apparently because the tip vortex structure is not circular. Note that very high tangential velocities occur in this region just at the trailing edge of the foil. The magnitude of these velocities were not observed to be strongly dependent on the reduced frequency of oscillation.

Measurements of the streamwise (axial) velocity in the core of the tip vortex (Figure 6.17) show a jet formation in the upstream direction inside the core of the vortex. Just outside the core, the axial velocity is greater than the freestream. The strength of these axial velocity components are observed to fluctuate with the phase of the hydrofoil oscillation.

6.5 Comparison Between 2-D Theoretical Predictions and Experimental Measurements

As presented in Appendix A, an expression for the rate of change of circulation of a two-dimensional foil was obtained from the theoretical analyses of Theodorsen [1935] and Garrick [1936]. This expression,

$$\frac{d\Gamma^*}{dt} = k2\pi C_o \Delta\alpha \cos(\omega t + \theta)$$

where C_o and θ are defined in Appendix A and plotted in Figures 6.18 and 6.19 respectively, is compared in Figure 6.20 with the measured rate of change in spanwise circulation of the two- and three-dimensional hydrofoils. The results for the two-dimensional foil compare extremely well while the results for the finite aspect ratio foil show a lower magnitude of the rate of change of circulation.

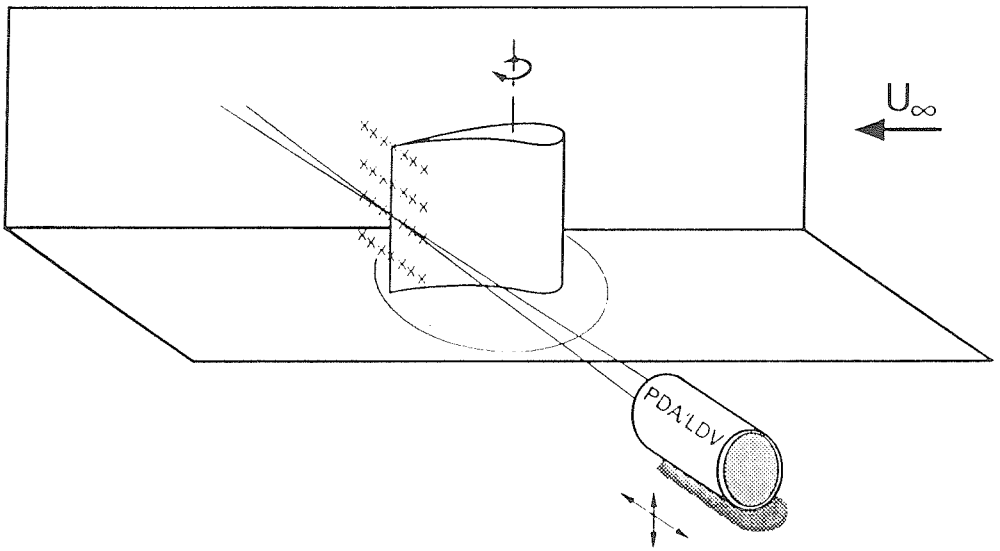

Figure 6.1 Graph of Data Locations in the Frame of Reference of the LTWT Test Section

The graph shows seven data locations where LDV data was taken at each of four span positions.

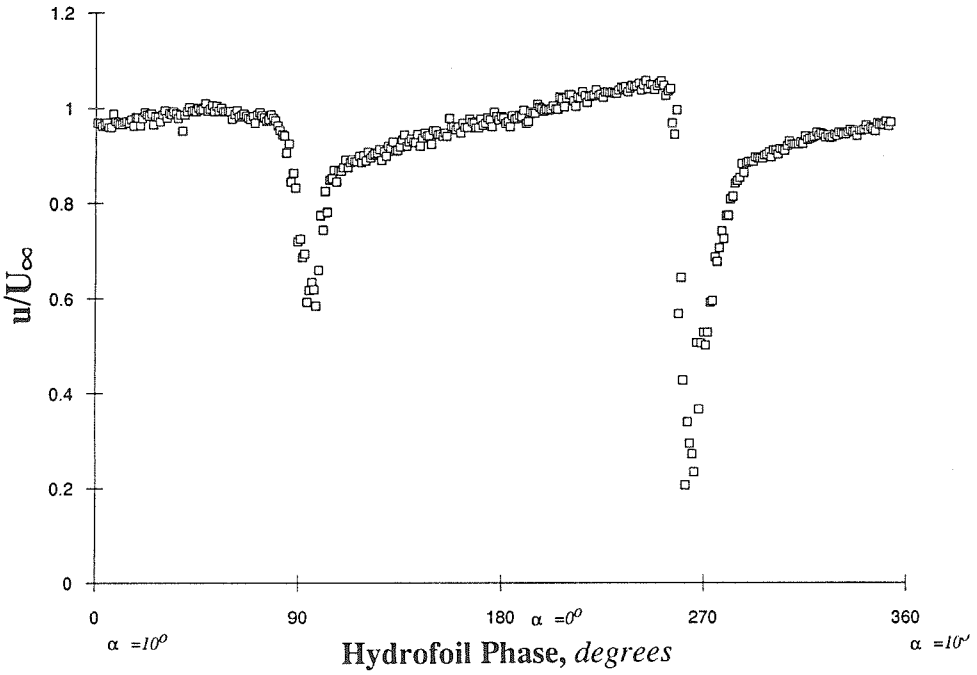

Figure 6.2 Graph of Typical Ensemble Phase Averaged LDV Measurements Taken Near the Trailing Edge of a Finite Aspect Ratio Hydrofoil and Encoded to the Phase of the Hydrofoil Oscillation

Data was collected over several hundred oscillations. The sudden drops in velocity are the locations where the boundary layer of the oscillating hydrofoil passes through the location at which these measurements were taken. The angle of attack of the hydrofoil is decreasing as the trailing edge passes through the data location at a phase of 90° and it is increasing as it passes through the data location at a phase of 180° accounting for the difference in the two velocity deficits ($Re=1.2x10^5$, $\Delta\alpha=\pm5°$, $k=1.92$).

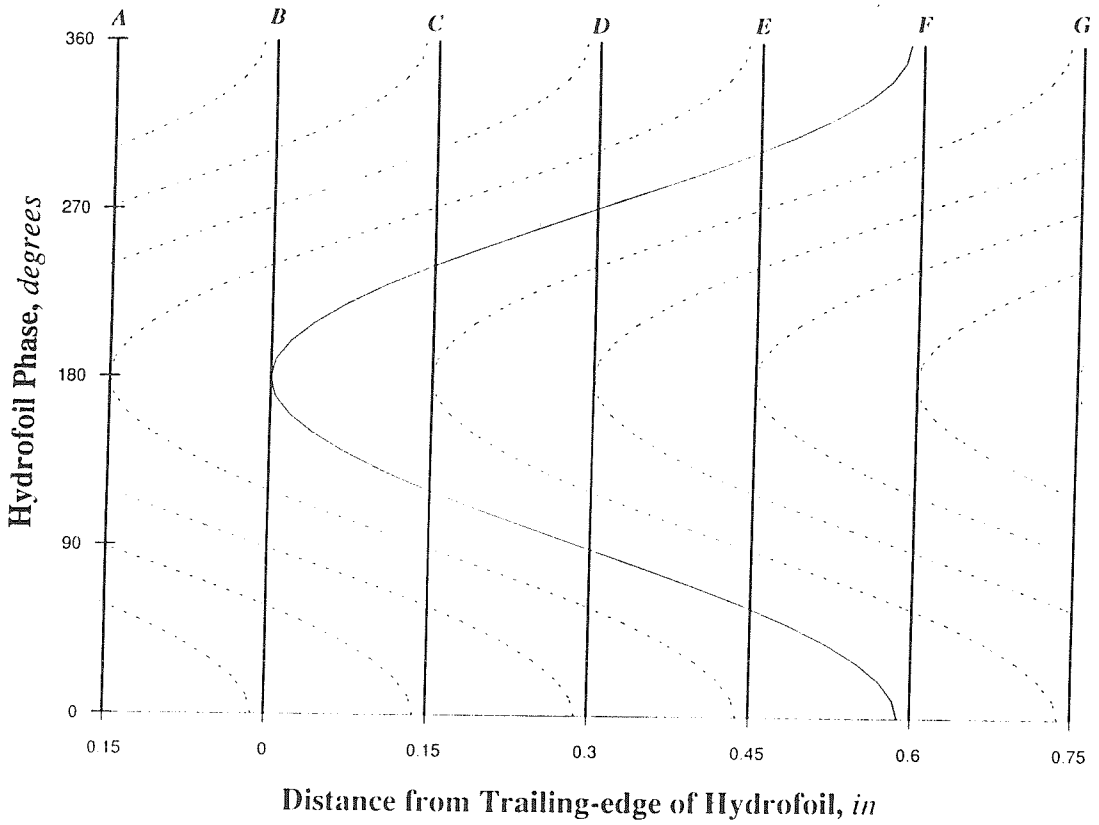

Figure 6.3 Schematic of LDV Data Locations Relative to the LTWT Test Section Centerline

LDV velocity measurements in the streamwise and spanwise directions were made at seven locations perpendicular to the hydrofoil at four locations along the span of the hydrofoil. This figure shows the relative locations at which the data was taken in phase with the hydrofoil motion. The solid sinusoidal line shows the location of the trailing edge of the hydrofoil as it passes through the seven data locations marked "A" through "G." The dotted lines are lines equi-distant from the trailing edge.

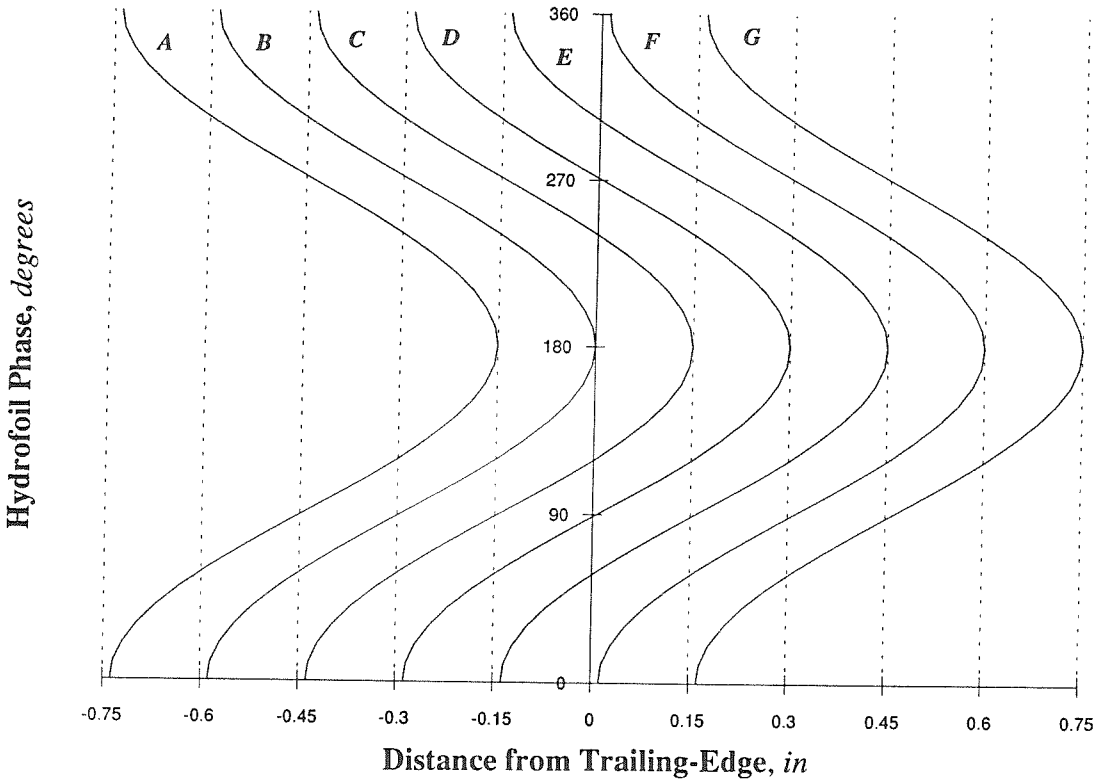

Figure 6.4 Schematic Showing Transformation From the LTWT Frame of Reference to the Frame of Reference of the Hydrofoil

LDV ensemble averaged data transformed to a Lagrangian frame of reference relative to the hydrofoil trailing edge allows harmonic interpolation of the data relative to hydrofoil phase. This technique provides a means of accurately analyzing the flow near the trailing edge of the hydrofoil with relatively few discrete measurements greatly simplifying the experimental procedure. The solid lines marked "A" through "G" are the transformed ensemble averaged LDV data locations relative to the trailing edge of the hydrofoil, η*=0.*

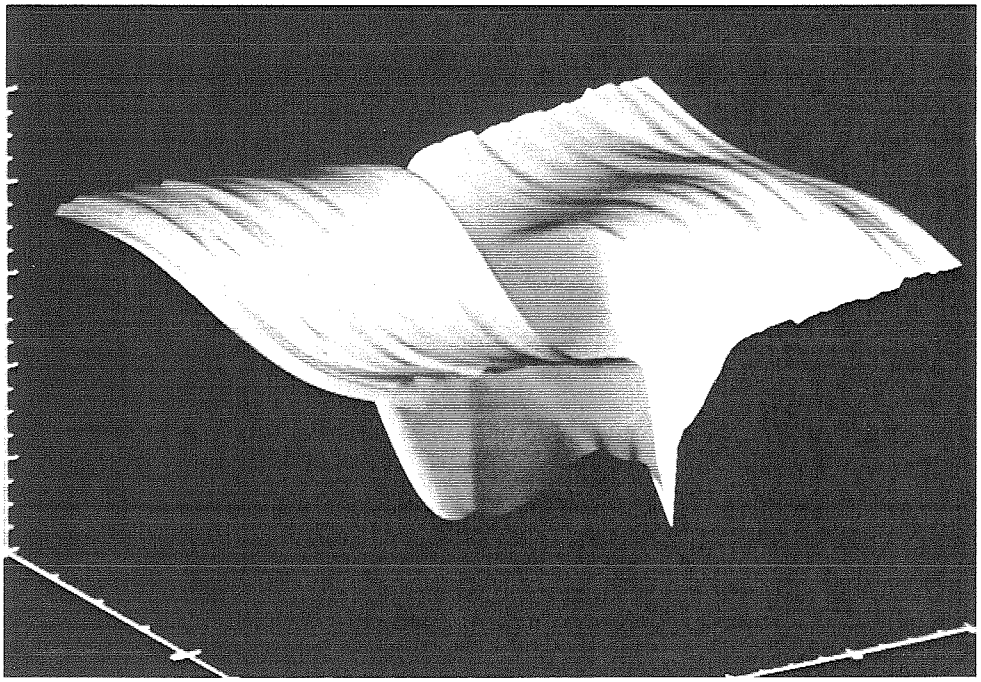

Figure 6.5 Surface Plot of the Data in the Frame of Reference of the Hydrofoil After Curve Fitting to the First and Second Harmonics

Ensemble averaged data transformed to the trailing edge of the hydrofoil and fit to the first and second harmonics of the hydrofoil oscillation frequency is shown here as a surface plot. The height of the surface shows the streamwise velocity non-dimensionalized with free stream velocity. The leading edge coordinate of the surface is the distance from the trailing edge of the hydrofoil and the left edge coordinate is the phase of the hydrofoil. The dip in the center of this plot is the velocity deficit of the boundary layer as it sheds from the foil. A phase shift between the pressure side and the suction side of the hydrofoil can be seen across this dip.

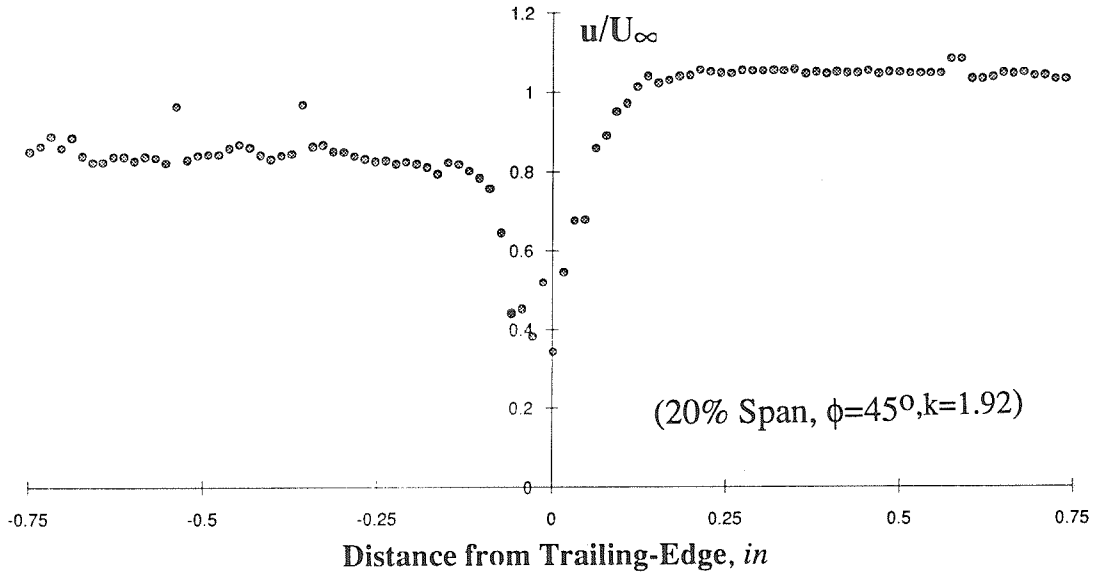

Figure 6.6 Streamwise Velocity Profile in the Wake of an Oscillating Hydrofoil
Linearly extrapolating the velocities through the boundary layer of the hydrofoil results in a slight increase in the estimated trailing edge velocities. Since the velocity of the streamwise flow tends toward the freestream velocity as the distance from the trailing edge of the hydrofoil is increased, the ensemble averaged data taken directly underestimates the velocity difference at the trailing edge.

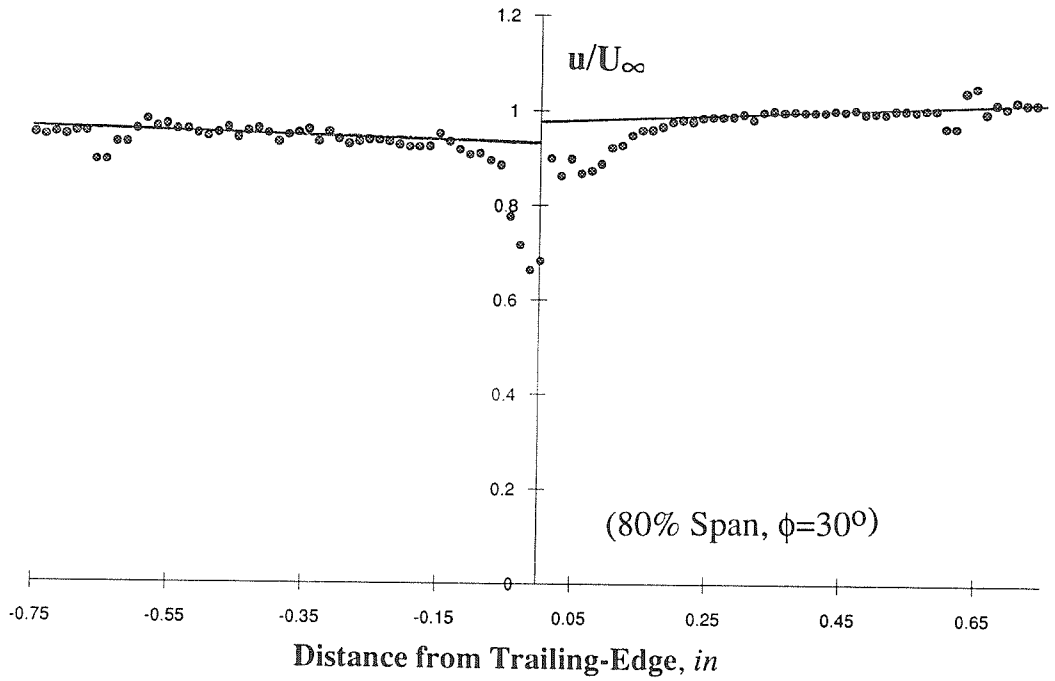

Figure 6.7 Illustration of Technique Used to Determine the Effective Jump in Velocity Across the Trailing-Edge of the Hydrofoil

Interpolated streamwise velocity normalized with the freestream velocity is shown here as a function of the distance from the trailing edge of the hydrofoil for a phase angle of 30°. The velocity jump across the trailing edge of the hydrofoil is determined by linearly fitting the data through the boundary layer. The resulting velocities are used to determine the change in circulation of the hydrofoil as a function of hydrofoil phase.

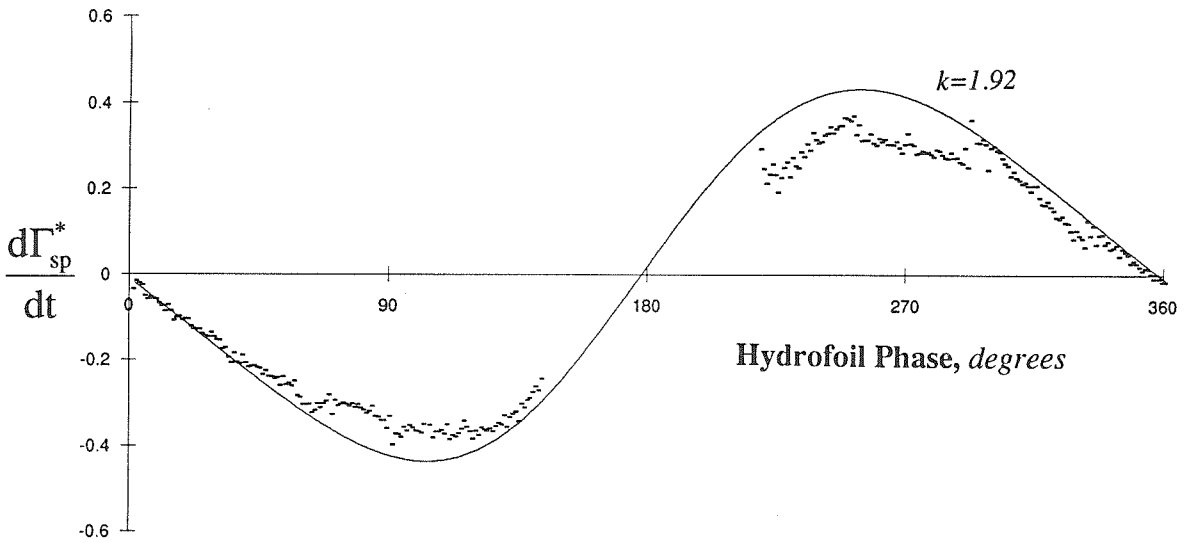

Figure 6.8 Comparison of Typical Interpolated Vorticity Calculation With Calculations Made Directly From Ensemble Averaged Data Taken Near the Trailing-Edge Outside the Boundary Layer

Interpolation through the boundary layer of the streamwise velocity component results in roughly a 5% correction in the calculated change in spanwise circulation. The actual change in streamwise velocity between the interpolated data and the velocity just outside the boundary layer of the hydrofoil is small. The ensemble averaged data taken with the LDV, however, falls at varying distances from the trailing edge depending on the phase of the hydrofoil. In addition, it is difficult to assess the location of the start of the boundary layer directly from the data. The result is an underestimation of the change in circulation.

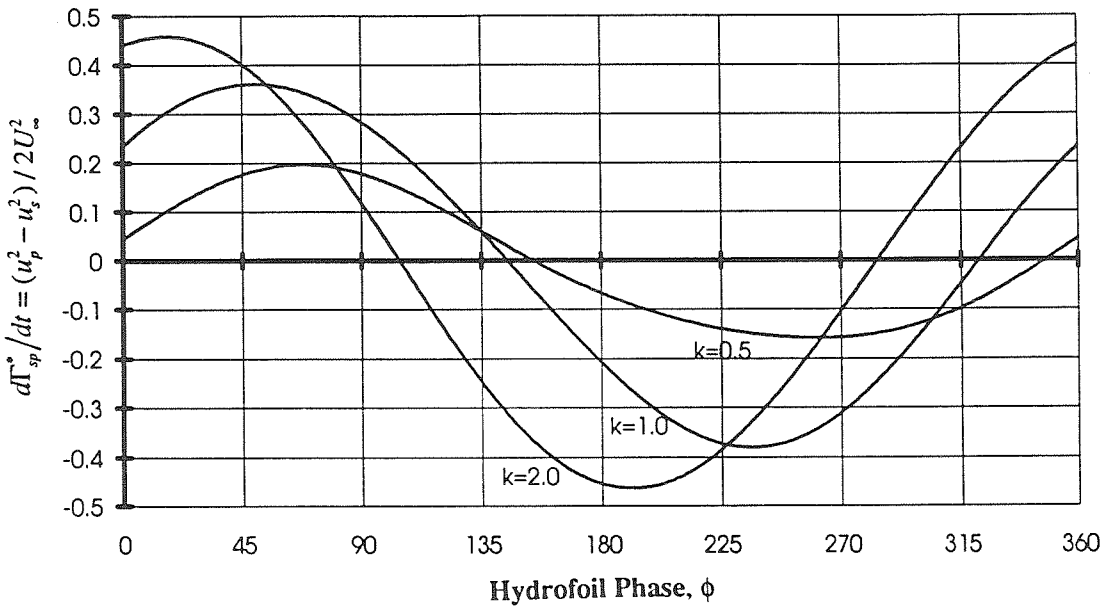

Figure 6.9 Graph of Rate of Change in Spanwise Circulation at the Trailing Edge of a Two-Dimensional Hydrofoil as a Function of Phase for Three Reduced Frequencies

The change in spanwise circulation is shown non-dimensionalized with the freestream velocity for reduced frequencies of k=0.48, 0.96, and 1.92. The hydrofoil is oscillating ±5° about a mean angle of attack of 5° The peak change in circulation increases linearly with reduced frequency. Note also that the phase of the loading of the hydrofoil shifts with increasing reduced frequency.

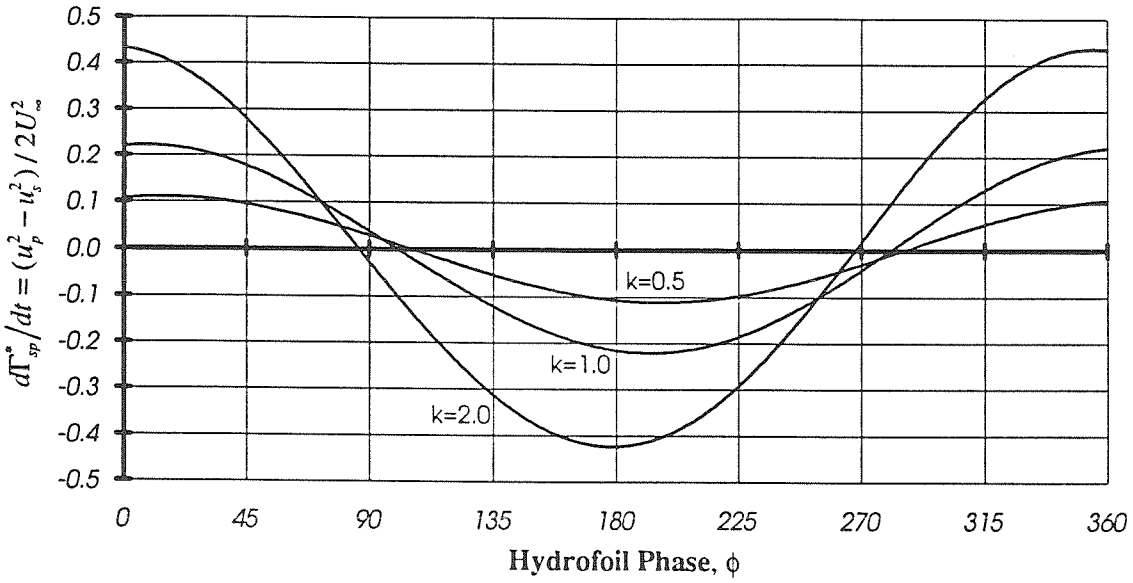

Figure 6.10 Graph of Rate of Change in Spanwise Circulation at the 20% span location as a Function of Hydrofoil Phase for Three Reduced Frequencies
The change in spanwise circulation is shown non-dimensionalized with the freestream velocity for reduced frequencies of k=0.48, 0.96, and 1.92. The hydrofoil is oscillating ±5° about a mean angle of attack of 5° The peak change in circulation increases linearly with reduced frequency. Note also that the phase of the loading of the hydrofoil shifts with increasing reduced frequency.

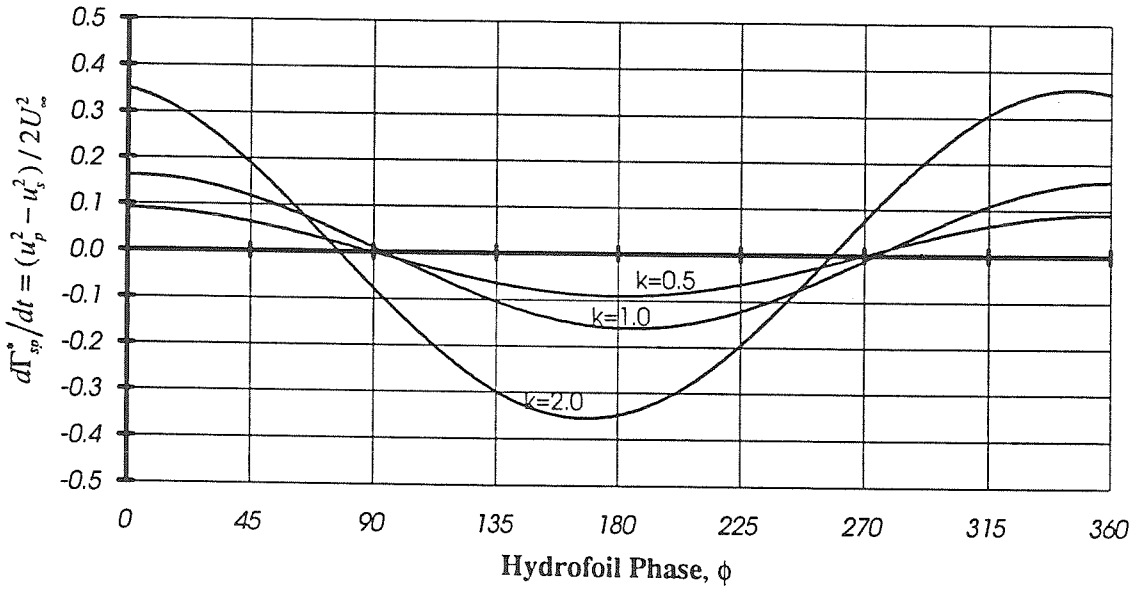

Figure 6.11 Measured Rate of Change of Spanwise Circulation as a Function of Hydrofoil Phase for Three Reduced Frequencies at the 80% Span Location
Peak change in streamwise circulation increases linearly with reduced frequency. In addition, a phase shift occurs. This phase shift is the result of a dynamic interaction between the oscillating hydrofoil and the surrounding fluid.

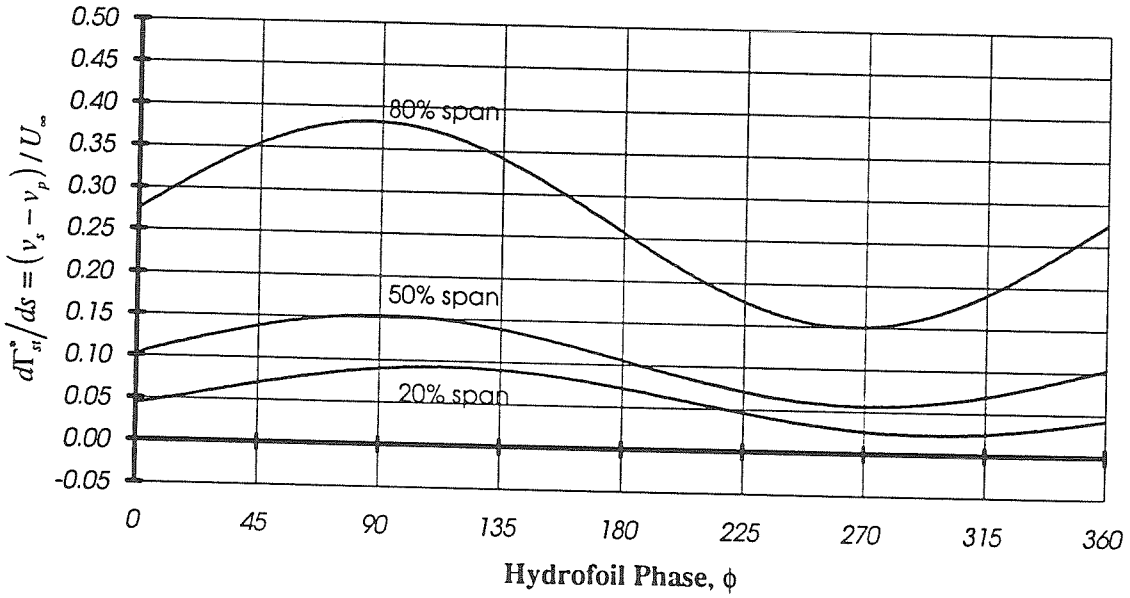

Figure 6.12 Graph of Change in Streamwise Circulation as a Function of Hydrofoil Phase at a Reduced Frequency of 1.92 for Three Span Locations
The change in streamwise circulation is shown non-dimensionalized with the freestream velocity for span locations of 20%,near the base of the foil, 50%, and 80%, near the tip of the foil.. The hydrofoil is oscillating ±5° about a mean angle of attack of 5° at a reduced frequency of 1.92. The hydrofoil is at its maximum angle of attack of 10° at the 0° phase position and at the minimum angle of attack, 0°, at the 180° phase position. The majority of change in streamwise circulation occurs within the last 30% of the span of the foil.

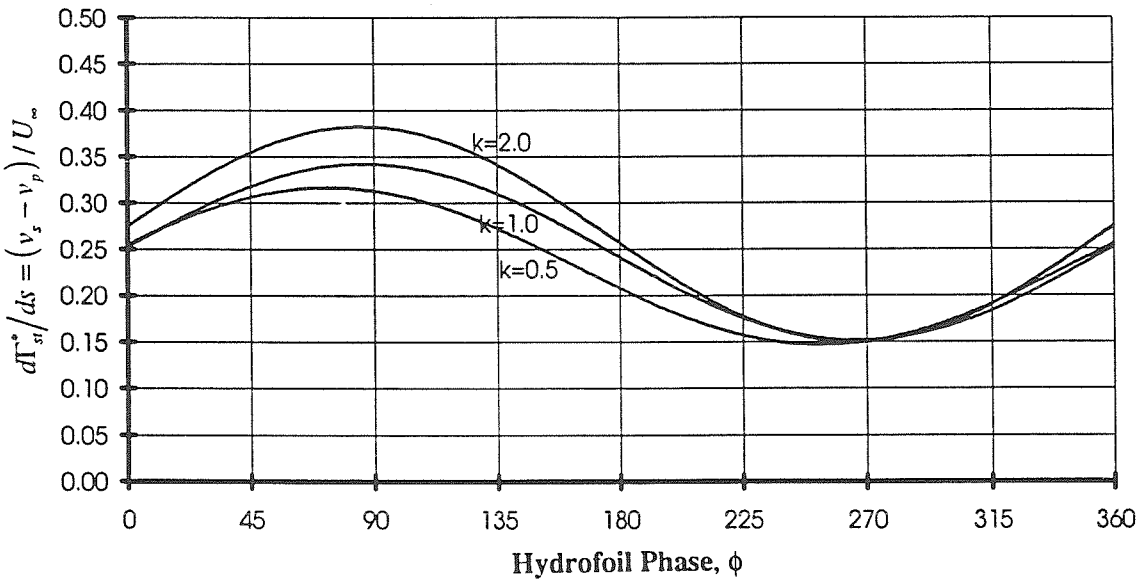

Figure 6.13 Measured Change Of Streamwise Circulation As A Function Of Hydrofoil Phase For Three Reduced Frequencies At The 80% Span Location
Near the tip of the hydrofoil, 80% span, there exists a large change in streamwise circulation with the phase of the hydrofoil. This change in circulation, however, is only slightly dependent on the reduced frequency of oscillation.

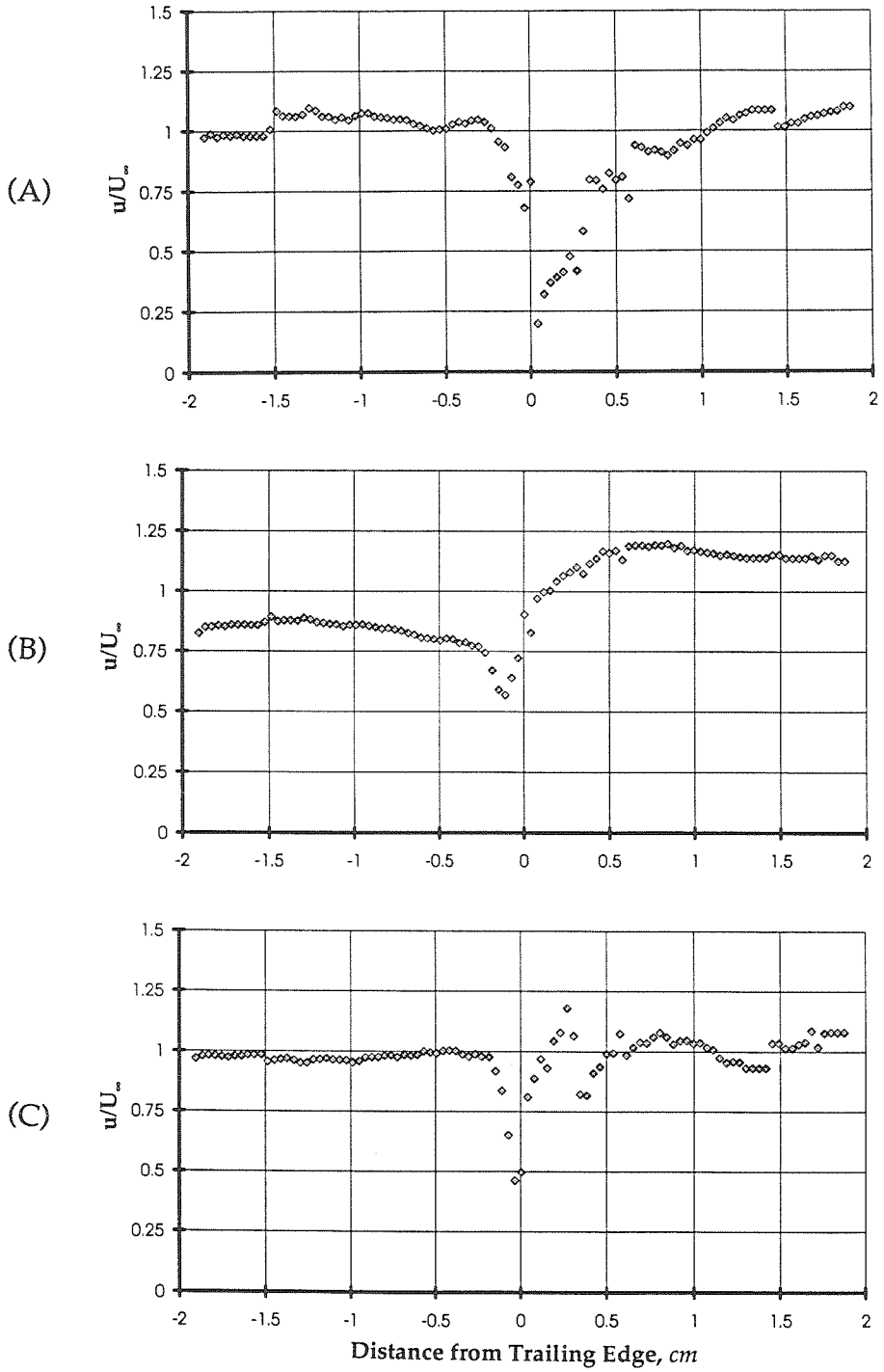

Figure 6.14 Comparison of Boundary Layer Profiles at the Trailing Edge of the Hydrofoil for Three Phase Angles

Three plots of the boundary layer profile at the trailing edge of the hydrofoil are shown for a hydrofoil reduced frequency of k=1.92. Each plot shows the profile at a different phase angle of the foil oscillation: (A) ϕ=0°, (B) ϕ=90°, (C) ϕ=180°.

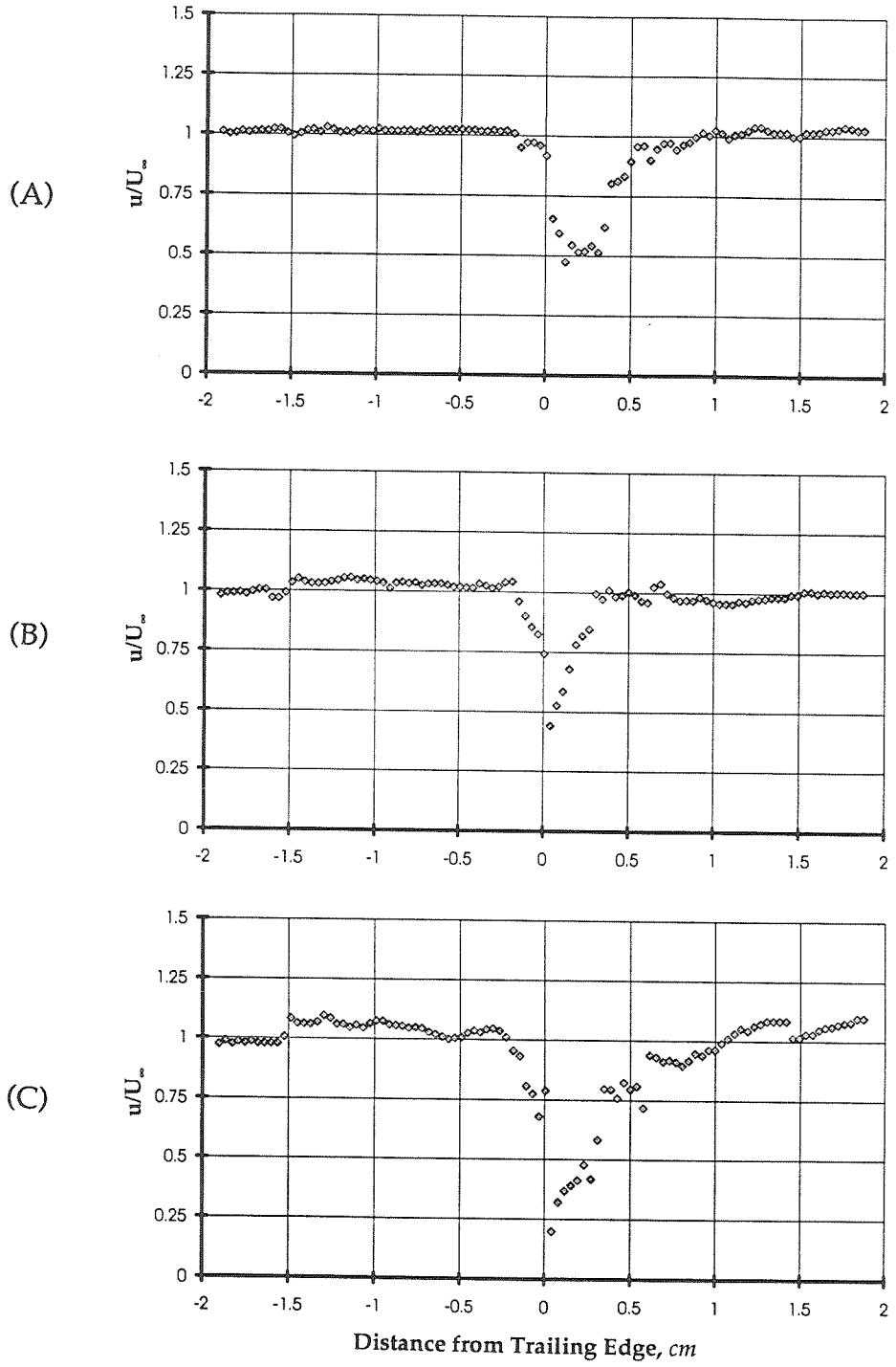

Figure 6.15 Comparison of Boundary Layer Profiles at the Trailing Edge of the Hydrofoil for Three Reduced Frequencies

Three plots of the boundary layer profile at the trailing edge of the hydrofoil are shown for a hydrofoil phase angle of 0°. Each plot shows the profile at a different reduced frequency of foil oscillation: (A) k=0.48, (B) k=0.96, (C) k=1.92.

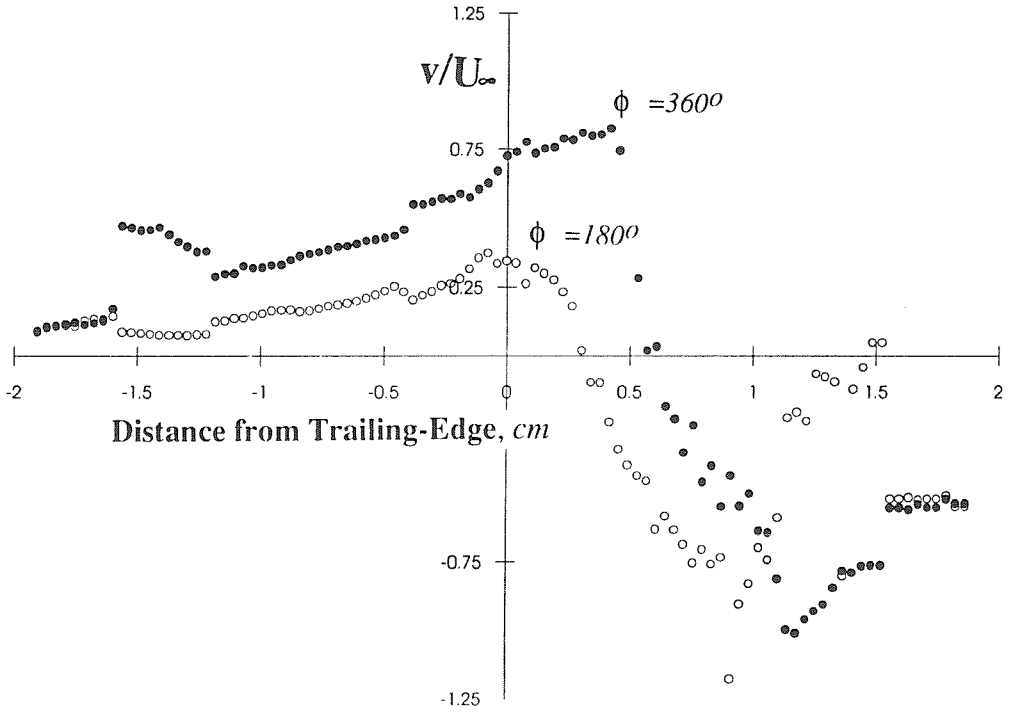

Figure 6.16 Tip Vortex Tangential Velocity at the Maximum and Minimum Angle of Attack of the Hydrofoil at a Reduced Frequency of 1.92
At the trailing edge of the hydrofoil, the tip vortex has already developed significant strength. The vortex, indicated here by the tangential velocity profile, is centered slightly to the suction side. The spanwise velocity continues to increase from the pressure side of the hydrofoil past the trailing edge until the flow rolls into the tip vortex.

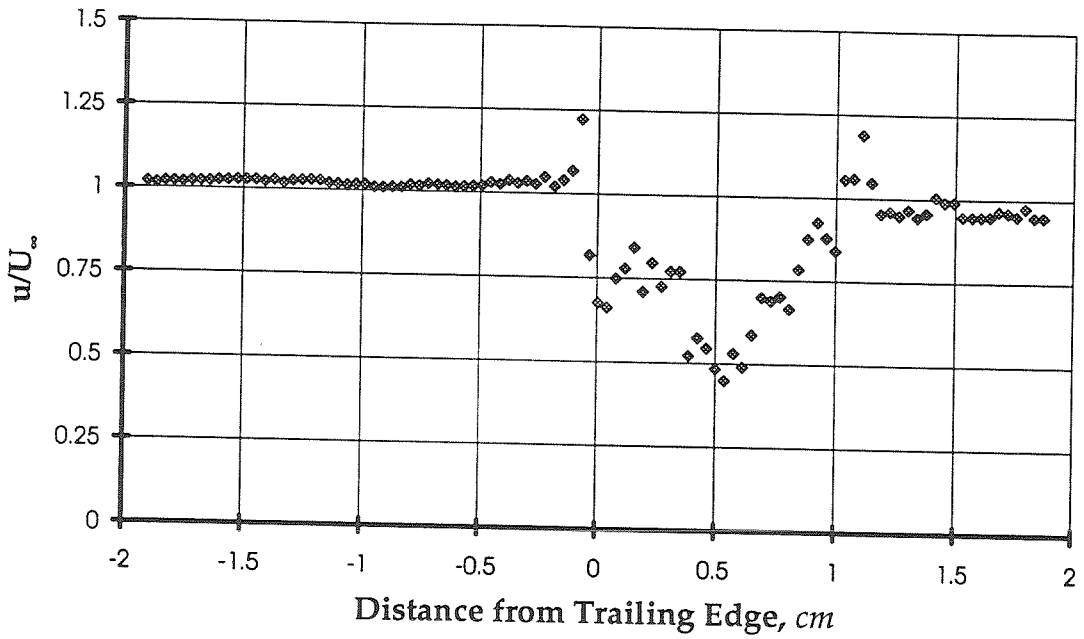

Figure 6.17 Streamwise Velocity at the Tip of the Hydrofoil Showing the Axial Velocity Profile of the Tip Vortex at a Reduced Frequency of 1.92
The streamwise velocity at the trailing edge of the hydrofoil just below the tip is shown. The tip vortex is apparent on the suction side of the hydrofoil. In the core of the tip vortex, the streamwise velocity is significantly less then the freestream velocity. Just outside the vortex core, the velocity is slightly higher than the freestream velocity.

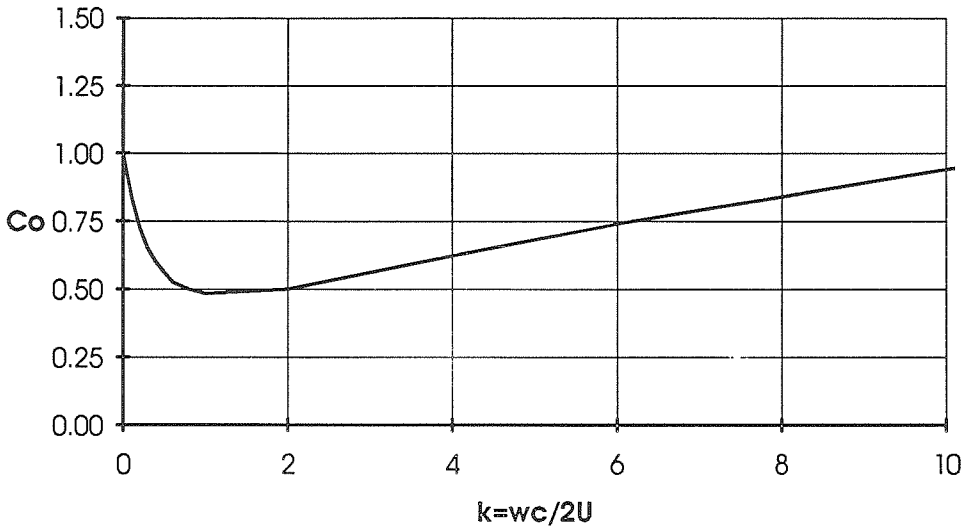

Figure 6.18 Circulation Rate of Change Coefficient
Graphic description of the magnitude of the circulation rate of change for a two-dimensional foil oscillating in pitch about the 38% chord position. The loading at first decreases as the reduced frequency increases and then increases. This is due to a shift from a predominantly circulatory change in loading of the foil to a predominately non-circulatory loading (added mass loading) of the foil at high reduced frequencies.

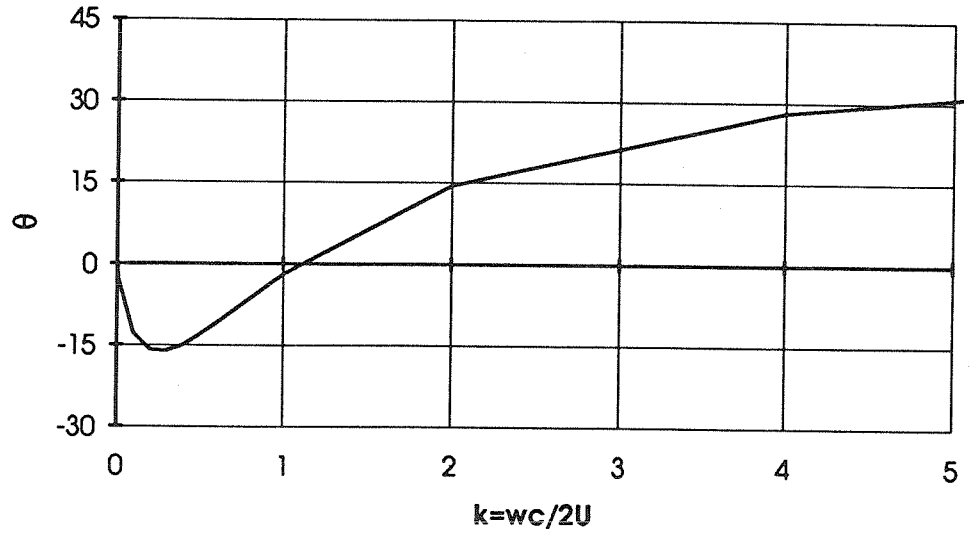

Figure 6.19 Phase Shift in Circulation Rate of Change
Phase shift due to oscillation of a two-dimensional foil about the 38% chord position. The phase shift lags the foil motion and then leads approaching 45 degrees as the reduced frequency increases. This is due to a shift from a predominantly circulatory change in loading of the foil to a predominately non-circulatory loading (added mass loading) of the foil at high reduced frequencies.

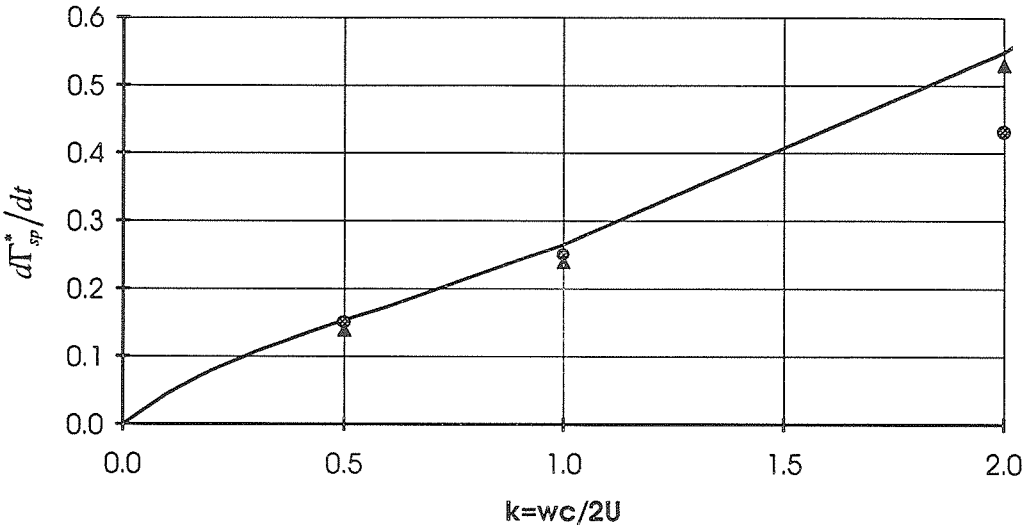

Figure 6.20 Comparison Between Experimental Measurements of Change in Circulation with Theoretical Predictions

Theoretical predictions, based on Theodorsen's analysis, of the time rate of change of circulation around a two-dimensional foil match closely with experimental measured time rate of change of circulation. Measurements taken near the root of the aspect ratio 2.3 foil (shown as circles) match closely with the two-dimensional foil measurements at low reduced frequencies, k<1.

CHAPTER 7

SUMMARY AND CONCLUSIONS

The research presented in this thesis was undertaken to acquire a basic understanding of the behavior of unsteady tip vortex flows and to bridge the gap between theoretical and numerical studies of unsteady flows and real-world applications. It investigates a small subset of the extremely complex flows that effect the performance of fluid based equipment and thus, is not intended to answer specific design concerns. It does, however, provide insight into unsteady flow behavior such as might be found in turbomachinery or propeller applications. For the first time, non-intrusive measurements of bound circulation, shed vorticity, and boundary layer and tip vortex velocity profiles of a harmonically pitching hydrofoil have been made. These measurements along with measurements of the effect of reduced frequency on the inception of cavitation, and observations of unsteady wake structures are the major experimental contributions of this work — providing a basis for an explanation of the intricacies of unsteady tip vortex flow behavior.

For the sake of brevity, this chapter has been broken into a number of sections in which the salient points have been highlighted in bullet fashion.

Experimental Setup

- *Developed foil oscillation system*

An oscillation mechanism was designed and constructed which oscillated a NACA 64A309 aspect ratio 2.3 hydrofoil with rounded tip in pitch near the center of pressure of the foil. This mechanism used a four bar linkage to harmonically drive the rectangular planform hydrofoil at frequencies up to 30Hz.

- *Developed two-dimensional experimental setup for studies of shed vorticity to compare with investigations made by others*

Studies of a two-dimensional oscillating hydrofoil were made by removing the tip of the three-dimensional foil and placing a Plexiglas panel on top. The panel was bolted to the top window of the LTWT. Nylon bushings were used to seal the bolts and to space the panel less than 1*mm* from the top of the foil.

- *Developed triple-pulsed holocamera control system for determining the sign of the wake vorticity vector*

The electronic controls of the holographic camera system, used in numerous experiments at Caltech, were modified to produce triple pulsed images with independent control of the time delay between each pulse. This modification allowed the sign of the local velocity vector in the fluid to be determined. The holocamera was used to determine the direction of rotation of the vorticity in the wake of the oscillating hydrofoil.

- *Developed synchronization system for matching instrumentation to the phase of the oscillating hydrofoil*

A synchronization circuit was designed and constructed to match instrumentation to the phase of the oscillating hydrofoil. This circuit input data from an optical shaft encoder at the base of the hydrofoil sent a trigger pulse to the RC Computerscope when a preset hydrofoil phase was reached. Software was written for the Computerscope to allow the incoming data to be clocked to the encoder output each time this trigger pulse was received.

- *Conducted surface flow visualization study to assess the suitability of various velocity measurement techniques by determine the complexity of the flow in the near wake of the foil*

Surface flow visualization studies were made of the finite aspect ratio oscillating hydrofoil to determine if recirculation was occurring near the trailing edge of the foil. Both paint dot surface flow visualization and telltales were used. The paint dots indicated the mean flow direction on the surface of the hydrofoil by forming streaks in the direction of the local flow. The telltales, on the other hand, provided more of an instantaneous view of the local flow direction near the surface. Strong recirculation of the flow was not

indicated in these studies, however, a phase lag in the motion of the fluid relative to the phase of the hydrofoil became apparent. The exact location of the telltales in the flow could not be controlled well. As a result, these flow studies were not used for quantitative information.

Wake Formations

- *Developed dye and air injection system for visualizing unsteady wake structures*

A tank was constructed to hold a dye solution for flow visualization. Pressurized air entering the top of the tank forced dye out a tube through the drive spindle of the hydrofoil oscillation mechanism, up through a shaft in the hydrofoil and out the tip into the core of the tip vortex. The dye solution was made from whole milk and alcohol (alcohol was added to adjust the density). By removing the tank and connecting the pressurized air line directly to a valve in the drive spindle, air could also be injected into the tip vortex core. The air and the dye were entrained into the low pressure region of the trailing vortices – tracing their intricate structures.

- *Developed hydrogen bubble flow visualization system*

A 25μm tungsten wire, held in place by a fiberglass bow, was connected to a 60V, 1 amp. DC power supply and used to generate a sheet of 50μm hydrogen bubbles. A traversing system was constructed to allow the wire to be positioned at any desired location along the span of the foil. Two halogen lamps illuminated the micro-bubble sheet from below. The hydrogen bubbles, because of their small size, closely followed the flow.

- *Completed detailed flow visualization study of three-dimensional vortex structures in the wake of an oscillating hydrofoil*

Using air and dye injection into the tip vortex core, a detailed study of the intricacies of the trailing wake structure of the finite aspect ratio hydrofoil was made. These studies showed that

- The wake formation of a harmonically pitching hydrofoil is composed of a complex vortex chain formed by pairs of spanwise vortices shed from the foil during each oscillation and the tip vortex of the foil.
- The structure of the trailing wake formation changes with reduced frequency and oscillation amplitude. At low reduced frequencies

and/or low oscillation amplitudes, strong links form between the spanwise vortices of one cycle of oscillation and link through the tip vortex formation to the vortices formed in the proceeding and subsequent cycles. At high reduced frequencies and/or large oscillation amplitudes, the spanwise vortices link strongly with the neighboring vortex formed during the same oscillation cycle. This change in structure is thought to be, in part, due to the observed phase shift in loading of the foil from a dynamic coupling of the fluid to the foil motion.

- The spanwise vortices generated by a finite aspect ratio foil differ significantly from those observed on a two-dimensional hydrofoil. Where only one vortex structure forms each half cycle of oscillation of a two-dimensional hydrofoil, two spanwise vortices form each half cycle of the finite aspect ratio foil.
- The lowest pressure region of the trailing wake structures formed under conditions of high reduced frequency or large oscillation amplitudes appears to be where the spanwise vortex structure, shed near the minimum angle of attack of the hydrofoil in an oscillation cycle, links with the tip vortex. The spanwise vortex formed near the minimum angle of attack rotates in a direction which appears to strengthen the rotation of the tip vortex. The spanwise vortex formed near the maximum angle of attack, on the other hand, appears to act against the rotation of the tip vortex.
- The spanwise vortices appear to roll up into the tip vortex – stretching them. This is believed to be a consequence of the velocity induced by each vortex structure on the other.

- *Examined unsteady wake structures behind a two-dimensional hydrofoil*

Using a hydrogen micro-bubble sheet, the two-dimensional flow structures in the wake of an infinite aspect ratio foil were observed. These observations showed that:

- A "rollup" regime exists where the reduced frequency of oscillation and the amplitude of oscillation is sufficient to cause the wake of the hydrofoil to roll up into spanwise vortex structures. This rollup regime appears to be a balance between the strength of the shed vorticity, the velocity of the flow, and the rate of diffusions of the shed vorticity into the wake flow.
- A consistent pattern of Kàrmàn vortices form near the trailing edge of the hydrofoil and travel downstream with the wake flow. When the reduced frequency of oscillation is near the Strouhal frequency of these

vortices, the Kàrmàn vortices appear to "adjust" to the frequency of the shed spanwise vortices – i.e. - their frequency matches the shedding frequency of the spanwise vortices and the phase at which they leave the foil adjusts to the phase of the spanwise vortices. As the reduced frequency of the hydrofoil is increased beyond this frequency, the Kàrmàn vortices continue to adjust to the shedding frequency of the spanwise structures.

Cavitation

- *Measured inception of cavitation on the surface of the oscillating hydrofoil*

Acoustical and visual techniques were used to detect cavitation on the surface of the oscillating hydrofoil. These measurements along with observations of the surface cavitation showed that:

- The inception of cavitation on the surface is strongly dependent on the reduced frequency of oscillation – the cavitation inception number at which surface cavitation occurs increases as the reduced frequency of oscillation increases.
- At high reduced frequencies, the inception of surface cavitation, the development of a leading edge vapor cavity, and the collapse of surfaced cavitation lags the phase of the hydrofoil oscillation. This phase lag phenomena was found to be the result of a change in angle of attack of the leading edge of the hydrofoil caused by an induced velocity from the pitching motion of the foil.
- A type of resonating condition occurs when the hydrofoil is oscillated at the same frequency that a surface cavity forms and collapses on a non-oscillating hydrofoil at the same mean angle of attack. This resonance takes the form of a loud pounding as the surface cavity collapses. This condition goes away at a slightly higher or slightly lower reduced frequency of oscillation and occurs only at the first harmonic of the surface cavity shedding frequency and not at higher harmonic excitation frequencies.

- *Developed a novel technique for quantitatively measuring cavitation in the tip vortex region*

An array of six photo-diodes mounted to an adjustable frame located against the test section window was used to detect the inception of cavitation in the tip vortex region. A halogen light illuminated the flow. Cavitation occurring in the trailing vortex cores cast shadows on the photo-diode array. A digital data taker recorded the cavitation events along with the phase of the

hydrofoil. By cross-correlating between diodes, the multiple diode array provided a means of detecting not only the cavitation event rate but also the phase at which the hydrofoil generated the vortex structure where cavitation first appeared as well as the downstream location where cavitation initiated.

- *Made quantitative measurements of cavitation inception in the tip vortex region of the oscillating hydrofoil*

Using the photo-diode detection technique, a series of experiments were done to determine the effects of pitching oscillation on the inception of cavitation in the tip vortex region of the oscillating hydrofoil. These measurements showed that:

  - At low reduced frequencies, cavitation first appears in the tip vortex formation, approximately three chords downstream, at a wake formation generated by the oscillating hydrofoil near its maximum angle of attack. At high reduced frequencies, cavitation first appears in the tip vortex formation where it links with the spanwise vortex formation formed when the hydrofoil is near its **minimum** angle of attack. These results relate well with the observations made of the wake flow using air and dye injection flow visualization and measurements of bound circulation and shed vorticity.
  - The cavitation number at which inception occurs **decreases** as the reduced frequency of oscillation increases up until a reduced frequency of about k=1.5 is reached and, then, the cavitation inception number increases with increasing reduced frequency. This is believed to be a consequence of a phase shift in the bound circulation of the hydrofoil.

Bound Circulation and Shed Vorticity

- *Developed method of determining the streamwise and spanwise velocity profiles at the trailing edge of the oscillating foil*

A Dantec Particle Dynamic Analyzer, PDA, was used as a single axis LDV to measure the velocity in the wake of the hydrofoil. LDV data was recorded along with the phase of the hydrofoil motion and ensemble averaged over several hundred oscillations. The data was then fit to a function based on the first and second harmonics of the foil oscillation frequency. By taking advantage of the periodicity of the ensemble averaged data in this way, a detailed interpolation of the velocity profile at the trailing edge of the hydrofoil was obtained. Calculations of bound circulation and shed vorticity

were made from these velocity profiles. Examination of the velocity profiles showed that;

- The boundary layer thickness of the hydrofoil expanded and shrank with the phase of oscillation. This effect was seen to increase with increased reduced frequency of oscillation

- *Made non-intrusive measurements of the bound circulation and shed vorticity of the oscillating foil*

Spanwise and streamwise velocity profiles were taken near the trailing edge of the hydrofoil at the 80%, 50%, and 20% span and at the tip of the hydrofoil at reduced frequencies of k=0.5, 1.0, and 2.0. From these non-intrusive measurements, the rate of change of spanwise circulation and the change in streamwise circulation were calculated based on the condition that the flow remained approximately parallel near the trailing edge of the foil. The following results were obtained from these calculations:

- The magnitude of the streamwise circulation leaving the trailing edge of the hydrofoil decreased as the reduced frequency of oscillation increased from k=0.5 to k=1.0 and then increased when the reduced frequency was increased to k=2.0. (This is consistent with observations of cavitation inception in the tip vortex region and with flow visualization studies done with air injection.)
- A phase lag occurs between the bound circulation and the angle of attack of the pitching hydrofoil – increasing with increasing reduced frequency of oscillation.
- A slight phase lag occurs between the shed streamwise circulation leaving the trailing edge of the hydrofoil near the tip and the shed streamwise circulation leaving the trailing edge of the hydrofoil near the root of the foil.
- The rate of change of the spanwise circulation was found to increase linearly with increased reduced frequency.
- The magnitude of the rate of change in spanwise circulation and streamwise circulation was found to change very little except near the tip of the foil.

- *Made measurements of the axial and tangential velocity of the tip vortex at the trailing edge of the hydrofoil*

Using the same technique used to measure the bound circulation and shed vorticity of the oscillating hydrofoil, tangential and axial velocity

measurements of the tip vortex were made at the trailing edge of the hydrofoil. These measurements showed that:

- A large axial velocity component (a jet) was observed in the core of the tip vortex in the upstream direction. Just outside of the core the axial velocity was found to be greater than the freestream velocity. The strength of the axial velocity components both inside the core and outside fluctuated with the phase of the hydrofoil oscillation.
- The tangential velocity profile of the tip vortex near the trailing edge of the hydrofoil was found to fluctuate very little with reduced frequency.
- Very high tangential velocities in the tip vortex were found to exist very close to the trailing edge of the foil.

- *Related measurements of the rate of change in bound circulation to theoretical predictions based on analyses by Theodorsen and Garrick*

The results of measurements of the rate of change in bound circulation of the two- and three-dimensional foil were compared with an expression for a two-dimensional oscillating plate based on analyses by Theodorsen [1935] and Garrick [1936]. The experimental measurements of the two-dimensional foil were found to be in good agreement while the measurements for the three-dimensional foil were found to be significantly lower in magnitude.

REFERENCES

Abbott, I. H., von Doenhoff, A. E., 1959. *Theory of Wing Sections*. Dover Publications, Inc., New York.

Abramson, H. N., Chu, Wen-Hwa, Irick, J. T., 1967. "Hydroelasticity with Special Reference to Hydrofoil Craft." Naval Ship Research and Development Center, Report 2557.

Acosta, A. J., Delong, R. K., 1971. "Experimental Investigations of Non-Steady Forces on Hydrofoils Oscillating in Heave." Non-Steady Flow of Water at High Speeds, Proceedings of the IUTAM Symposium, Leningrad, June 22-23, pp. 95-104.

Basu, B. C., Hancock, G. J., 1978. "The Unsteady Motion of a Two-Dimensional Aerofoil in Incompressible Inviscid Flow." *J. Fluid Mech.*, Vol. 87, pp. 159-178.

Chen, D. R., Sheu, M. J., 1989. "Numerical Solutions for Oscillatory Aerofoil at High Reduced Frequency." *Computer Methods in Applied Mechanics and Engineering*, Vol. 74, pp. 55-68.

Commerford, G. L., Carta, F. O., 1974. "Unsteady Aerodynamic Response of a Two-Dimensional Airfoil at High Reduced Frequency." *AIAA Journal*, Vol. 12, No. 1, pp. 43-48.

DeLaurier, J. D., Harris, J. M., 1981. "Experimental Study of Oscillating-Wing Propulsion." *J. Aircraft*, Vol. 19, No. 5, pp. 368-373.

Dengler, M. A., Goland, M., 1952. "The Subsonic Calculation of Circulatory Spanwise Loadings for Oscillating Airfoils by Lifting-Line Techniques." *Journal of Aeronautical Sciences*, November, pp. 751-759.

Faler, J. H., Leibovich, S., 1977. "Disrupted States of Vortex Flow and Vortex Breakdown." *The Physics of Fluids*, Vol. 20, No. 9, pp. 1385-1400.

Fleeter, S., 1980. "Trailing Edge Conditions for Unsteady Flows at High Reduced Frequency." *AIAA Journal*, Vol. 18, No. 5, pp. 497-503.

Franc, J. P., Michel, J. M., 1988. "Unsteady Attached Cavitation on an Oscillating Hydrofoil." *J. Fluid Mech.*, Vol. 193, pp. 171-189.

Fujita, H., Kovasznay, L. S. G., 1974. "Unsteady Lift and Radiated Sound from a Wake Cutting Airfoil." *AIAA Journal*, Vol. 12, No. 9, pp. 1216-1221.

References

Garrick, I. E., 1936. "Propulsion of a Flapping and Oscillating Airfoil." *NACA T.R.* No. 567.

Gates, E. M., 1977. "The Influence of Freestream Turbulence, Freestream Nuclei Populations, and Drag-Reducing Polymer on Cavitation Inception on Two Ansymmetric Bodies." Calif. Inst. of Tech., Div. of Eng. and Appl. Sci., Report No. E182-2.

Giesing, J. P., 1969. "Vorticity and Kutta Condition for Unsteady Multienergy Flows." *ASME J. Appl. Mech.*, Vol. 19, pp. 608-613.

Giesing, J. P., 1968. "Nonlinear Two-Dimensional Unsteady Potential Flow with Lift." *J. Aircraft*, Vol. 5, No. 2, pp. 135-143.

Green, S. I., 1988. "Tip Vortices - Single Phase and Cavitating Flow Phenomena." Ph.D. Thesis, Calif. Inst. of Tech., Div. of Eng. and Appl. Sci., Report No. 183-17.

Gustafson, K. E., Sethian, J. A., 1991. *Vortex Methods and Vortex Motion*. Society for Industrial and Applied Mathematics, Philadelphia, Pennsylvania.

Hart, D. P., 1991. "Cavitation Inception in the Tip Vortex Region of an Oscillating Hydrofoil." Proceedings of the ASME Cavitation and Multiphase Flow Forum, pp. 35-41.

Hart, D. P., Brennen, C. E., Acosta, A. J. 1990. "Observations of Cavitation on a Three-Dimensional Oscillating Hydrofoil." Proceedings of the ASME Cavitation and Multiphase Flow Forum, Toronto, pp. 49-52.

Hart, D. P., Acosta, A., Leonard, A., 1992. "Observations of Cavitation and Wake Structure of Unsteady Tip Vortex Flows." International STG Symposium on Propulsors and Cavitation, June 22-24, Hamburg, Germany.

Johnson, W., 1980. *Helicopter Theory*. Princeton University Press, Princeton, New Jersey, pp. 471-498.

Johnston, R. T., Sullivan, J. P., 1991. "The Vortex Interactions in a Propeller/Stator Flow Field." Proceedings of the AIAA 22nd Fluid Dynamics, Plasma Dynamics & Lasers Conference, June 24-26, Honolulu, Hawaii.

Jones, R. T., 1990. *Wing Theory*. Princeton University Press, Princeton, New Jersey.

References

Jones, R. T., 1938. "The Unsteady Lift of a Finite Wing." N.A.C.A. T.R. No. 682.

Katz, J., 1981. "Cavitation Inception In Separated Flows." Ph.D. Thesis, California Institute of Technology, Report No. 183-5.

Katz, J., 1984. "Cavitation Phenomena Within Regions of Flow Separation." *J. Fluid Mechanics*, 140, pp. 397-436.

Katz, J., Plotkin, A., 1991. *Low-Speed Aerodynamics From Wing Theory to Panel Methods*. McGraw-Hill Series in Aeronautical and Aerospace Engineering, pp. 421-495.

Katz, J., Weihs, D., 1981. "Wake Rollup and the Kutta Condition for Airfoils Oscillating at High Frequency." *AIAA Journal*, Vol 19, No. 12, pp. 861-863.

Katz, J., Weihs, D., 1978. "Behavior of Vortex Wakes from Oscillating Airfoils." *J. Aircraft*, December, pp. 861-863.

Koochesfahani, M. M., 1989. "Vortical Patterns in the Wake of an Oscillating Airfoil." *AIAA Journal*, Vol. 27, No. 9, pp. 1200-1205.

Kundu, P. K., 1990. *Fluid Mechanics*. Academic Press Inc., San Diego.

Lawrence, H. R., Gerber, E. H., 1952. "The Aerodynamic Forces on Low Aspect Ratio Wings Oscillating in an Incompressible Flow." *Journal of Aeronautical Sciences*, November, pp. 769-781.

Lorber, P. F., Covert, E. E., 1982. "Unsteady Airfoil Pressures Produced by Periodic Aerodynamic Interferences." *AIAA Journal*, Vol. 20, No. 9, pp. 1153-1159.

Lugt, H. J., 1983. *Vortex Flow in Nature and Technology*. John Wiley & Sons, New York.

Merzkirch, W. 1974. *Flow Visualization*. Academic Press Inc., New York.

Marchaj, C. A., 1979. *Aero-Hydrodynamics of Sailing*. Dodd, Mead & Company, New York, pp. 343-347.

McCroskey, W. J., 1982. "Unsteady Airfoils." *Annual Review of Fluid Mechanics*, Vol. 14, pp. 285-311.

References

O'Hern, T. J., 1987. "Cavitation Inception Scale Effects, I. Nuclei Distribution in Natural Waters, II. Cavitation Inception in a Turbulent Shear Flow." Ph.D. Thesis, California Institute of Technology, Report No. 183-15.

Ooi, K. K., 1981. "Scale Effects on Cavitation Inception in Submerged Jets." Ph.D. Thesis, California Institute of Technology, Report No. 183-6.

Postel, E. E., Leppert, E. L., Jr., 1948. "Theoretical Pressure Distributions for a Thin Airfoil Oscillating in Incompressible Flow." *J. of the Aeronautical Sciences*, August, pp. 486-492.

Ravindra, K., 1989. "Experimental Investigation of the Behavior of Cavities Behind a Wedge Oscillating in Pitch." International Conference on Mechanics of Two-Phase Flows, June, Taipei, Taiwan.

Satyanarayana, B., Davis, S., 1978. "Experimental Studies of Unsteady Trailing-Edge Conditions." *AIAA Journal*, Vol. 16, No. 2, pp. 125-129.

Sclavounos, P. D., 1987. "An Unsteady Lifting-Line Theory." *J. of Eng. Mathematics*, Vol. 21, pp. 201-226.

Sears, W. R., "Some Aspects of Non-Stationary Airfoil Theory and Its Practical Applications." *J. of the Aeronautical Sciences.*

Shen, Y, Gowing S., 1986. "Pressure Measurements on an Oscillating Foil in Fully Wetted and Cavitating Conditions." International Symposium on Cavitation, April, Sendai, Japan, pp. 95-102.

Shen, Y. T., Peterson, F. B.,1978. "Unsteady Cavitation on an Oscillating Hydrofoil." Proceedings of the 12th Symposium on Naval Hydrodynamics, June, Washington, D.C..

Shen, Y. T., Peterson, F. B.,1980. "The Influence of Hydrofoil Oscillation on Boundary Layer Transition and Cavitation Noise." Proceedings of the 13th Symposium on Naval Hydrodynamics, October 6-10, Tokyo, pp. 221-241.

Spalart, P. R., and Leonard, A., 1981. "Computation of Separated Flows by a Vortex-Tracing Algorithm." AIAA-81-1246.

Spalart, P. R., 1985. Simulation of Rotating Stall by the Vortex Method. *J. of Propulsion and Power*, 1, p. 235.

Theodorsen, T., 1935. "General Theory of Aerodynamic Instability and the Mechanism of Flutter." NACA T.R. No. 496.

References

Ueda, T., Dowell, E. H., 1981. "A New Solution Method for Lifting Surfaces in Subsonic Flow." *AIAA Journal*, Vol. 20, No. 3, pp. 348-355.

von Kármán, T., Sears, W. R. 1938. "Airfoil Theory for Nonuniform Motion." *J. Aeronautical Sciences*, Vol. 5, pp. 379-390.

Weihs, D., 1972. "Semi-Infinite Vortex Trails, and Their Relation to Oscillating Airfoils." *J. Fluid Mech.*, Vol. 54, part 4, pp. 679-690.

Zabusky, N. J., Melander, M. V., 1989. "Three-Dimensional Vortex Tube Reconnection: Morphology for Orthogonally-Offset Tubes." *Physica D*, Vol. 37, pp. 555-562.

APPENDIX A

DERIVATION OF 2-D UNSTEADY CIRCULATION

This appendix presents a derivation of the rate of change in circulation of a harmonically pitching two-dimensional foil based on the theoretical analyses of Theodorsen [1935] and Garrick [1936].

Theodorsen in 1935 formulated a theoretical expression for the unsteady forces experienced by a two-dimensional flat plate oscillating at a small-amplitude. He showed that the lift of a flat plate oscillating harmonically in pitch only can be expressed as

$$L = \pi\rho U_\infty c C_{(k)}\left[U_\infty \alpha + \frac{c}{2}\left(\frac{1}{2} - a\right)\dot{\alpha}\right] + \pi\rho\frac{c^2}{4}\left[U_\infty \dot{\alpha} - \frac{c}{2}a\ddot{\alpha}\right], \qquad \text{(A.1)}$$

where a is the point of oscillation (see Figure A.1) and the term $C(k)$, defined in Equation A.16, is the Theodorsen's *lift deficiency factor* which results from the downwash of the unsteady wake. This lift equation is a combination of a circulatory lift component and a non-circulatory (added mass) lift component

$$L = L_C + L_{N.C.} \qquad \text{(A.2)}$$

or in terms of the quasi-steady lift component of the oscillating foil

$$L = C_{(k)}L_Q + L_{N.C.},$$

where

$$L_Q = \tfrac{1}{2}\rho U_\infty c 2\pi\left[U_\infty \alpha + \tfrac{c}{2}\left(\tfrac{1}{2} - a\right)\dot{\alpha}\right] \qquad \text{(A.3)}$$

and

$$C_{(k)} = F + iG \qquad \text{(A.4)}$$

$$F_{(k)} = \frac{J_1(J_1 + Y_0) + Y_1(Y_1 - J_0)}{(J_1 + Y_0)^2 + (Y_1 - J_0)^2} \qquad \text{(A.5)}$$

$$G_{(k)} = -\frac{Y_1(J_1+Y_0)+J_1(Y_1-J_0)}{(J_1+Y_0)^2+(Y_1-J_0)^2} \tag{A.6}$$

Y_0, Y_1, and J_0, J_1 are solutions to the Bessel functions.

$C_{(k)}$ shifts the phase of the loading of the foil by ϖ where

$$\varpi = \tan^{-1}(G/F) \tag{A.7}$$

(ϖ and the magnitude of $C_{(k)}$ are tabulated as a function of the foil reduced frequency k in Table A.1. These terms are also plotted in Figures A.1 and A.2 along with the aspect ratio corrected values formulated by Jones [1938])

Setting $\alpha = \Delta\alpha e^{i\omega t}$ and taking the imaginary part of the solution of Equation A.1 (the part of the solution corresponding to the foil motion $\alpha = \Delta\alpha\sin(\omega t)$) we obtain

$$L = \tfrac{1}{2}\rho U^2 c\pi\Delta\alpha\left\{\left[k+2kF(\tfrac{1}{2}-a)+2G\right]\cos(\omega t)+\left[ak^2+2F-2kG(\tfrac{1}{2}-a)\right]\sin(\omega t)\right\} \tag{A.8}$$

which can be written

$$L = \tfrac{1}{2}\rho U_\infty^2 c2\pi C_L\Delta\alpha\sin(\omega t+\delta), \tag{A.9}$$

where

$$C_L = \sqrt{A_L^2+B_L^2} \tag{A.10}$$

$$A_L = \left[\tfrac{1}{2}ak^2+F-Gk(\tfrac{1}{2}-a)\right]$$

$$B_L = \left[\tfrac{1}{2}k+Fk(\tfrac{1}{2}-a)+G\right] \tag{A.11}$$

and

$$\delta = \tan^{-1}(B_L/A_L). \tag{A.12}$$

Using Theodorsen's expression for the vorticity in the wake and the definition of the circulation about the foil as the integral of the vorticity in the wake, an expression for the circulation around the foil can be found –

$$\Gamma = \int_{\frac{c}{2}}^{\infty}\gamma_{(x}dx = -i\frac{c}{2k}\gamma_o e^{i\phi}e^{i\omega t}, \tag{A.13}$$

where $\gamma_o e^{i\phi}$ is a complex quantity defined by Garrick [1936] to be

$$\gamma_o e^{i\phi} = -4U_\infty \Delta\alpha\left[1 + ik\left(\tfrac{1}{2} - a\right)\right](J + iM)e^{-ik}, \tag{A.14}$$

where

$$J = \frac{J_1 + Y_0}{D},\ M = \frac{Y_1 - J_0}{D} \tag{A.15}$$

$$D = (J_1 + Y_0)^2 + (Y_1 - J_0)^2 \tag{A.16}$$

and

$$J^2 + M^2 = \frac{1}{D}. \tag{A.17}$$

Thus, the non-dimensionalized change in circulation with time is

$$\frac{d\Gamma^*}{dt} = \frac{1}{U_\infty}\gamma_o e^{i\phi} e^{i\omega t}. \tag{A.18}$$

Taking the expression for the quasi-steady lift,

$$L_Q = \rho U_\infty \Gamma_Q = \tfrac{1}{2}\rho U_\infty c 2\pi\left[U_\infty \alpha + \tfrac{c}{2}\left(\tfrac{1}{2} - a\right)\dot{\alpha}\right] \tag{A.19}$$

and differentiating it in time, the quasi-steady time rate of change of circulation, non-dimensionalized with freestream velocity, is found to be

$$\frac{d\Gamma_Q^*}{dt} = i\frac{2\pi k}{U_\infty}\left[U_\infty \alpha + \tfrac{c}{2}\left(\tfrac{1}{2} - a\right)\dot{\alpha}\right]. \tag{A.20}$$

Thus, the non-dimensionalized time rate of change of circulation around the foil is

$$\frac{d\Gamma^*}{dt} = C_{\Gamma(k)}\frac{d\Gamma_Q^*}{dt}, \tag{A.21}$$

where

$$C_{\Gamma(k)} = -\frac{2(M - iJ)}{k\pi}e^{-ik} \tag{A.22}$$

which shifts the phase of the quasi-steady time rate of change of circulation around the foil by φ where

$$\varphi = \tan^{-1}(-J/M) - k. \tag{A.23}$$

The phase shift φ and the magnitude of $C_\Gamma(k)$ as a function of reduced foil oscillation frequency k is tabulated in Table A.2.

Setting $\alpha = \Delta\alpha e^{i\omega t}$ and taking the imaginary part of the solution

$$\frac{d\Gamma^*}{dt} = -4\Delta\alpha\left\{A_o \sin(\omega t - k) + B_o \cos(\omega t - k)\right\}, \tag{A.24}$$

where

$$A_o = J - Mk\left(\tfrac{1}{2} - a\right)$$

$$B_o = M + Jk\left(\tfrac{1}{2} - a\right). \tag{A.25}$$

Thus,

$$\frac{d\Gamma^*}{dt} = k2\pi C_o \Delta\alpha \cos(\omega t + \theta), \tag{A.26}$$

where

$$C_o = \frac{2}{\pi k}\sqrt{A_o^2 + B_o^2} \tag{A.27}$$

and

$$\theta = -\left[\tan^{-1}(A_o/B_o) + k\right] \tag{A.28}$$

C_o and θ are tabulated in Table A.2 as a function of k and plotted in Figures A.4 and A.5.

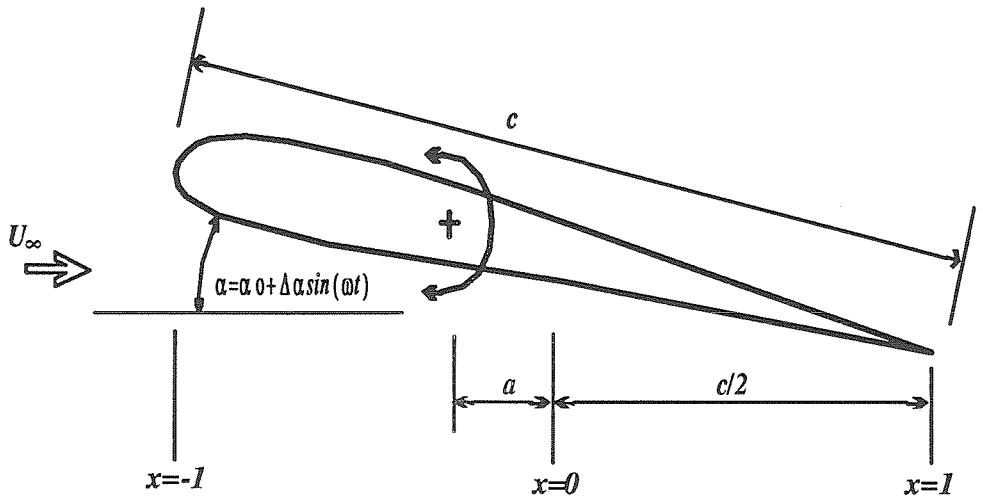

Figure A.1 Theodorsen's 2-D Unsteady Foil Analysis
Nomenclature for the oscillatory pitching motion of a two-dimensional flat plate.

Table A.1 Theodorsen's Lift Deficiency Function

k	1/k	F	G	|C(k)|	ϖ	C_{I_c}	δ
0.00	∞	1.000000	0.00000	1.0000	0.00	1.0000	0.00
0.01	100.0	0.982427	-0.04565	0.9835	-2.66	0.9833	-1.95
0.10	10.00	0.831924	-0.17230	0.8496	-11.70	0.8457	-4.12
0.20	5.00	0.727581	-0.18862	0.7516	-14.53	0.7509	1.45
0.30	3.33	0.664972	-0.17932	0.6887	-15.09	0.7040	9.67
0.40	2.50	0.664972	-0.16498	0.6464	-14.79	0.6906	18.58
0.50	2.00	0.624978	-0.15071	0.6166	-14.15	0.7012	27.20
0.60	1.67	0.570938	-0.13583	0.5869	-13.38	0.7213	35.39
0.80	1.25	0.554148	-0.11650	0.5663	-11.87	0.8200	48.23
1.00	1.00	0.539437	-0.10028	0.5487	-10.53	0.9391	58.29
2.00	0.50	0.512955	-0.05769	0.5162	-6.42	1.7056	86.02
4.00	0.25	0.503673	-0.03049	0.5046	-3.46	3.7058	110.97
6.00	0.17	0.501687	-0.02060	0.5021	-2.35	6.4032	125.59
10.00	0.10	0.500618	-0.01245	0.5008	-1.42	14.3415	142.69

Table A.2 Parameters Defining Circulation Rate of Change

k	1/k	J	M	$\|C_\Gamma\|$	φ	C_o	θ
0.00	∞	0.00000	0.00000	1.0000	0.00	1.0000	0.00
0.01	100.0	-0.00072	-0.01542	0.9829	-3.23	0.9830	-2.80
0.10	10.00	-0.02568	-0.12900	0.8374	-16.99	0.8397	-12.75
0.20	5.00	-0.05015	-0.22040	0.7195	-24.28	0.7274	-15.86
0.30	3.33	-0.05920	-0.29382	0.6360	-28.58	0.6515	-16.06
0.40	2.50	-0.0537	-0.35681	0.5742	-31.43	0.5989	-14.94
0.50	2.00	-0.03458	-0.41205	0.5265	-33.45	0.5614	-13.14
0.60	1.67	-0.00449	-0.45401	0.4818	-34.95	0.5271	-11.00
0.80	1.25	0.08276	-0.53533	0.4311	-37.05	0.5010	-6.42
1.00	1.00	0.19783	-0.57908	0.3896	-38.44	0.4847	-1.93
2.00	0.50	0.84187	-0.25627	0.2801	-41.52	0.5004	14.43
4.00	0.25	-0.12986	1.24421	0.1991	-43.23	0.6221	28.10
6.00	0.17	-1.32871	-0.76601	0.1627	-43.82	0.7406	33.49
10.00	0.10	0.38910	1.94251	0.1261	-44.30	0.9418	38.00

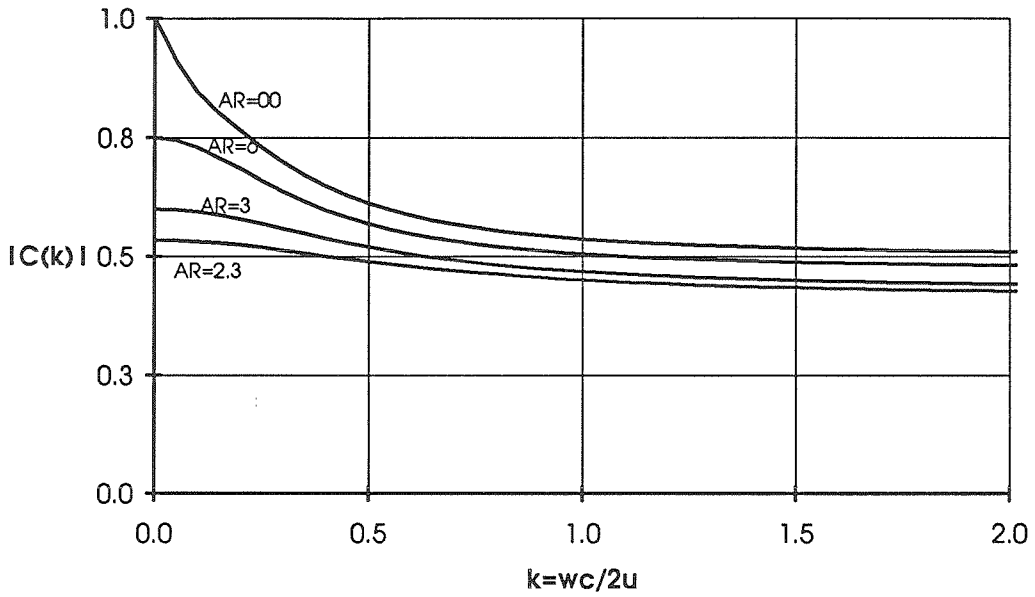

Figure A.2 Theodorsen's Lift Deficiency Factor
Graphic description of the magnitude of the Theodorsen lift deficiency function C(k), AR=∞. Corrections, formulated by Jones [1938], for other aspect ratios are also shown.

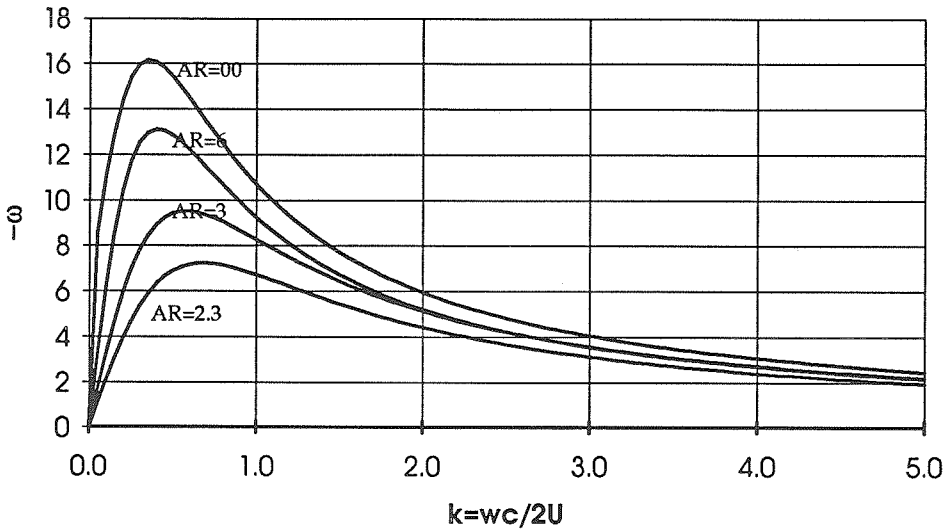

Figure A.3 Phase Shift from Theodorsen's Lift Deficiency Factor
Graphic description of the phase lag due to the Theodorsen lift deficiency function C(k), AR= ∞. Corrections, formulated by Jones [1938], for other aspect ratios are also shown.

APPENDIX B

CATALOGUE OF EXPERIMENTAL RESULTS

This appendix serves as a reference for comparisons with numerical solutions of unsteady tip vortex flows and as an elaboration of the results presented in the body of this thesis.

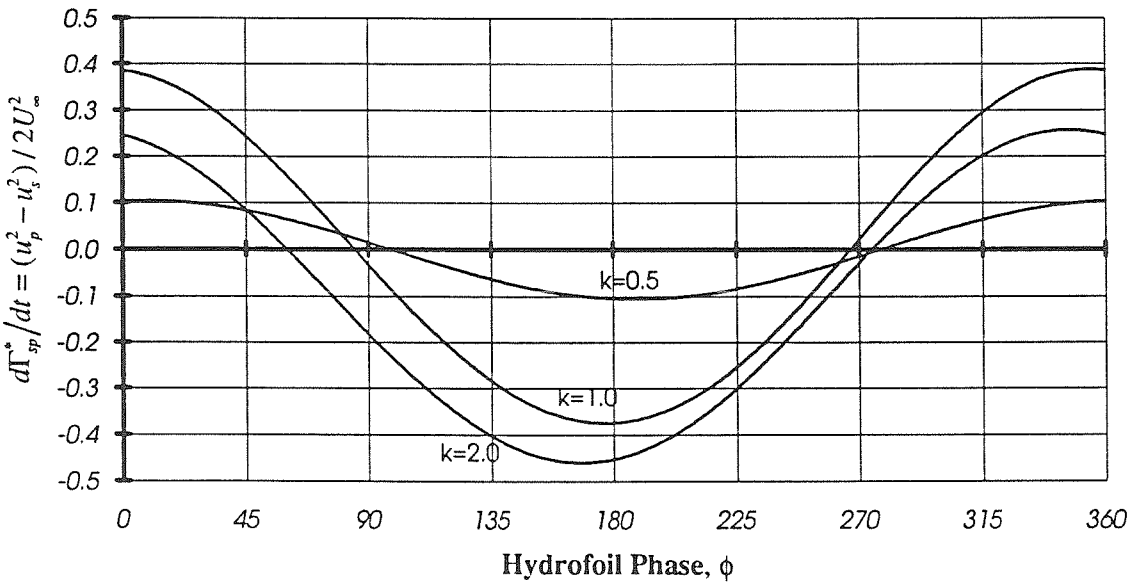

Figure B.1 Graph of Change in Spanwise Circulation at the 50% Span Location as a Function of Hydrofoil Phase for Three Reduced Frequencies
The change in spanwise circulation is shown non-dimensionalized with the freestream velocity for reduced frequencies of k=0.48, 0.96, and 1.92. The hydrofoil is oscillating ±5° about a mean angle of attack of 5°. The peak change in circulation increases linearly with reduced frequency. Note also that the phase of the loading of the hydrofoil shifts with increasing reduced frequency.

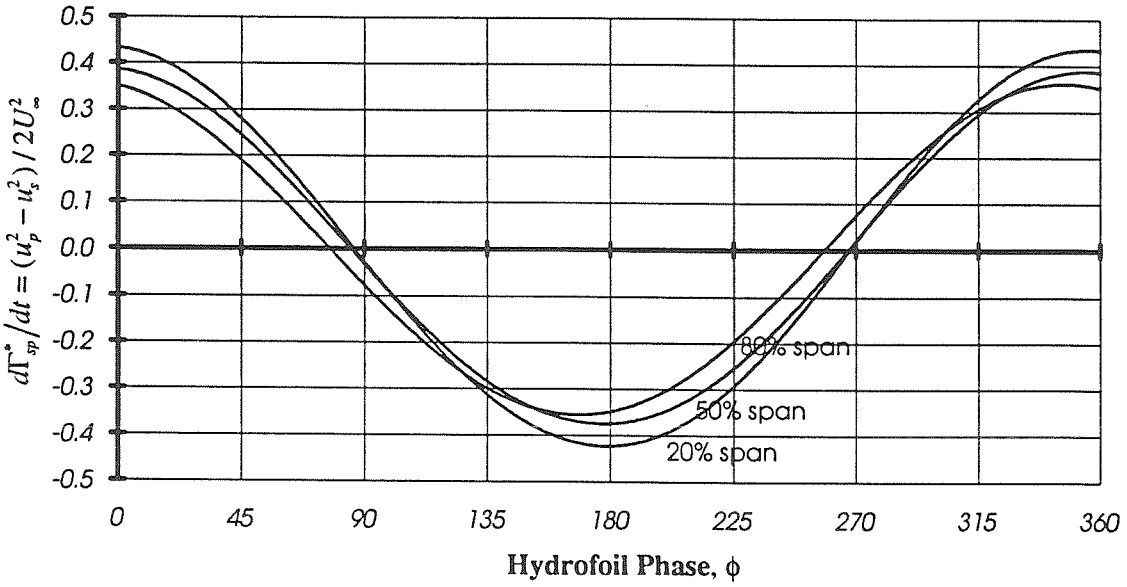

Figure B.2 Measured Rate of Change of Spanwise Circulation as a Function of Hydrofoil Phase at a Reduced Frequency of 1.92 for Span Locations of 80%, 50%, and 20%

The change in spanwise circulation varies little with the span of the hydrofoil. This indicates, by the continuity of vorticity, that most of the change in circulation in the streamwise direction occurs near the tip of the hydrofoil.

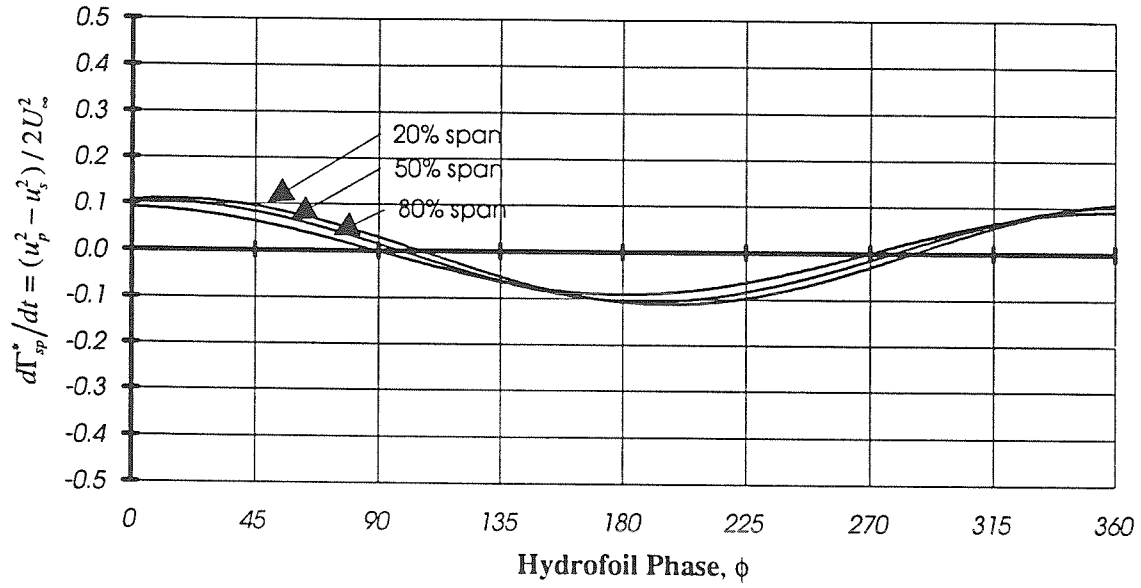

Figure B.3 Measured Rate of Change of Spanwise Circulation as a Function of Hydrofoil Phase at a Reduced Frequency of 0.48 for Span Locations of 80%, 50%, and 20%

The change in spanwise circulation varies little with the span of the hydrofoil. This indicates, by the continuity of vorticity, that most of the change in circulation in the streamwise direction occurs near the tip of the hydrofoil.

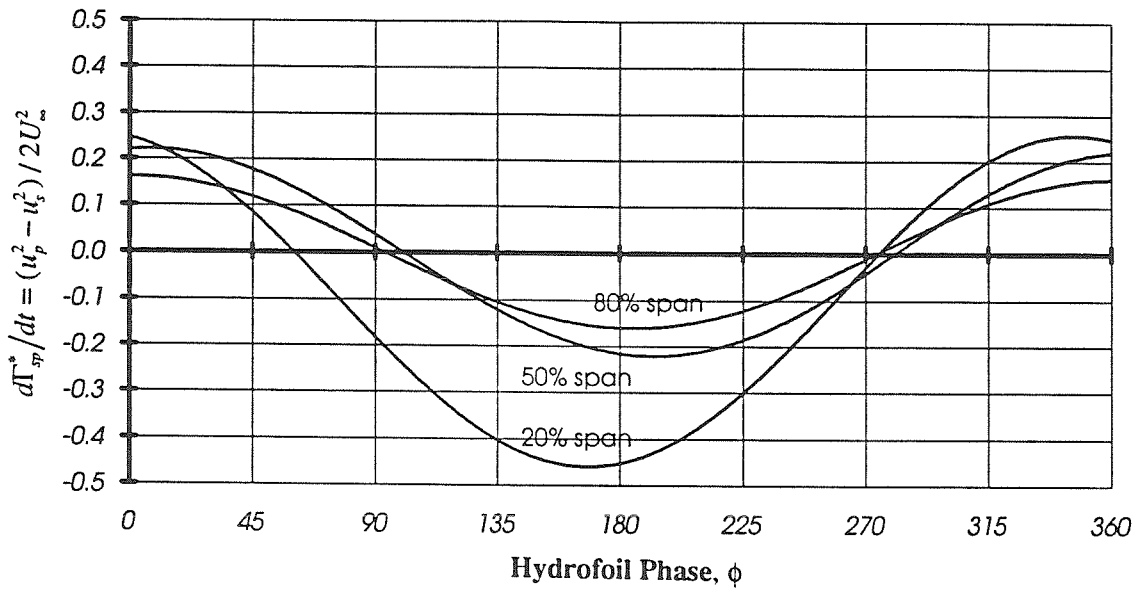

Figure B.4 Measured Rate of Change of Spanwise Circulation as a Function of Hydrofoil Phase at a Reduced Frequency of 0.96 for Span Locations of 80%, 50%, and 20%

The change in spanwise circulation varies little with the span of the hydrofoil. This indicates, by the continuity of vorticity, that most of the change in circulation in the streamwise direction occurs near the tip of the hydrofoil.

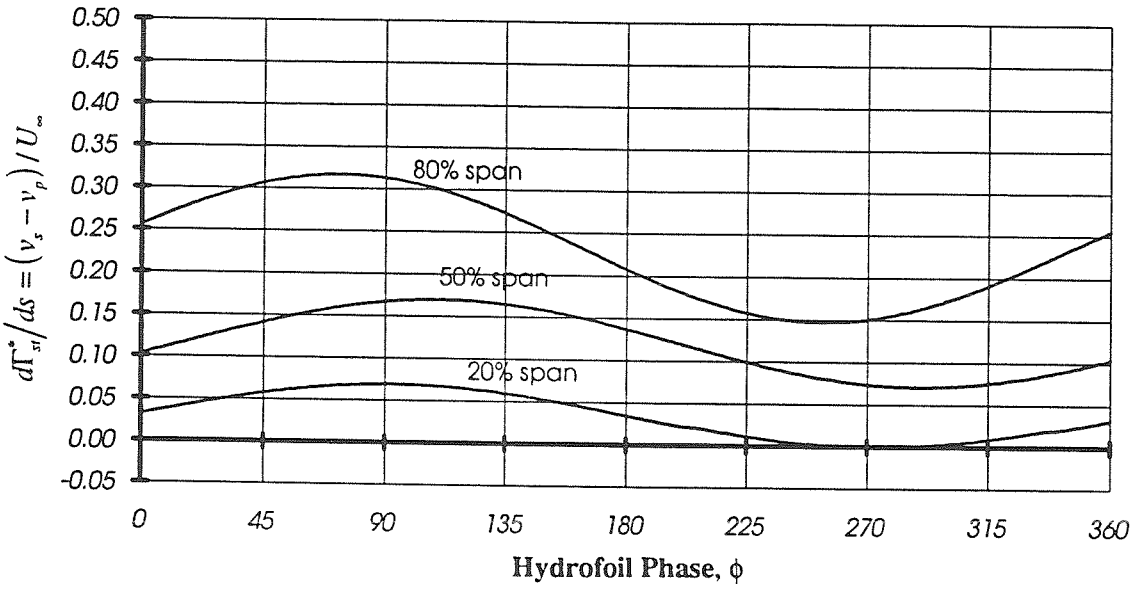

Figure B.5 Graph of Change in Streamwise Circulation as a Function of Hydrofoil Phase at a Reduced Frequency of 0.48 for Three Span Locations
The change in streamwise circulation is shown non-dimensionalized with the freestream velocity for span locations of 20%,near the base of the foil, 50%, and 80%, near the tip of the foil.. The hydrofoil is oscillating ±5° about a mean angle of attack of 5° at a reduced frequency of 1.92. The hydrofoil is at its maximum angle of attack of 10° at the 0° phase position and at the minimum angle of attack, 0°, at the 180° phase position. The majority of change in streamwise circulation occurs within the last 30% of the span of the foil.

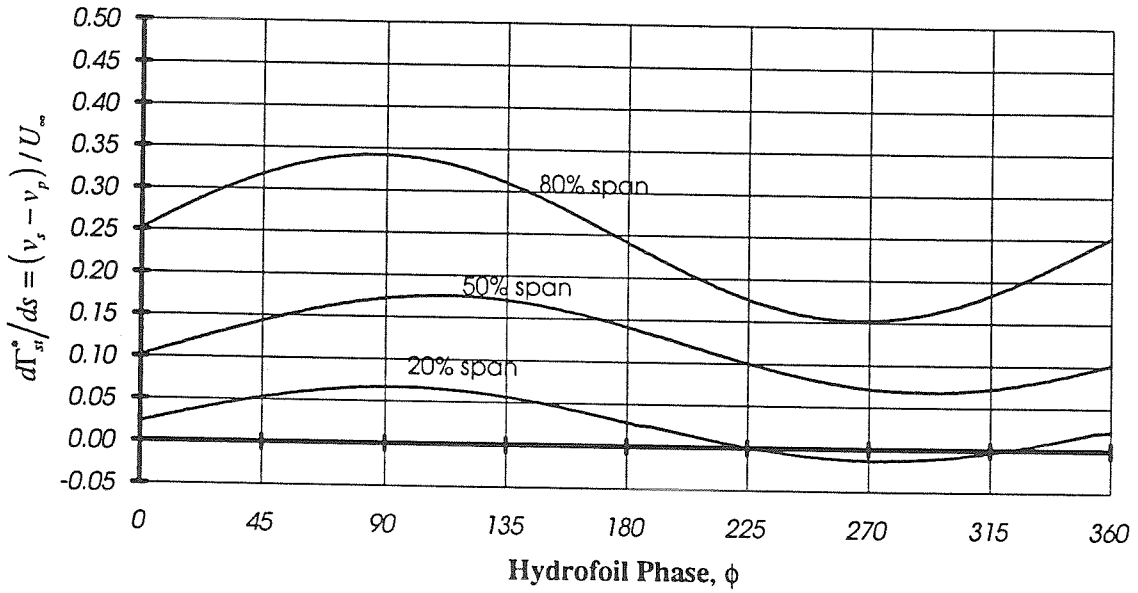

Figure B.6 Graph of Change in Streamwise Circulation as a Function of Hydrofoil Phase at a Reduced Frequency of 0.96 for Three Span Locations
The change in streamwise circulation is shown non-dimensionalized with the freestream velocity for span locations of 20%,near the base of the foil, 50%, and 80%, near the tip of the foil. The hydrofoil is oscillating ±5° about a mean angle of attack of 5° at a reduced frequency of 1.92. The hydrofoil is at its maximum angle of attack of 10° at the 0° phase position and at the minimum angle of attack, 0°, at the 180° phase position. The majority of change in streamwise circulation occurs within the last 30% of the span of the foil.

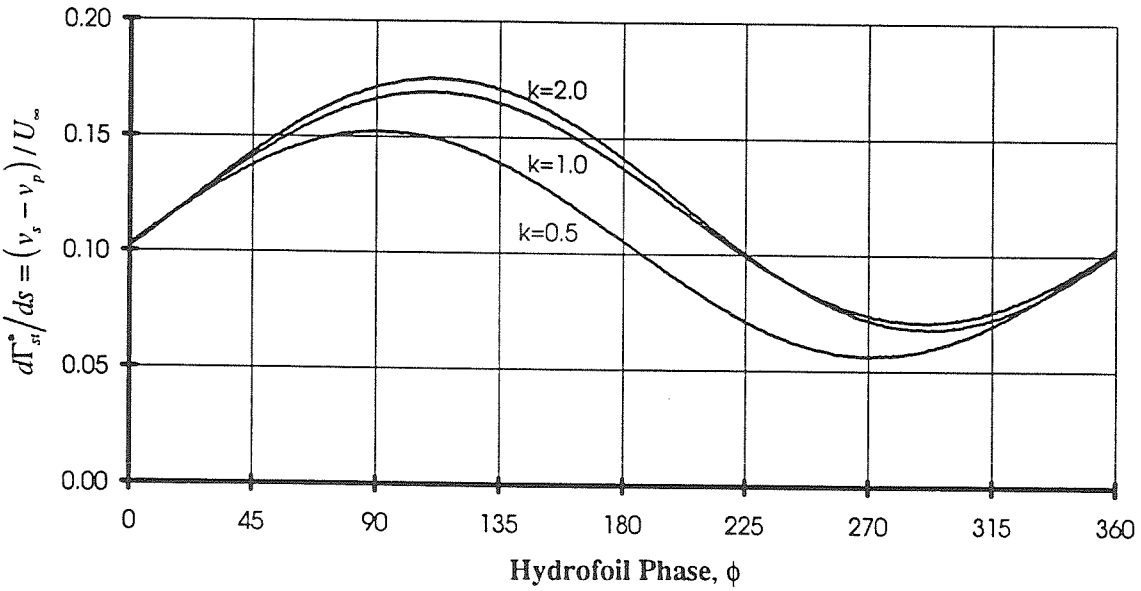

Figure B.7 Measured Rate of Change of Streamwise Circulation as a Function of Hydrofoil Phase for Three Reduced Frequencies at the 50% Span Location
Near the tip of the hydrofoil, 50% span, there exists a large change in streamwise circulation with the phase of the hydrofoil. This change in circulation, however, is only slightly dependent on the reduced frequency of oscillation.

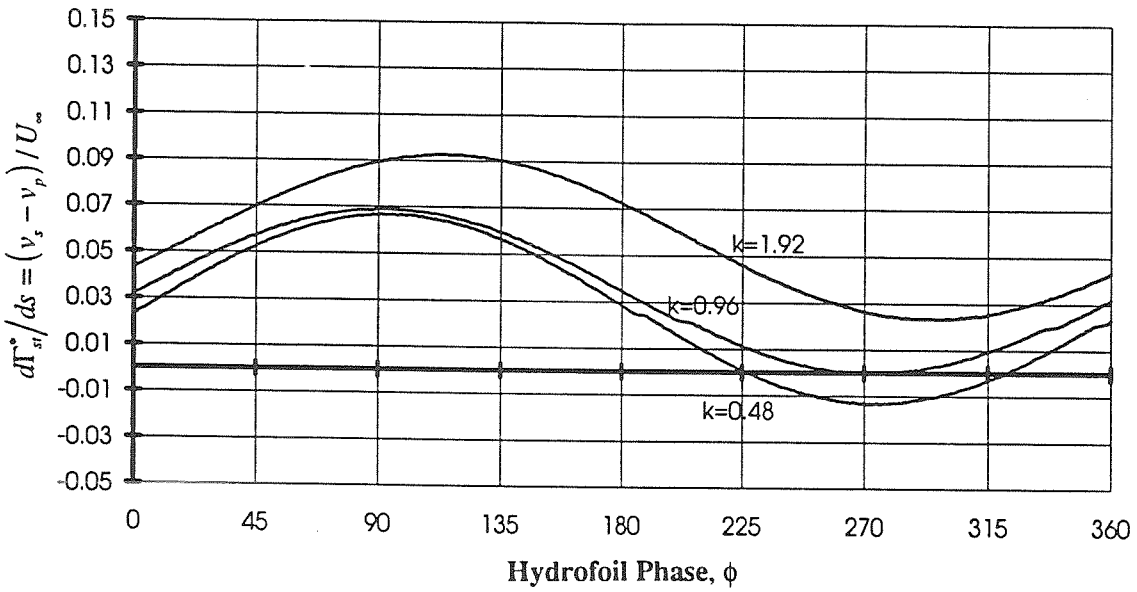

Figure B.8 Measured Rate of Change of Streamwise Circulation as a Function of Hydrofoil Phase for Three Reduced Frequencies at the 20% Span Location
Near the tip of the hydrofoil, 20% span, there exists a large change in streamwise circulation with the phase of the hydrofoil. This change in circulation, however, is only slightly dependent on the reduced frequency of oscillation.

APPENDIX C

HOLOGRAPHIC CAMERA CONTROL SYSTEM

This appendix explains the holocamera control system and contains electrical schematics for the control system and related circuits. This system is a modification of the one contained in Appendix I of O'Hern [1987]. It was modified to provide a third laser pulse and to increase the reliability and safety of the existing system.

C.1 System Overview

The holocamera, described in Chapter 2, is controlled by the digital Pulsed Laser Timing Circuit. This timing circuit, as shown in Figure C.1, connects to a number of components in the laser system. The function of each of these components is described in Table C.1. The Pulsed Laser Timing Circuit is the heart of the holocamera control sytem. It initiates a sequence of events and monitors the output of the ruby laser. Table C.2 lists the control sequences initiated by the timing circuit under normal operation.

The Pulsed Laser Timing Circuit has a number of inputs and outputs located on the front and back panel of the box (see Figure C.3). The function of each of these is described in Table C.3. The inputs and outputs of the Pulsed Laser Timing Circuit are protected against short-circuits. The outputs have been designed to drive 50Ω or greater loads. All BNC connectors are isolated ceramic bulkhead types to protect external circuitry from ground shorts and to reduce problems associated with electromagnetic induced noise caused by the discharge of the Pockels Cell. Care should be taken when connecting BNC cables to these connectors to prevent them from breaking off.

C.2 Electronic Design of Pulsed Laser Timing Circuit

The Pulsed Laser Timing Circuit is built on two boards with edge connectors. These boards mount inside a cage in the main box. The three digital time delay circuits are contained on one board and the camera control, laser control, and lase monitors are contained on the other. Figures C.4 through C.7 show the electrical schematics of the circuit. Included on these schematics are the pin location of the inputs and outputs. Not included are various chokes used to filter electronic noise which caused premature triggering of the time delays. The circuit is constructed using CMOS IC's. CMOS is considerably more immune to electronic noise than TTL due to the high threshold *on* voltage and the low *off* voltage. All switch inputs to the circuit pass through a debounce circuit isolating them from the main timing electronics. Outputs are protected and driven by transistors for high current sourcing.

C.3 Electronic Design of Pockels Cell Power Circuit

The Pockels Cell Power Circuit contains three Krytron trigger modules. These modules are housed in aluminum boxes helping to isolate them from the rest of the circuitry. Krytrons are very high speed, high current switches. They use a radioactive source to maintain a plasma gas which carries the current during discharge. Krytrons require a keep-alive during operation. This is essentially a cathode heating element. This element is prone to burnout much in the same way as a light bulb. Therefore, it is recommended that the Pockels Cell Power Circuit be used as little as possible. Each of the trigger modules contain a circuit like the one in Figure C.8. They are powered by a high voltage switching power supply. A separate power supply is used to drive a voltage regulating circuit which controls power to the switching

power supply. Yet another power supply is used to provide power to a sensing circuit which monitors the Pockels Cell pulses and outputs this information through a BNC on the front panel.

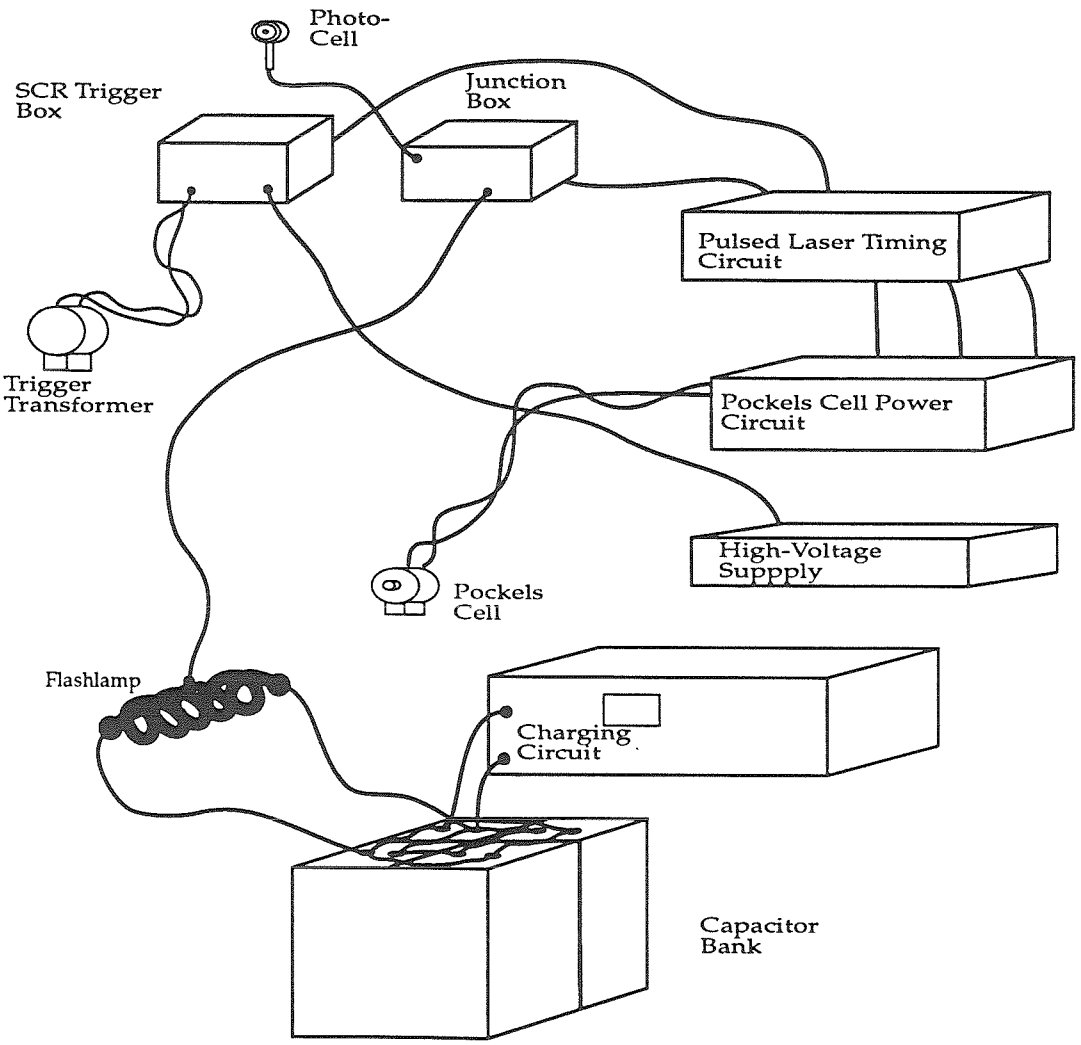

Figure C.1 Schematic of Holocamera Control System
Schematic showing connection of holocamera control components.

Table C.1 Holocamera Control System

Capacitor Bank	Stores high-voltage charge used to drive the laser flashlamp
Charging Circuit	Controls charging of the capacitor bank - regulates voltage and sounds alarm when capacitors are fully charged
High Voltage Source	Generated high-voltage needed to trigger the flashlamp - normally set to 700 volts
Junction Box	Provides convenient connection point for camera circuit, photo-cell, Pockels Cell, and flashlamp trigger voltage input
Photo-cell	Detects lasing - beam splitter diverts laser light onto this photo-diode. Used to monitor laser output
Pockels Cell	Electronic polarized shutter controlling lasing - mounts inside the laser cavity
Pockels Cell Power Circuit	Generates high-voltage for the Pockels Cell and triggers the extremely fast (1*ns*) discharge needed to operate the Pockels Cell effectively
Pulsed Laser Timing Circuit	Controls the timing of each of the holocamera system components
SCR Flashlamp Control Box	Contains SCR circuit which triggers the laser flashlamp on command from the Pulsed Laser Timing Circuit

Table C.2 Standard Control Sequence of the Pulsed Laser Timing Circuit

Time	Event
(System Triggered)	• Initiation of timing sequence
0.0*s*	• Camera shutter opened • Lasing monitors reset • Sync. pulse triggered • Pulse timers loaded with user set values • Laser flash lamp triggered
0.25*ms*	• Pulse timers started
0.25*ms* + Delay	• Pockels Cell triggered • Delay indicator LED lit if lasing occurs correctly
0.13*s*	• Camera shutter closed
0.15*s*	• Camera advanced if lasing detected • Camera advance LED lit if film advances • Photo counter and lasing counter advanced • Master lase LED lit if lasing detected

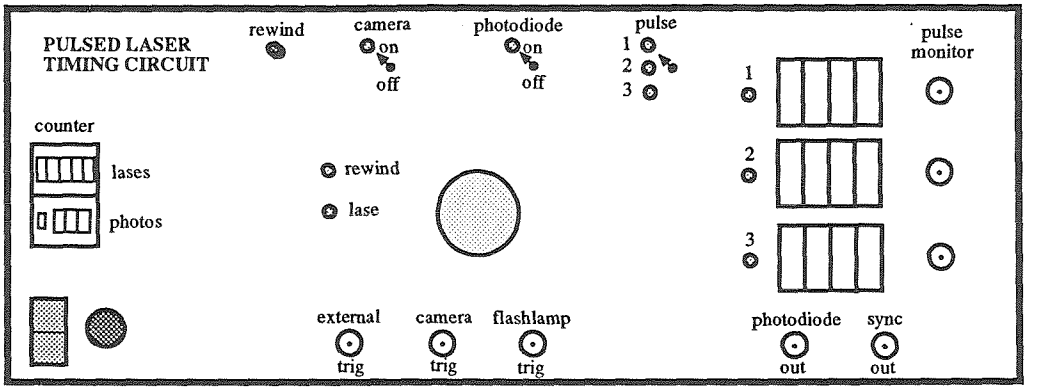

FRONT

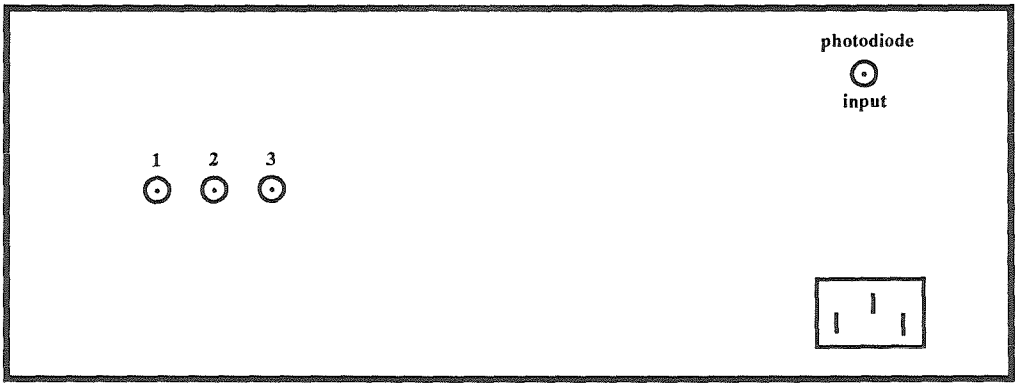

BACK

Figure C.2 Schematic of Pulsed Laser Timing Circuit Panel Layout
Schematic showing location of inputs, outputs and switches.

Table C.3 Inputs and Outputs of the Pulsed Laser Timing Circuit

Front Panel:	
Camera Enable (switch)	Used to enable and disable camera - allows laser system to be tested without exposing film.
Delay 1,2,3 (BNC)	Outputs TTL level pulse when delay times out. (Used to monitor operation of timing circuit.)
Delay (thumbwheel switches)	Sets time delay of pulses in micro-seconds.
Ext. Camera Trigger (BNC)	Controls the camera shutter: Closed - shutter open. Open - shutter closed, film advanced. (Used to manually control the camera when holocamera is synchronized to an external device.)
Ext. Lase (BNC)	Manually controls laser timing control sequence independent of the camera; Open - nothing. Closed - laser timing control sequence started. (Used to synchronized the holocamera to an external device.)
Ext. Trigger (BNC)	Same as the Fire Button: Open - nothing. Closed - starts standard timing control sequence.
Fire (Trigger) Button	Starts standard timing control sequence.
Photo Cell Enable (switch)	Enables the photo cell used to detect lasing. If this switch is off, the camera must be advanced manually.
Photo Cell Level Adjustment (pot)	Used to adjust the sensitivity of the photo cell detection circuit to laser output.
Pulse Enable (3 position switch)	Used to select the number of laser pulses per hologram.
Rewind (switch)	Miss-named switch - advances film manually. Must have the Photo Cell Enable switch off and the Camera Enable switch on for this switch to work.
Sync. Out (BNC)	Outputs a 10μs TTL level pulse when the laser timing control sequence starts. (Used to synchronize external devices to the holocamera.)
Back Panel:	
1, 2, 3 (BNC)	Outputs CMOS level pulse to Pockels Cell Power Circuit to trigger Pockels Cell.
Camera Plug	Feeds power to the camera and opens shutter and advances film (pin-outs compatible with old design).
Laser Exciter Output (BNC)	Outputs CMOS level pulse to laser trigger circuit to fire laser flashlamp.
Photo Cell Input (BNC)	Input for photo cell used to detect lasing.

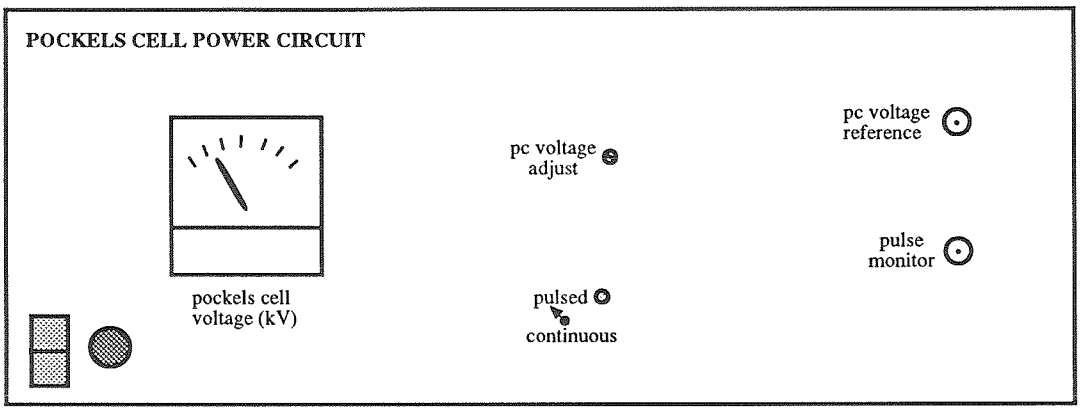

Figure C.3 Schematic of Pockels Cell Power Circuit Panel Layout
Schematic showing location of inputs, outputs and switches.

Table C.4 Inputs and Outputs of Pockels Cell Power Circuit

Front Panel:	
High Voltage Adjustment (pot)	Adjust the level of voltage which triggers the Pockels Cell (note - too high a voltage setting will cause EMI noise prematurely triggering time delays 2 and 3 when delay 1 triggers).
Pulse Monitor (BNC)	Outputs an analog signal proportional to the signal received by the Pockels Cell - must be connected to a monitoring source with a very high input impedance and frequency response to get accurate readings.
Back Panel:	
Delay 1,2,3	Inputs from the Pulsed Laser Timing Circuit for triggering the Pockels Cell after the corresponding time delay.

MASTER TIMING CIRCUIT (Board A)

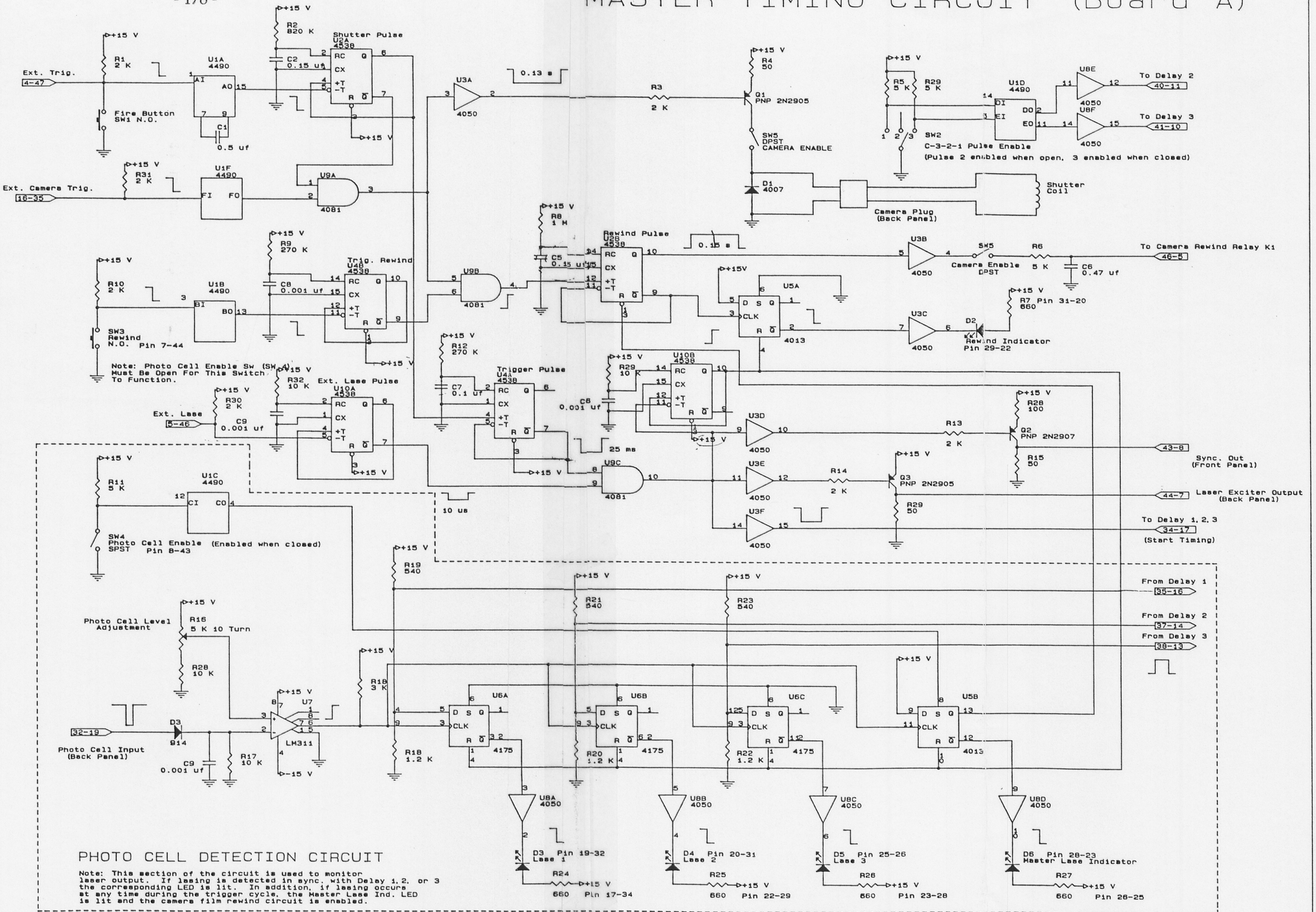

PHOTO CELL DETECTION CIRCUIT

Note: This section of the circuit is used to monitor laser output. If lasing is detected in sync. with Delay 1, 2, or 3 the corresponding LED is lit. In addition, if lasing occurs at any time during the trigger cycle, the Master Lase Ind. LED is lit and the camera film rewind circuit is enabled.

U1: pins 10, 8 GND, 16 V+
U2: pins 1, 8, 15 GND, 16 V+
U3: pins 8 GND, 1 V+ -
U4: pins 1, 8, 15 GND, 16 V+
U5: pins 7 GND, 14 V+
U6: pins 13 GND, 16 V+
U7: -
U8: pins 11, 8 GND, 1 V+
U9: pins 5, 6, 8, 9, 12, 13, 7 GND, 14 V+ Note - Pin numbers (eg. Pin 25-32) refers to the edge conector pin numbers

Figure C.4 Electrical Schematic of Timing Circuit (Board A-Main Control Circuit)

DOUGLAS P. HART		
Size C	Document Number MASTER TIMING CIRCUIT	REV A
Date: October 30, 1989	Sheet 1 of 4	

TIME DELAY #1 (Board B1)

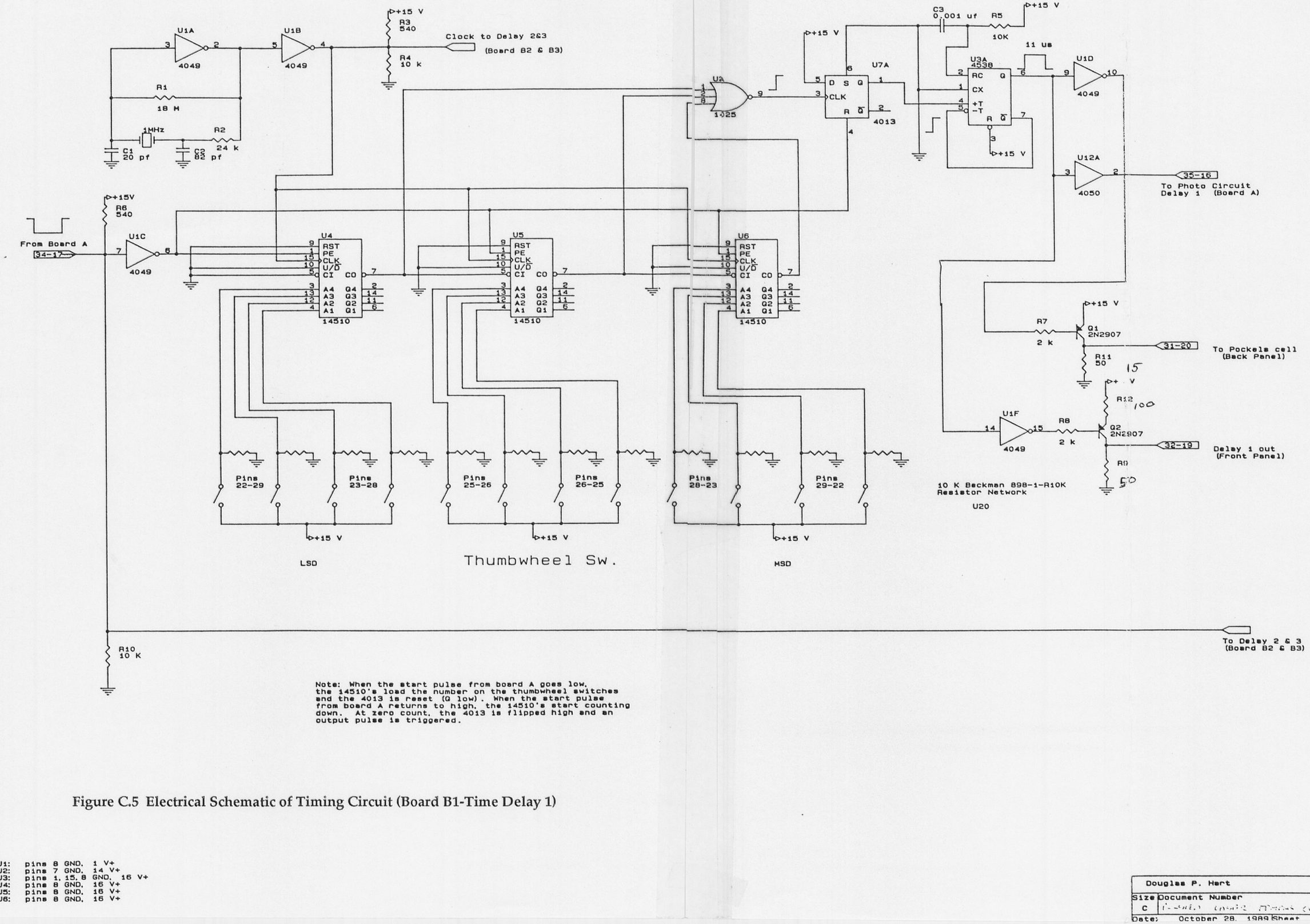

Note: When the start pulse from board A goes low, the 14510's load the number on the thumbwheel switches and the 4013 is reset (Q low). When the start pulse from board A returns to high, the 14510's start counting down. At zero count, the 4013 is flipped high and an output pulse is triggered.

Figure C.5 Electrical Schematic of Timing Circuit (Board B1-Time Delay 1)

U1: pins 8 GND, 1 V+
U2: pins 7 GND, 14 V+
U3: pins 1, 15, 8 GND, 16 V+
U4: pins 8 GND, 16 V+
U5: pins 8 GND, 16 V+
U6: pins 8 GND, 16 V+

Douglas P. Hart		
Size C	Document Number	REV A
Date: October 28, 1989	Sheet 2 of 4	

TIME DELAY #2 (Board B2)

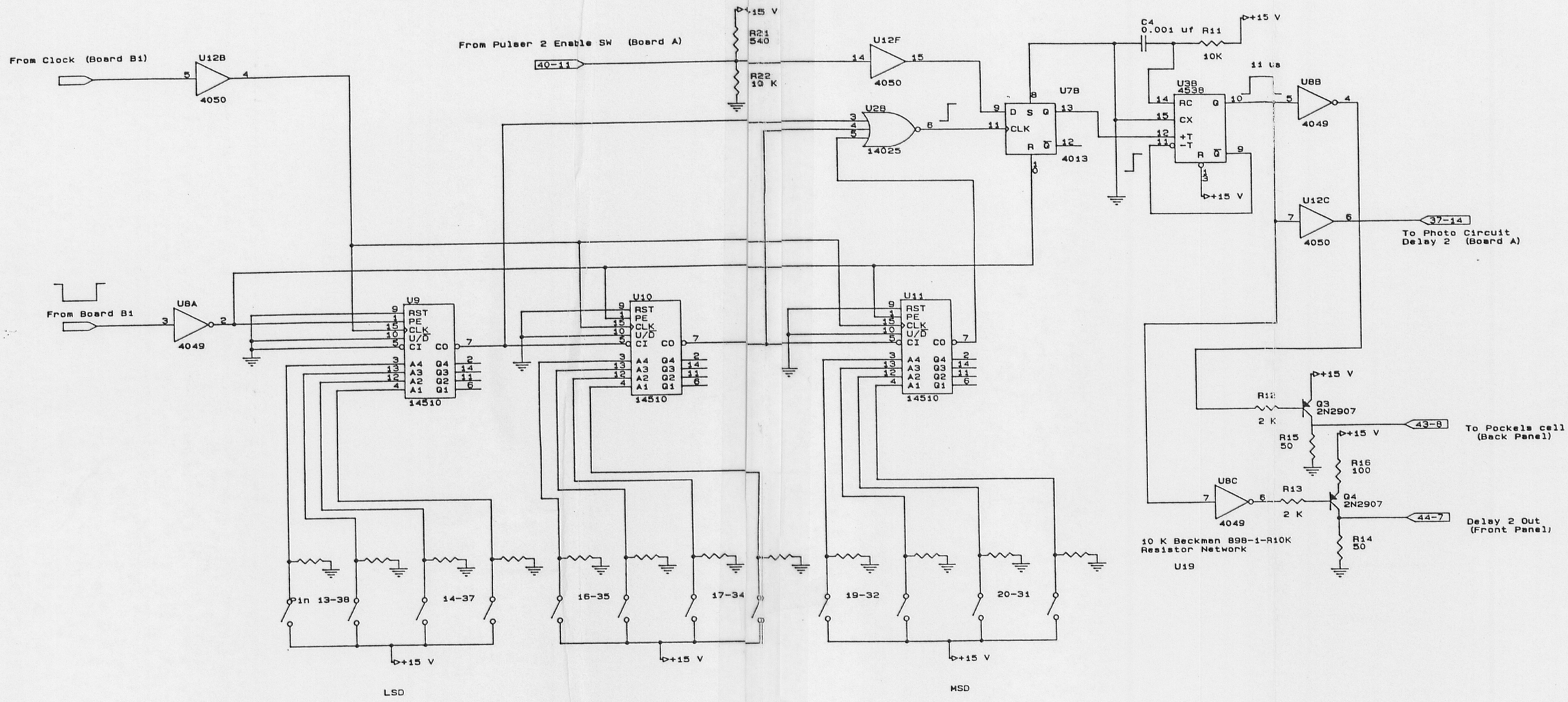

Figure C.6 Electrical Schematic of Timing Circuit (Board B2-Time Delay 2)

U7: pins 7 GND, 14 V+
U8: pins 8 GND, 1 V+
U9: pins 8 GND, 16 V+
U10: pins 8 GND, 16 V+
U11: pins 8 GND, 16 V+
U12: pins 8 GND, 1 V+

Douglas P. Hart

Size C | Document Number | REV A

Date: October 20, 1990 Sheet 2 of 4

TIME DELAY #3 (Board B3)

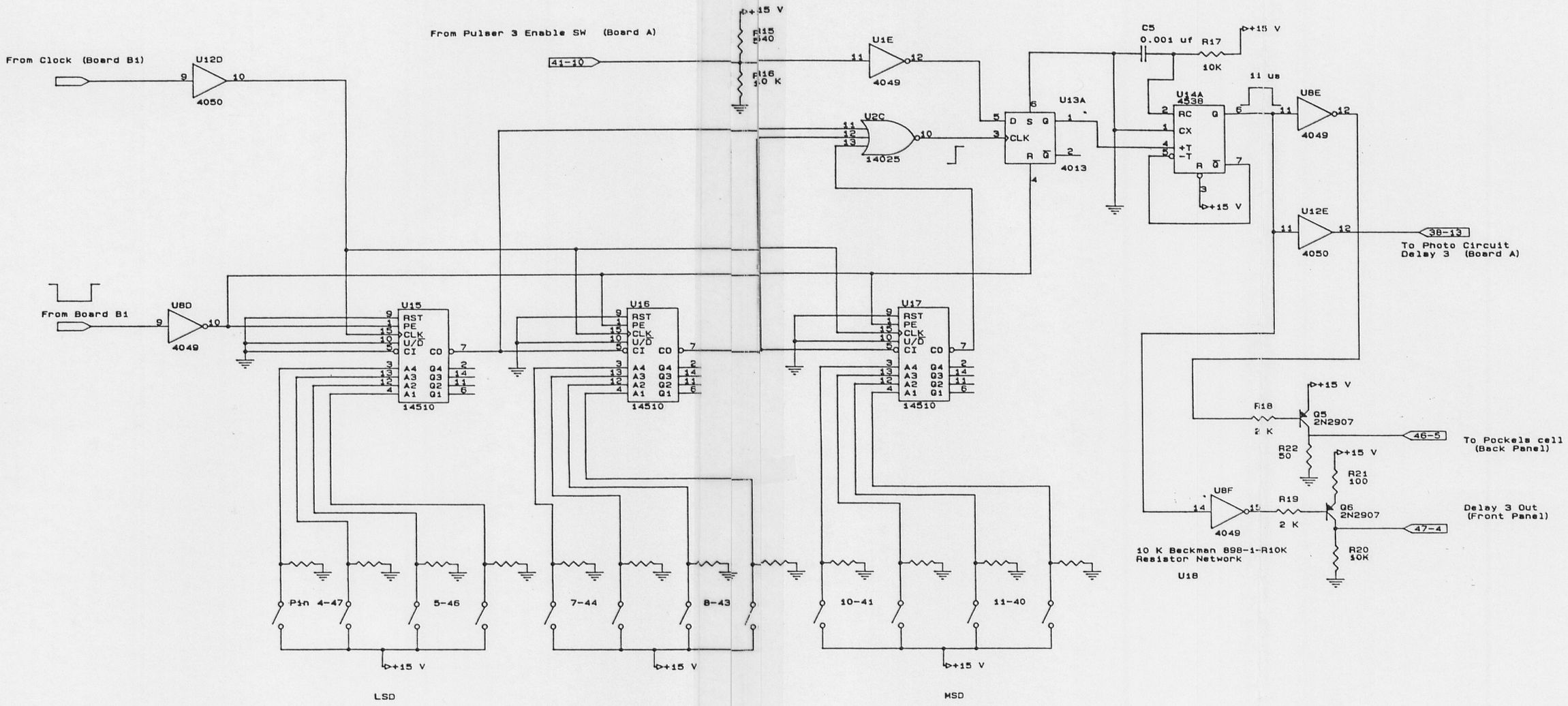

Figure C.7 Electrical Schematic of Timing Circuit (Board B3-Time Delay 3)

U13: pins 8, 9, 11, 10, 7 GND, 14 V+
U14: pins 1, 15, 8, 12, 11, 13, 14 GND, 16 V+
U15: pins 8 GND, 16 V+
U16: pins 8 GND, 16 V+
U17: pins 8 GND, 16 V+

Douglas P. Hart		
Size C	Document Number [illegible]	REV A
Date: October 29, 1989	Sheet 4 of 4	

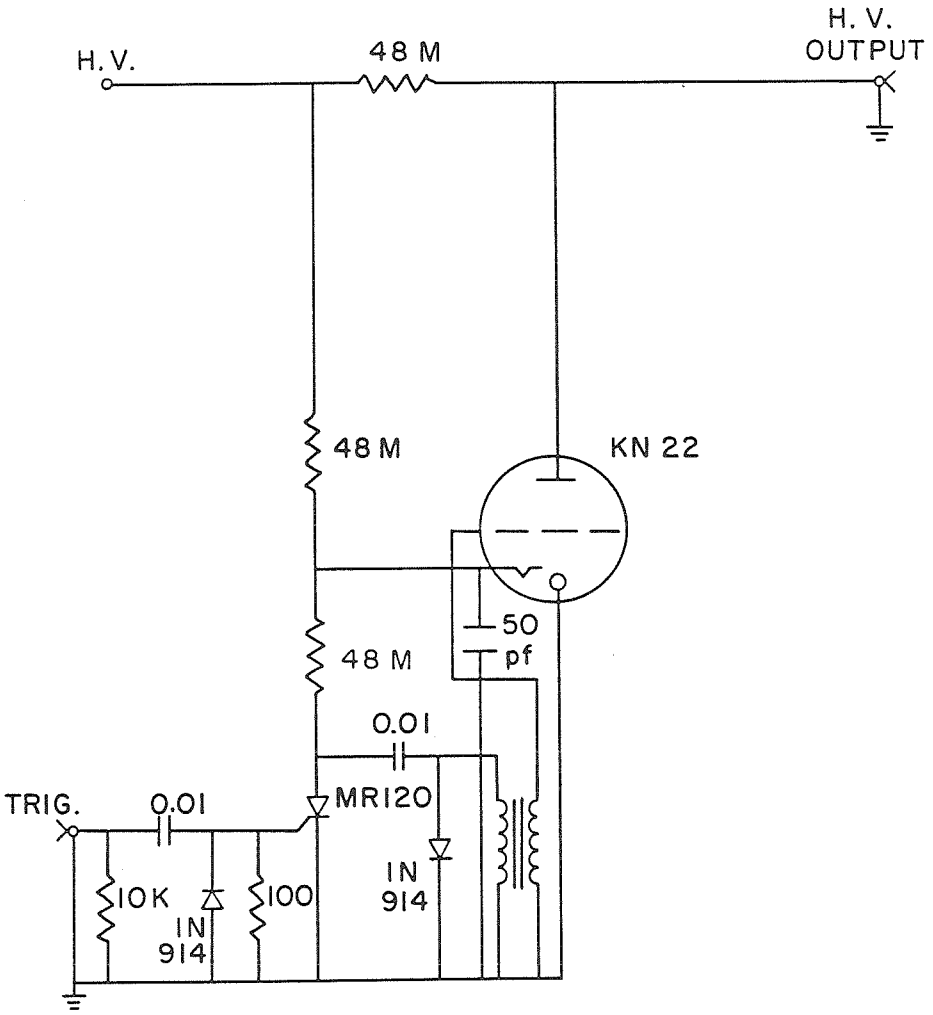

Figure C.8 Electrical Schematic of Pockels Cell Pulsing Circuit

APPENDIX D

SYNCHRONIZATION CIRCUIT

This appendix describes the Synchronization Circuit used to synchronize instrumentation to the phase of the oscillating hydrofoil. Included is a description of the principle of operation and details of the circuit design.

D.1 Principle of Operation

The synchronization circuit takes inputs from the encoder on the shaft of the oscillating hydrofoil mechanism and outputs the oscillation frequency in hertz and outputs a pulse when the phase of oscillation is equal to the phase set on a series of thumbwheel switches (see Table D.1). In addition, the Synchronization Circuit is set up to control the motor of the oscillation mechanism via a Sabina Motor Controller (see Chapter 2). Unfortunately, this circuit was never designed to provide feedback to stabilize the oscillation frequency. As the DC motor of the oscillation mechanism warms up, the oscillation frequency slowly creeps up. Since the Sabina Motor Controller requires only a resistive type of element to adjust the motor output, a simple JFET based circuit could be added to this circuit to provide frequency stabilization.

The optical shaft encoder used in the experiments described in this thesis has five lines coming out of it; a ground line, a +28V (+V) line, a -28V (-V) line, a zero pulse line, and a 1024 pulse line. The zero pulse line puts out a signal from -V to +V and back to -V each time the shaft encoder passes through its zero phase position. The 1024 pulse line outputs 1024 equally spaced pulses from -V to +V and back to -V with each rotation of the encoder. The synchronization circuit loads an internal counter with the number set on a

series of thumbwheel switches each time a zero pulse is received and then counts down incrementally each time one of the 1024 pulses is received. When zero on the counter is reached, a TTL level pulse is output on the SYNC line of the circuit. The outputs of the Synchronization Circuit, as shown in Figure D.1 are designed to both source and sink current. If a device with a voltage source greater than +5V is connected to any of the outputs, the Synchronization Circuit will sink the voltage source to ground each time an output pulse is sent. If, however, a source less than +5V is connected to one of the outputs, the Synchronization Circuit will output +5V through a 50Ω output protection resistor. The reason this is done is to provide both a signal for synchronizing data with the phase of the oscillating hydrofoil and to provide a means to trigger a strobe or the holographic camera at a particular phase of the hydrofoil.

The frequency of oscillation is determined simply by multiplying the pulses per revolution from the 1024 pulse line of the optical shaft encoder by 1/1024 seconds. This is done by counting the pulses from a 1*kHz* crystal oscillator until a pulse is received from the 1024 pulse line at which time the total count is latched and displayed. This method results in a slight error (2.4%) in determining the oscillation frequency, but this error is small relative to other sources of error in the experimental system.

D.2 Electronic Design of Synchronization Circuit

Table D.1 Inputs and Outputs of the Synchronization Circuit

Front Panel:	
1024 Pulses (BNC)	Outputs a CMOS level pulse each time an encoder pulse is received
Digital Display	Displays the frequency of rotation in *Hz*
Ext. Trigger (BNC)	Same as the Trigger Button: Open - nothing Closed - starts standard timing control sequence
Run - Jog	Controls the status of the motor Start/Stop switch Run - motor keeps running until Stop switch is pressed Jog - motor stops when Start switch is not pressed
Sync. Out (BNC)	Outputs a 10μs CMOS level pulse when the preset number of encoder pulses is received
Thumbwheel Switches	Sets number of encoder pulses before outputting a pulse - note that the encoder outputs 1024 pulses per revelation
Trigger Button	Starts counting down preset number of encoder pulses
Trigger Enable (switch)	Sets Trigger mode; Single - one output pulse when encoder count is reached Continuous - resets count and outputs a pulse each time the same encoder count is reached
Zero (BNC)	Outputs a CMOS level pulse each time the zero encoder pulse is received
Back Panel:	
Encoder Cable	Feeds power to the optical encoder and inputs the zero and 1024 pulses from the encoder.
Motor Control Cable	Cable connecting motor controls to Sabina motor control circuit

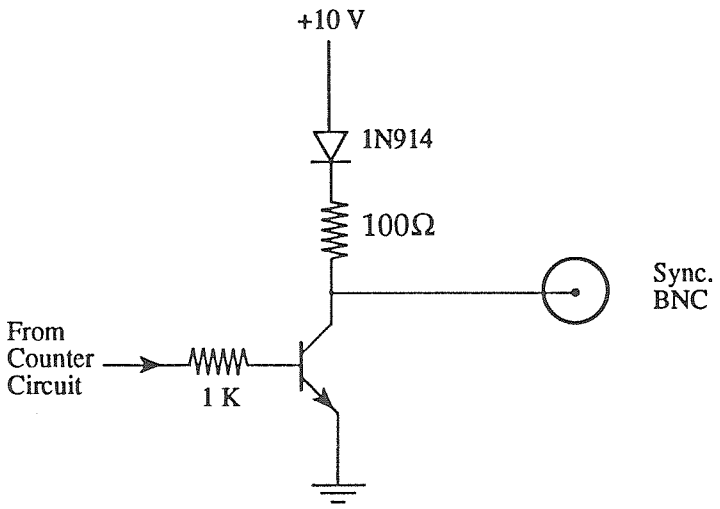

Figure D.1 Schematic of Synchronization Circuit SYNC. Output

APPENDIX E

RESEARCH SPECIFIC SOFTWARE

This appendix documents a number of computer programs that were used to take and process data acquired during the course of investigations of the oscillating hydrofoil research presented in this thesis. These programs are listed here so that, should the reader desire, they may duplicate the authors work. In addition, the reader may find the fundamental basis of these programs useful in their own research even though some of these programs are hardware specific. The author is well aware that advances in computers, data takers, and packaged software are likely to make these programs obsolete in a short period of time from the date of publication.

E.1 RC Ensemble Averaging Software

The RC Ensemble Averaging Program was written to take a data trace from the RC Computerscope, described in Chapter 2, and average it with a previously acquired trace. This program takes advantage of the RC Computerscopes duel internal memory buffers to continually acquire data as it averages. The number of channels and the number of traces averaged can be set in advance. The program was originally set up to use an external trigger and clock source. In this manner, the data could be synchronized to the phase of the oscillating hydrofoil by connecting the zero pulse of the shaft encoder output to the external trigger input and connecting the 1024 pulse output to the clock input with the RC Computerscope buffer set at 1K.

The RC Ensemble Averaging Program is written in Turbo Pascal with an external Assembly Language routine for an 8086 based machine. The Assembly Language routine is used to transfer the data from the RC

Computerscope buffer to the computers memory and average the data. In addition, this routine can be used to acquire statistical information about the data by storing the square of the sums, the sums, etc.. It should be noted that the Assembly Language routine requires a bit of time to download the data. It is possible to get ahead of this routine by inputting an external clock pulse that is faster than data can be downloaded. When this happens, the program simply ignores the incoming data until downloading is complete. This is usually not a problem if many data traces are to be averaged and sequential data traces are not needed. Variables in the Turbo Pascal portion of this program used to hold the data are forced to reside at a particular location in the computers memory. This allows the data to be easily downloaded from the RC Computerscope buffer directly into the arrays in the Turbo Pascal program. The difficulty with this is that the computer may be using the specified memory address for other programs or devices. The user can change these addresses to fit his needs.

```
Program DataGetter;    {Takes data from 16 channel A/D }

Uses  Dos, Crt, GDriver, GKernel, GWindow, GShell;

Type  ar1024 = Array[1..1024] of Real;  {size of FFT arrays}

Var   Data      :Array[1..4096] of LongInt;  {main data array filled by assembly program}
    OldData     :Array[1..4096] of LongInt;
    NumChannel :Word;          {assembly program number of channels to look at}
    NumPoints  :Word;          {assembly program total number of data points to take}
    DataSeg    :Word;    {assembly program segment to put data}
    DataOfs    :Word;    {assembly program offset to put data}
    NSweep     :Word;    {number of traces to average}
```

DataGetter (cont'd)

```
    NSweepOld :Word;
    A,B,C     :PlotArray;
    cr1,ci1   :ar1024;
    Trace     :Integer;          {Controls old trace drawings}
    npts      :Integer;
    i,j       :Integer;          {loop control variables}
    Channel   :Integer;          {Number of channel selected to draw}
    XPos,YPos :Integer;          {location of cursor}
    XLow,XHi  :Integer;
    YLow,YHi  :Integer;
    Step      :Integer;          {adjusts cursor movement step size}
    DeltaX    :Integer;
    DeltaY    :Integer;
    ScaleX    :Real;             {adjusts scale of drawing window}
    ScaleY    :Real;
    ZoomX     :Boolean;
    ZoomBack  :Boolean;
    BaseLine  :Boolean;
    ch        :Char;             {used as keyboard character}

{*************************************************************************}

{$L Getter}    {Location of external assembly program File Getter.OBJ}

Procedure GetData; External;  {external assembly program used for fast data taking}

{*************************************************************************}

Procedure Msg;

Begin
ClrScr;
Writeln('    This program was written to take data synchronized to an external clock    ');
Writeln('using the RC card.  By connecting the CLK input of the RC card to the 1024    ');
Writeln('output of the Oscillating Foil Motor Control box and connecting the TRG input ');
Writeln('of the RC card to the Zero output of the Oscillating Foil Motor Control box,  ');
Writeln('data can be taken in phase with the hydrofoil oscillations.  In addition,     ');
Writeln('a number of traces can be averaged together over many foil oscillations.      ');
Writeln('The program uses an external assembly language program called Getter to       ');
Writeln('collect the data from the RC card at a high rate of speed. The program is'    ');
Writeln('menu driven and should be self explanatory.  Note that the FFT part           ');
Writeln('is based on the CLK input ie. freq.= foil freq.* X pos..                      ');
Writeln('The following functions are not listed in the menu:                           ');
Writeln;
Writeln('     1.  ^PrtSc     Prints the present screen                                 ');
Writeln('     2.  Shift-F3   Zooms in on the Y scale but not the X                     ');
Writeln('     3.  Shift-F4   Zooms out on the Y scale but not the X                    ');
Writeln('     4.  ^F4        Returns to a 1 to 1 scale                                 ');
```

DataGetter (cont'd)

```
Writeln('      5.  Shift-F6     Takes a baseline trace and subtracts                    ');
Writeln('                      it from another trace                                   ');
Writeln;
Writeln('                              Have Fun!                                       ');
Writeln;
Writeln('                                  D.P.Hart                                    ');

ch:=ReadKey;

End;

{*************************************************************************}

Procedure Int3Handler; Interrupt;      {handles IRQ3 interrupt}

Begin
   Inline($B8/$00/$31/$8E/$D8/$BF/$00/$00/$C6/$05/$01/$B0/$20/$E6/$20);
End;

{*************************************************************************}

Function XtoY(x,y:Integer) :Integer;      {takes care of pascal's little problem}

Var  r: Real;

Begin

 r := y*ln(x);
 If r > 88.0296  then r :=88.0296;
 If r < -88.0296 then r := -88.0296;
 XtoY := Round(exp(r));

End;

{*************************************************************************}

Procedure FFT(index:Integer);

Var k,l,m,qn,m1,m2,mz,n,mp,mq : Integer;
   sn,rtre,rtim : Real;
   cr2 : ar1024;
   ci2 : ar1024;
   W   : ar1024;
   Z   : ar1024;
   IP  : Array[1..11] of Integer;

Begin

N    :=npts;
qN   := -1;
```

DataGetter (cont'd)

```
SN    := 0.5;

IF INDEX < 0 then
 Begin
  SN := 1;
  qN := 1;
 End;

IP[1] := 1;
For i := 2 to N+1 do IP[I] := IP[I-1]*2;

{*** NOW FIND THE M ROOT OF UNITY ***}

RTRE  := 0;

IF N <> 2 then
 For i := 3 To N Do RTRE := SQRT((1+RTRE)/2);

RTIM := qN*SQRT(1-RTRE*RTRE);
W[1] := 1;
Z[1] := 0;

For i := 2 to ip[n+1] do
Begin
 W[I] := W[I-1]*RTRE-Z[I-1]*RTIM;
 Z[I] := Z[I-1]*RTRE+W[I-1]*RTIM;
End;

{*** START BIG LOOP, K=1,N ***}

For K := 1 to N do
 Begin
  For L := 1 to IP[N-K+1] do
   Begin
    For J := 1 to IP[K] do
     Begin
       M      := L + (J-1)*IP[N-K+1];
       M1     := L + (J-1)*IP[N-K+2];
       M2     := M1 + IP[N-K+1];
       MZ     := (J-1)*IP[N-K+1] + 1;
       CR2[M]   := SN*(CR1[M1]+W[MZ]*CR1[M2]-Z[MZ]*CI1[M2]);
       MP     := IP[K]*IP[N-K+1];
       CI2[M]   := SN*(CI1[M1]+Z[MZ]*CR1[M2]+W[MZ]*CI1[M2]);
       CR2[M+MP] := SN*(CR1[M1]-W[MZ]*CR1[M2]+Z[MZ]*CI1[M2]);
       CI2[M+MP] := SN*(CI1[M1]-Z[MZ]*CR1[M2]-W[MZ]*CI1[M2]);
     End;
   End;
    For I := 1 to IP[N+1] do
     Begin
       CR1[I] := CR2[I];
```

DataGetter (cont'd)

```
        CI1[I] := CI2[I];
      End;
  End;
End;

{*************************************************************************}

Procedure  Correlate;

Var  M,j,k,Mat      : Integer;
     ChanOne,ChanTwo : Integer;
     Max            : Real;

Begin

GotoXY(37,23);Write('Enter number of first channel  (1..',NumChannel:2,') :  ');
Read(ChanOne);
GotoXY(37,23);Write('Enter number of second channel (1..',NumChannel:2,') : ');
Read(ChanTwo);
GotoXY(37,23);Write('This is going to take a bit of time !                ');

For i:=1 to MaxPlotGlb Do
 Begin
  M:=Trunc((i-1)*2.844444)*NumChannel;
  cr1[i]:=Data[M+ChanOne]/NSweep;
  ci1[i]:=Data[M+ChanTwo]/NSweep;
 End;

Max:=0;

For i:=1 To MaxPlotGlb do
  Begin
   A[i,1]:=i;
   A[i,2]:=0;
   For j:=1 to MaxPlotGlb do
    Begin
     k:=i+j-1;
     If k>360 then k:=k-360;
     A[i,2]:=A[i,2]+cr1[j]*ci1[k];
    End;
   If A[i,2]>Max Then Begin; Max:=A[i,2]; Mat:=i; End;
End;


GotoXY(37,23);Write('Maximum at X: ',Mat:4,'                ');

FindWorld(2,A,MaxPlotGlb,1,1.08);
SetBackGround(0);
DrawPolygon(A,1,-MaxPlotGlb,0,0,0);
SelectWorld(1);
```

DataGetter (cont'd)

```
End;

{*************************************************************************}

Procedure DrawFFT;          {Calculates and draws the FFT of Data}

Begin

npts:=1024;

GotoXY(37,23);Write('This is going to take a bit of time !              ');

npts:=Round(ln(npts)/ln(2));

 For i:=1 to 1024 Do
  Begin
   cr1[i]:=Data[(i-1)*NumChannel+Channel]/NSweep;
   ci1[i]:=0;
  End;

 FFT(-1);

 For i:=1 To MaxPlotGlb Do
  Begin
   A[i,1]:=i;
   A[i,2]:=sqrt(cr1[i]*cr1[i]+ci1[i]*ci1[i]);
  End;

 A[1,2]:=A[2,2];  {get rid of dc offset on FFT plot}

GotoXY(37,23);Write('                                          ');
SetBackGround(0);

FindWorld(2,A,MaxPlotGlb,1,1.08);
DrawPolygon(A,1,-MaxPlotGlb,0,0,0);
SelectWorld(1);

End;

{*************************************************************************}

Procedure SortIt;          {sorts selected channel out of data}

Var M    :Integer;

Begin
 For i:=1 to MaxPlotGlb Do          {loads drawing array with data from selected channel}
  Begin
   M:=Trunc((i-1)*2.84444);
```

DataGetter (cont'd)

```
    C[i,2]:=B[i,2];
    B[i,2]:=A[i,2];
    A[i,2]:=Data[M*NumChannel+Channel]/NSweep;
  End;

  Trace:=1;
  GotoXY(37,23);Write('Trace: ',Trace:2,'                    ');

End;

{************************************************************************}

Procedure SetUp;        {Initial screen SetUp}

Begin

  InitGraphic;

  DefineWindow(1,0,0,XMaxGlb,YMaxGlb-30);
  SelectWindow(1);
  SetBackGround(0);
  DrawBorder;

  DefineWindow(2,1,1,XMaxGlb-1,YMaxGlb-31);
  DefineWorld(1,0,4070,MaxPlotGlb+1,-1);
  SelectWorld(1);
  SelectWindow(2);
  SetClippingOn;
  SetBackGround(0);

  DrawTextW(XPos,YPos,1,'X');  {puts an X for cursor locaation}

  GotoXY(1,23);
  Write('  X: ',XPos:4,'  Y: ',YPos:4,'  Channel: ',Channel:2);
  GotoXY(1,24);
  Write('   F1 DRAW  F2 AUTO  F3 ZOOM IN  F4 ZOOM OUT  F5 CLEAR  F6 DATA  F7
CHANNEL');
  GotoXY(1,25);
  Write('      F8 TRACE   F9 RESTART   F10 EXIT   ^F FFT   ^R READ   ^S SAVE   ^X
CORRELATE');

End;

{************************************************************************}

Procedure ClearData;

Begin

   For i:=1 to 4096 do
```

DataGetter (cont'd)

```
    Data[i]:=0;

End;

{*************************************************************************}

Procedure MoveV;

Begin

 SetColorBlack;
 DrawTextW(Xpos,YPos,1,'X');
 YPos:=YPos+Step;
 SetColorWhite;
 DrawTextW(XPos,YPos,1,'X');
 GotoXY(2,23);Write('   X: ',XPos:4,'  Y: ',YPos:4);

End;


{*************************************************************************}

Procedure MoveH;

Begin

 SetColorBlack;
 DrawTextW(Xpos,YPos,1,'X');
 XPos:=XPos+Step;
 SetColorWhite;
 DrawTextW(XPos,YPos,1,'X');
 GotoXY(2,23);Write('   X: ',XPos:4,'  Y: ',YPos:4);

End;

{*************************************************************************}

Procedure  InPut;     {input initial parameters and initialize variables}

Var dummy,Mask :Integer;

Begin

 ClrScr;
 GotoXY(20,14);Write('ENTER NUMBER OF TRACES TO AVERAGE :');Read(NSweep);
 NSweepOld:=NSweep;
 NumChannel:=4;
 NumPoints:=4096;

 dummy:=Port[33];       {Enable IRQ3}
```

DataGetter (cont'd)

```
 Mask:=Trunc(dummy/8);
 If Mask <> (Trunc(Mask/2)*2) then Port[33]:=dummy-8;

 XPos   :=Round(MaxPlotGlb/2);
 YPos   :=2047;
 ScaleX :=1;
 ScaleY :=1;
 Trace  :=1;
 Channel :=1;
 XLow   :=0;XHi:=MaxPlotGlb;
 YLow   :=0;YHi:=4069;
 BaseLine:=True;
 ZoomX:=True;
 ZoomBack:=False;
 DataSeg:=Seg(Data[1]);
 DataOfs:=Ofs(Data[1]);
 For i:=1 to MaxPlotGlb Do
  Begin
   A[i,1]:=i;
   A[i,2]:=2047;
   B[i,1]:=i;
   B[i,2]:=2047;
   C[i,1]:=i;
   C[i,2]:=2047;
  End;

End;

{*************************************************************************}

Procedure ZoomIn;

Begin

 ScaleY:=ScaleY*0.50;                {Reduce window by 50%}
 DeltaY:=Round(4069*ScaleY/2);

If ZoomX Then
 Begin
  ScaleX:=ScaleX*0.50;
  DeltaX:=Round(MaxPlotGlb*ScaleX/2);
  XLow:=XPos-DeltaX;
  XHi:=XPos+DeltaX;
 End;

 ZoomX:=True;
 YLow:=YPos-DeltaY;
 YHi:=YPos+DeltaY;

 DefineWorld(2,XLow,YHi,XHi,YLow);
```

DataGetter (cont'd)

```
 SelectWorld(2);
 SetBackGround(0);

GotoXY(37,23);Write('XScale = ',ScaleX:4:2,' YScale = ',ScaleY:4:2);

 DrawPolygon(A,1,-MaxPlotGlb,0,0,0);

End;

{*************************************************************************}

Procedure ZoomOut;

Begin

ScaleY:=ScaleY/0.50;
DeltaY:=Round(4069*ScaleY/2);

If ZoomX Then
 Begin
  ScaleX:=ScaleX/0.50;
  DeltaX:=Round(MaxPlotGlb*ScaleX/2);
  XLow:=XPos-DeltaX;
  XHi:=XPos+DeltaX;
 End;

 YLow:=YPos-DeltaY;
 YHi:=YPos+DeltaY;

If ZoomBack Then          {Ctrl F4}
 Begin
 ScaleX:=1;
 ScaleY:=1;
 YLow:=0;
 YHi:=4069;
 XLow:=0;
 XHi:=MaxPlotGlb;
End;

ZoomX:=True;
ZoomBack:=False;

 DefineWorld(2,XLow,YHi,XHi,YLow);
 SelectWorld(2);
 SetBackGround(0);

 GotoXY(37,23);Write('XScale = ',ScaleX:4:2,' YScale = ',ScaleY:4:2);

 DrawPolygon(A,1,-MaxPlotGlb,0,0,0);
```

DataGetter (cont'd)

```
End;

{*************************************************************************}

Procedure SaveData;

Var   FilVar   :File;
      Result   :Word;
      FileName :String[30];     {holds filename to save data in}

Begin

  GotoXY(37,23);
  Write('Enter file name :              ');Readln;
  Read(FileName);
    FileName:=Concat('C:\Turbo\Photdat\',FileName,'.dat');

  GotoXY(37,23);
  Write('                              ');

  Assign(FilVar,FileName);
  ReWrite(FilVar);

  BlockWrite(FilVar,NSweep,1,Result);
  BlockWrite(FilVar,Data,130,Result);

  Close(FilVar);

  GotoXY(37,23);
  If Result < 130 Then
   Begin
     Sound(400);
     Write('WARNING - DISK IS FULL !!!');
     Delay(500);
     NoSound;
     Delay(3000);
     GotoXY(37,23);
     Write('                          ');
   End;

End;

{*************************************************************************}

Procedure ReadData;

Var   FilVar   :File;
      Result   :Word;
      FileName :String[30];     {holds filename to save data in}
```

DataGetter (cont'd)

```
Begin

  GotoXY(37,23);
  Write('Enter file name :              ');Readln;
  Read(FileName);
   FileName:=Concat('C:\Turbo\Photdat\',FileName,'.dat');

  GotoXY(37,23);
  Write('                              ');

  Assign(FilVar,FileName);
  Reset(FilVar);

  BlockRead(FilVar,NSweep,1,Result);
  BlockRead(FilVar,Data,130,Result);

  Close(FilVar);

End;

{*****************************************************************************}

Procedure  TipCav;        {Procedure to subtract one data trace from another}

Var i     :Integer;


Begin

If Baseline Then
 Begin

 GotoXY(37,23);Write('Set baseline conditions and hit a key');
 ch:=ReadKey;
 GotoXY(37,23);Write('                              ');

 ClearData;
 GetData;
 NSweep:=NSweepOld;

 For i:=1 to 4096 Do OldData[i]:=Data[i];

 DefineWindow(3,0,0,XMaxGlb,YMaxGlb);
 SelectWindow(3);
 SetBackGround(0);
 DrawBorder;
 DefineWindow(4,1,1,XMaxGlb-1,YMaxGlb-1);
 SelectWindow(4);
 SetBackGround(0);
 Ypos:=0;
```

DataGetter (cont'd)

```
End;

 BaseLine:=False;

 GotoXY(37,23);Write('Set conditions and hit a key');
 ch:=ReadKey;
 GotoXY(37,23);Write('                          ');

 ClearData;
 GetData;
 NSweep:=NSweepOld;

 For i:=1 to 4096 do Data[i]:=Data[i]-OldData[i];
 sortIt;
 DrawPolygon(A,1,-MaxPlotGlb,0,0,0);

End;

{***************************** MAIN PROGRAM *********************************}

Begin

 Msg;        {display information about the program}
 Input;      {Initialize the system}
 SetUp;
 SetIntVec(11,@Int3Handler); {Set IRQ3 interrupt vector to Int3Handler procedure}

Repeat       {get a character from the keyboard and execute it}

 ch:=ReadKey;

 CASE ord(ch) of

  6:DrawFFT;        {^F}
 18:ReadData;       {^R}
 19:SaveData;       {^S}
 24:Correlate;      {^X}
 59:Begin           {F1}
    SortIt;
    DrawPolygon(A,1,-MaxPlotGlb,0,0,0);
    End;
 60:Begin           {F2}
     Repeat
      ClearData;
      GetData;
      NSweep:=NSweepOld;
      SortIt;
      SetBackGround(0);
      DrawPolygon(A,1,-MaxPlotGlb,0,0,0);     {linked drawing routine}
     Until KeyPressed;
```

DataGetter (cont'd)

```
    End;
  61:ZoomIn;          {F3}
  86:Begin            {Shift F3}
      ZoomX:=False;
      ZoomIn;
    End;
  89:TipCav;          {Shift F6}
  62:ZoomOut;         {F4}
  87:Begin            {Shift F4}
      ZoomX:=False;
      ZoomOut;
    End;
  97:Begin;           {Ctrl F4}
      ZoomBack:=True;
      ZoomOut;
    End;
  63:SetBackGround(0); {F5}
  64:Begin
     ClearData;
     GetData;         {F6}
     NSweep:=NSweepOld;
    End;
  65:Begin            {F7}
      If Channel < NumChannel then Channel:=Channel+1 else Channel:=1;
      GotoXY(37,23);Write('                                    ');
      GotoXY(32,23);Write(Channel:2);
    End;
  66:Begin            {F8}
      If Trace<3 Then Trace:=Trace+1 else Trace:=1;;
      GotoXY(37,23);Write('Trace: ',Trace:2,'                  ');
      Case Trace of
       1:DrawPolygon(A,1,-MaxPlotGlb,0,0,0);
       2:DrawPolygon(B,1,-MaxPlotGlb,0,0,0);
       3:DrawPolygon(C,1,-MaxPlotGlb,0,0,0);
      End; {Case}
    End;
  67:Begin LeaveGraphic; Input; Setup; End;      {F9 ReStart}
  72:Begin Step:=Round(20*ScaleY); MoveV; End;   {up}
  80:Begin Step:=Round(-20*ScaleY); MoveV; End;  {Down}
  75:Begin Step:=-1; MoveH; End;                 {Left}
 115:Begin Step:=-4; MoveH; End;                 {Ctrl Left}
  77:Begin Step:=1; MoveH; End;                  {Right}
 116:Begin Step:=4; MoveH; End;                  {Ctrl Right}
 114:HardCopy(false,6);                          {^PrtSc}
 End; {Case}

Until Ch = #68;       {Exit if F10 is pressed}
LeaveGraphic;

End.
```

E.2 LDV Data Reduction

The following program was written in Turbo Pascal for an 8086 base machine. This program takes ASCII stored LDV data from the Dantec PDA, described in Chapter 2, throws out suspect and unused data, sorts the data according to encoder counts and averages it into 360 bins (one bin/degree). The program outputs a file with the suffix **.ave*.

```
Program Reduce;

Uses  Dos, Crt;

Var
   Uv,Enc       :Array[1..5000] of Single;
   Index        :Array[1..5000] of Byte;
   Um,U2,Rms          :Array[0..360] of Real;
   N            :Array[0..360] of Integer;
   Pt,St        :Integer;
   TT           :Single;
   Old          :Single;
   i,j,k        :Integer;          {loop control variables}
   NumData      :Integer;    {Constant}
   NFileName          :String[30];

{************************ Mean      *********************************}

Procedure Mean;

 Begin

   For i:=0 to 360 do
    Begin
     Um[i]:=0;U2[i]:=0;N[i]:=0;
    End;

   For i:=1 to NumData do
    Begin
     If Index[i]=1 then
       Begin
        k:=Round(Enc[i]);
        Um[k]:=Um[k]+Uv[i];
        U2[k]:=U2[k]+Uv[i]*Uv[i];
        N[k]:=N[k]+1;
       End;
    End;
```

Reduce (cont'd)

```
nd;

{************************ Standard Deviation ***************************}

Procedure StD;
Begin

   For i:=0 to 360 Do
    Begin
     If N[i]>1 Then
       Begin
        Um[i]:=Um[i]/N[i];
        Rms[i]:=Sqrt(Abs((U2[i]-N[i]*Um[i]*Um[i])/(N[i]-1)));
       End;
    End;

 End;

{************************  Calculate  *********************************}

Procedure Calculate;

 Begin

  GotoXY(23,12);Write('   Sorting: ',NFileName);

  For i:=1 to NumData do
   Begin
    Index[i]:=1;
    For j:=i+1 to NumData do
     Begin
      If Enc[i]>Enc[j] then
        Begin
         Old:=Enc[i];  Enc[i]:=Enc[j]; Enc[j]:=Old;
         Old:=Uv[i];  Uv[i]:=Uv[j]; Uv[j]:=Old;
        End;
     End;
   End;

 End;

{************************ Re-Sort ******************************}
Procedure ReSort;

Begin
  For i:=1 to NumData do
   Begin
    k:=Round(Enc[i]);
    If N[k]>2 Then
      Begin
```

Reduce (cont'd)

```
        If (Abs(Uv[i]-Um[k]))>(Rms[k]) Then Index[i]:=0;
       End
      Else Index[i]:=0;
    End;
End;

{************************  Save Data  ***************************}

Procedure SaveData;

Var   FilVar   :Text;
     Result   :Word;
     FileName  :String[30];     {holds filename to save data in}

Begin

  FileName:=Concat(NFileName,'.Ave');
  Assign(FilVar,FileName);
  ReWrite(FilVar);

  For i:=0 to 360 do
    If N[i]>1 Then Writeln(FilVar,i,chr(9),Um[i]:5:3,chr(9),Rms[i]:5:3);

  Close(FilVar);

  GoToXY(23,13);Write('Averaged data saved into ',FileName:12);

  FileName:=Concat(NFileName,'.red');
  Assign(FilVar,FileName);
  ReWrite(FilVar);

  For i:=1 to NumData do
   Begin
    If Index[i]=1 Then Writeln(Filvar,enc[i]:5:3,chr(9),uv[i]:5:3);
   End;

  Close(FilVar);

  GoToXY(23,12);Write('Reduced data saved into  ',FileName:12);

End;

{************************  Read Data  ***************************}

Procedure ReadData;

Var   FilVar   :Text;
     Result   :Word;
     x,y,z    :Single;
     FileName  :String[30];     {holds filename to save data in}
```

Reduce (cont'd)

```
Begin

  GotoXy(23,12);Write('Reading ',NFileName:10);

  FileName:=ConCat(NFileName,'.dat');

  Assign(FilVar,FileName);
  Reset(FilVar);

  For i:=1 to 20 do Readln(FilVar);

  i:=0;

  While Not Eof(FilVar) and (i<5000) do
   Begin
    Readln(Filvar,Pt,St,x,TT,y,z);
      If z<>0 then
       Begin
        i:=i+1;
        Uv[i]:=y;
        ENC[i]:=z;
       End;
   End;

  NumData:=i;

  Close(FilVar);

End;

{************************      Sort      ******************************}

Procedure Sort;

Begin

 ClrScr;
 ReadData;
 Calculate;
 Mean;
 StD;
 ReSort;
 Mean;
 StD;
 SaveData;

End;
```

Reduce (cont'd)

```
{************************  Main Program  ******************************}
Begin

 NFileName:='c:\sizeware\a05205u';
  Sort;

End.
```

E.3 LDV Data Interpolation

The following programs were written in C for a UNIX based machine. They were written to accurately determine the change in circulation around an oscillating hydrofoil based on a limited number of LDV measurements taken at the trailing edge of the foil. These programs are included here for reference. The reader will find them useful only after an extensive study of the interpolation technique described in Chapter 6. *(The programs listed in this section were written with the help of graduate student Elizabeth A. McKenney.)*

E.3.1 Shape2.c

This program was written to interpolate the velocities at the trailing edge of the hydrofoil by transforming the LDV data to the coordinate frame of the hydrofoil and fitting it to a first and second harmonic function. This program reads in the ensemble averaged LDV data, corrects for slight errors in positioning of the LDV, fits the data, and then outputs the coefficients in a file **.tor*.

```
#include <stdio.h>
#include <ctype.h>
#include <math.h>

#define DEBUG 1
#define DEBUG2 1
#define DEBUG3 0
#define MAXLEN 30
```

Shape2.c (cont'd)

```
#define PI 3.141592
#define FOILEN 6.0                      /* chord length of foil, inches */
#define FOILSPAN 6.0                    /* span of foil, inches */
#define FRONT 0.38                      /* fraction of foil upstream of rotation axis
*/
#define L_EDGE FRONT*FOILSPAN           /* position of leading edge */
#define T_EDGE (FRONT-1.0)*FOILSPAN     /* position of trailing edge */
#define MEAN_ALPHA 5.3                  /* mean angle of attack, degrees */
#define ENCMAX 360                      /* encoder counts/cycle (effective) */
#define D_ENC (360/ENCMAX)
#define PHI 5.0                         /* amplitude of oscillation, degrees */
#define NHTS 1                          /* number of heights to consider */
#define NPOS 7                          /* number of data locations to consider */
#define UNUSED (-1000.0)                /* initial vel. value, before reading data */
#define CORR 1.20                       /* correction for beam bending through
glass */
#define PT_SPC (0.125*CORR)             /* spacing between data locations */
#define PT_SIZE 0.02                    /* radius of circles denoting data locations
*/
#define MAG 50.0                        /* magnitude magnification */

#define AMPL 0.2942
#define ETA_OFST AMPL
#define ETA_BINS 100
#define DEL_ETA ((6.1*PT_SPC + 2*AMPL)/ETA_BINS)
#define MIN_ETA (-5*PT_SPC)
#define Uinf 5.0
#define EPSILON 0.00001                 /* compare to error to stop opt. */
#define MAX_ITERS 100
  /* indices into coeff arrays */
#define A 0
#define B 1
#define C 2
#define D 3
#define E 4

  /* starting ranges for bisection search */
#define A_START 0.0
#define B_START 0.0
#define C_START 0.0
#define D_START 0.0
#define E_START 1.0

#define P_MIN (-2.0)
#define P_MAX 2.0

char poschar[] = "ABCDEFG";             /* chars identifying data locations */

float u[ETA_BINS][ENCMAX];              /* velocity component being considered */
```

Shape2.c (cont'd)

```
int good_data[ETA_BINS];                /* number of good points in bin */
float coeff[7][ETA_BINS];               /* current values of parameters A,B,C */
float del_eta = DEL_ETA;                /* use variable so only calc once */

char comp;                              /* velocity component of interest */
int freq;                               /* oscillation frequency of interest */
char htchar;                            /* letter denoting height of interest */

/*************************************************************************/
/*  readdata -- read velocity data into arrays, transforming coordinates  */
/*************************************************************************/
int readdata()
{
  float eta, vel,Vmin,Xpos;
  float V[ENCMAX];
  int pos, etai, enct, rc, gd_sum,phimin;
  char fname[MAXLEN];
  FILE *u_datafile, *v_datafile;

   /* initialise vel. arrays */

  for (enct=0; enct<ENCMAX; enct++)
    {
        V[enct]=UNUSED;
   for (etai=0; etai<ETA_BINS; etai++)
        {
        u[etai][enct]=UNUSED;
        good_data[etai]=0;
        }
    }

  for (pos=1; pos>-NPOS+1; pos--)  /* position 'a' = 1 ... pos. 'g' = -5 */
  {
          /* open data file for u velocities */
    sprintf(fname,"%c5%c%02d%c.AVE",poschar[-pos+1],htchar,freq,comp);
#if (DEBUG)
printf("Opening file %s...\n",fname);
#endif
    u_datafile = fopen(fname,"r");

        Vmin = 1000.0;

    if (u_datafile==NULL)
    {
        printf("\007Error in fopen(\"%s\").\n",fname);
        sleep(1);
    }

    else                    /* read u velocity data into array */
```

Shape2.c (cont'd)

```
    {
        do
        {
          rc = fscanf(u_datafile,"%d%f%*f\n",&enct,&vel);
          V[enct] = vel/Uinf;
          if ((fabs(V[enct])<Vmin)&&(fabs(V[enct])>0.005))
            {
                Vmin=fabs(V[enct]);
                phimin=enct;
            }

        } while (rc!= EOF);

        fclose(u_datafile);

        Xpos = -AMPL*(cos(phimin*D_ENC*PI/180.0)+1);
        if (fabs(Xpos-pos*PT_SPC)>0.08) Xpos=pos*PT_SPC;

#if (DEBUG)
  printf("Xpos = %0.3f\n",Xpos);
#endif

        for (enct=0; enct<ENCMAX; enct++)
         {
           eta = Xpos + AMPL*cos(enct*D_ENC*PI/180.0) + ETA_OFST;
           etai = (eta-MIN_ETA)/del_eta;
           if (fabs(V[enct])>2.0) V[enct]=UNUSED;

           if ((etai<0) || (etai>=ETA_BINS))
                printf("\007etai out of range! [%d]",etai);

           u[etai][enct] = V[enct];

           if(V[enct]!=UNUSED) good_data[etai]++;

               V[enct]=UNUSED;

               if (DEBUG3 || (etai<0) || (etai>=ETA_BINS))
                 printf("u(%0.3f,%0.3f) [%d] = %0.3f\n",
                                        eta,enct*1.0,etai,u[etai][enct]);
         } /* for (enct) */

    } /* else */

 } /* for (pos) */

#if (DEBUG2)
    gd_sum = 0;
    for (etai=0; etai<ETA_BINS; etai++) gd_sum += good_data[etai];
    printf("total points = %d\n",gd_sum-good_data[0]);
```

Shape2.c (cont'd)

```
#endif

    /* create eta-phi file for PV-WAVE */
  sprintf(fname,"%c5%c%02d%c.ETA",'X',htchar,freq,comp);
#if (DEBUG)
printf("Opening file %s...\n",fname);
#endif

  v_datafile = fopen(fname,"w");

   for(enct=0; enct<ENCMAX; enct++)
    for (etai=0; etai<ETA_BINS; etai++)
        if (u[etai][enct]!=UNUSED)
          fprintf(v_datafile,"%0.3f\n",u[etai][enct]);
        else
          fprintf(v_datafile,"%0.3f\n",0.0);

  fclose(v_datafile);

#if (DEBUG)
printf("Closing file %s...\n",fname);
#endif

}  /* readdata() */

/*************************************************************************/
/*        std_dev  -- calculate error in fit                             */
/*************************************************************************/
float std_dev(etai)
int etai;
{
  int enct;
  float phi, guess, sum=0.0;

  for (enct=0; enct<ENCMAX; enct++)  /* note we are calculating B in radians */
    if (u[etai][enct]!=UNUSED)
    {
        phi = (enct*D_ENC*PI/180.0);
        guess = coeff[A][etai]*sin(phi)+coeff[B][etai]*cos(phi)+
                coeff[C][etai]*sin(2.0*phi)+coeff[D][etai]*cos(2.0*phi)+
                coeff[E][etai];
        sum += (u[etai][enct] - guess)*(u[etai][enct] - guess);
    }

  return(sqrt(sum/(good_data[etai]-1)));

}  /* std_dev() */
```

Shape2.c (cont'd)

```
/*************************************************************************/
/*                          Vary                                         */
/*     * "Golden Section" search routine*                                */
/*************************************************************************/

float vary(param,etaval)
char param;
int etaval;
{
  float k = 1.618034;        /* Golden Ratio of interval sizes    */
  float xL, xR, xA, xB, err1, err2;   /* interval limits          */
  float old;

  param -='A';

  old = coeff[param][etaval];
  xL = P_MIN;
  xR = P_MAX;

  while (fabs(xL-xR) > EPSILON)
  {
    xB = xL + (xR - xL)/k;
         coeff[param][etaval]=xB;
         err1=std_dev(etaval);

    xA = xR + (xL - xR)/k;
         coeff[param][etaval]=xA;
         err2=std_dev(etaval);

    if (err2 > err1)     /* keep xR the same, old xA is new left limit */
         xL = xA;
    else                 /* keep xL the same, old xB is new right limit */
         xR = xB;

  }  /* while */

  return(fabs((old-coeff[param][etaval])/coeff[param][etaval]));

}  /* vary() */

/*************************************************************************/
/*         optimise                                                      */
/*************************************************************************/
void optimise()
{
  int etai, enct, iter;
  float total_err;

  for (etai=0; etai<ETA_BINS; etai++)
    if (good_data[etai]>2)
```

Shape2.c (cont'd)

```
{
        iter=0;

          coeff[A][etai] = A_START;
        coeff[B][etai] = B_START;
        coeff[C][etai] = C_START;
        coeff[D][etai] = D_START;
        coeff[E][etai] = E_START;

        do
        {
          total_err = vary('E',etai);
          total_err += vary('A',etai);
          total_err += vary('B',etai);
          total_err += vary('C',etai);
          total_err += vary('D',etai);
        } while ((total_err>7*EPSILON)&&(++iter<MAX_ITERS));

    if (iter>=MAX_ITERS) printf("timed out on etai= %d\n",etai);


        } /*for (eta) if (good_data) */

} /* optimise() */

/*************************************************************************/
/*  savedata -- save coefficient data into file                          */
/*************************************************************************/
int savedata()
{
  int etai, enct;
  float u_val;
  float coefs[7];
  char fname[MAXLEN];
  FILE *c_datafile, *v_datafile;

          coefs[A]= coeff[A][etai];
          coefs[B]= coeff[B][etai];
          coefs[C]= coeff[C][etai];
          coefs[D]= coeff[D][etai];
          coefs[E]= coeff[E][etai];

  sprintf(fname,"%c5%c%02d%c2.COE",'X',htchar,freq,comp);
#if (DEBUG)
printf("Opening file %s...\n",fname);
#endif

  c_datafile = fopen(fname,"w");

  if (c_datafile==NULL)
```

Shape2.c (cont'd)

```
            printf("\007Error in fopen(\"%s\").\n",fname);
  else
     for (etai=0; etai<ETA_BINS; etai++)
           if (good_data[etai]>6)
            {
            coefs[A]= coeff[A][etai];
            coefs[B]= coeff[B][etai];
            coefs[C]= coeff[C][etai];
            coefs[D]= coeff[D][etai];
            coefs[E]= coeff[E][etai];

             fprintf(c_datafile,"%0.3f\t%0.6f\t%0.6f\t%0.6f\t%0.6f\t%0.6f\t%0.6f\n",
                                                    etai*DEL_ETA+MIN_ETA,
                                                    coeff[A][etai],
                                                    coeff[B][etai],
                                                    coeff[C][etai],
                                                    coeff[D][etai],
                                                    coeff[E][etai],
                                                    std_dev(etai));
            }
           else
            fprintf(c_datafile,"%0.3f\t%0.6f\t%0.6f\t%0.6f\t%0.6f\t%0.6f\t%0.6f\n",
                                                    etai*DEL_ETA+MIN_ETA,
                                                    coefs[A],
                                                    coefs[B],
                                                    coefs[C],
                                                    coefs[D],
                                                    coefs[E],0.0);

  fclose(c_datafile);

    /* create eta-phi file for PV-WAVE */
  sprintf(fname,"%c5%c%02d%c2.SURF",'X',htchar,freq,comp);
#if (DEBUG)
printf("Opening file %s...\n",fname);
#endif

  v_datafile = fopen(fname,"w");

  for (enct=0; enct<ENCMAX; enct++)
    for (etai=0; etai<ETA_BINS; etai++)
    {
          if (good_data[etai]>6)
            u_val = coeff[A][etai]*sin(enct*PI/180.0)+coeff[B][etai]*cos(enct*PI/180.0)+
                    coeff[C][etai]*sin(enct*PI/90.0)+coeff[D][etai]*cos(enct*PI/90.0)+
                    coeff[E][etai];



          fprintf(v_datafile,"%0.6f\n",u_val);
```

Shape2.c (cont'd)

```
}

#if (DEBUG)
printf("Closing file %s...\n",fname);
#endif
  fclose(v_datafile);

}  /* savedata() */

/*************************************************************************/
/*        main program                                                   */
/*************************************************************************/
main(argc,argv)
int argc;
char *argv[];
{
  char h,f,d;
  char choice[MAXLEN];
/*
  comp = 'U';

  if (argc<2)
  {
    printf("Enter oscillation frequency (5, 10, 20):\t");
    scanf("%d",&freq);
  }
  else freq = atoi(argv[1]);

  if (freq==0) exit(-1);

  if (argc<3)
  {
    printf("Enter desired height (a, b, c, d):\t");
    scanf("%s",choice);
    htchar = choice[0];
  }
  else htchar = argv[2][0];

  if (islower(htchar))
    htchar += ('A' - 'a');
*/
/* htchar should be upper case */

  for (htchar='C'; htchar<='C'; htchar++)
    for (freq=5; freq<=20; freq*=2)
          for (comp='U'; comp<='V'; comp++)
          {

            readdata();
            optimise();
```

Shape2.c (cont'd)

```
            savedata();
          }

} /* maine() */
```

E.3.2 DvFit.c

This program was written to linearly extrapolate the velocity jump across the trailing edge of the hydrofoil through the boundary layer. It uses the **.coe* files generated by Shape2.c as input and outputs a file **.tor* that contains the left and right trailing edge velocities and the standard deviation of the curve fit.

```
#include <stdio.h>
#include <ctype.h>
#include <math.h>

#define DEBUG 1
#define DEBUG2 0
#define MAXLEN 30

#define PI 3.141592
#define FOILEN 6.0                      /* chord length of foil, inches */
#define FOILSPAN 6.0                    /* span of foil, inches */
#define FRONT 0.38                      /* fraction of foil upstream of rotation axis */
#define L_EDGE FRONT*FOILSPAN           /* position of leading edge */
#define T_EDGE (FRONT-1.0)*FOILSPAN     /* position of trailing edge */
#define MEAN_ALPHA 5.3                  /* mean angle of attack, degrees */
#define ENCMAX 360                      /* encoder counts/cycle (effective) */
#define D_ENC (360/ENCMAX)
#define PHI 5.0                         /* amplitude of oscillation, degrees */
#define NHTS 1                          /* number of heights to consider */
#define NPOS 7                          /* number of data locations to consider */
#define UNUSED (-1000.0)                /* initial vel. value, before reading data */
#define CORR 1.20                       /* correction for beam bending through glass */
#define PT_SPC (0.125*CORR)             /* spacing between data locations */
#define PT_SIZE 0.02                    /* radius of circles denoting data locations */
#define MAG 50.0                        /* magnitude magnification */

#define AMPL 0.2942
#define ETA_OFST AMPL
#define ETA_BINS 100
#define DEL_ETA ((6.1*PT_SPC + 2*AMPL)/ETA_BINS)
#define MIN_ETA (-5*PT_SPC)
```

DvFit2.c (cont'd)

```
#define Uinf 5.0
#define EPSILON 0.0001                    /* compare to error to stop opt. */
#define MAX_ITERS 120
#define MAX 0
#define MIN 1

/* indices into coeff arrays */

#define A 0
#define B 1
#define C 2
#define D 3
#define E 4

#define A0 0
#define A1 1
#define A2 2


  /* starting ranges for bisection search */
#define A0_MIN (-2.0)
#define A0_MAX (2.0)
#define A1_MIN (-10.5)
#define A1_MAX (10.5)
#define A2_MIN (-2.0)
#define A2_MAX (2.0)

#define A0_START 0.0
#define A1_START 0.0
#define A2_START 1.0

char poschar[] = "ABCDEFG";          /* chars identifying data locations */

int  LBOUND[3];
int  RBOUND[3];
float u[ETA_BINS][ENCMAX];           /* velocity component      */
float eta[ETA_BINS];                 /* corresponding values of eta for etai=0 to 99 */
float coeff[7][ETA_BINS];            /* current values of parameters A,B,C */
float p_range[7][2];                 /* range of parameters GAMMA,L,M */
float vcoeff[7][ENCMAX];             /* current values of parameters GAMMA,L,M */
float Ur[ENCMAX];
float Ul[ENCMAX];
float stdev[ENCMAX];

char comp;                           /* velocity component of interest */
int freq;                            /* oscillation frequency of interest */
int index;
char htchar;                         /* letter denoting height of interest */
```

DvFit2.c (cont'd)

```
/*************************************************************************/
/*  readdata -- read velocity data into arrays, transforming coordinates */
/*************************************************************************/
int readdata()
{
  int etai, enct, rc;
  char fname[MAXLEN];
  FILE *u_datafile;

            /* open data file for coefficients */
  sprintf(fname,"X5%c%02d%c2.COE",htchar,freq,comp);
#if (DEBUG)
printf("Opening file %s...\n",fname);
#endif
  u_datafile = fopen(fname,"r");

  if (u_datafile==NULL)
    printf("\007Error in fopen(\"%s\").\n",fname);

  else                    /* read coefficients into array */
    for (etai=0; etai<ETA_BINS; etai++)
          rc = fscanf(u_datafile,"%f%f%f%f%f%f%f%*f\n",&eta[etai],&coeff[A][etai],
                                                       &coeff[B][etai],
                                                       &coeff[C][etai],
                                                       &coeff[D][etai],
                                                       &coeff[E][etai]);
#if (DEBUG)
printf("Closing file %s...\n",fname);
#endif
  fclose(u_datafile);

     /* generate array of velocity values from coeffs in .COE file */
  for (enct=0; enct<ENCMAX; enct++)
    for (etai=0; etai<ETA_BINS; etai++)
          u[etai][enct] = coeff[A][etai]*sin(enct*PI/180.0) +
                          coeff[B][etai]*cos(enct*PI/180.0)+
                          coeff[C][etai]*sin(enct*PI/90.0) +
                          coeff[D][etai]*cos(enct*PI/90.0)+coeff[E][etai];

}  /* readdata() */

/*************************************************************************/
/*        fit_fn  -- test function to fit data                           */
/*************************************************************************/
float fit_fn(enct,etai)
int enct,etai;
{
float calc_fit;
```

DvFit2.c (cont'd)

```
    /* linear fit, i.e. y = mx + b */
  calc_fit = vcoeff[A0][enct]*eta[etai]+ vcoeff[A1][enct];

  return(calc_fit);

}  /* fit_fn() */

/*************************************************************************/
/*        std_dev  -- calculate error in fit                             */
/*************************************************************************/
float std_dev(enct)
int enct;
{
  int etai;
  float guess, sum=0.0;

  for (etai=LBOUND[index]; etai<RBOUND[index]; etai++)
  {
    guess = fit_fn(enct,etai);
    sum += (u[etai][enct] - guess)*(u[etai][enct] - guess);
  }

  stdev[enct]= sqrt(sum/(-LBOUND[index]+RBOUND[index]));
  return(stdev[enct]);

}  /* std_dev() */

/*************************************************************************/
/*                        Vary                                           */
/*     * "Golden Section" search routine *                               */
/*************************************************************************/
float vary(param,phival)
char param;
int phival;
{
  float k = 1.618034;        /* Golden Ratio of interval sizes    */
  float xL, xR, xA, xB, err1, err2;   /* interval limits          */
  float old;

  old = vcoeff[param][phival];
  xL = p_range[param][MIN];
  xR = p_range[param][MAX];

  while (fabs(xL-xR) > EPSILON)
  {
    xB = xL + (xR - xL)/k;
        vcoeff[param][phival]=xB;
        err1=std_dev(phival);

xA = xR + (xL - xR)/k;
```

DvFit2.c (cont'd)

```
        vcoeff[param][phival]=xA;
        err2=std_dev(phival);

    if (err2 > err1)     /* keep xR the same, old xA is new left limit */
        xL = xA;
    else                 /* keep xL the same, old xB is new right limit */
        xR = xB;

  }  /* while */

  return(fabs((old-vcoeff[param][phival])/vcoeff[param][phival]));

}   /* vary() */

/*************************************************************************/
/*        optimise --                                                    */
/*************************************************************************/
void optimise()
{
  int etai, enct, iter;
  float total_err;

  p_range[A0][MIN] = A0_MIN;
  p_range[A0][MAX] = A0_MAX;
  p_range[A1][MIN] = A1_MIN;
  p_range[A1][MAX] = A1_MAX;
  p_range[A2][MIN] = A2_MIN;
  p_range[A2][MAX] = A2_MAX;

  LBOUND[1]=20;
  LBOUND[2]=65;
  RBOUND[1]=40;
  RBOUND[2]=80;

  for (enct=0; enct<ENCMAX; enct++)
  {
    iter=0;

    vcoeff[A0][enct] = A0_START;
    vcoeff[A1][enct] = A1_START;
    vcoeff[A2][enct] = A2_START;
    do
    {
        total_err  = vary(A0,enct);
        total_err += vary(A1,enct);
        iter++;

    } while ((iter<MAX_ITERS) && (total_err>3*EPSILON));

   if (index==1) Ul[enct]=vcoeff[A1][enct];
```

DvFit2.c (cont'd)

```
 if (index==2) Ur[enct]=vcoeff[A1][enct];

#if (DEBUG)
  printf("index=%d enct %d iter=%d Ul=%g Ur=%g stdev=%g\n",
          index,enct,iter,Ul[enct],Ur[enct],stdev[enct]);
#endif

   }

}  /* optimise() */

/*************************************************************************/
/*   savedata -- save coefficient data into file                         */
/*************************************************************************/
int savedata()
{
  int etai, enct;
  float u_val;
  char fname[MAXLEN];
  FILE *c_datafile, *v_datafile;

  sprintf(fname,"%c5%c%02d%c2.TOR",'X',htchar,freq,comp);
#if (DEBUG)
printf("Opening file %s...\n",fname);
#endif

  c_datafile = fopen(fname,"w");
   fprintf(c_datafile,"enct\tUl\tUr\tstdev\n");

  if (c_datafile==NULL)
         printf("\007Error in fopen(\"%s\").\n",fname);
  else
    for (enct=0; enct<ENCMAX; enct++)
          fprintf(c_datafile,"%d\t%0.6f\t%0.6f\t%g\n",enct,
                                                    Ul[enct],
                                                    Ur[enct],
                                                    stdev[enct]);
#if (DEBUG)
printf("Closing file %s...\n",fname);
#endif
  fclose(c_datafile);

}  /* savedata() */

/*************************************************************************/
/*        main program                                                   */
/*************************************************************************/
main(argc,argv)
int argc;
char *argv[];
```

DvFit2.c (cont'd)

```
{
 char h,f,d;
  char choice[MAXLEN];

  for (htchar='B'; htchar<='B'; htchar++)
    for (freq=20; freq<=20; freq*=2)
          for (comp='U'; comp<='V'; comp++)
          {
            readdata();

           index=1;
            optimise();
           index=2;
            optimise();

            savedata();

          }

} /* maine() */
```

APPENDIX F

OSCILLATING HYDROFOIL SCHEMATICS

This appendix contains schematics of the oscillating hydrofoil mechanism. They are included here as a record to aid the reader in modifying, understanding, and using this equipment.

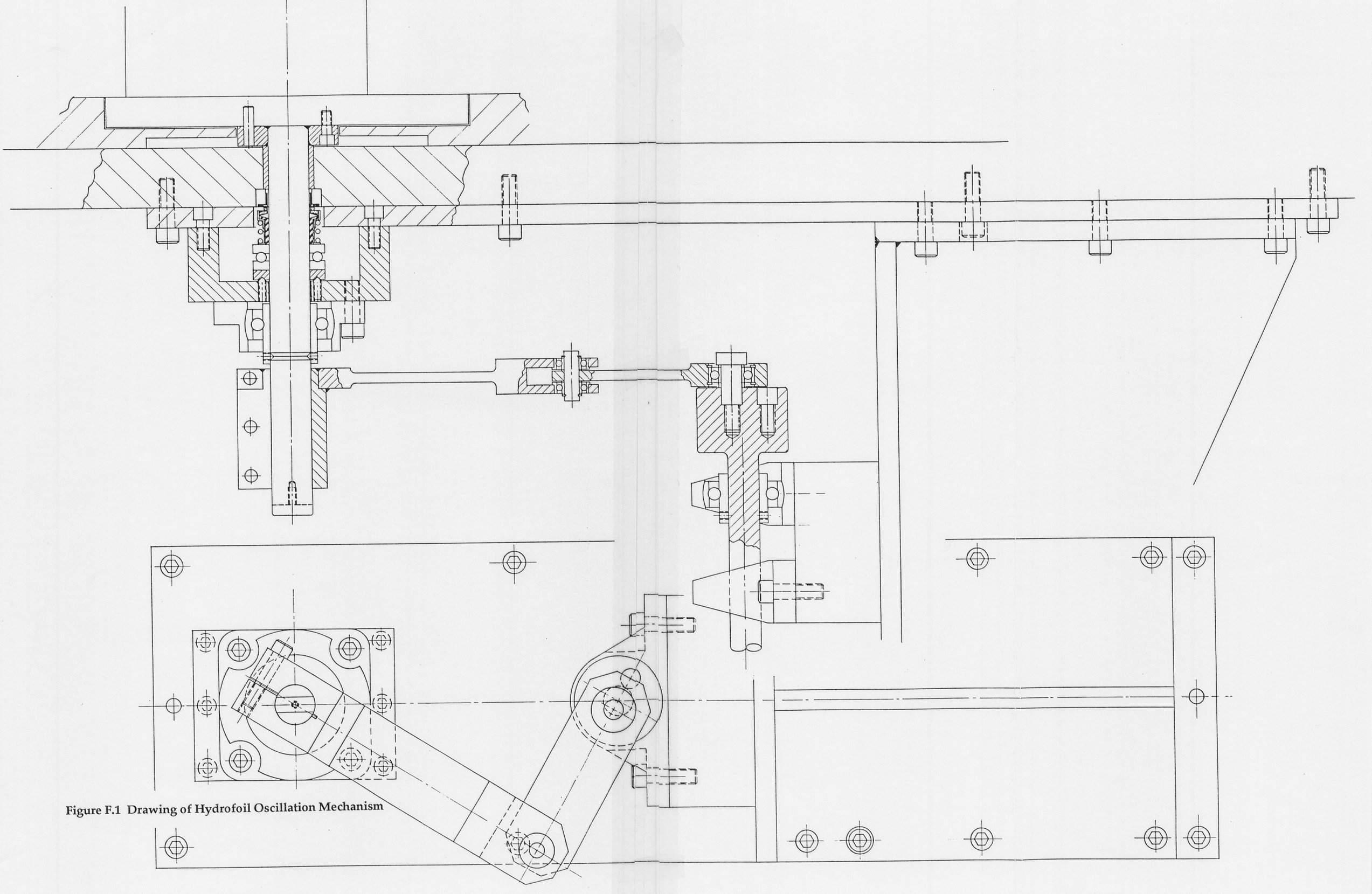

Figure F.1 Drawing of Hydrofoil Oscillation Mechanism

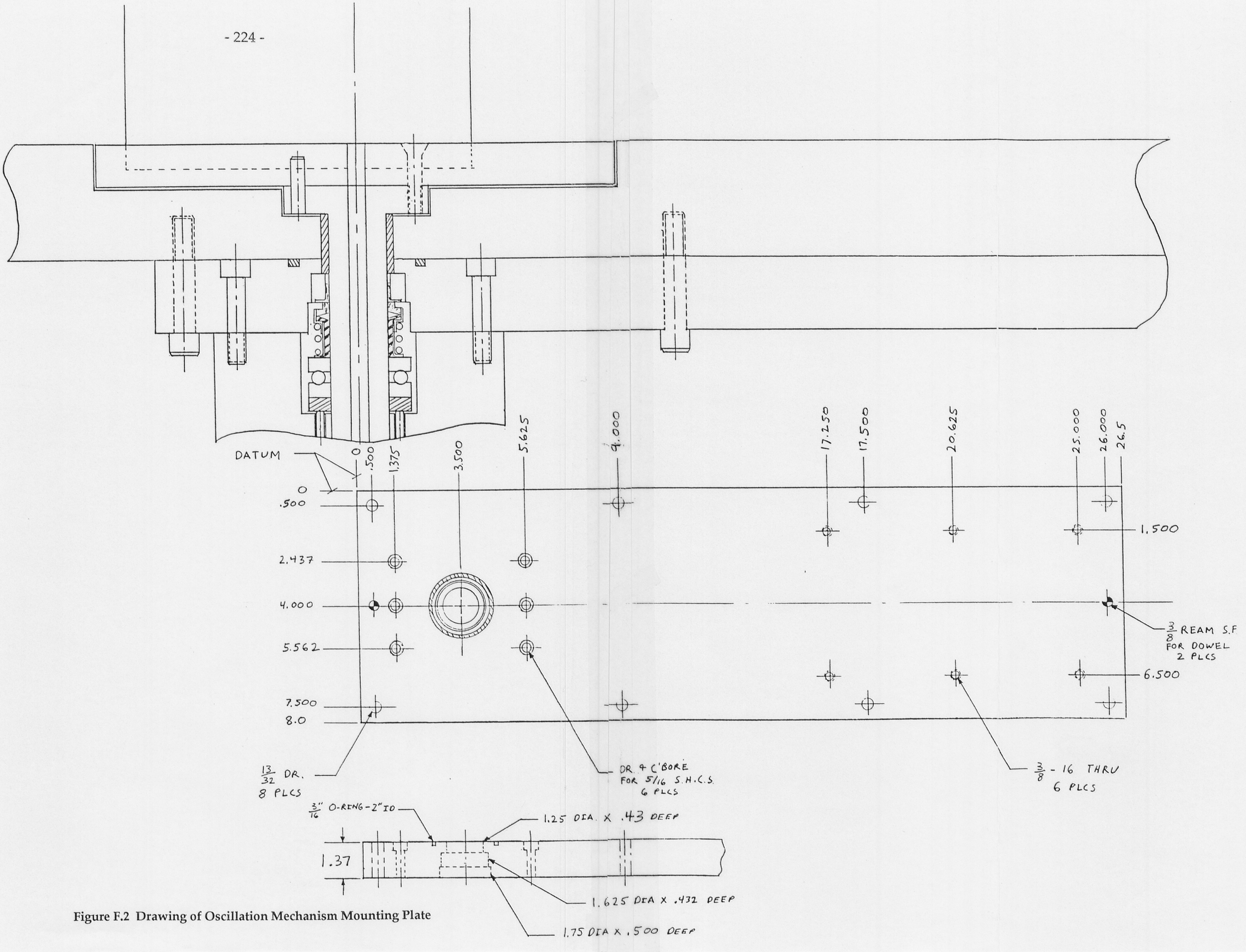

Figure F.2 Drawing of Oscillation Mechanism Mounting Plate

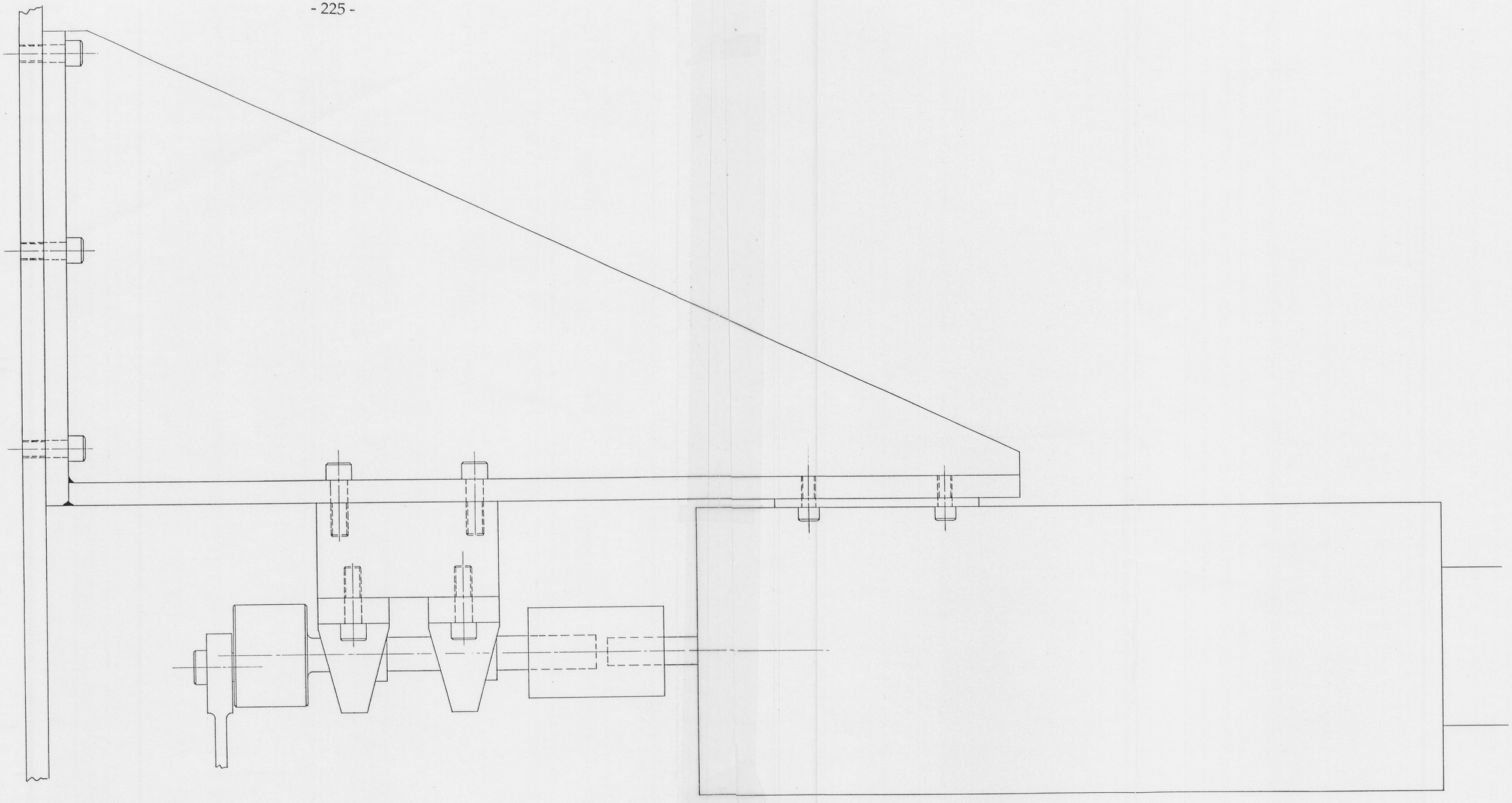

Figure F.3 Drawing of Oscillation Motor Mount and Coupling